

REPORT DOCUMENTATION PAGE

Form Approved
OMB No. 0704-0188

Public reporting burden for this collection of information is estimated to average 1 hour per response, including the time for reviewing instructions, searching existing data sources, gathering and maintaining the data needed, and completing and reviewing the collection of information. Send comments regarding this burden estimate or any other aspect of this collection of information, including suggestions for reducing this burden, to Washington Headquarters Services, Directorate for Information Operations and Reports, 1215 Jefferson Davis Highway, Suite 1204, Arlington, VA 22202-4302, and to the Office of Management and Budget, Paperwork Reduction Project (0704-0188), Washington, DC 20503.

1. AGENCY USE ONLY (Leave blank)		2. REPORT DATE March 18, 1997	3. REPORT TYPE AND DATES COVERED Final; 1 Oct. 89 - 15 May 96	
4. TITLE AND SUBTITLE Physics and Technology of III-V Pseudomorphic Structures			5. FUNDING NUMBERS PE61153N R&T#414s002	
6. AUTHOR(S) C. W. Tu				
7. PERFORMING ORGANIZATION NAME(S) AND ADDRESS(ES) Dept. of Electrical & Computer Engineering University of California, San Diego La Jolla, CA 92093-0407			8. PERFORMING ORGANIZATION REPORT NUMBER TU-ONR-97	
9. SPONSORING / MONITORING AGENCY NAME(S) AND ADDRESS(ES) Office of Naval Research Code 1114 800 North Quincy Street Arlington, VA 22217-5000			10. SPONSORING / MONITORING AGENCY REPORT NUMBER	
11. SUPPLEMENTARY NOTES				
12a. DISTRIBUTION / AVAILABILITY STATEMENT Approved for public release; Distribution Unlimited			12b. DISTRIBUTION CODE	
13. ABSTRACT (Maximum 200 words) We have shown that pseudomorphic InAsP on InP is a viable alternative to the conventional InGaAsP for long-wavelength optical-fiber communications. The layer thickness and composition are independently controlled in gas-source molecular beam epitaxy. We developed, for the first time, an in situ technique for composition calibration in growing InAsP by group III- and group V-induced intensity oscillations of reflection high-energy electron diffraction. By a systematic growth optimization procedure with respect to growth temperature, V/III incorporation ratio and substrate misorientation, high-quality InAsP/InP strained multiple quantum wells were successfully grown on both InP(111)B and (100) substrates. The valence-band offset was obtained from the best fit of a model calculation to the photoluminescence excitation spectra. Excellent electroabsorption and photocurrent spectra were obtained for 1.3 μm InAsP/InP MQW modulator structures. We have also developed a growth kinetic model for composition control on InGaAsP. In addition, besides pseudomorphic phosphide-base heterostructures on InP, we have obtained very good results from the use of a linearly graded buffer layer for growing lattice-mismatched phosphide-base heterostructures on GaAs substrates.				
14. SUBJECT TERMS InAsP, InGaAsP, GSMBE, strain, modulator, (111)B, band offset			15. NUMBER OF PAGES	
			16. PRICE CODE	
17. SECURITY CLASSIFICATION OF REPORT	18. SECURITY CLASSIFICATION OF THIS PAGE	19. SECURITY CLASSIFICATION OF ABSTRACT	20. LIMITATION OF ABSTRACT	

TABLE OF CONTENTS

List of Figures	iv
List of Tables	xii

I. Introduction

1.1 Motivation of studying InAsP/InP heterostructures	1
1.2 Brief survey of related studies	5
1.3 Overview of the final report	6
References	9

II *In situ* Composition Calibration for Mixed-Group-V Compounds by Group-V-Induced RHEED Oscillations

2.1 Introduction	12
2.2 Brief description of GSMBE	14
2.3 Group-V-induced RHEED oscillations	17
2.4 As incorporation behavior in $\text{GaAs}_{1-x}\text{P}_x$	23
2.4.1 <i>In situ</i> technique of determining the P composition	23
2.4.2 Dependence on the substrate temperature	28
2.4.3 Dependence on the growth under different strain states	31
2.5 <i>In situ</i> calibration of As composition in $\text{InAs}_x\text{P}_{1-x}$	33
2.6 <i>In situ</i> composition calibration in $\text{In}_{1-x}\text{Ga}_x\text{As}_y\text{P}_{1-y}$	38
2.7 Conclusion	41
References	43

III Growth and Structural Characterizations of InAsP/InP Strained Multiple Quantum Well Structures Grown on InP (100) and (111)B Substrates

3.1 Introduction	45
3.2 Strain limitation and critical layer thickness	47
3.2.1 Model calculations of the critical layer thickness	47
3.2.2 CLT determination by PL and TEM measurements	50
3.3 Growth of InAsP/InP strained multiple quantum wells on InP (100)	53
3.3.1 Typical growth conditions	53
3.3.2 Growth interruption and interface asymmetry	53
3.3.3 Approaches for composition control over a wide range	56

DTIC QUALITY INSPECTED 8

19970408 043

3.3.4	Structural characterizations for (100) InAsP/InP strained MQWs	58
3.4	Growth of InAsP/InP strained quantum wells on InP (111)B	59
3.4.1	Stoichiograph and miscut of the (111)B substrate	59
3.4.2	Optimization of the growth condition for homoepitaxial InP	60
3.4.3	Optimization of the growth condition for InAsP/InP heterostructures	65
3.4.4	Characterization (111)B InP epilayers	68
3.4.5	Characterization of (111)B InAsP/InP strained MQWs	71
3.5	Simulation of x-ray rocking curves	73
3.5.1	High-resolution x-ray rocking curves	73
3.5.2	Elastic deformation and anisotropy of the elastic tensor	74
3.5.3	Computer simulation and structural parameter determination	76
3.6	Conclusion	79
	References	80

IV Optical Properties of InAsP/InP Strained Quantum Wells Grown on InP (100) and InP (111)B Substrates

4.1	Introduction	82
4.2	Band structure and energy-level calculations	84
4.2.1	Envelope-function model	84
4.2.2	Strain-induced change of the band structure	86
4.2.3	Piezoelectric effect of (111) InAsP/InP strained quantum wells	89
4.2.4	Energy calculation of excitonic transitions	96
4.3	Optical characterization techniques	96
4.3.1	Photoluminescence measurements	96
4.3.2	Photoluminescence excitation measurements	98
4.3.3	Absorption measurements	100
4.4	Optical property of (111)B InAsP/InP strained quantum wells	106
4.4.1	PL spectra	106
4.4.2	Low-temperature absorption spectra	108
4.4.3	PLE spectra and valence band offset determination for (111) heterostructures	109
4.5	Screening of piezoelectric field in (111)B InAsP/InP strained quantum wells	114
4.5.1	Low-temperature PL measurements at various pumping densities	114
4.5.2	Field screening and blue energy shift	117
4.5.3	Deduction of the valence band anisotropy	121
4.6	Conclusion	122
	References	124

V Electrooptical Properties of (100) InAsP/InP Strained Quantum Wells

5.1	Introduction	127
5.2	Device principle, fabrication and measurement	129
5.2.1	Quantum-confined Stark effect and effective well-width model	129
5.2.2	Device processing technology	132
5.2.3	Electroabsorption and photocurrent spectra	136

5.3 Electroabsorption at 1.06 and 1.3 μm	137
5.3.1 $\text{InAs}_x\text{P}_{1-x}/\text{InP}$ MQWs for 1.3 μm waveguide modulators	137
5.3.2 Optical modulators at 1.06 μm	144
5.4 Effect of strain relaxation on electro-absorption properties	148
5.5 Conclusion	152
References	155
 Appendix A	
A kinetic model for As and P incorporation in III-V's	157
 Appendix B	
Lattice-mismatched structures with linearly graded Buffer Layers	167
 Appendix C	
List of Publications	180

List of Figures

1.1	Room-temperature bandgap of III-V semiconductor compounds vs. the lattice constant. This relation is shown by solid and dashed curves for ternary compounds with direct and indirect bandgap, respectively.	2
1.2	Calculated photon energies of room-temperature heavy-hole excitonic emissions based on the envelope-function model, as a function of As compositions in $\text{InAs}_x\text{P}_{1-x}/\text{InP}$ quantum wells.	3
2.1	Schematic diagram of the GSMBE setup.	17
2.2	Schematic diagrams of the cause of RHEED oscillations.	19
2.3	RHEED oscillations induced by In ($t_1 < t < t_2$) and As ($t_3 < t < t_4$). Note that the As-induced oscillations occurred on an In-rich surface caused by depositing excess In during $t_2 < t < t_3$. The incorporation rates of indium and arsenic can be determined, respectively, from the first and second part of the oscillations.	20
2.4	(a) The indium (InAs) growth rate as a function of the furnace temperature. The Arrhenius plot indicates the thermal effusion behavior of the furnace. The substrate temperature ($\sim 460^\circ\text{C}$) and the AsH_3 flow rate (3 sccm) are kept constant; (b) the As incorporation rate is shown as a function of the AsH_3 flow rate calibrated at the substrate temperature of 460°C for InAs grown on a thick InAs layer. The linear dependence implies that the In supply is infinite to the injected As on the surface during RHEED oscillations.	21
2.5	Typical group-V-limited RHEED intensity oscillations on a Ga-rich GaAs surface. The oscillation is induced by (a) As, and (b) As+P.	24
2.6	Phosphorus composition in $\text{GaAs}_{1-x}\text{P}_x$ as a function of the PH_3 flow-rate fraction. The data shown by open circles are determined from RHEED oscillations; the full circles represent the x-ray simulation data.	25
2.7	The phosphorus composition as a function of the V/III incorporation ratio. The solid marks represent the <i>ex situ</i> determined data; the open marks indicate the <i>in situ</i> determinations at the same corresponding phosphine flow fractions.	27

2.8	The phosphorus composition in GaAsP grown with the same hydride flow rates as a function of the substrate temperature. The curve through the data points is drawn to guide the eye.	29
2.9	X-ray rocking curves taken from GaAsP-containing multilayered heterostructures. (a) 15-period GaAs(40 Å)/GaAs _{1-x} P _x (40 Å) SLS grown on GaAs; (b) 15-period GaP(40 Å)/GaAs _{1-x} P _x (40 Å) SLS grown on GaP substrates. The computer simulation results show that the phosphorus incorporation does not depend on strain states.	32
2.10	The incorporation rate of (As+P), determined by group-V-induced RHEED oscillations during InAsP growth, as a function of the PH ₃ flow rate at several fixed AsH ₃ flow rates (0, 0.5, 0.75, 1 sccm). The lines through the data points are drawn to guide the eye.	34
2.11	The As composition in InAs _x P _{1-x} determined from x-ray rocking curve measurements versus the incorporation ratio of As to In obtained from RHEED oscillations.	35
2.12	The normalized As composition in InAs _x P _{1-x} (<i>ex situ</i> / <i>in situ</i>) as a function of the flow-rate ratio of PH ₃ to AsH ₃ at fixed AsH ₃ flow rates, 0.25 sccm (full circles) and 0.4 sccm (open circles).	37
2.13	An x-ray rocking curve of (004) diffraction from a 20-period In _{0.7} Ga _{0.3} As _{0.65} P _{0.35} (101.5 Å)/ InP(152 Å) MQW structure. Some satellite peaks are missing because of the intermixing at InGaAsP/InP interface.	40
3.1	The critical layer thickness of InAs _x P _{1-x} , pseudomorphically grown on InP, as a function of the As composition. The solid and dotted curves are for multiple and single epitaxial layers, respectively. The open and full squares represent strained and relaxed quantum wells, respectively, examined by PL measurements.	49
3.2	Number of periods for pseudomorphic growth of InAs _x P _{1-x} /InP strained MQWs as a function of the room-temperature emission wavelength. The solid and dotted curves are for multiple and single epitaxial layers, respectively. The open and full squares represent InAsP MQW layers without and with dislocations, examined by TEM images.	50
3.3	XTEM images taken from (a) HI06 and (b) HI11. Note that in (a) the misfit dislocations lie in the buffer layer; in (b) interfaces are sharp, uniform and free from dislocations.	52

3.4	The diagram of the shutter operation sequence for growing InAsP/InP MQW structures. The lower part indicates the growth of InAs _x P _{1-x} layer by short-period superlattices.	54
3.5	XTEM images from two InAs _x P _{1-x} /InP MQW structures. (a) for a sample grown with interruption; Asymmetry in the interfaces is evidenced by the darker contrast at the InAsP/InP interface. (b) for a sample grown without interruption (using two crackers); Sharp and symmetric interfaces are obtained.	55
3.6	High-resolution x-ray rocking curves with (400) diffraction taken from two highly strained (100) InAsP/InP MQW samples, with (a) from HI06 (lattice mismatch ~2.1%) and (b) from HI11 (lattice mismatch ~1.7%).	57
3.7	An XTEM microimage for an InAs _{0.5} P _{0.5} /InP strained MQW sample, in which the InAs _x P _{1-x} layer was grown with SPSL as resolved by the fine structures in the dark region of the picture.	58
3.8	Stereograph for a fcc cubic structure along the (111) pole.	61
3.9	Nomarski micrographs of the surface of 1 μm InP epilayers grown on InP (111)B substrates with misorientation of 0.5° toward <110> under different substrate temperatures and V/III incorporation ratios. (a) T _s =470 °C, V/III~1; (b) T _s =470 °C, V/III~3; (c) T _s =490 °C, V/III~1; and (d) T _s =490 °C, V/III~3.	62
3.10	RHEED oscillations during modulated phosphorus beam growth with different V/III incorporation ratios. The sequence of the shutter operation is also indicated.	64
3.11	Nomarski micrographs of surfaces of 15-period InAsP(80 Å)/InP(120 Å) strained MQW structures grown on InP (111)B substrates with various misorientations. (a) 0.5° off toward <110>; (b) 1° toward <110>; (c) 0.5° toward <211>; and (d) 1° toward <211>.	66
3.12	A symmetric (333) x-ray rocking curve taken from a 1 μm thick InP (111)B epilayer with 0.5° misorientation.	67
3.13	Low-temperature PL spectra taken from 1 μm thick homoepitaxial InP layers grown at T _s = 450, 470 and 490 °C. The FWHMs for these three samples are 5.3, 3.5 and 9.7 meV, respectively.	69
3.14	A typical x-ray rocking curve of a symmetric (333) diffraction from a 15-period InAs _{0.21} P _{0.79} (80 Å)/InP(120 Å) strained MQW structure. Intense and	

sharp satellite peaks can be seen up to the third order, and Pendellösung fringes appear on the wings of the substrate and adjacent satellite peaks.	70
3.15 XTEM micrographs taken from InAsP/InP MQWs grown on InP (111)B substrates with a 1° misorientation toward to (a) <110> direction, and (b) <100> direction. The inset of (b) shows the Nomarski microscopic picture of the surface morphology. Hatch lines are due to strain relaxation.	72
3.16 Schematic diagram of the diffraction configuration of the x-ray diffractometry.	73
3.17 (a) A high-resolution x-ray rocking curve and (b) a dynamic-theory simulation for a 15-period (100) InAs _{0.5} P _{0.5} (76 Å)/InP(162 Å) strained MQW structure. The best fit allows a precise determination of the arsenic composition and well and barrier layer thicknesses.	76
3.18 (a) An x-ray rocking curve from (111)B 15-period InAs _{0.21} P _{0.79} (80 Å)/InP(120 Å) strained MQWs in the vicinity of symmetric (333) diffraction. Satellite peaks and Pendellösung fringes show good crystalline quality. (b) A dynamical-theory simulation considering the anisotropy of the strain tensor in (111) orientation.	78
4.1 Schematic diagram of the tetragonal distortion of a strained InAsP layer grown on an InP substrate. The InAsP layer is biaxially strained, while there is no strain in the InP layer.	85
4.2 Schematic diagram of the band structure modification for InAs _{0.21} P _{0.79} /InP heterostructures pseudomorphically grown on InP (111)B and (100) substrates, respectively. The energy changes due to hydrostatic pressure, uniaxial stress and shear components are designated respectively.	89
4.3. The magnitude of the piezoelectric field in an InAs _x P _{1-x} /InP strained quantum well grown on an InP (111)B substrate.	91
4.4. Energy shift of the first electron, hh and lh levels in InAs _{0.21} P _{0.79} (80 Å)/InP(120 Å) strained MQWs under an electric field due to QCSE. The calculation is based on the effective well width model. Larger shifts are obtained from levels with smaller confined energies.	94
4.5 Energy shift of different hh subbands as a function of the applied electric field across the quantum well region. Significant difference of the energy shift is predicted. This result indicates that the energy shift of the higher subband excitonic transition is very small.	95

4.6	(a) Schematic diagram of PL setup; (b) Low-temperature PL spectrum taken from a 1.3 μm modulator structure consisting of 30-period $\text{InAs}_{0.4}\text{P}_{0.6}$ (92 Å)/ InP (138 Å) MQWs. Sharp and intense peak is attributed to the heavy-hole excitonic emission. The arrows in the figure indicate the calculated transition energies.	97
4.7	(a) Schematic diagram of PLE setup; (b) PLE spectra taken at 15 K for two highly-strained InAsP/InP MQW samples. Also shown are PL spectra measured at the same temperature. The labels refer to the identifications for spectral features and the vertical bars indicate calculated interband transitions using $Q_v=0.3$	99
4.8	(a) Schematic diagram of absorption setup; (b) Room-temperature absorption spectra from three InAsP/InP strained MQW samples. Very sharp absorption peaks are obtained at 1.06, 1.3 and 1.55 μm for these samples, respectively, indicative of their potential usefulness for optoelectronic devices.	101
4.9	Absorption spectra taken from a 1.3 μm modulator structure consisting of 30-period $\text{InAs}_{0.4}\text{P}_{0.6}$ (92 Å)/ InP (138 Å) MQWs at various temperatures. The narrower absorption peak at lower temperature is due to reduced thermal scattering. The energy bandedge shifts to higher energy, resulting in an increase of transition energy at low temperature.	103
4.10	The energy of the 1e-1hh excitonic transition as a function of the measuring temperature. The curve through the data points is the calculated temperature dependence of the bandgap energy of $\text{InAs}_{0.4}\text{P}_{0.6}$ interpolated from the known temperature coefficients of InAs and InP	104
4.11	Comparison of a photo-modulated transmission (PT) spectrum, transmission spectrum and the first-order derivative of a transmission spectrum for a $\text{InAs}_{0.21}\text{P}_{0.79}$ (100 Å)/ InP strained MQW structure taken at low temperature. It is apparent that the PT spectrum reveals the same information as the transmission derivative, yet the PT is a more sensitive technique.	105
4.12	Low-temperature PL spectra taken from two $\text{InAs}_{0.21}\text{P}_{0.79}$ (80 Å)/ InP (120 Å) strained MQW samples grown on InP (111)B and (100) substrates, respectively. Comparable emission intensity was obtained from these two samples. The slight broadening of the emission peak from (111) MQWs may be due to the internal QCSE.	107
4.13	Low-temperature absorption spectra from $\text{InAs}_{0.21}\text{P}_{0.79}$ (80 Å)/ InP (120 Å) strained MQWs grown on (a) (100), and (b) (111)B substrates. The different absorption behavior is believed to result from the internal QCSE in the (111) quantum structure.	108

4.14	PLE spectra taken at low temperature from $\text{InAs}_{0.21}\text{P}_{0.79}(80 \text{ \AA})/\text{InP}(120 \text{ \AA})$ strained MQWs grown on (a) (100) and (b) (111)B substrates. Very distinct transitions from higher subbands, and parity-forbidden transitions are observed. The assignments for the transitions are based on an energy-level calculation from the envelope-function model and the effective well width model [for the (111) quantum well only]. The vertical bars indicate calculated results.	110
4.15	Energy difference between 2e-2hh and 1e-1hh, and between 1e-1lh and 1e-1hh excitonic transitions calculated as a function of Q_v . The best fit between experimental and theoretical results can be obtained for $Q_v \sim 0.3$	111
4.16	Schematic diagram of the band lineup for strained InAsP layers grown on (111)B and (100) substrates with respect to the InP layer. The energy reference of the InAsP bandedges is obtained from Fig. 4.2.	116
4.17	Low-temperature PL spectra taken from a (111) $\text{InAsP}(100 \text{ \AA})/\text{InP}$ single QW under different pumping density. The PL peaks shift to higher energy and broaden in linewidth as the pumping density increases.	115
4.18	Schematic diagram of the screening effect of the piezoelectric field by photo-generated carriers during PL measurements at high pumping power. A flat band condition can be reached when the built-in field is screened entirely.	116
4.19	Emission energy shift as a function of the pumping density for a highly strained $\text{InAsP}(100 \text{ \AA})/\text{InP}$ QW with a lattice-mismatched of $\epsilon_0 \sim 0.9\%$. The energy shift is as high as 35 meV when the sample was pumped with a very high density.	118
4.20	The FWHM of the PL peaks measured from for an InAsP/InP strained quantum well as a function of the pumping density.	119
4.21	Emission energy shift as a function of the pumping density for a slightly strained $\text{InAsP}(100 \text{ \AA})/\text{InP}$ QW with a lattice-mismatched of $\epsilon_0 \sim 0.65\%$. A saturation of the energy shift ($\sim 13.8 \text{ meV}$) indicates a flat-band condition.	120
5.1	(a) Schematic diagram of electroabsorption effect in MQWs. The left figure shows quantum wells formed by conduction and valence bandedges. The energy levels of the ground states for electrons and holes are shown, along with the wavefunction envelopes. The right figure shows these items when an electric field is applied perpendicular to the quantum well layers. (b) Schematic diagram of the absorption spectra from the corresponding quantum wells with and without field. Changes of the absorption energy, intensity and the line shape are due to QCSE.	130

5.2	Universal curve for the energy of the first confined state in an infinite quantum well in the presence of a uniform electric field perpendicular to the well. The variables are energy and electric field normalized to those of the ground state.	131
5.3	(a) Schematic diagram of the cross section of a <i>p-i-n</i> ring diode consisting of 10 periods of InAsP/InP strained MQWs in the intrinsic layer region. (b) The top view for the <i>p</i> -type ohmic contact of a ring diode.	133
5.4	Flow chart of the processing procedure for fabricating <i>p-i-n</i> ring diodes.	134
5.5	I-V curve for a 1.3 μm InAsP/InP strained MQWs <i>p-i-n</i> diode modulator. Sharp turn-on under forward bias and hard breakdown under reverse bias suggest good electrical characteristics.	135
5.6	EA spectra taken at various reverse biases for a 1.3 μm modulator structure. The sharp excitonic transition shows a significant red energy shift, a reduction of the absorption intensity, and a broadening of the linewidth due to QCSE and field ionization effect.	138
5.7	Energy shift from the heavy-hole excitonic absorption as a function of the electric field across the quantum well. The calculated results are illustrated for the shift of electron (dashed curve) and heavy-hole (dotted curve) subbands, as well as for the energy of excitonic transitions (solid curve). A good agreement between theoretical and experimental (solid circles) results is obtained.	139
5.8	(a) Change of the absorption coefficient as a function of the detuning energy with respect to the zero-field excitonic absorption; (b) $\Delta\alpha/\alpha_0$ as a function of the detuning energy. Both $\Delta\alpha$ and $\Delta\alpha/\alpha_0$ have to be maximized for waveguide modulator applications.	142
5.9	$\Delta\alpha/F^2$ as a function of the detuning energy with various $\Delta\alpha/\alpha_0$. A large magnitude of $\Delta\alpha/F^2$ represents a high modulator depth with a small driving power.	143
5.10	Electro-absorption spectra taken at various reverse biases for a 1.06 μm InAsP/InP strained MQW modulator. The sharp excitonic transition shows a significant red energy shift, a reduction of the absorption intensity, and a broadening of the linewidth due to QCSE and field ionization effect.	144
5.11	Energy shift from the heavy-hole excitonic absorption as a function of the electric field across the quantum well for an InAs _{0.19} P _{0.81} (100 Å)/InP (120 Å) MQW structure. The calculated results are illustrated for the shift of	

electron (dashed curve) and heavy-hole (dotted curve) subbands, as well as for the energy of excitonic transitions (solid curve). A good agreement between theoretical and experimental (solid circles) results is obtained.	145
5.12 $\Delta T/T$ data taken at various modulation voltages for a 1.06 μm $\text{InAs}_{0.19}\text{P}_{0.81}(100 \text{ \AA})/\text{InP} (120 \text{ \AA})$ MQW modulator.	147
5.13 XTEM micrograph for a 50-period $\text{InAs}_{0.39}\text{P}_{0.61}(100 \text{ \AA})/\text{InP} (120 \text{ \AA})$ MQW structure for a 1.3 μm modulator.	148
5.14 EA spectra from two 1.3 μm modulators consisting of $\text{InAs}_{0.39}\text{P}_{0.61}(100 \text{ \AA})/\text{InP} (120 \text{ \AA})$ MQWs (a) with 20 periods, and (b) with 50 periods.	149
5.15 Change of the absorption coefficient from two 1.3 μm modulators consisting of $\text{InAs}_{0.39}\text{P}_{0.61}(100 \text{ \AA})/\text{InP} (120 \text{ \AA})$ MQWs (a) with 20 periods, and (b) with 50 periods. Reduced $\Delta\alpha$ [compared to Fig. 5.8(a)] is observed for the structure with more number of periods, in which a more severe strain relaxation is expected.	150
5.16 Energy shift of the absorption peak as a function of the electric field across the quantum well for a 1.3 μm $\text{InAsP}(100 \text{ \AA})/\text{InP} (120 \text{ \AA})$ MQW modulator. The calculated results are illustrated for the shift of electron (dashed curve) and heavy-hole (dotted curve) subbands, as well as for the energy of excitonic transitions (solid curve). Experimental results from a 20- and 50-period MQWs are denoted with solid and open circles, respectively.	152
6.1 Hall mobility vs. InP mole fraction for n -type InAsP. Experimental points were measured from strain relaxed InAsP layers at 0.5 T (from Ref. 1).	162
6.2 EA spectra from a 1.3 μm $\text{InAs}_{0.4}\text{P}_{0.6}(93 \text{ \AA})/\text{InP} (142 \text{ \AA})$ strained MQW modulator. The absorption peak shows no energy shift under bias.	164

List of Tables

3.1 Description of the sample structures.	53
4.1 Physical constants of InP and InAs used in the present calculation.	92
4.2 Description of the sample structures.	102

Chapter I

Introduction

1.1 Motivation of studying $\text{InAs}_x\text{P}_{1-x}/\text{InP}$ heterostructures

Research on semiconductor quantum wells and superlattices was initiated with a proposal by Esaki and Tsu[1] in 1969 for a one-dimensional potential structure "engineered" with epitaxy of alternating ultrathin layers. At the same time, the advent of a new growth technique, molecular beam epitaxy (MBE), opened the way to the growth of semiconductor heterostructures, with an accuracy of atomic-layer thickness control.[2] These quantum structures were quickly realized to be extremely useful for various electronic and optoelectronic devices.[3] In fact, materials, physics and device studies of semiconductor quantum structures have been the most attractive research activities for the last three decades.[3] III-V semiconductor compounds provide a great selection of bandgap, lattice constant, as well as various physical properties. Figure 1.1 shows the room-temperature bandgap of III-V semiconductor compounds vs. lattice constant. Solid and dashed curves show this relationship for ternary compounds with direct and indirect bandgaps, respectively. These materials possess, in many aspects, superior electrical and optical properties to the elemental semiconductors, Si and Ge. The bandgap can be tuned by choosing different materials or different composition of the ternary and quaternary compounds. However, for good epitaxial growth, the heterostructure constituents should have the same lattice structures and constants. This limits the choices of material combinations. In 1974, it was demonstrated that an epitaxial growth can be achieved pseudomorphically from lattice-mismatched materials with the lattice mismatch accommodated by elastic strain provided that the strained layer is grown within a

thickness limit.[4] The choice for heterostructure materials has thus been greatly expanded.

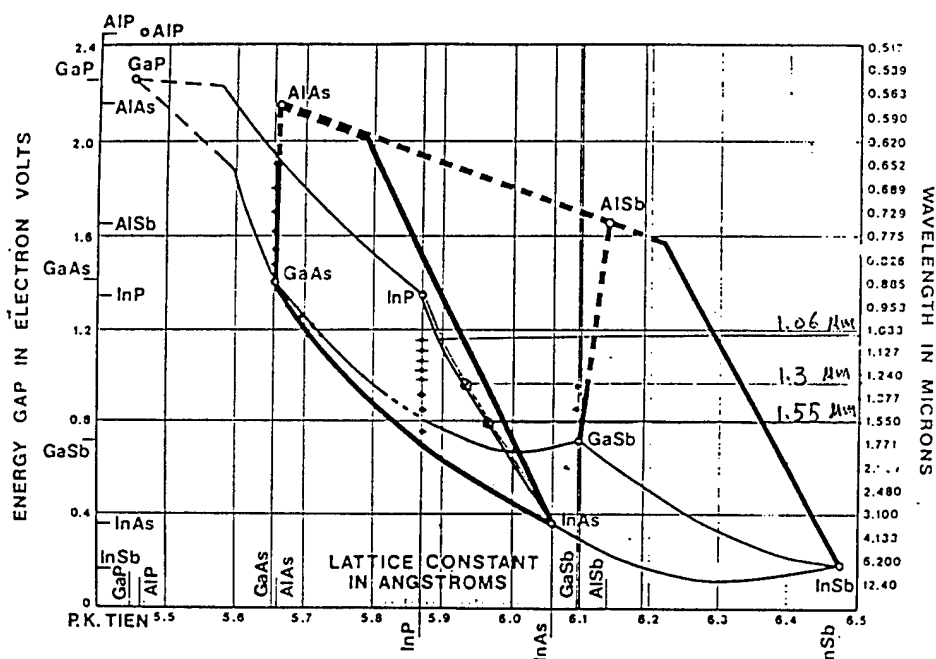


FIG. 1.1 Room-temperature bandgap of III-V semiconductor compounds vs. the lattice constant. This relation is shown by solid and dashed curves for ternary compounds with direct and indirect bandgap, respectively.

One class of the many novel electronic and optoelectronic devices made of semiconductor quantum structures includes optical emitters, modulators and detectors operated at 1.3 μm . This is the optimum wavelength for minimum dispersion in several varieties of optical fibers that are the transmission medium for modern fiberoptic

communication systems. Quaternary compound $\text{In}_{1-y}\text{Ga}_y\text{As}_x\text{P}_{1-x}$ grown on InP is used for these long-wavelength optoelectronic devices because its fundamental band gap is suitable for devices operated between 0.9 and 2.0 μm . However, the composition control of the quaternary layers can be difficult, particularly when a specific absorption wavelength has to be obtained.[6] The quaternary-alloy quantum-well layer also possesses a high level of alloy disorder.[7] Another material system for 1.3 μm emission is InGaAlAs/InAlAs quantum well structures[8] lattice-matched to InP substrates. In addition to the above difficulties, this Al-containing compound has an additional problem of deterioration of the cleaved facets due to oxidation.

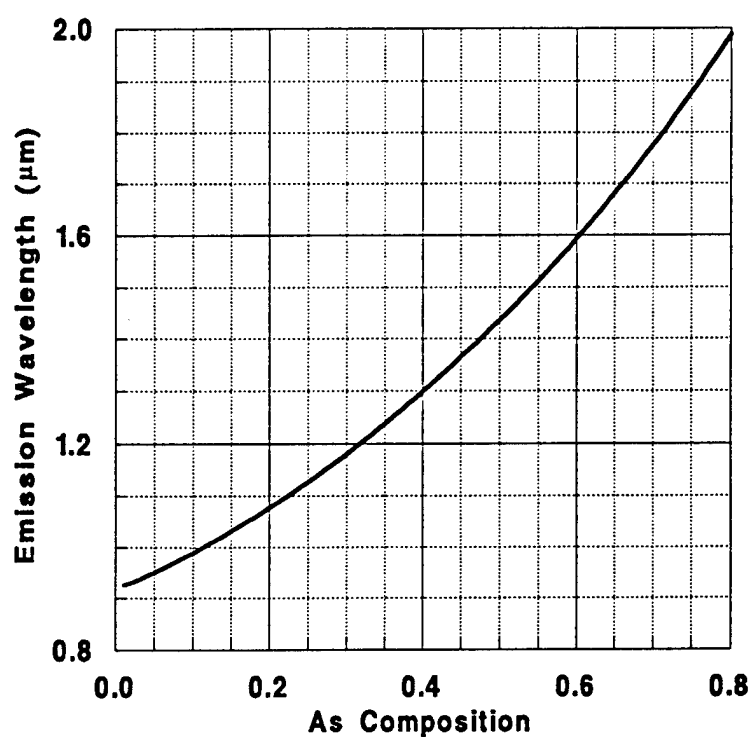


FIG. 1.2 Calculated photon energies of room-temperature heavy-hole excitonic emission based on the envelope-function model, as a function of As compositions for $\text{InAs}_x\text{P}_{1-x}/\text{InP}$ quantum wells.

One objective for the study performed as part of this dissertation is to explore a material system which can be a good alternative to these quaternary compounds for 1.3 μm waveguide modulators. These devices provide high-speed light switching and modulation based on the change of the absorption coefficient of the quantum wells under a modulated electrical bias.[9] Typical structures consist of multiple quantum well (MQW) with a well width of 100 Å. With the quantum-size effect taken into account, the well material should have a fundamental bandgap of about 1.35 μm (~0.92 eV) for 1.3 μm emission. As shown in Fig. 1.1, $\text{In}_{0.7}\text{Ga}_{0.3}\text{As}_{0.65}\text{P}_{0.35}$ and $\text{In}_{0.53}\text{Al}_{0.09}\text{Ga}_{0.38}\text{As}$ are two quaternary quantum well materials, which are lattice matched to InP, with a fundamental bandedge emission at 1.35 μm (or 0.92 eV). In addition, two strained ternary compounds, $\text{In}_{0.38}\text{Ga}_{0.62}\text{As}$ and $\text{InAs}_{0.4}\text{P}_{0.6}$, can be alternative materials. $\text{InAs}_{0.4}\text{P}_{0.6}$, however, may be more favorable since the layer thickness and composition of this $\text{IIIV}_x\text{V}_{1-x}$ compound can be controlled independently in gas-source molecular beam epitaxy (GSMBE).[10] This can greatly simplify the tuning procedure of the emission from a quantum well to a specific wavelength.[10] The energy levels confined in a 100-Å $\text{InAs}_x\text{P}_{1-x}/\text{InP}$ quantum well[11] was calculated as a function of the As composition in $\text{InAs}_x\text{P}_{1-x}$. As shown in Fig. 1.2, an excitonic emission can be obtained at 1.3 μm for an $\text{InAs}_{0.4}\text{P}_{0.6}$ (100 Å)/InP quantum well structure. Moreover, the emissions at 1.06 and 1.55 μm could also be obtained with quantum structures with $x=0.2$ and 0.6, respectively. These wavelengths are also very important for optical information processing[12] and long-haul fiberoptic communication.[9]

Quantum-well modulator devices operate on the basis of modulating optical absorption by applying an electric field due to the quantum-confined Stark effect.[9] Strained heterostructures grown on (111)B substrates have been demonstrated to possess a *built-in electric field* due to the piezoelectric effect.[13] Some devices utilizing this internal piezoelectric field have unique characteristics. Therefore, we also extended our

study to $\text{InAs}_x\text{P}_{1-x}/\text{InP}$ quantum structures grown on InP (111)B substrates. A successful synthesis of $\text{InAs}_x\text{P}_{1-x}/\text{InP}$ (111)B quantum structures can be expected to provide more flexibility in designing novel devices.

In spite of these potential device applications, research has not been conducted extensively on some of the very important issues on growth, structural and optical characteristics of InAsP/InP heterostructures; for instance, how to achieve an easy and repeatable composition control for $\text{IIIIV}_x\text{V}_{1-x}$ compounds, how good the structural and optical qualities can be, can this quantum structure be superior for some device applications, and how good the heterostructure on InP (111)B can be. Answers to these questions are apparently very important and valuable to the studies of materials and devices. This motivated our research presented in this dissertation.

1.2 Brief survey of related studies

$\text{InAs}_x\text{P}_{1-x}$ bulk materials received attention primarily because of the advantageous transport property.[14,15] Thick strain-relaxed layers grown by metalorganic chemical vapor deposition (MOCVD)[15,16] and MBE[17] were used for studying As incorporation in InAsP and the electrical and optical properties of bulk $\text{InAs}_x\text{P}_{1-x}$. InAsP/InP heterostructures with good structural and optical properties were first demonstrated in 1988 by MOCVD.[18] In 1991, Woodward[12] and we ourselves[10,19] reported studies on this quantum structure, grown by GSMBE, for device applications. Since then a variety of device and fundamental studies have been presented. Optical modulators operated at $1.06\text{ }\mu\text{m}$ [12,20] and $1.3\text{ }\mu\text{m}$ [21], as well as $1.3\text{ }\mu\text{m}$ lasers[22], have been fabricated. Furthermore, magneto-transport properties of two-dimensional electron systems were also investigated.[23]

Epitaxial growth on (111)B substrates is and has been an interesting and potentially rewarding research topic for materials science,[24,25] physics[13] and device

applications. Mirror-like surfaces were achieved either by controlling growth in a step-flow mode[26] on vicinal substrates, or by migration-enhanced epitaxy,[27] or by carefully choosing growth conditions.[28] A reduction of threshold current for a laser,[29] enhanced QCSE shift for a modulator structure,[30] and frequency doubling of the laser emission[31] are among the novel device studies for (111)B GaAs/AlGaAs quantum structures. More interestingly, an internal electric field can be produced in strained (111)B quantum structures due to the piezoelectric effect.[13,32] This makes possible novel nonlinear optical devices, such as self electrooptic-effect devices (SEEDs)[33] and optical switches using the inherent large optical nonlinearity.[34] Work to date in the study of (111)B heterostructures has been primarily limited to structures grown on GaAs substrates. Little has been accomplished for the epitaxial growth on InP (111)B substrates.[35]

1.3 Overview of this final report

The emphasis of this final report is on the growth and optical properties of $\text{InAs}_x\text{P}_{1-x}$ /InP quantum wells grown on InP (100) and (111)B substrates.

The composition control is the first important issue for material synthesis, particularly because of a preferential incorporation of As in the $\text{InAs}_x\text{P}_{1-x}$ over P. In Chapter 2, we present a comprehensive study of the As and P incorporation behavior in GaAsP, InAsP, and InGaAsP as a function of the group-III elements, substrate temperature and different strain states. We developed an *in situ* composition determination procedure for these materials using group-V-induced intensity oscillations of reflection high-energy electron diffraction (RHEED). In particular, the calibration for the As composition in $\text{InAs}_x\text{P}_{1-x}$ is simply achieved by controlling the incorporation-rate ratio of As over In.

Chapter 3 describes growth and structural characterization of InAsP/InP strained multiple quantum wells (MQWs) grown on InP (100) and (111)B substrates. The comprehensive discussion includes (1) calculation and determination of the critical layer thickness for pseudomorphic growth; (2) different approaches to controlling the As composition in $\text{InAs}_x\text{P}_{1-x}$ over a wide range; (3) optimization of growth conditions for epitaxial growth on InP (111)B substrates with respect to growth temperature, V/III incorporation ratio, and substrate misorientation; and (4) structural characterizations by transmission electron microscopy and x-ray rocking curve measurements, along with computer simulations. The results presented in this chapter show our samples possessing excellent material quality and precise structural parameters, which are essential for interpreting optical properties presented in Chapters 4 and 5.

In Chapter 4, optical properties of (100) and (111)B InAsP/InP quantum wells are examined by various optical techniques to resolve subband excitonic transitions. Excellent optical properties are evidenced by sharp and intense excitonic transitions. A comparative study for (100) and (111)B quantum structures reveal the significant difference of spectral signatures in these two substrate orientations. The difference is well accounted for by considering the valence band anisotropy, strain-induced band structure modulation and the piezoelectric effect in the (111)B quantum wells. The valence band discontinuity is determined from the best fit of the theoretical calculation to the experimental result. A direct evidence of the existence of the piezoelectric field in (111)B InAsP/InP quantum wells is also presented by photoluminescence measurements with various pumping densities. An identification of the complete screening of the piezoelectric field allows an extraction of the heavy-hole effective mass along [111]. The theoretical and experimental examinations of optical properties of InAsP/InP strained quantum wells allow the determination of the band discontinuity and hole effective mass

and provide a better understanding of the quantum-size effect in $\text{InAs}_x\text{P}_{1-x}/\text{InP}$ quantum wells.

The first demonstration of the electroabsorption (EA) property of a $1.3\ \mu\text{m}$ InAsP/InP strained MQW modulator will be given in Chapter 5. In spite of the strain limitation, this material structure has shown excellent EA property with a significant red shift of the absorption peak and a large change of the absorption coefficient under a reverse bias due to QCSE. The energy shift is well accounted for in the effective well-width model. With the superior EA property to the more complex quaternary materials, $\text{InGaAsP}/\text{InP}$ and $\text{InGaAlAs}/\text{InAlAs}$ MQW's, InAsP/InP strained MQW's are promising for $1.3\ \mu\text{m}$ waveguide modulators. Furthermore, a correlation of EA with structural properties of MQW structures with different numbers of periods shows that the strain relaxation can degrade the EA property by having a reduced energy shift and a smaller absorption coefficient. The InAsP/InP strained MQW structure is also demonstrated for $1.06\ \mu\text{m}$ spatial light modulators.

Finally, included in Appendix A are two papers on our growth kinetic model for As and P incorporation behaviors in GaAsP and InGaAsP grown by gas-source MBE. Appendix B contains four papers on the use of linearly graded buffer layers for lattice-mismatched growth. In one case we grew a green light-emitting InGaP diode structure on a GaP substrate, and in other cases we investigated an InGaAs or InGaP compositionally graded buffer layer for phosphide-based heterostructures. Appendix C lists a total of 43 publications.

References

- [1] L. Esaki and R. Tsu, IBM J. Res. Dev. **14**, 61 (1970).
- [2] A. Y. Cho, J. Appl. Phys. **41**, 2780 (1970); **42**, 2074 (1971); and Appl. Phys. Lett. **19**, 467 (1971).
- [3] For reviews, see for example, IEEE J. Quantum Electron. **QE-22**, 1609-1915 (1986); Semicon. and Semimet. vol 24, edited by R. Dingle, (Academic, San Diego, 1987).
- [4] J. W. Matthews and A. E. Blakeslee, J. Cryst. Growth **27**, 118 (1974).
- [5] H. C. Casey, Jr. and M. B. Panish, *Heterostructure Lasers*, (Academic, New York, 1978).
- [6] M. B. Panish, Prog. Cryst. Growth Charact. **12**, 1 (1986), and M. B. Panish and H. Temkin, Annu. Rev. Mater. Sci. **19**, 209 (1989).
- [7] T. H. Chiu, J. E. Zucker, and T. K. Woodward, Appl. Phys. Lett. **59**, 3452 (1991).
- [8] A. N. Cheng *et al.* personal communications.
- [9] T. H. Wood, J. Light. Tech. **6**, 743 (1988), and references therein.
- [10] H. Q. Hou, C. W. Tu, and S. N. G. Chu, Appl. Phys. Lett. **58**, 2954 (1991).
- [11] H. Q. Hou, T. P. Chin, B. W. Liang, and C. W. Tu, Mat. Res. Soc. Symp. Proc. **228**, 231 (1992).
- [12] T. K. Woodward, T. Sizer, and T. H. Chiu, Appl. Phys. Lett. **58**, 1366 (1991).
- [13] D. L. Smith and C. Mailhot, Solid State Commun. **57**, 919 (1986), and Phys. Rev. Lett. **58**, 1264(1987).
- [14] A. El-Sabbathy, A. R. Adams, and M. L. Young, Solid State Electron. **21**, 83 (1987).
- [15] P. J. Wang and B. W. Wessels, Appl. Phys. Lett. **44**, 766 (1984).
- [16] T. Fukui and N. Kobayashi, J. Cryst. Growth, **71**, 9 (1985).
- [17] W. T. Tsang, J. Appl. Phys. **55**, 2901 (1984).

- [18] P. J. Wang and B. W. Wessels, *Superlattices and Microstructures* **4**, 251 (1988); K. Huang and B. W. Wessels, *J. Cryst. Growth* **92**, 547 (1988), and *J. Appl. Phys.* **60**, 4342 (1986); and R. P. Schneider, Jr. D. X. Li, and B. W. Wessels, *J. Electrochem. Soc.* **136**, 3490 (1989).
- [19] H. Q. Hou and C. W. Tu, *J. Electron. Mater.* **21**, 137 (1992).
- [20] T. K. Woodward, T. H. Chiu and T. Sizer, *Appl. Phys. Lett.* **60**, 2846 (1992).
- [21] H. Q. Hou, A. N. Cheng, H. H. Wieder, W. S. C. Chang, and C. W. Tu, *Appl. Phys. Lett.* **63**, Sept. 27 (1993).
- [22] Y. Imajo, A. Kasukawa, T. Namegaya, and T. Kikuta, *Appl. Phys. Lett.* **61**, 2506 (1992).
- [23] W. -P. Hong, R. Bhat, J. Hayes, F. DeRosa, M. Leadbeater, and M. Koza, *Appl. Phys. Lett.* **60**, 109 (1992); and D. Yang, P. K. Bhattacharya, W. P. Hong, R. Bhat, and J. R. Hayes, *J. Appl. Phys.* **72**, 174 (1992).
- [24] A. Y. Cho, *J. Appl. Phys.* **41**, 2780 (1970).
- [25] L. Vina and W. I. Wang, *Appl. Phys. Lett.* **48**, 36 (1986).
- [26] K. Tsutsui, H. Mizukami, O. Ishiyama, S. Nakamura, and S. Furukawa, *Jpn. J. Appl. Phys.* **29**, 468 (1990).
- [27] Y. Takano, Y. Kanaya, T. Orihaya, K. Pak, and H. Yonezu, *J. Cryst. Growth* **102**, 343 (1990).
- [28] P. Chen, K. C. Rajkumar, and A. madhukar, *Appl. Phys. Lett.* **58**, 1771 (1991).
- [29] T. Hayakawa, K. Takahashi, M. Kondo, T. Suyama, S. Yamamoto, and T. Hijikata, *Jpn. J. Appl. Phys.* **26**, L302 (1987).
- [30] Y. Kajikawa, M. Hata, N. Sugiyama, and Y. Katayama, *Phys. Rev. B* **42**, 9540 (1990); Y. Kajikawa, N. Sugiyama, T. Komijoh, Y. Katayama, *Jpn. J. Appl. Phys.* **28**, L1022 (1989).

- [31] E. A. Caridi, T. Y. Chang, K. W. Goossen, and L. F. Eastman, *Appl. Phys. Lett.* **56** 659 (1990).
- [32] D. Vakhshoori, R. J. Fischer, M. Hong, D. L. Sivco, G. J. Zydzik, S. N. G. Chu, and A. Y. Cho, *Appl. Phys. Lett.* **59**, 896 (1991).
- [33] K. W. Goossen, E. A. Caridi, T. Y. Chang, J. B. Stark, D. A. B. Miller, and R. A. Morgan, *Appl. Phys. Lett.* **56**, 715 (1990).
- [34] I. Sela, D. E. Watkins, B. K. Laurich, D. L. Smith, S. Subbanna, and H. Kroemer, *Phys. Rev. B* **43**, 11884 (1991).
- [35] K. Nishi and T. Anan, *J. Appl. Phys.* **70**, 5004 (1991).

Chapter II

In situ Composition Calibration for Mixed-Group-V Compounds by Group-V-Induced RHEED Oscillations

2.1 Introduction

Phosphide-based semiconductors, such as $\text{In}_{1-x}\text{Ga}_x\text{As}_y\text{P}_{1-y}$, as well as the end member ternary alloys $\text{GaAs}_{1-x}\text{P}_x$, $\text{InAs}_x\text{P}_{1-x}$, $\text{In}_x\text{Ga}_{1-x}\text{As}$, and $\text{In}_x\text{Ga}_{1-x}\text{P}$, are useful materials for electronic and optoelectronic device applications. Among these materials, InGaAsP/InP [1-3] and strained InAsP/InP [4-6] quantum well structures are of great importance for long-wavelength optoelectronic applications, because the fundamental bandgaps of $\text{In}_{1-x}\text{Ga}_x\text{As}_y\text{P}_{1-y}$ and $\text{InAs}_x\text{P}_{1-x}$ can be tuned to achieve bandedge emissions from 0.9 to 2 μm . [1] This range includes the optimum wavelengths for minimum dispersion and minimum absorption loss in several varieties of optical fibers that are the transmission media for modern fiberoptic communications systems. Various kinds of state-of-the-art light-emitting, modulating and detecting devices made of the $\text{In}_{1-x}\text{Ga}_x\text{As}_y\text{P}_{1-y}/\text{InP}$ material system have been demonstrated. [3] Previously, the growth of phosphorus-containing materials have been mainly accomplished by liquid phase epitaxy (LPE), vapor phase epitaxy (VPE), and metalorganic chemical vapor deposition (MOCVD), but not by molecular beam epitaxy (MBE).

MBE possesses a unique ability to prepare abrupt interfaces at heterojunctions, and extremely abrupt doping profiles and layer-thickness control down to the monolayer range. Consequently, this capability permits us to engineer the band structure by changing the alloy composition, the layer thickness, or the doping levels. By using As_2 and P_2 from cracked gaseous hydrides, arsine (AsH_3) and phosphine (PH_3), in an MBE

system, we can grow arsenides, phosphides and mixed-group-V compounds. However, achieving precise composition control in mixed group-V compounds, e.g., the quaternary $\text{In}_{1-x}\text{Ga}_x\text{As}_y\text{P}_{1-y}$, has proven to be difficult[3] owing to the different incorporation behavior of As and P.[7] Furthermore, this incorporation behavior also depends on group-III elements, since the As incorporation is different in GaAsP and InAsP.[8,9] There is no simple relation between gaseous flows and solid-phase compositions of the group-V elements.[10] The arsenic composition in $\text{In}_{1-x}\text{Ga}_x\text{As}_y\text{P}_{1-y}$ reported so far has been determined by composition calibrations with x-ray diffraction, optical and other *ex situ* measurements for thick as-grown layers. Two composition parameters in $\text{In}_{1-x}\text{Ga}_x\text{As}_y\text{P}_{1-y}$ have to be determined by at least two independent methods. Based on these *ex situ* calibrations, the data are then fed back to fine tune the growth parameters in order to obtain the desired compositions. It is very important, therefore, to develop an *in situ* technique for composition calibration.

To determine the composition of mixed group-III alloys, on the other hand, intensity oscillations of reflection high-energy electron diffraction (RHEED)[11] are extensively used. By measuring the growth rates of different group-III elements, the composition can be obtained readily. However, the RHEED technique cannot be simply applied to determine the As composition in mixed-group-V compounds, such as InAsP, since its growth rate is governed only by the In beam flux under normal growth conditions (group-V rich) with an arsenic and/or phosphorus over pressure. In 1984, Neave *et al.*[12] reported a modified RHEED oscillation technique to determine the As incorporation rate. They observed RHEED oscillations on a Ga-rich GaAs surface, where the oscillation period, or "growth rate", is controlled by the As flux. Hereafter, we will call this RHEED technique as group-V-induced RHEED oscillations.

In this chapter, we describe a technique for composition control of mixed-group-V compounds by group-V-induced RHEED oscillations. A systematic study is presented

on the incorporation behavior of As and P with In and Ga in gas-source molecular beam epitaxy (GSMBE). The As composition in $\text{GaAs}_{1-x}\text{P}_x$ and $\text{InAs}_x\text{P}_{1-x}$ can be controlled by an *in situ* incorporation-rate calibration. The viability of this *in situ* technique was verified by extensive *ex situ* composition determinations. Combining the knowledge for *in situ* composition calibration of both $\text{InAs}_x\text{P}_{1-x}$ and $\text{GaAs}_{1-x}\text{P}_x$, we were able to determine the composition in quaternary $\text{In}_{1-x}\text{Ga}_x\text{As}_y\text{P}_{1-y}$. This chapter is organized as follows. A brief description is given of the GSMBE technology, and of our GSMBE setup; general growth conditions will be presented in Section 2. In Section 3 the group-V-induced RHEED oscillations will be described as a method for determining the As or P incorporation rate. The *in situ* technique for composition control for $\text{GaAs}_{1-x}\text{P}_x$ is described in Section 4; and that applied to $\text{InAs}_x\text{P}_{1-x}$ in Section 5. We then briefly introduce the implementation of the As and P incorporation studies to composition control of the quaternary $\text{In}_{1-x}\text{Ga}_x\text{As}_y\text{P}_{1-y}$ in Section 6. In Section 7 a summary of this work will be given as a conclusion.

2.2 Brief description of GSMBE

During the past two decades there has been a parallel development in the physics and device applications of heterostructures and in the growth of a variety of semiconductor heterostructure materials. Epitaxy methods have provided new degrees of freedom for basic research and device development. Achievement in device studies, such as the first success of heterostructure lasers,[13] in turn provided a powerful incentive to improve the epitaxial growth process in thickness, composition, doping profile, and more abrupt interfaces for more complex structures. MBE is an advanced and versatile technique for semiconductor thin film preparation. It is based on the thermal evaporation of highly pure elemental sources in an ultra-high vacuum chamber ($\sim 10^{-10}$ torr).

Tremendous efforts, with Cho paving the way,[14] have been made towards developing MBE into a practical epitaxy technology for growing high-quality materials.

However, the reproducible growth of high-quality P-containing compounds is not among the many achievements of the conventional MBE. Though a pioneering MBE growth of GaAsP was carried out by Arthur and Lepore by using a solid effusion source of phosphorus,[15] the result was not satisfactory. A major difficulty arose because the elemental phosphorus source, which initially consists of red phosphorus, contains a mixture of allotropic forms. Each allotropic form has a different vapor pressure, and the amount present depends on the subsequent thermal history of the effusion cell. A further severe difficulty is that the low incorporation efficiency of P_4 necessitates a very high phosphorus pressure (such as $P_4/In \sim 100$) to maintain a good surface morphology.[16] This in turn leads to a short life time of the source and a very large buildup of flammable white phosphorus in the MBE chamber. Worst of all, the large capacity and low vaporization temperature of the solid arsenic and phosphorus sources result in a poor conductivity and slow thermal response. Therefore, it is very difficult to achieve the necessary control over the ratio of As to P by using solid phosphorus.[10,15,16]

The gas-source method was reported by Panish in 1980 with the intention of growing InGaAs(P)/InP heterostructures.[17] The atomic beams of the group-III elements were generated, as in conventional MBE, by evaporation of Ga and In from effusion cells. However, the arsenic and phosphorus beams were generated as a result of the decomposition of AsH_3 and PH_3 through a high-temperature cracker. Thermally cracked AsH_3 and PH_3 can provide high purity As_2 and P_2 beams,[18] and the arsenic and phosphorus fluxes can be controlled precisely and conveniently by controlling the flow rates of AsH_3 and PH_3 with electronic mass-flow controllers or controlling the upstream pressure of a leak valve with a baratron. The switching and changing of the gas stream can be very fast and stable by a run-vent technique, in which the gas flow is

temporarily directed to an exhaust line when the flux is not in use for growth.[18] The only drawback for using AsH_3 and PH_3 in this epitaxy method is that the AsH_3 and PH_3 are very toxic gases; thus, a comprehensive exhaust system has to be built to ensure the operation safety. A variety of efforts are being made to explore other As- and P-containing compounds with less toxicity.[19] In addition to the advancement in gas-source technology, the valved cracker, using a needle valve to control the flux from red solid phosphorus, has been demonstrated to be a promising technology to grow phosphide in a conventional MBE system.[20]

Our experiments were carried out in an Intevac (Varian) Modular GEN-II MBE machine, which was modified to handle gas sources. Two 2200 l/s cryopumps are equipped to evacuate the growth chamber. They are used alternately so that one pump can be regenerated while the other pump is being used. Pure AsH_3 and PH_3 sources, as well as scrubbers, are housed in two separate gas cabinets. The hydride gas sources for As_2 and P_2 are introduced into the growth chamber through a single Varian four-channel hydride injector, which is operated nominally at 1000 °C. A second home-made hydride cracker is also incorporated into the system to provide more flexibility for the gas switching when mixed- or alternating-group-V compounds are grown. In addition, the growth chamber is accommodated with two indium sources, one gallium, one aluminum, one silicon, and one beryllium source. The chamber is also equipped with a nude ion gauge for flux calibration and a Dycor quadrupole mass spectrometer for residual mass determination and leak detection. The temperature of the elemental sources is set such that a typical growth rate is approximately 1 $\mu\text{m/hr}$. The hydride flow rates are 2 to 4 sccm, and the working pressure in the growth chamber is typically 1×10^{-5} torr. Figure 2.1 shows a schematic drawing of our GSMBE system with the gas manifold. $\text{GaAs}_{1-x}\text{P}_x$ and $\text{InAs}_x\text{P}_{1-x}$ were grown at 580 °C and 460 °C, respectively. The substrate temperature was calibrated by a pyrometer and the melting point of InSb.

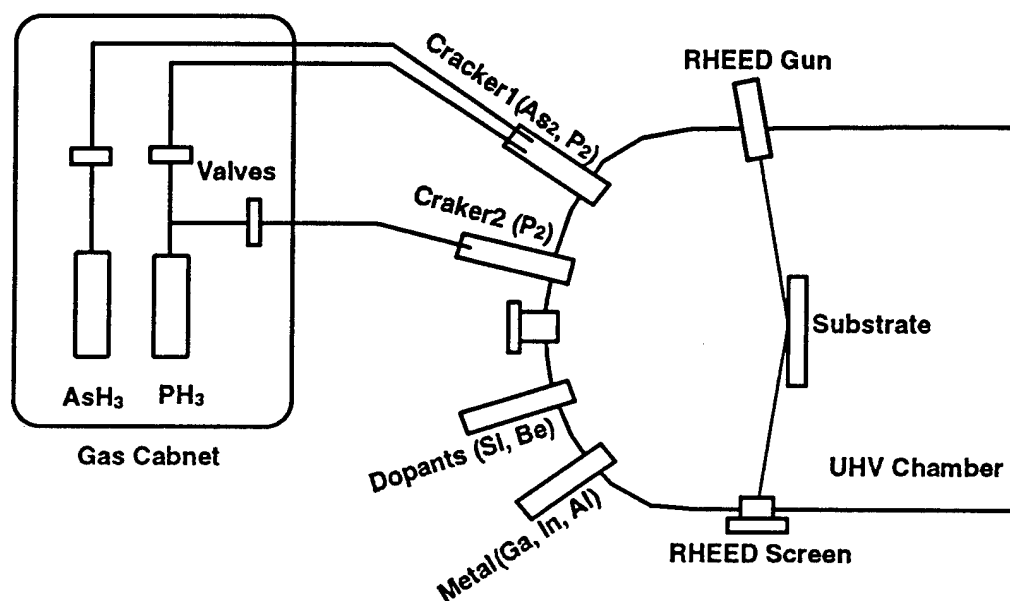


FIG. 2.1 Schematic diagram of the GSMBE setup.

2.3 Group-V-induced RHEED oscillations

For electrons with energies of 5-50 keV the wavelength is of the order of 0.1 Å. When a narrow beam of such electrons impinges on a single crystalline surface at a glancing angle, it is diffracted by the crystal lattice within a few atomic layers of the surface. The diffraction pattern thus observed is characteristic of the arrangement of

atoms on and within a small distance of the surface. Two particularly interesting and useful manifestations of RHEED are surface structural transitions observed as a function of the group-V coverage of the surface,[14] and intensity oscillations during growth.[11] In 1983, Neave *et al.*[11] reported that the intensity of the RHEED specular beam oscillated when the supply of Ga flux was resumed after an interruption of GaAs growth. The detailed mechanism that leads to the oscillations is not well understood, but it is clear that each oscillation corresponds to one monolayer of growth of GaAs. A qualitative picture, frequently cited, is shown in Fig. 2.2, in which the growth proceeds by coalescence of molecular-layer islands. It is intuitive that the diffraction intensity is small when the island population is about 50% of a monolayer coverage, whereas a strong diffraction occurs when the entire layer is formed. The layer-by-layer growth will therefore result in intensity oscillations. This RHEED oscillation technique provides a simple, yet accurate *in situ* approach to determining the growth rate and therefore the composition for ternary compounds (such as AlGaAs) from the difference of the GaAs and AlGaAs growth rates. In our MBE system, the intensity of the RHEED specular beam is detected by an optical-fiber-coupled photodiode, and the signal is recorded by a computer after it is enhanced with a dual-channel differential amplifier.[21] We use this technique routinely to calibrate the incorporation rate of group-III elements.

Now we will go into the details of group-V-induced RHEED oscillations. A *metallic* (group-III-rich) surface is *intentionally* formed by stopping the hydride injection and keeping only the shutter for the group-III element open. Thus, metal atoms accumulate on the surface of the substrate. When the shutter for the group-V element is opened, the excess metal atoms on the surface will react with the group-V element, causing layer-by-layer two-dimensional growth, and the RHEED intensity oscillates.[12,22]

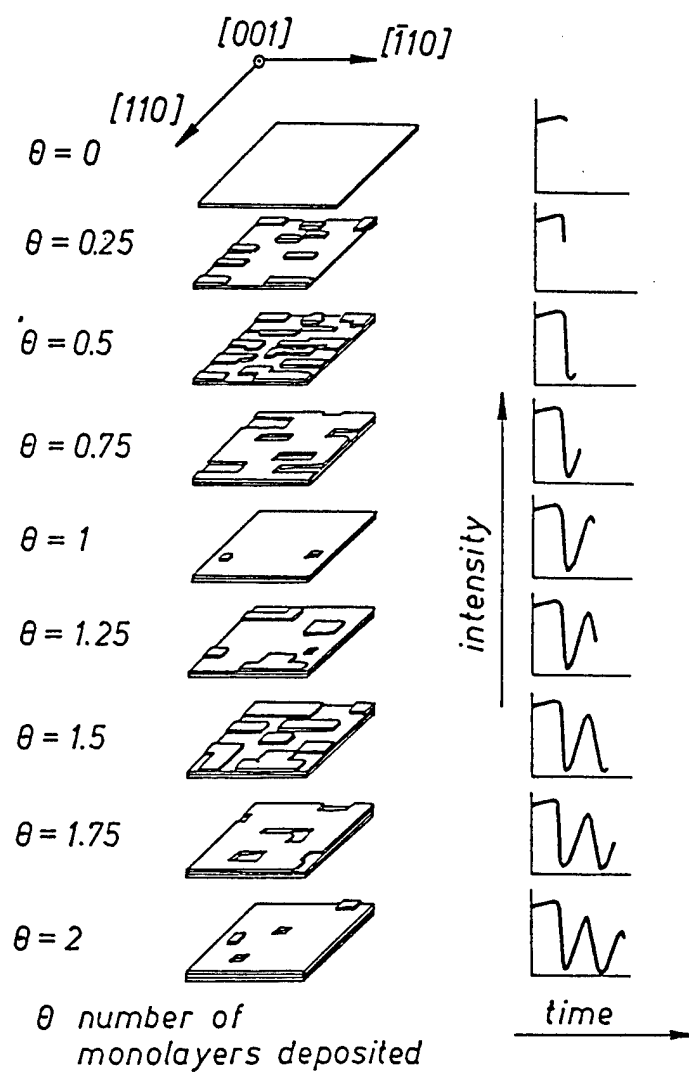


FIG. 2.2 Schematic diagrams of the cause of RHEED oscillations.

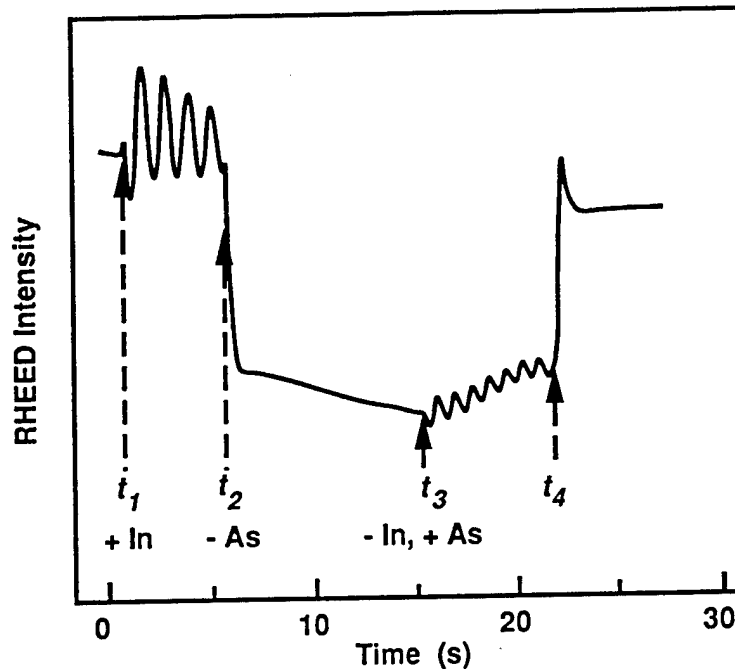


FIG. 2.3 RHEED oscillations induced by In ($t_1 < t < t_2$) and As ($t_3 < t < t_4$). Note that the As-induced oscillations occurred on an In-rich surface caused by depositing excess In during $t_2 < t < t_3$. The incorporation rates of indium and arsenic can be determined, respectively, from the first and second part of the oscillations.

Fig. 2.3 shows a typical trace of the group-III- ($t_1 < t < t_2$) and group-V-induced ($t_3 < t < t_4$) RHEED oscillations during InAs homoepitaxial growth.[11,12] A thick ($\sim 3 \mu\text{m}$) and totally strain-relaxed InAs layer was grown on InP so that a high-quality surface was achieved for RHEED oscillation measurements. During $t_1 < t < t_2$, the growth rate is limited by the arrival rate of the In flux as normally applied.[11] However, the growth rate is limited by the As arrival rate during $t_3 < t < t_4$ since excess In atoms were deposited on the InAs surface during $t_2 < t < t_3$. [12] Therefore, the incorporation rates of In and As, R_{In} and R_{As} , at a given growth temperature can be determined from these oscillations, respectively.

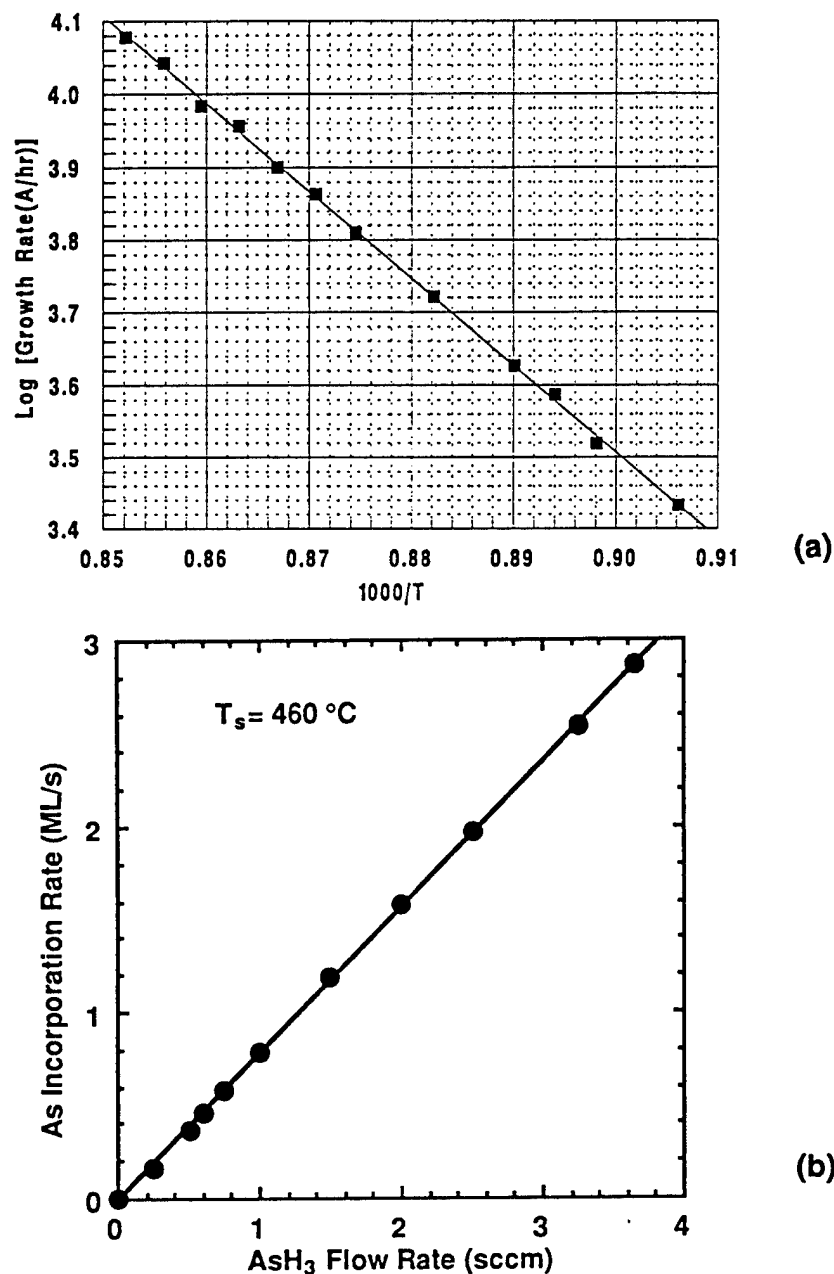


FIG. 2.4 (a) The indium (InAs) growth rate as a function of the furnace temperature. The Arrhenius plot indicates the thermal effusion behavior of the furnace. The substrate temperature ($\sim 460^\circ\text{C}$) and the AsH_3 flow rate (3 sccm) are kept constant; (b) the As incorporation rate is shown as a function of the AsH_3 flow rate calibrated at the substrate temperature of 460°C for InAs grown on a thick InAs layer. The linear dependence implies that the In supply is infinite to the injected As on the surface during RHEED oscillations.

Figs. 2.4 (a) and (b) show calibration curves of incorporation rates for In and As from the group-III and group-V-induced RHEED oscillations, respectively. An Arrhenius dependence of the indium incorporation (or growth) rate on the furnace temperature is obtained. On the other hand, Figure 2.4 (b) shows that the As incorporation rate, calibrated at a substrate temperature of 460 °C, is proportional to the AsH₃ flow rate. This linear dependence runs through the whole range of the AsH₃ flow rate, as high as 4 sccm, implying that the amount of metal deposited on the surface is an infinite supply source to the injected As during RHEED oscillations. This As incorporation rate also has an Arrhenius dependence on the substrate temperature.[22]

Now, we will discuss the surface state in the metal-rich condition. Up to what extent of the excess metal population can the surface resume layer-by-layer growth? Isu *et al.*[23] studied the micro-morphology of a group-III-rich surface by incorporating a scanning electron microscopy (SEM) into an MBE growth chamber. Their experimental results obtained by directly monitoring the surface morphology on an atomic scale showed that the excess metal atoms form droplets on the surface rather than a uniform layer. The higher the substrate temperature is, the smaller yet denser the droplets form. When the group-V flux is injected, the size and the density of the droplets decrease. In the area between droplets is a metal-rich surface reconstruction. A stable surface state is a *dynamic equilibrium* of the diffusions between droplets and group-III-rich area. When the group-V flux impinges, excess group-III atoms on the surface are consumed. As a result, group-III atoms diffuse away from the droplets constantly to maintain the equilibrium. After all excess group-III atoms are incorporated into the lattice, the RHEED intensity recovers to the level of group-V-rich surface at $t > t_4$ in Fig. 2.3. However, the surface is not recoverable if too many group-III atoms are deposited such that the droplet density is too high. From our experience, an amount of In or Ga deposited on a substrate surface is usually less than that which can cause 10 oscillations.

2.4 As incorporation behavior in $\text{GaAs}_{1-x}\text{P}_x$

2.4.1 *In situ* technique of determining the P composition

We initiated our incorporation study of mixed-group-V compounds with $\text{GaAs}_{1-x}\text{P}_x$ because theoretical and experimental studies of As incorporation for this material have been substantially examined previously, and the data are readily available for comparison.[8-10,16] Considerable attention has been focused on the preparation, characterization and application of this material system since pseudomorphic GaAsP/GaAs heterostructures were first grown by MOCVD.[24] In addition, $\text{GaAs}_{1-x}\text{P}_x$, a ternary member of the quaternary InGaAsP, is the simplest mixed-group-V compound for understanding the incorporation behavior of group-V elements. The growth study on GaAsP will aid the growth control for the InGaAsP quaternary compound.[25] Although the incorporation behavior of As and P in GaAsP has been extensively investigated in MOCVD [7-9,26,27] and even in solid-source MBE,[10,16] only a limited amount of work has been done on the growth study of GaAsP by GSMBE. A comprehensive understanding of the incorporation behavior of As and P into GaAsP, however, would be very useful for composition control. We will report an *in situ* method to calibrate the phosphorus composition in GaAsP by measuring the group-V-induced RHEED intensity oscillations. We will also discuss a study of the incorporation behavior of phosphorus as a function of the substrates temperature and different strain states.[28,29]

Figures. 2.5(a) and (b) illustrate typical group-V-limited RHEED oscillations for GaAs and $\text{GaAs}_{1-x}\text{P}_x$ growth on a GaAs substrate, respectively. The AsH_3 flow rate was fixed at 1.6 sccm in both cases, whereas PH_3 was also introduced with a flow rate of 2.4 sccm for the oscillations shown in Fig. 2.5(b). The (As+P)-limited growth rate was found to be higher than the As-limited growth rate. Such measurements were performed at a fixed AsH_3 flow rate (1.6 sccm) and various PH_3 flow rates ranging from 0 to 4.0 sccm.

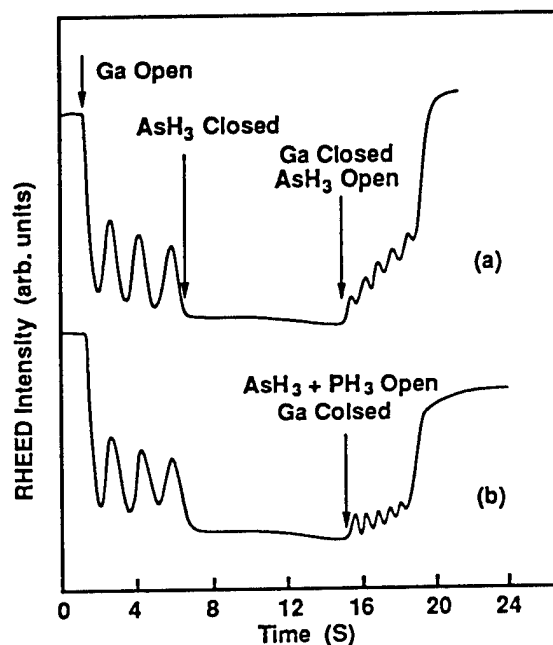


FIG. 2.5 Typical group-V-limited RHEED intensity oscillations on a Ga-rich GaAs surface. The oscillation is induced by (a) As, and (b) As+P.

Generally speaking, the As incorporation rate into $\text{GaAs}_{1-x}\text{P}_x$ might change upon the injection of P due to the displacement of As by P. Foxon *et al.* [16] reported a slight decrease of As_4 sticking coefficient when P_4 was injected during $\text{GaAs}_{1-x}\text{P}_x$ MBE growth under a limited Ga supply ($8 \times 10^{13} \text{ atoms cm}^{-2} \text{ s}^{-1}$), where As_4 is 50 times more effective at displacing P_4 than vice versa. In our case, excess Ga atoms are deposited on the surface before the group-V-limited RHEED oscillation measurements; hence the

displacement of As by P may be negligible. It is then reasonable to assume that the increase in the growth rate shown in Fig. 2.5(b) is uniquely due to the addition of P. Therefore, the difference in the group-V growth rates gives the net incorporation rate of phosphorus from which the phosphorus composition, x , can be deduced.

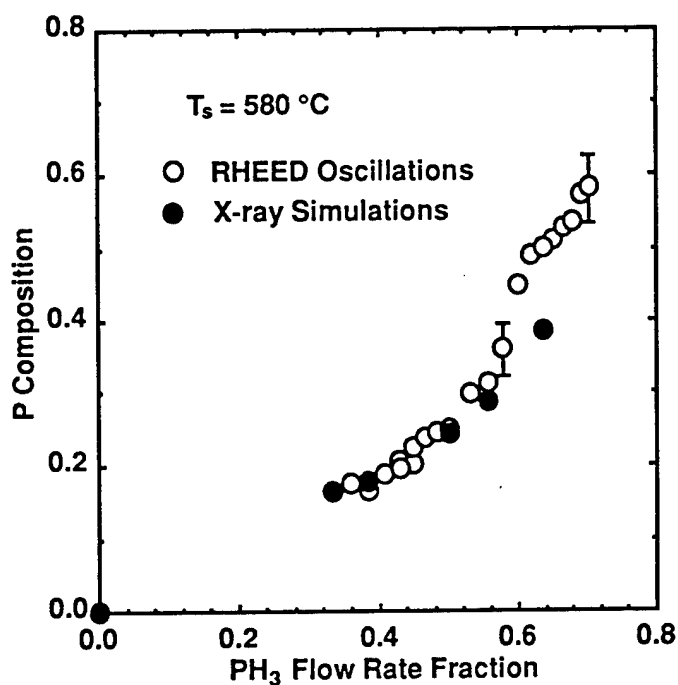


FIG. 2.6 Phosphorus composition in $\text{GaAs}_{1-x}\text{P}_x$ as a function of the PH_3 flow-rate fraction. The data shown by open circles are determined from RHEED oscillations; the full circles represent the x-ray simulation data.

The RHEED-determined phosphorus composition in $\text{GaAs}_{1-x}\text{P}_x$ is plotted in Fig. 2.6 (indicated by open circles) versus the PH_3 flow-rate fraction (PH_3 flow rate over the total hydride flow rate). Typical errors in determining x from the RHEED oscillations are indicated with error bars for $0.3 < x < 0.6$. This uncertainty is significant when the phosphorus composition is greater than 0.3 since the relatively large surface strain reduces the number of oscillations, which causes errors in reading the time scale. As shown in Fig. 2.6, the composition of phosphorus incorporated in the solid is different from the PH_3 flow-rate fraction in the gas phase. This is attributed to different sticking coefficients and arrival rates (a factor of square root of the As_2 to P_2 molecule mass ratio) of arsenic and phosphorus.[16,18]

The *in situ* determined composition was examined by x-ray rocking curve measurements of strained-layer superlattice (SLS) structures. Five samples, typically consisting of 15-period $\text{GaAs}(95 \text{ \AA})/\text{GaAs}_{1-x}\text{P}_x(95 \text{ \AA})$ superlattices, were grown with the same fixed AsH_3 flow rate (1.6 sccm) and substrate temperature (580°C) as RHEED measurements and PH_3 flow rates ranging from 0.8 to 2.8 sccm. The thickness of the $\text{GaAs}_{1-x}\text{P}_x$ layer is less than the critical layer thickness so that pseudomorphic $\text{GaAs}_{1-x}\text{P}_x$ growth is expected. In such a case, by assuming Vegard's law the structural parameters can be determined accurately from the x-ray diffraction simulation based on a dynamical theory (this is discussed in greater detail in Chapter 3). X-ray results for these five samples are shown in Fig. 2.6 with closed circles. It is remarkable that the RHEED oscillation data and x-ray diffraction data are in very good agreement for $x < 0.3$. However, a significant deviation in composition exists for the sample with the highest phosphorus composition.

In order to understand the viability of this *in situ* determination of the phosphorus composition, several more 15-period $\text{GaAs}(95 \text{ \AA})/\text{GaAs}_{1-x}\text{P}_x(95 \text{ \AA})$ SLS samples were grown with the same phosphine flow fraction, but different V/III incorporation ratios.

Here, the *incorporation ratio* refers to the ratio of the group-V and group-III incorporation rates determined by group-V- and group-III-limited RHEED oscillations, respectively.[12,22] As shown in Fig. 2.7, solid circles and triangles represent phosphorus compositions versus the V/III incorporation ratio when the phosphine flow-rate fractions are fixed at 0.50 (by triangles) and 0.56 (by circles), respectively. The open marks indicate the *in situ* determined composition from RHEED oscillations at the same flow-rate fraction and substrate temperature as those prepared for above SLS samples.

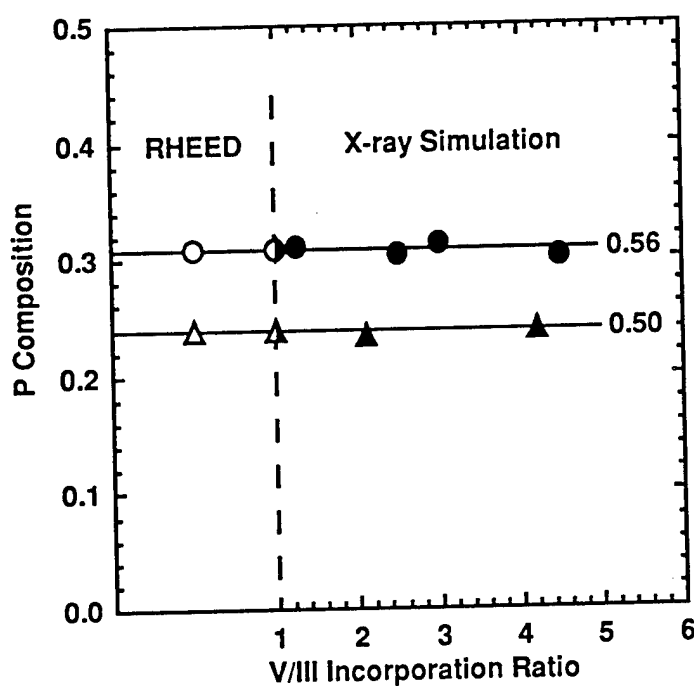


FIG. 2.7 The phosphorus composition as a function of the V/III incorporation ratio. The solid marks represent the *ex situ* determined data; the open marks indicate the *in situ* determinations at the same corresponding phosphine flow fractions.

As seen in Fig. 2.7, the phosphorus composition is almost independent of the V/III incorporation ratio in the current ratio range as long as the phosphine flow-rate fractions are the same. In other words, the phosphorus compositions are the same when the samples are grown with V/III incorporation ratio greater or close to unity. On the other hand, when the V/III ratio is unity, the phosphorus composition determined by the group-V-limited RHEED oscillation is naturally the same as that determined from the group-III-limited oscillation. Therefore, the *in situ* derived composition ($V/III < 1$) agrees with the x-ray *ex situ* determination ($V/III > 1$).

The dynamic growth model[8] of Seki and Koukitu proposes that the phosphorus composition depends on the V/III beam-flux ratio for MOCVD growth of $GaAs_{1-x}P_x$. *It is important to note that the V/III incorporation ratio is different from the beam-flux ratio, since the incorporation rate is a function of the beam flux and the sticking coefficient, which is different for arsenic and phosphorus. Therefore, the incorporation ratio is more relevant to growth studies. Our data also show that the phosphorus composition depends on the substrate temperature. However, the in situ method is still valid provided that the in situ calibration and real growth are carried out at the same substrate temperature.*

2.4.2 Dependence on the substrate temperature

We studied the P incorporation in $GaAs_{1-x}P_x$ as a function of the phosphine flow rate and the flow-rate fraction. Another related issue is the growth-temperature dependence of the As and P incorporation in $GaAs_{1-x}P_x$. This is important not only as shown above, but also for implementation of the *in situ* technique to composition control of the quaternary InGaAsP layer, which is usually grown under different substrate temperature (T_s) and strain states. A series of 15-period $GaAs(95 \text{ \AA})/GaAsP(95 \text{ \AA})$ SLS samples were grown. The phosphorus compositions were determined from the x-ray

rocking curve measurements and computer simulations. Fig. 2.8 shows the substrate-temperature dependence of the P composition obtained for a series of SLS samples grown with the same AsH_3 and PH_3 flow rates (therefore the same PH_3 flow-rate fraction). A change of the P composition occurs in the temperature region between 520 and 620 °C, whereas the P composition is independent of the substrate temperature when $T_s > 620$ °C or < 520 °C.

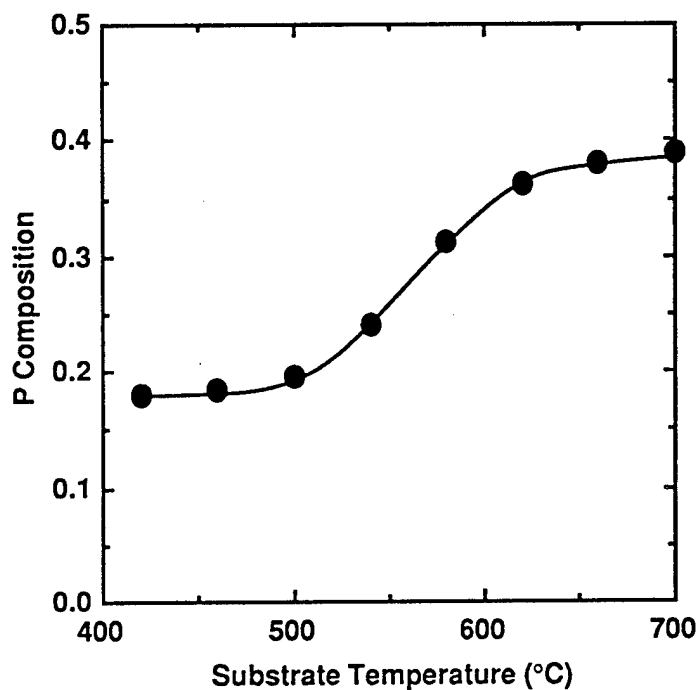


FIG. 2.8 The phosphorus composition in GaAsP grown with the same hydride flow rates as a function of the substrate temperature. The curve through the data points is drawn to guide the eye.

Chow *et al.* [30] and Chin *et al.* [22] reported the incorporation rates of As and P in GaAs and GaP, respectively, versus the substrate temperature. These incorporation rates were measured by the group-V-induced RHEED oscillations for GaAs (GaP) growth on a GaAs (GaP) substrate under different T_s . The incorporation of As and P was found to decrease starting at around 540 and 650 °C, respectively, due to increasing desorption. The activation energies related to As and P desorption were deduced to be about 0.9 eV for both GaAs and GaP.[22,30] The two corners of the P composition in GaAsP shown in Fig. 2.8 then coincide with the temperatures at which As and P begin to desorb. Therefore, it is easy to understand that the ratio of As to P incorporation into GaAsP is the same for $T_s < 520$ °C, where no significant desorption occurs, and for $T_s > 620$ °C, where As and P desorb at about the same rate (since they have similar activation energy). In the temperature region of 500 °C $< T_s < 620$ °C, the As desorption results in an increase of the P composition in GaAsP.

Recently, Nomura *et al.*[10] reported a very similar result for GaAsP grown by conventional MBE. The significant composition change was found between 450 and 520°C owing to the different dissociation temperatures for As and P.[10] In MOCVD growth of GaAsP, however, the P composition was found to be strongly dependent on the substrate temperature over a wider temperature range (650~850 °C).[27] This different behavior from the GSMBE growth is probably due to the fact that, in MOCVD, the arsine and phosphine are cracked on the substrate surface with different cracking efficiency at a given substrate temperature. From the point of view of composition control in GSMBE, it is better to grow GaAsP at either $T_s > 620$ °C or < 520 °C because small fluctuations in T_s may result in a significant change of x when 520 °C $< T_s < 620$ °C.

2.4.3 Dependence on the growth under different strain states

It has been reported that the As composition in InAsP depends on the strain in MOCVD growth at the substrate temperature of 600 °C.[29] A detailed study was also reported on the In incorporation coefficient in strained and unstrained InAlAs layers grown by MBE at various substrate temperatures.[31] An observable difference was found when $T_s > 570$ °C. From thermodynamic considerations, the difference is due to the increase of the strain-related energy in the growing layer[31]. To understand whether the P incorporation depends on the strain state in the growing layer under normal growth conditions, GaAsP(40 Å)/GaAs(40 Å) and GaAsP(40 Å)/GaP(40 Å) SLSs were grown on GaAs and GaP substrates, respectively. The same hydride flow rates and substrate temperature were used, but the GaAsP layer would experience a biaxial tensile strain in the former and a biaxial compressive strain in the latter if an elastic tetragonal distortion is assumed for deformations. Figures 2.9(a) and (b) show respective x-ray rocking curves taken from these two samples. The compositions, given in the figure, were based on computer simulations to x-ray rocking curves. The proposed increase[31] of the strain-related energy in the growing GaAsP layer comes from the additional incorporation of P and As into GaAs and GaP, respectively. The strain would be expected to be a barrier for additional incorporation of elements that would increase the strain. Therefore, the P composition in GaAsP should be smaller when it is grown on GaAs than when grown on GaP. However, the P compositions determined by x-ray rocking curves for these two SLSs are 0.49 and 0.485, respectively. The other pair at $x = 0.43$ gives almost the same composition results within the uncertainty of the composition determination by x-ray rocking curve measurements. Hence, no observable difference of the incorporation of group-V is detected for the different strain states under normal growth conditions. In other words, the composition calibration for GaAsP on GaAs may also be applicable to GaAsP grown on GaP. We have found that the respective *in situ* composition calibrations

for GaAsP and InAsP grown on GaAs and InP substrates provide a very good guideline for the composition control in InGaAsP quaternary compounds grown on InP substrates. This will be discussed in Section 2.6.[25]

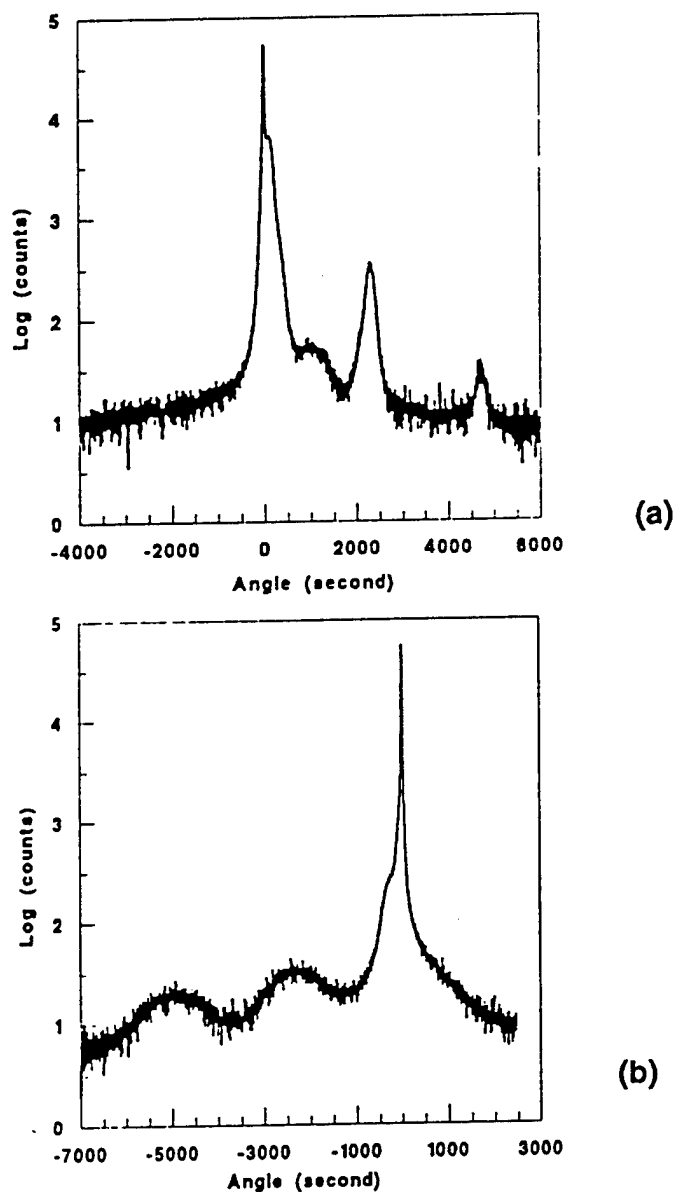


FIG. 2.9 X-ray rocking curves taken from GaAsP-containing multilayered heterostructures. (a) 15-period GaAs(40 Å)/GaAs_{1-x}P_x(40 Å) SLS grown on GaAs; (b) 15-period GaP(40 Å)/GaAs_{1-x}P_x(40 Å) SLS grown on GaP substrates. The computer simulation results show that the phosphorus incorporation does not depend on different strain states.

2.5 *In situ* calibration of As composition in $\text{InAs}_x\text{P}_{1-x}$

We discussed the *in situ* calibration of the phosphorus composition in GaAsP by measuring the difference in the incorporation rate of (As+P) and As with group-V-induced RHEED oscillations.[32] Because of the metal-rich condition on the surface, this difference was inferred to be due to the addition of P. The P compositions determined from RHEED oscillations agreed with *ex situ* measurements for the samples grown under the same PH_3 flow-rate fractions (PH_3 flow rate over the total hydride flow rate) and at the same substrate temperature. However, the As and P incorporation behavior is somewhat different for InAsP and GaAsP growth. In this section, we will discuss another application of the group-V-induced RHEED oscillations to the composition determination.

When both As and P were injected onto the substrate surface at t_3 shown in Fig. 2.3, we see a higher growth rate, due to the addition of P, than when only As was introduced. In Fig. 2.10 the growth rates limited by (As+P) are plotted against PH_3 flow rates at several fixed AsH_3 flow rates (0, 0.5, 0.75 and 1 sccm). The lines through the data points are drawn to guide the eye. It appears that the incorporation rate of (As+P) has qualitatively the same linear dependence on the PH_3 flow rate as the incorporation rate of only P itself (calibrated for InP grown on InP). The only difference is a constant offset corresponding to the additional incorporation of As. (The jump in the incorporation rate for the results grown with 0.5 sccm AsH_3 may be due to the change of the RHEED pattern for a highly strained InAsP surface). We can, therefore, conclude that the As incorporation into $\text{InAs}_x\text{P}_{1-x}$ is independent of the presence of P under the In-rich growth condition. This behavior agrees with the prediction of Seki and Koukiku.[8] Now we can assume that the As incorporation into $\text{InAs}_x\text{P}_{1-x}$ is dominant in our normal growth conditions (group-V rich but $R_{\text{As}}/R_{\text{In}} < 1$) with substrate temperature at around 460 °C and a small PH_3 flow rate, which is sufficient to provide a higher total group-V

flux than In. In other words, phosphorus reacts with In only when there is not enough As to react with all of the In. This situation makes controlling the As composition in $\text{InAs}_x\text{P}_{1-x}$ very simple. Once we calibrate the As and In incorporation rates at a desired growth temperature by As- and In-induced RHEED oscillations, respectively, as shown in Figs. 2.4(a) and (b), the ratio of the As to In incorporation rates (when ≤ 1) is basically the As composition in $\text{InAs}_x\text{P}_{1-x}$.

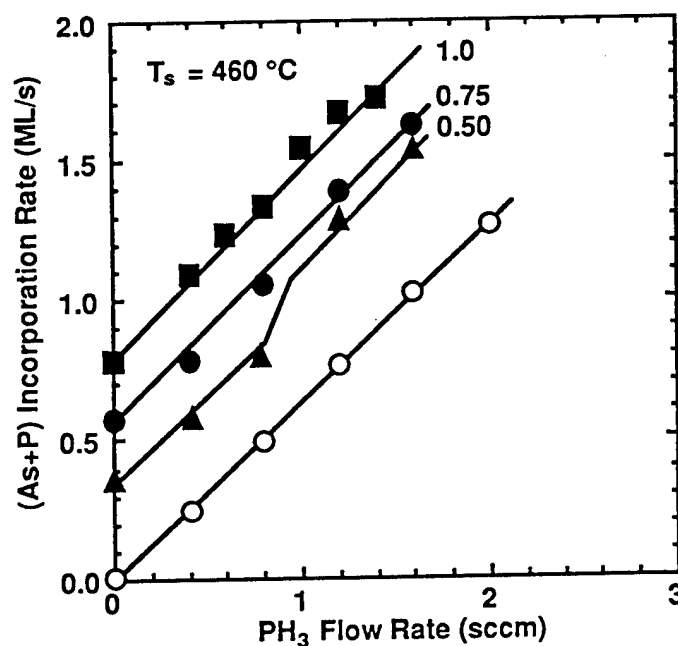


FIG. 2.10 The incorporation rate of (As+P), determined by group-V-induced RHEED oscillations during InAsP growth, as a function of the PH_3 flow rate at several fixed AsH_3 flow rates (0, 0.5, 0.75, 1 sccm). The lines through the data points are drawn to guide the eye.

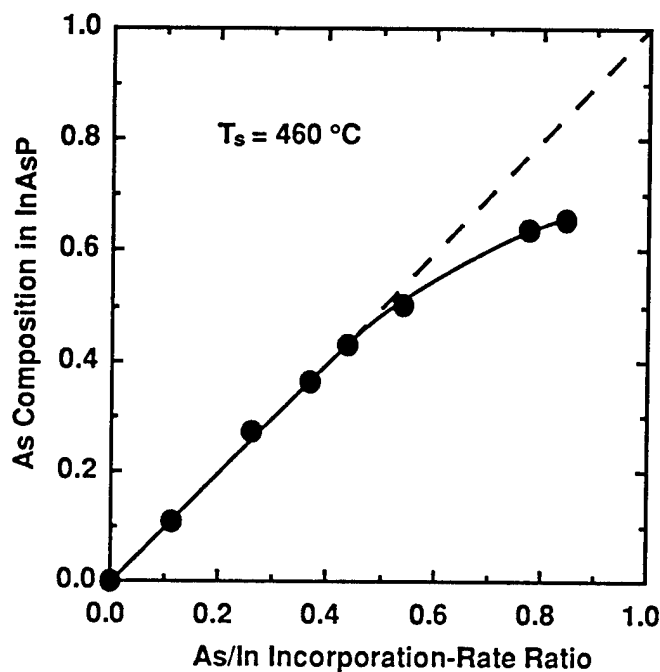


FIG. 2.11 The As composition in $\text{InAs}_x\text{P}_{1-x}$ determined from x-ray rocking curve measurements versus the incorporation ratio of As to In obtained from RHEED oscillations.

Based on this idea of *in situ* control of the As composition in InAsP, a series of InAsP/InP SLS structures were grown at 2 sccm PH_3 flow rates and different $R_{\text{As}}/R_{\text{In}}$ ratios. High-resolution (400) x-ray rocking curves and computer simulations yielded a precise determination of the As composition in $\text{InAs}_x\text{P}_{1-x}$. Shown in Fig. 2.11 is the *ex*

situ determined As composition versus the R_{As}/R_{In} ratio. An excellent agreement can be seen when $x < 0.5$. This implies that our assumption of As being dominantly incorporated in InAsP under normal growth conditions is valid, and that this *in situ* method to determine the composition is viable. The discrepancy for $x > 0.5$ is presently not well understood. A possible reason for this is that the large surface strain may affect the incorporation behavior of As and P. Chang *et al.*[33] reported a similar result of composition control in MBE grown GaAsSb. They found that the control of the Sb composition can best be achieved by maintaining the ratio of Sb/Ga below unity. They attributed this behavior to the higher sublimation energy (longer surface lifetime), and lower atomization energy (more reactions with Ga surface atoms) of Sb_4 than of As_4 .

The SLS samples used for *ex situ* composition determination by x-ray rocking curves and simulations shown in Fig. 2.11 were all grown at a PH_3 flow rate of 2 sccm (except 1.5 sccm for the sample with $x=0.1$). However, when the PH_3 flow rate is much higher than the AsH_3 flow rate, the As flux concentration may be greatly diluted on the substrate surface.[34] As a result, the As composition in InAsP would be dependent on the PH_3 flow rate. Therefore, a series of InAsP/InP SLS samples were grown with a fixed AsH_3 flow rate (0.25 and 0.5 sccm, respectively) and various PH_3 flow rates ranging from 1.25 to 4 sccm. Shown in Fig. 2.12 is the normalized As composition determined from x-ray rocking curves to the As/In incorporation-rate ratio as a function of the PH_3/AsH_3 flow-rate ratio. The full and open circles represent the respective cases with AsH_3 flow rate of 0.25 and 0.4 sccm. The As composition decreases when the PH_3 flow rate is about 5 times as much as the AsH_3 flow rate. The corresponding surface concentration ratio is even enhanced by a factor of $\sqrt{m_{As_2}/m_{P_2}}$, where m_{As_2} and m_{P_2} are the molecular mass of As_2 and P_2 , respectively. In this case, the *ex situ* determined As composition is no longer consistent with the *in situ* calibration. *Therefore, to keep this in situ method valid it is important to use as small V/III incorporation ratio as possible.*

Although the As composition in InAsP is dependent on the substrate temperature, the *in situ* calibrated composition should be correct as long as the calibration (RHEED oscillations) and real growth are performed at the same substrate temperature within a reasonable range.

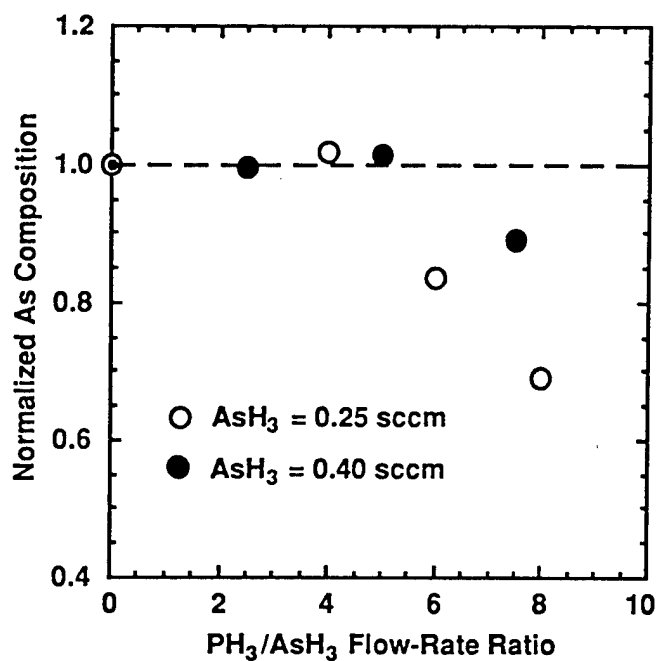


FIG. 2.12 The normalized As composition in InAs_xP_{1-x} (*ex situ/in situ*) as a function of the flow-rate ratio of PH₃ to AsH₃ at fixed AsH₃ flow rates, 0.25 sccm (full circles) and 0.4 sccm (open circles).

To use this *in situ* technique, RHEED calibrations are not necessary for every run provided that the substrate temperature and gas flow rates are relatively stable over a period of time. It is important to note that with this RHEED calibration of the composition in $\text{InAs}_x\text{P}_{1-x}$ we have established a composition determination scheme which provides a linear dependence of the As composition in $\text{InAs}_x\text{P}_{1-x}$. Furthermore, we see that the As incorporation rate is also proportional to the AsH_3 flow rate from Fig. 2.4(b). These results imply the possibility for simplification of the *ex situ* composition calibration procedure of InAsP. Once the As composition from a calibration sample is known in $\text{InAs}_x\text{P}_{1-x}$, then a linear interpolation or extrapolation of the AsH_3 flow rate can provide an accurate prediction of the desired As composition. This procedure has actually been often used in the InAsP growth of this work.

2.6 *In situ* composition calibration in $\text{In}_{1-x}\text{Ga}_x\text{As}_y\text{P}_{1-y}$

In this section, we will present an *in situ* procedure for controlling the composition in $\text{In}_{1-x}\text{Ga}_x\text{As}_y\text{P}_{1-y}$ by considering As and P incorporation behavior in $\text{GaAs}_{1-x}\text{P}_x$ and $\text{InAs}_x\text{P}_{1-x}$, as studied by group-V-induced RHEED oscillations.[32,35] We succeeded in growing $\text{In}_{1-x}\text{Ga}_x\text{As}_y\text{P}_{1-y}/\text{InP}$ MQWs with desired structural parameters. Characterizations by x-ray rocking curve, absorption, and low-temperature photoluminescence (PL) measurements suggest that high-quality samples were obtained.

We have elucidated the *in situ* procedures used for composition determination of GaAsP and InAsP. It should be noted that the *in situ* composition determination for these ternary compounds requires that the incorporation rate of As not be changed by adding P. Therefore, the compositions of GaAsP and InAsP are calculated with respect to the As-limited growth rates of GaAs and InAs, respectively. A direct *in situ* composition calibration for InGaAsP would be difficult because no one simple binary compound can be chosen as a reference. We can, however, control the composition in InGaAsP by

combining the knowledge of the *in situ* determination for GaAsP and InAsP. The growth rates of Ga and In are calibrated first by measuring group-III-induced RHEED oscillations on GaAs and InP substrates, respectively. The Ga composition in $\text{In}_{1-x}\text{Ga}_x\text{As}_y\text{P}_{1-y}$ is then obtained as normally done for $\text{III}_x\text{III}_{1-x}\text{V}$ compounds. It is reasonable to assume that the distribution of As flux to In and Ga is $(1-x)F_{\text{As}}$ and $x F_{\text{As}}$, respectively, where F_{As} denotes the As beam flux. Since the As composition in $\text{In}_{1-x}\text{Ga}_x\text{As}_y\text{P}_{1-y}$ derives from As incorporation with both In and Ga, it can be estimated individually for InAsP and GaAsP as discussed above. Arsenic incorporates with In at almost 100% efficiency, but incorporates with Ga with an efficiency p , which depends on the presence of P, as shown in Fig. 2.6. Once p is determined for a given substrate temperature and PH_3 flow rate, the As composition in $\text{In}_{1-x}\text{Ga}_x\text{As}_y\text{P}_{1-y}$ can be found from $(1-x)R_{\text{As}}/R_{\text{In}} + xpR_{\text{As}}/R_{\text{Ga}}$. Here R denotes the incorporation rate. We grew a series of InGaAsP/InP MQW structures with growth rates of 0.67 ML/s for In and 0.28 ML/s for Ga as measured on InP and GaAs substrates, respectively. The PH_3 flow rate was fixed at 2 sccm, but the AsH_3 flow rate varied from 0.8 sccm to 1.2 sccm. Combining x-ray rocking curve, PL and absorption measurements with simulations and calculations, we found the As composition to be very close to what is expected.

To examine the lattice-match condition, we grew a series of MQW samples for x-ray rocking curve measurement. A typical structure consisted of 20-period $\text{In}_{0.7}\text{Ga}_{0.3}\text{As}_{0.65}\text{P}_{0.35}$ (100 Å)/InP (150 Å) undoped MQWs grown on an Fe-doped semi-insulating (100) InP substrate and capped with a 300 Å InP layer. Mirror-like surface morphology was obtained. High-resolution x-ray rocking curve was recorded for the symmetric (004) diffraction from a monochromatic line of Cu $K\alpha_1$ through four Ge crystals. The full width at half maximum (FWHM) for a 2 µm thick $\text{In}_{0.7}\text{Ga}_{0.3}\text{As}_{0.65}\text{P}_{0.35}$ was as narrow as 30 arc seconds, indicating good crystalline quality. In Fig. 2.13, very sharp and distinct satellite peaks are observed, suggesting good

periodicity of the multi-layered structure. The zeroth order peak from these MQWs is only 38 arc seconds away from that of the InP substrate, corresponding to a lattice mismatch of 0.1%. This indicates that a lattice match condition is obtained. Thus, the *in situ* composition determination procedures described here provide a general guideline for composition control in InGaAsP quaternary compounds.

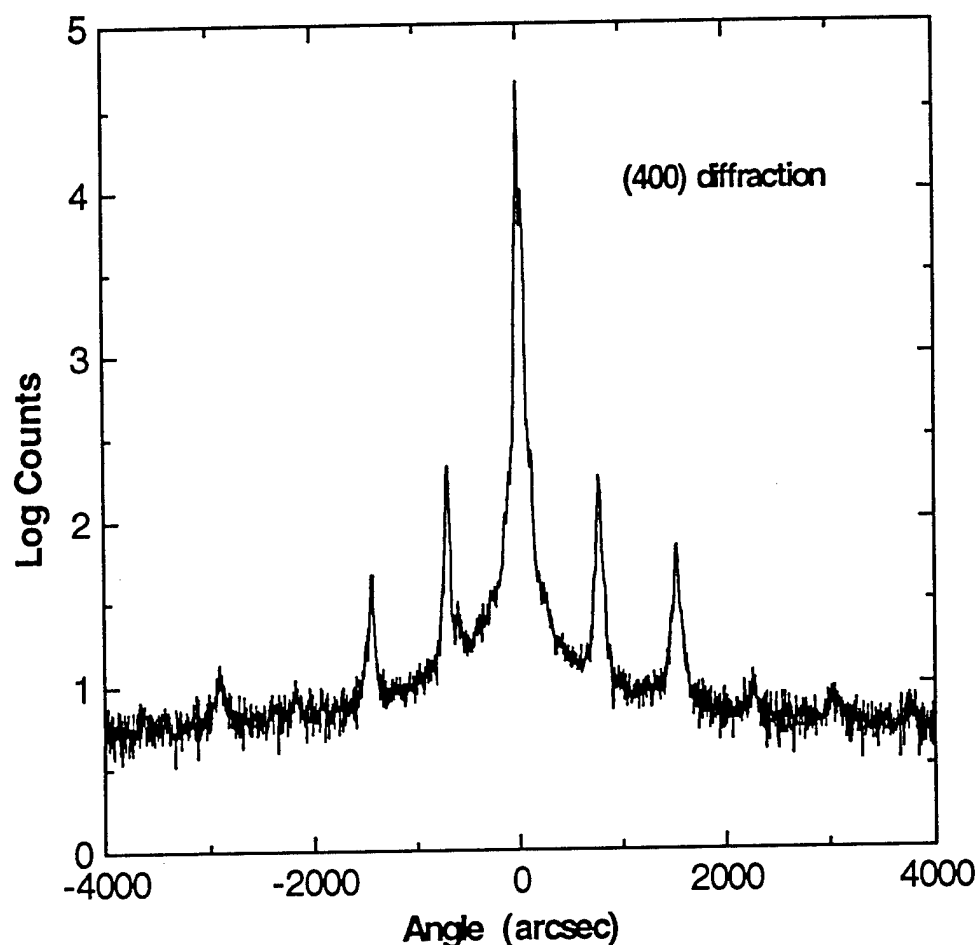


FIG. 2.13. An x-ray rocking curve of (004) diffraction from a 20-period $\text{In}_{0.7}\text{Ga}_{0.3}\text{As}_{0.65}\text{P}_{0.35}$ (101.5 Å)/InP (152 Å) MQW structure. Some satellite peaks are missing because of the intermixing at InGaAsP/InP interfaces.

2.7 Conclusion

A simple *in situ* approach to determining the phosphorus composition in $\text{GaAs}_{1-x}\text{P}_x$ grown by GSMBE has been presented. The different incorporation rates of As and As+P, hence, the composition in the alloy layer, were deduced by observing the RHEED intensity oscillations of the group-V-limited growth on a Ga-rich surface ($\text{V/III} < 1$). The results agree favorably with the x-ray examination of as-grown ($\text{V/III} > 1$) superlattice samples. This calibration technique is viable provided that the same substrate temperature and phosphine flow-rate fraction are used for RHEED oscillation calibration and real growth. The incorporation behavior of phosphorus in GaAsP was, furthermore, studied as a function of the substrate temperature and under different strain states. An increase of the phosphorus composition at the substrate temperature region between 520 and 620 °C was observed. This increase is attributable to different desorption temperatures of As and P. Moreover, the phosphorus incorporation into GaAsP was found to be the same when grown at normal temperature, even when different strains were involved.

However, the As incorporation behavior is somewhat different in InAsP growth. An *in situ* control of the As composition in $\text{InAs}_x\text{P}_{1-x}$ was achieved in GSMBE growth by controlling the ratio (when less than unity) of the incorporation rates of As to In as determined from As- and In-induced RHEED oscillations, respectively. The composition determination for as-grown InAsP/InP strained-layer superlattice structures by x-ray rocking curve measurements verified the viability of this *in situ* method when the PH_3 flow rate was not too large. The As composition in $\text{InAs}_x\text{P}_{1-x}$ is proportional to the AsH_3 flow rate. This implies that *ex situ* As composition calibrations can be simplified by using interpolation or extrapolation of the AsH_3 flow rate for a known As composition from a calibration sample.

The difference of the composition determination procedures for $\text{GaAs}_{1-x}\text{P}_x$ and $\text{InAs}_x\text{P}_{1-x}$ is that when compared to phosphorus, arsenic is more dominant in

incorporating with In than with Ga. Therefore, the As incorporation in the $\text{InAs}_x\text{P}_{1-x}$ can be considered to be a special situation of $\text{GaAs}_{1-x}\text{P}_x$ with the factor p , as defined above, close to unity. Combining the *in situ* techniques of composition control for $\text{GaAs}_{1-x}\text{P}_x$ and $\text{InAs}_x\text{P}_{1-x}$, the two ternary end members of the quaternary, we have succeeded in controlling the compositions for quaternary compounds $\text{In}_{1-x}\text{Ga}_x\text{As}_y\text{P}_{1-y}$. This *in situ* technique is extremely useful when different compositions have to be grown in a given structure. The reduction in the number of calibrations needed to determine compositions will result in a great deal of savings of time and resources.

It has been reported[33] that the sticking coefficient is smaller for the group-V element with a smaller atomic number, as a result of the smaller atomization energy — the sequence being P, As and Sb, from small to large. A dominant incorporation of one element is always expected for mixed-group-V compounds, including $\text{IIIAs}_x\text{Sb}_{1-x}$, [33] $\text{IIIAs}_x\text{P}_{1-x}$, $\text{IIIP}_x\text{Sb}_{1-x}$ and even $\text{IIIP}_x\text{As}_y\text{Sb}_{1-x-y}$. Therefore, we would suggest that this *in situ* technique for composition control of mixed-group-V compounds can be extended beyond the $\text{IIIAs}_x\text{P}_{1-x}$ and $\text{IIIAs}_x\text{Sb}_{1-x}$ systems. A further study for the incorporation behavior of other mixed-group-V compounds will be very interesting.

References

- [1] H. C. Casey, Jr. and M. B. Panish, *Heterostructure Lasers*, (Academic, New York, 1978).
- [2] T. P. Pearsall, *GaInAsP alloy semiconductors*, (Wiley, New York, 1982).
- [3] M. B. Panish and H. Temkin, *Gas Source Molecular Beam Epitaxy: Growth and Properties of Phosphorus Containing III-V Heterostructures*, (Springer-Verlag, Heidelberg, 1993).
- [4] T. K. Woodward, T. Sizer, and T. H. Chiu, Appl. Phys. Lett. **58**, 1366 (1991).
- [5] H. Q. Hou, C. W. Tu, and S. N. G. Chu, Appl. Phys. Lett. **58**, 2954 (1991); and H. Q. Hou, A. N. Cheng, H. H. Wieder, W. S. C. Chang, and C. W. Tu, Appl. Phys. Lett. (submitted).
- [6] T. Fukushima, A. Kasukawa, M. Iwase, T. Namegaya, T. Kikuta, IEEE Photon. Technol. Lett. **5**, 117 (1993); and Y. Imajo, A. Kasukawa, T. Namegaya, and T. Kikuta, Appl. Phys. Lett. **61**, 2506 (1992).
- [7] T. Fukui and N. Kobayashi, J. Cryst. Growth **71**, 9 (1985).
- [8] H. Seki and A. Koukitu, J. Cryst. Growth, **74**, 172 (1986).
- [9] L. Samuelson, P. Omling, and H. G. Grimmeiss, J. Cryst. Growth **61**, 425 (1983).
- [10] T. Nomura, H. Ogasawara, M. Miyao, and M. Hagino, J. Cryst. Growth **111**, 61 (1992).
- [11] J. H. Neave, B. A. Joyce, P. J. Dobson, and N. Norton, Appl. Phys. **A31**, 1 (1983).
- [12] J. H. Neave, B. A. Joyce, and P. J. Dobson, Appl. Phys. **A34**, 179 (1984).
- [13] M. Panish, I. Hayashi, and S. Sumski, IEEE J. Quantum Electron. **QE-5**, 210 (1969).
- [14] A. Y. Cho, J. Appl. Phys. **41**, 2780 (1970); **42**, 2074 (1971); and Appl. Phys. Lett. **19**, 467 (1971).
- [15] J. R. Arthur and J. J. Lepore, J. Vac. Sci. Technol. **6**, 545 (1969).
- [16] C. T. Foxon, B. A. Joyce, and M. T. Norris, J. Cryst. Growth **49**, 132 (1980).

- [17] M. B. Panish, *J. Electrochem. Soc.* **127**, 2729 (1980).
- [18] For reviews, see M. B. Panish, *Prog. Cryst. Growth Charact.* **12**, 1 (1986), and M. B. Panish and H. Temkin, *Annu. Rev. Mater. Sci.* **19**, 209 (1989).
- [19] C. R. Abernathy, P. W. Wisk, S. J. Pearton, F. Ren, *et al.* *J. Cryst. Growth*, **124**, 64 (1992).
- [20] G. W. Wicks, M. W. Koch, J. A. Varriano, F. G. Johnson, C. R. Wie, H. M. Kim, and P. Colombo, *Appl. Phys. Lett.* **59**, 342 (1991).
- [21] C. E. Chang, T. P. Chin, and C. W. Tu, *Rev. Sci. Instrum.* **62**, 655 (1991).
- [22] T. P. Chin, B. W. Liang, H. Q. Hou, M. C. Ho, C. E. Chang, and C. W. Tu, *Appl. Phys. Lett.* **58**, 254 (1991).
- [23] T. Isu, M. Hata, and A. Watanabe, *J. Cryst. Growth* **111**, 83 (1991).
- [24] J. W. Matthews and A. E. Blakeslee, *J. Cryst. Growth* **27**, 118 (1974).
- [25] H. Q. Hou and C. W. Tu, *J. Cryst. Growth*, **120**, 167 (1992).
- [26] G. B. Stringfellow, *J. Cryst. Growth* **62**, 225 (1983).
- [27] L. Samuelson, P. Omring, H. Titze, and H. G. Grimmeiss, *J. Phys. Paris Colloq.* **43**, C5-323 (1982), and *J. Cryst. Growth* **61**, 425 (1983).
- [28] H. Q. Hou, B. W. Liang, M. C. Ho, T. P. Chin, and C. W. Tu, *J. Vac. Sci. Technol. B* **10**, 953 (1992).
- [29] R. P. Schneider, D. X. Li, and B. W. Wessels, *J. Electrochem. Soc.* **136**, 3491 (1989).
- [30] R. Chow and R. Fernandez, *Mat. Res. Soc. Symp. Proc.* **145**, 13 (1989).
- [31] F. Turco and J. Massies, *Appl. Phys. Lett.* **51**, 1989 (1987).
- [32] H. Q. Hou, B. W. Liang, T. P. Chin, and C. W. Tu, *Appl. Phys. Lett.* **59**, 292 (1991).
- [33] C. A. Chang, R. Ludeke, L. L. Chang, and L. Esaki, *Appl. Phys. Lett.* **31**, 759 (1977).
- [34] H. Q. Hou, C. W. Tu, and S. N. G. Chu, *Appl. Phys. Lett.* **58**, 2954 (1991).
- [35] H. Q. Hou and C. W. Tu, *Appl. Phys. Lett.* **60**, 1874 (1992).

Chapter III

Growth and Structural Characterizations of InAsP/InP Strained Multiple Quantum Well Structures Grown on InP (100) and (111)B Substrates

3.1 Introduction

It was shown in Chapter 1 that the fundamental bandgap of $\text{InAs}_x\text{P}_{1-x}$ can be tuned over a wide range of emission wavelengths, covering 1.06, 1.3 and 1.55 μm which are useful for optoelectronic devices intended for use in both optical information processing and fiberoptic communication. Among various optoelectronic devices, we concentrate on optical modulators using InAsP/InP multiple quantum wells (MQWs). As shown in Fig. 1.2, the emissions at 1.06, 1.3 and 1.55 μm from 100-Å $\text{InAs}_x\text{P}_{1-x}$ quantum wells can be obtained for As composition at ≈ 0.2 , 0.4 and 0.6, respectively. In Chapter 2, we have presented an *in situ* technique for controlling the arsenic composition in $\text{InAs}_x\text{P}_{1-x}$ based on the fact that the arsenic incorporation is dominant over phosphorus in the growth of InAsP. The remaining two of the growth issues are how to control the As composition in $\text{InAs}_x\text{P}_{1-x}$ over a wide range, and how to obtain a high-quality material from this strained heterostructure. The layer thickness of the strained quantum well has to be constrained within a critical value to ensure pseudomorphic growth.[1]

Heterostructures grown on (111)B substrates possess novel properties, but the epitaxial growth was reported to be more difficult. Facet growth along (100) direction dominates and pyramid surface defects are often observed.[2] An effective approach to suppress the surface defect density is to introduce a small misorientation for the (111)B substrate and to control the growth in a step-flow mode.[3]

The interpretation of optical experiments relies quite heavily on the structural information for the sample under investigation. Two techniques, cross-sectional transmission electron microscopy (XTEM) and high-resolution x-ray diffraction, were found particularly useful in studying quantum wells and superlattices. The XTEM reveals the well and barrier thicknesses and provides some measures of the structural perfection. Cross-sectional images taken with the (002) reflection yield detailed information on the strain distribution in the sample. The contrast of wells and barriers allows an evaluation of the interface abruptness. High-resolution x-ray diffraction provides very detailed structural information averaged over a sample area of several square millimeters. The x-ray rocking curve can be simulated with a computer, based on the dynamical theory, to a remarkable precision and sensitivity. These measurements indicate that controlling the superlattice period and interfacial abruptness to about one monolayer can be achieved in samples grown by gas-source molecular beam epitaxy (GSMBE).

This chapter discusses the growth techniques and structural characterization of $\text{InAs}_x\text{P}_{1-x}/\text{InP}$ heterostructures. The structural parameters obtained are essential to the discussion of optical properties in the following chapters. $\text{InAs}_x\text{P}_{1-x}$ has been grown with an arsenic composition ranging from 0.10 to 0.70 by three different techniques for composition control. Highly strained samples are characterized by x-ray rocking curve and XTEM measurements. Low-temperature photoluminescence (PL) and Hall measurements will also be presented. This chapter is organized as follows. In Section 3.2, we present a calculation of the critical layer thickness (CLT) and also experimental determination of CLT by low-temperature PL and XTEM measurements. In Section 3.3, we present several techniques for effective composition control of the As composition in $\text{InAs}_x\text{P}_{1-x}$. In Section 3.4 an optimization procedure of the surface morphology with respect to the substrate misorientation, V/III ratio, and growth temperature is presented

for the epitaxial growth on InP (111)B substrates. Section 3.5 is devoted to a comprehensive discussion of computer simulations of x-ray rocking curves.

3.2 Strain limitation and critical layer thickness

3.2.1 Model calculations of the critical layer thickness

In the early stage of developing heterostructure lasers, it was found that when a high current was injected, the performance of lasers degraded due to dark-line defects. These were quickly realized to be from strain relaxation.[4] In 1974, Matthews and Blakeslee[2] demonstrated that a pseudomorphic growth can be achieved for lattice-mismatched materials by limiting the strained layer thickness to a certain value, called CLT. They developed a model based on a mechanical equilibrium principle by assuming that the absence of mechanical equilibrium for grown-in threading dislocations results in the onset of the generation of interfacial misfit dislocations. The resultant CLT (h_c) for a single epitaxial layer is given by:

$$h_c = \frac{b}{8\pi f} \frac{(1 - \nu \cos^2 \theta)}{(1 + \nu) \cos \lambda} \left(\ln \frac{h_c}{b} + 1 \right), \quad (3.1)$$

where f is the lattice mismatch; b is the magnitude of Burger's vector ($a/\sqrt{2}$); ν is the Poisson's ratio [$C_{11}/(C_{11} + C_{12})$]; C_{11} and C_{12} are elastic stiffness constants; θ is the angle between the dislocation line and its Burger's vector; and λ is the angle between the slip direction and the direction in the film plane that is perpendicular to the line of intersection of the slip plane and the interface.

Recently, People and Bean[5] proposed an energy equilibrium model, in which the generation of misfit dislocations is assumed to be solely determined by energy imbalance. Their result is very different from Eq. 3.1, the CLT being almost an order-of-magnitude higher. More recently, Hu has reexamined[6] the energy equilibrium model in

a more rigorous manner. His result turned out to be identical to Matthew and Blakeslee's result. Hu further argued that misfit dislocations do not appear en masse catastrophically when the CLT is reached. Rather, their density increases gradually with the epitaxial thickness, approaching asymptotically a value required for a complete relief of the film stress as the thickness tends to infinity. Equation 3.1 is for a single epitaxial layer. The CLT for epitaxial *multi-layers* is four times as large as that for a single layer, due to the strain being shared in two adjacent interfaces of a conjunction pair of misfit dislocations at these interfaces. Figure 3.1 shows calculated CLTs. The dashed and solid curves are for single and multiple epitaxial layers, respectively. We see that the 100 Å well width of $\text{InAs}_x\text{P}_{1-x}$ layers with $x=0.2, 0.4$ and 0.6 for 1.06, 1.3, and 1.55 μm emissions, respectively, are well below the critical limit.

Another important aspect of the CLT is the upper limit of the number of periods MQW samples. The strained MQW structure, as a whole, has an average lattice constant, which is given by

$$a_{\text{MQW}} = \frac{a_1 d_1 + a_2 d_2}{d_1 + d_2}, \quad (3.2)$$

where the subscripts 1 and 2 refer to the InAsP and InP layers, respectively; a is the lattice constant; and d is the layer thickness. This strained MQW structure is also lattice-mismatched to the InP substrate. Thus the total thickness of the quantum well, or the number of periods, must be constrained within a limit.

For a typical modulator structure consisting of 100 Å InAsP and 100 Å InP, the critical number of periods was calculated as a function of the As composition in $\text{InAs}_x\text{P}_{1-x}$. The results are illustrated in Fig. 3.2 as a function of the room-temperature photoluminescence emission wavelength, converted from the As composition for 100-Å wide $\text{InAs}_x\text{P}_{1-x}$ quantum wells in Fig. 1.2. We see that, for instance, $\text{InAs}_{0.4}\text{P}_{0.6}(100 \text{ Å})/$

InP(100 Å) quantum wells for 1.3 μm modulators can be grown with a maximum of 15 period to ensure pseudomorphic layers.

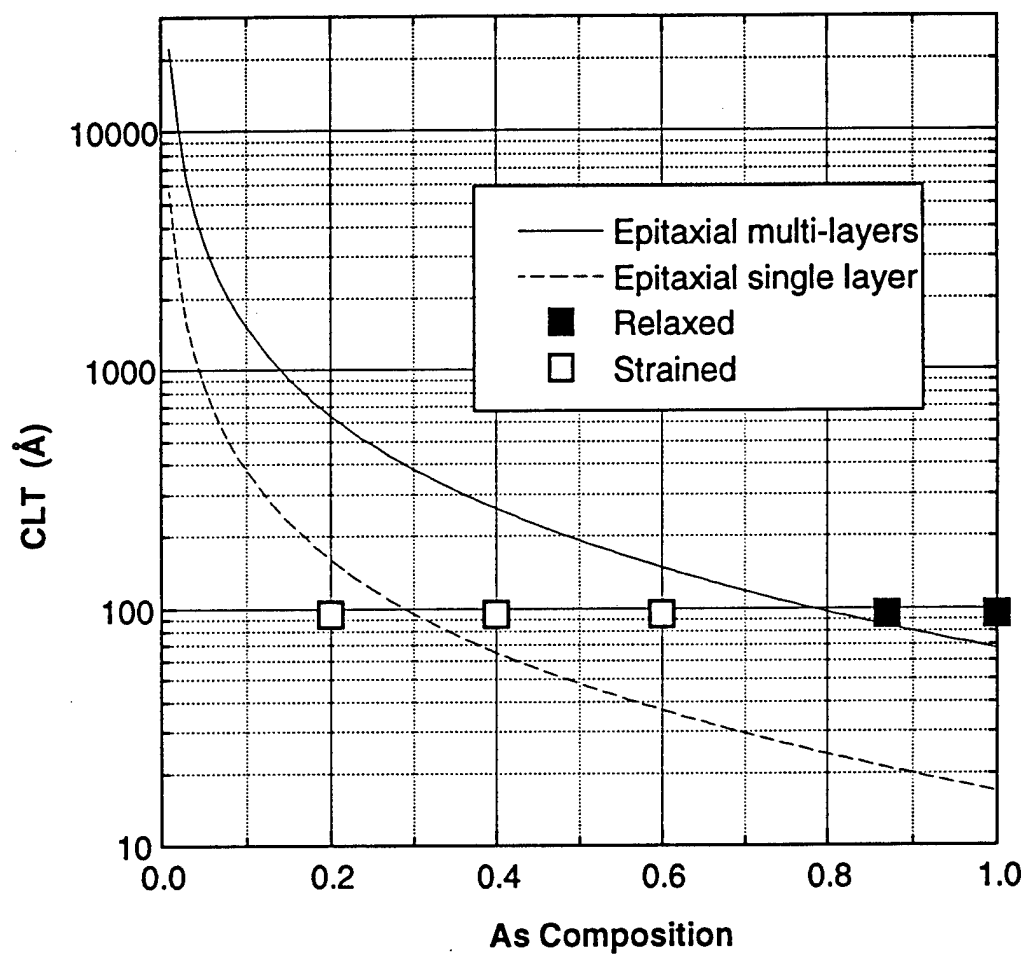


FIG. 3.1 The critical layer thickness of $\text{InAs}_x\text{P}_{1-x}$, pseudomorphically grown on InP, as a function of the As composition. The solid and dashed curves are for multiple and single epitaxial layers, respectively. The open and full squares represent strained and relaxed quantum wells, respectively, examined by PL measurements.

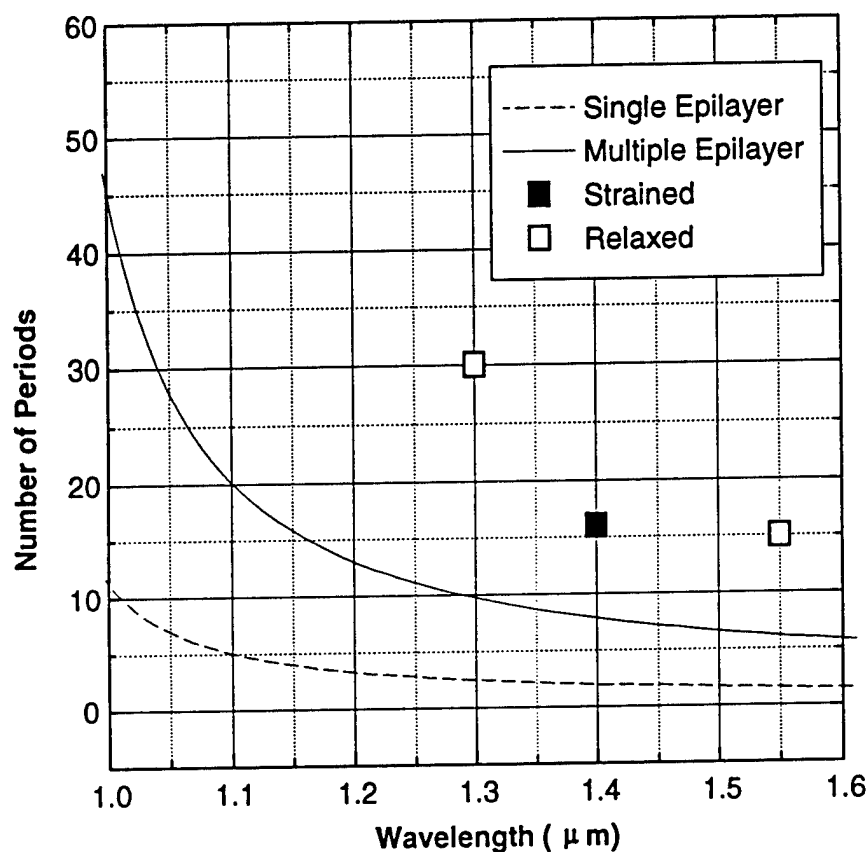


FIG. 3.2 Number of periods for pseudomorphic growth of $\text{InAs}_x\text{P}_{1-x}/\text{InP}$ strained MQWs as a function of the room-temperature emission wavelength. The solid and dashed curves are for multiple and single epitaxial layers, respectively. The open and full squares represent InAsP MQW layers without and with dislocations, examined by TEM images.

3.2.2 CLT determination by PL and TEM measurements

Many experimental approaches have been reported to determine the CLT, e.g., optical[7] (PL spectrum and PL mapping), electrical[8] (Hall) and structural[1,9] (plan-

view TEM, XTEM, and x-ray diffraction) measurements. However, the experimental data have been very scattered, resulting from their different sensitivities for detecting dislocations. In this work, a sample composed of five 95 Å wide single quantum wells with different As compositions, grown on the same substrate, was used to examine the CLT. The emission energy from a strained quantum well should agree with the transition energy calculation considering the bandedge shift due to strain, while a relaxed quantum well would give a smaller emission energy and a broader peak.[7,10] By theoretically fitting the photon energy of the low-temperature PL emission from quantum wells with different depths, the strained and relaxed quantum wells can be identified. Open and full squares in Fig. 3.1 represent strained and relaxed InAsP layers, respectively, identified from the PL spectra. It appears that the CLT determined from PL measurements agrees with the calculation for multiple epilayers. Therefore, we took this calculated curve as a reference for epitaxial growth, and we should be able to obtain a pseudomorphic 100 Å wide $\text{InAs}_x\text{P}_{1-x}$ quantum well with x as high as 0.78.[11]

Another experimental determination of CLT is from the XTEM measurement. XTEM images were taken for the above strained MQW samples (HI06, HI11, and HI35), whose structural parameters are listed in Table 3.1. The XTEM micrographs for two of these three MQW samples are shown in Figs. 3.3(a) and (b). The image from Sample HI11 shows very sharp, flat and dislocation-free InAsP/InP interfaces. In the picture for Sample HI06, however, some dislocation nets, due to strain relaxation, are present at the interface of the strained MQWs and the InP buffer layer. For Sample #35 (not shown) some dislocations and stacking faults appear in the quantum well layers. The number of periods and emission wavelength of these three samples are also plotted in Fig. 3.2. Full and open squares represent strained MQWs with and without dislocations respectively. The experimental results show that more periods, than the calculated value, can be pseudomorphically grown with a proper growth condition.

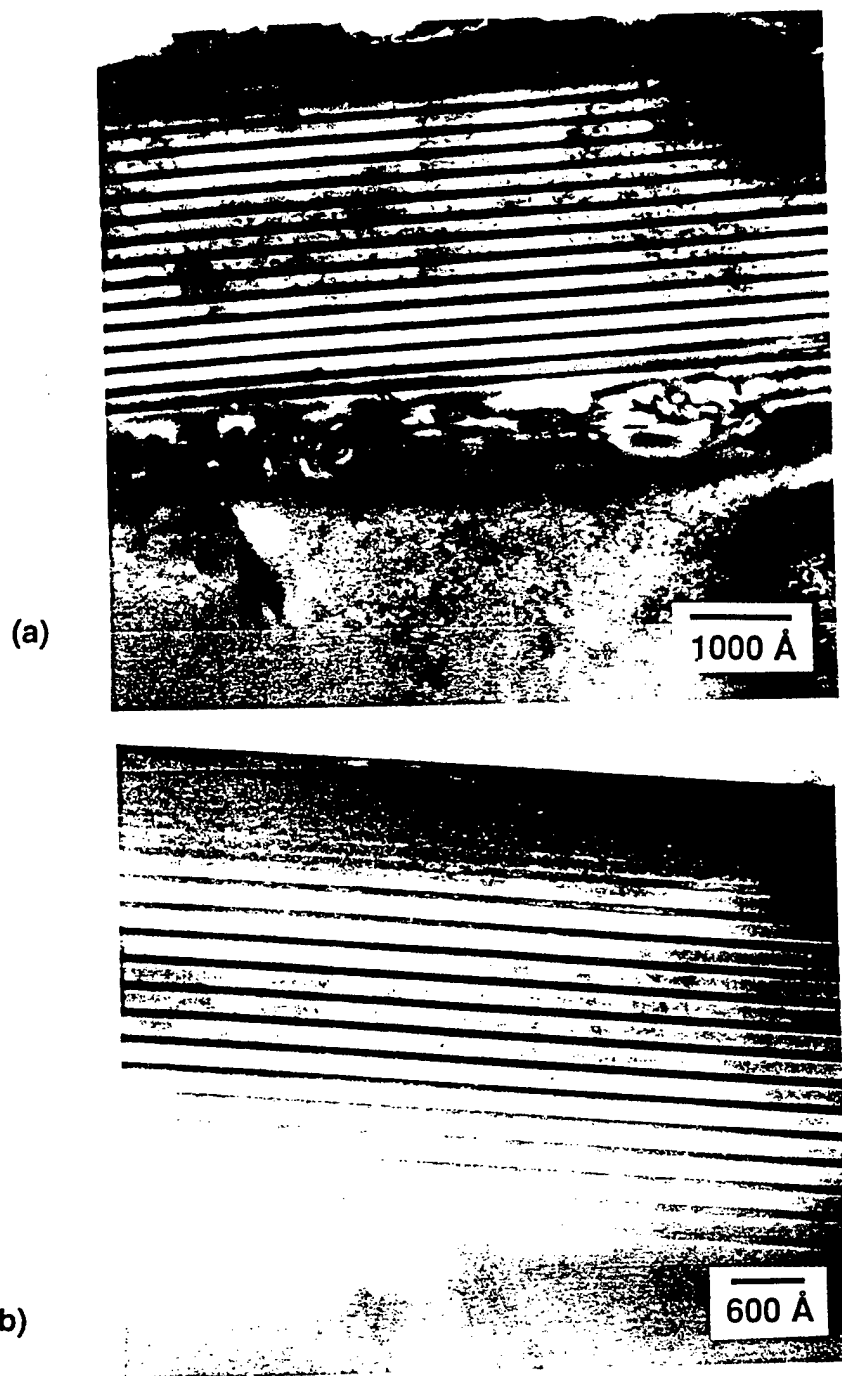


FIG. 3.3 XTEM images taken from (a) HI06 and (b) HI11. Note that in (a) the misfit dislocations lie in the buffer layer; in (b) interfaces are sharp, uniform and free from dislocations.

Table 3.1. Description of the sample structures.

Sample	x	$L_{\text{InAs}_x\text{P}_{1-x}} (\text{\AA})$	$L_{\text{InP}} (\text{\AA})$	Period	Emission (μm)
HI06	0.60	78	144	15	1.55
HI11	0.50	76	162	16	1.40
HI35	0.40	92	138	30	1.30

3.3 Growth of InAsP/InP strained multiple quantum wells on InP (100)

3.3.1 Typical growth conditions

InAs_xP_{1-x}/InP strained MQW structures were grown on (100) Fe-doped semi-insulating or S-doped n^+ InP substrates in a modified Varian Modular GEN-II MBE machine. The growth was performed with elemental indium and thermally cracked hydrides, AsH₃ and PH₃, at a substrate temperature of 460 °C. The gas-source supplies (100% arsine and 100% phosphine) were introduced into the growth chamber through different channels of a single hydride injector or two separate gas injectors, which were operated nominally at 1000 °C. The growth chamber was evacuated with two 2200 l/s cryopumps. The typical working pressure was 1×10^{-5} Torr. The indium flux was set such that the growth rate was typically about 1 $\mu\text{m/hr}$ as calibrated by RHEED oscillation measurements discussed in the previous chapter. The growth rate, therefore, the thickness of InAs_xP_{1-x}, is determined only by the indium beam flux, so the layer thickness of InAs_xP_{1-x} can be controlled independently of the composition, which is related to only the AsH₃ and PH₃ flow-rate fraction.

3.3.2 Growth interruption and interface asymmetry

Initially, we used only one gas cracker for both AsH₃ and PH₃. Since we do not use run-vent mode for switching hydride sources (so as not to vent uncracked hydrides)

during the growth of mixed-group-V compounds, we have to consider carefully the shutter and valve operations when we use different channels of the same injector. Figure 3.4 shows a typical shutter operation procedure. Growth interruptions were performed at each interface to purge out the residual gases and to stabilize beam fluxes. However, we have found that the interruption causes a substitution of the phosphorus by arsenic when we used both AsH_3 and PH_3 to preserve the InP surface.

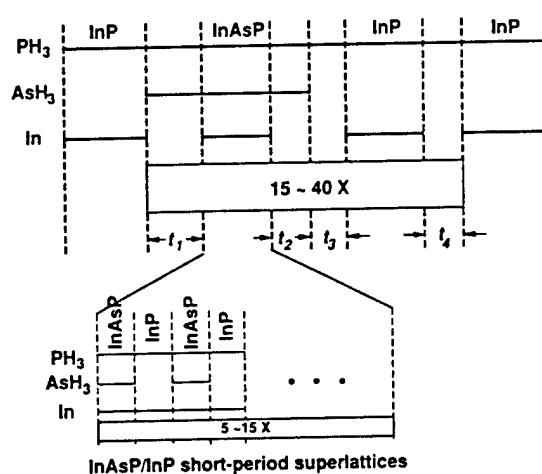


FIG. 3.4 The diagram of the shutter operation sequence for growing InAsP/InP MQW structures. The lower part indicates the growth of $\text{InAs}_x\text{P}_{1-x}$ layer by short-period superlattices.

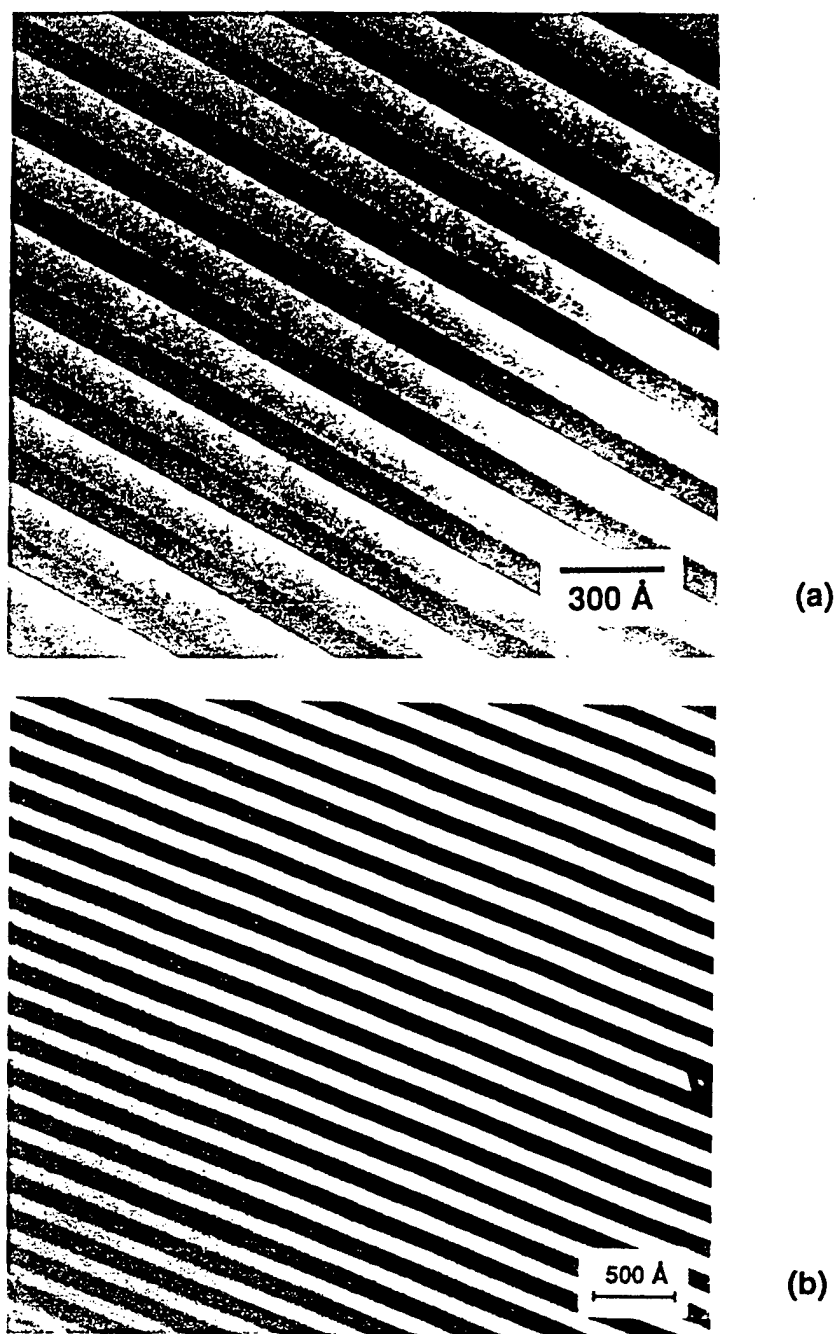


FIG. 3.5 XTEM images from two InAs_xP_{1-x}/InP MQW structures (a) for a sample grown with interruption; Asymmetry in the interfaces is evidenced by the darker contrast at the InAsP/InP interface. (b) for a sample grown without interruption (using two crackers); Sharp and symmetric interfaces are obtained.

Shown in Fig. 3.5(a) is a bright-field XTEM picture for an InAsP/InP MQW structure grown by this interruption technique. It can be seen clearly from Fig. 3.5(a) that the upper interface (from InP to InAsP) is somewhat darker than the lower interface (from InAsP to InP). This was attributed to excess As incorporation or substitution on the InP surface. Therefore, we modified the initial configuration of the MBE machine by installing another home-made gas cracker in the growth chamber to switch gases more conveniently. Two separate crackers for AsH₃ and PH₃, respectively, provide a great flexibility for gas switching by simply operating the shutters in front of the individual gas crackers. Figure 3.5(b) shows a XTEM image from a MQW sample grown by separate crackers. Very sharp and uniform interfaces were obtained, indicative of an improvement of the structural accuracy during this growth.

3.3.3 Approaches for composition control over a wide range

The As composition in InAs_xP_{1-x} was achieved over a wide range by three different methods: As-limited incorporation, As-concentration dilution, and short-period superlattice (SPSL). As discussed in Chapter 2, the As composition can be controlled by a small setting of the AsH₃ flow so that the As composition was limited by the injected As amount when the PH₃ flow rate is not very high. This is actually very convenient and the As composition calibration can be performed *in situ*. However, to achieve an InAs_xP_{1-x} layer with a very small As composition by this growth method is limited by the stability of the mass flow controller at very low flow rate. An alternative method is to use a relatively large PH₃ flow rate, compared to AsH₃, to *dilute* the arsenic fraction in the flux on the growth front. The AsH₃ flow rate was typically fixed at 0.6 sccm, and PH₃ flow rate was varied from 3 to 6 sccm; correspondingly, the x in InAs_xP_{1-x} was varied from 0.65 to 0.10. Another method, as shown at the lower part of Fig. 3.4, is alternately introducing AsH₃ flow during InP growth so that the As composition in the

$\text{InAs}_x\text{P}_{1-x}$ quantum well layer was averaged to a smaller value by these short-period (2 to 5 monolayers per period) InAs/InP superlattices. The x can be controlled with the ratio of the open and close duration of AsH_3 easily with this technique. However, such frequent shutter and valve operation may wear out shutter mechanisms in the long run. Employing these three techniques, we could control x from 0.1 to 0.7 for the growth of strained InAsP layers.

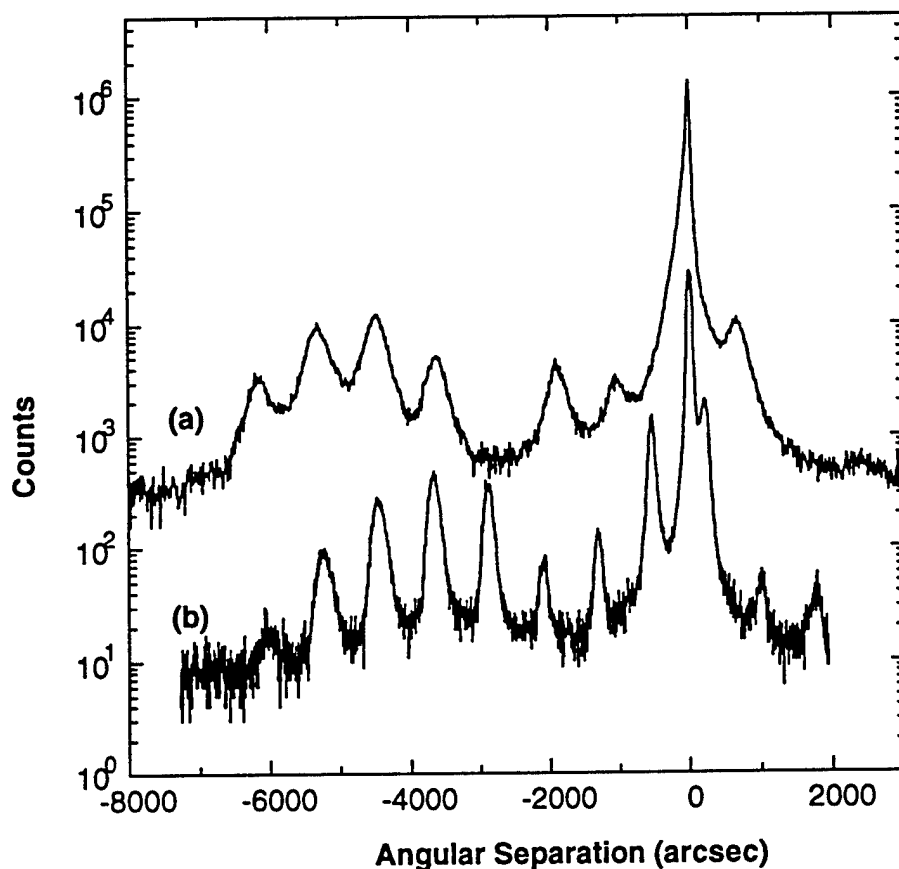


FIG. 3.6 High-resolution x-ray rocking curves with (400) diffraction taken from two highly strained (100) InAsP/InP MQW samples, with (a) from HI06 (lattice mismatch ~2.1%) and (b) from HI11 (lattice mismatch ~1.7%).

3.3.4 Structural characterizations of (100) InAsP/InP strained MQWs

High-resolution x-ray diffraction were recorded with the symmetric (400) diffraction. Figures 3.6(a) and (b) show respective x-ray rocking curves from two highly strained InAsP/InP MQW samples, HI06 and HI11. The mismatches between $\text{InAs}_x\text{P}_{1-x}$ and InP layers for these two samples are 2.1% and 1.7%, respectively. Satellite peaks, resulted from diffraction of strained MQWs, can be observed up to the seventh order, and they are sharp and distinct. This suggests that good periodicity of these multi-layered

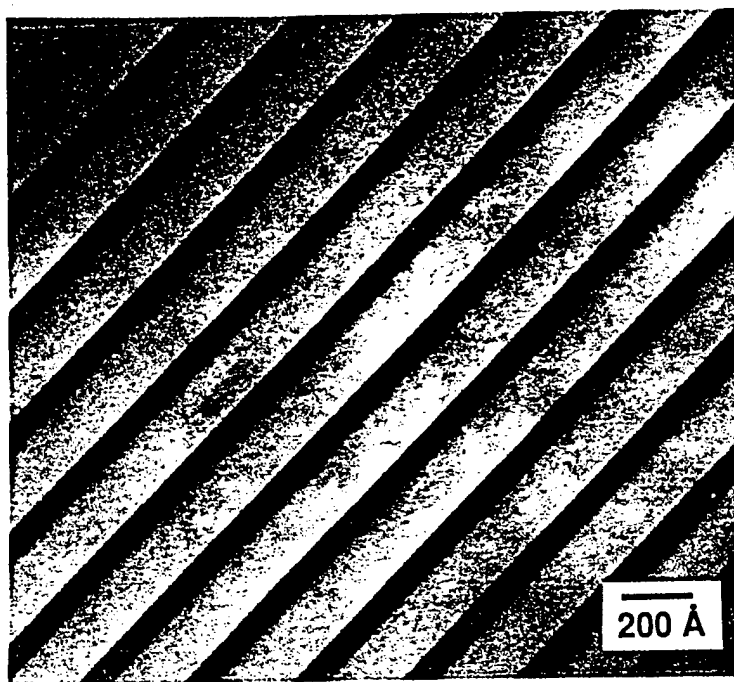


FIG. 3.7 An XTEM microimage for an $\text{InAs}_{0.5}\text{P}_{0.5}/\text{InP}$ strained MQW sample, in which the $\text{InAs}_x\text{P}_{1-x}$ layer was grown with SPSL as resolved by the fine structures in the dark region of the picture.

structures was obtained. The broadening of the peaks in Fig. 3.6(a) is attributed to the partial strain relaxation and As carryover into the InP layer at the interface during growth interruption. Furthermore, the ratio of layer thicknesses of InAs to InP is exactly the same as the ratio of the growth duration of these two layers, because the growth rates of both InAs and InP are determined only by the indium flux.

Figure 3.7 shows a XTEM image taken from Sample HI11, a strained MQW structure with the $\text{InAs}_{0.5}\text{P}_{0.5}$ layer consisting of an $\text{InAs(P)}(2.5 \text{ ML})/\text{InP}(2.5 \text{ ML})$ SPSL. It appears that strained MQW interfaces are very flat and abrupt. No dislocations are observed. Furthermore, five SPSL periods in the $\text{InAs}_{0.5}\text{P}_{0.5}$ layer can be seen clearly, suggesting that the inter-diffusion at the interface of InAsP/InP is not serious enough to degrade the SPSL structure.[12]

3.4 Growth of InAsP/InP strained quantum wells on InP (111)B

3.4.1 *Stereograph and miscut of the (111)B substrate*

Epitaxial growth on low-index surfaces other than (100), namely (111) and (110), is of considerable interest because of associated novel physical properties[13] and also because of the possibility for fabricating quantum wires[14]. For the (111) orientation, there are two different types of surfaces: one terminated with group-III atoms, referred normally as the (111)A surface; and the other terminated with group-V atoms, referred as the (111)B or $(\bar{1}\bar{1}\bar{1})$ surface. Epitaxial growth is primarily performed on (111)B substrates because of the difficulty of chemical cleaning of the (111)A surface.

The growth on (111) substrates is of great importance from the material science point of view. The etched V-grooves belong to a set of $\{111\}$ planes, which are the surface for regrowth of heterostructures.[15] The initial MBE study can be dated back to 1970, when Cho conducted the first homoepitaxial growth on a GaAs(111)B substrate.[2] He reported a very distinguishable RHEED pattern for a clean Ga-rich (111)B surface.

The reconstruction was identified to be $\sqrt{19} \times \sqrt{19}$ $R23.4^\circ$. However, he failed to obtain a specular surface from the epitaxial layer. Pyramid-like surface defects existed on the surface, and the size and density were a strong function of the substrate temperature and the As beam flux. Vina and Wang[16] advanced the surface quality by using a slightly miscut GaAs (111)B substrate. Their intention was to create some surface steps by introducing misorientation to help nucleation and migration of the group-III elements on the surface. Neave *et al.*[3] in 1986 elucidated the function of the surface step in aiding the growth by the so-called step-flow mode. The atoms nucleate preferentially on the step, so the step edge advances. The growth of one-monolayer thickness corresponds to the surface step flows from the original place to an adjacent edge. Under this condition physically absorbed molecules are incorporated in the crystal at steps where the molecular incorporation direction is uniquely determined. Therefore, it is very important to know how the surface steps change with different miscut directions.

Shown in Fig. 3.8 is a stereograph of a face-centered cubic (fcc) structure with a (111) pole direction. Arsenides and phosphides are zincblende structures, which consist of two fcc lattices interlaid a quarter of the diagonal length along the (111) direction. As can be seen, there are two major directions of the miscut with respect to the (111) pole, $\langle 100 \rangle$ and $\langle 110 \rangle$; and several minor directions, such as $\langle 310 \rangle$, $\langle 210 \rangle$, and $\langle 320 \rangle$. Different miscut directions result in different shapes of the surface step; consequently, very different surface morphology can be expected.[17] In this dissertation, we use the convention defined in this stereograph to express the substrate misorientation.

3.4.2 Optimization of the growth condition for homoepitaxial InP

The growth rate of InP was approximately 0.4 ML/sec from the calibration with In-induced RHEED intensity oscillations on an InP(100) substrate. InP (111)B substrates were cleaned and etched with our standard recipe for (100) substrates. The surface oxide

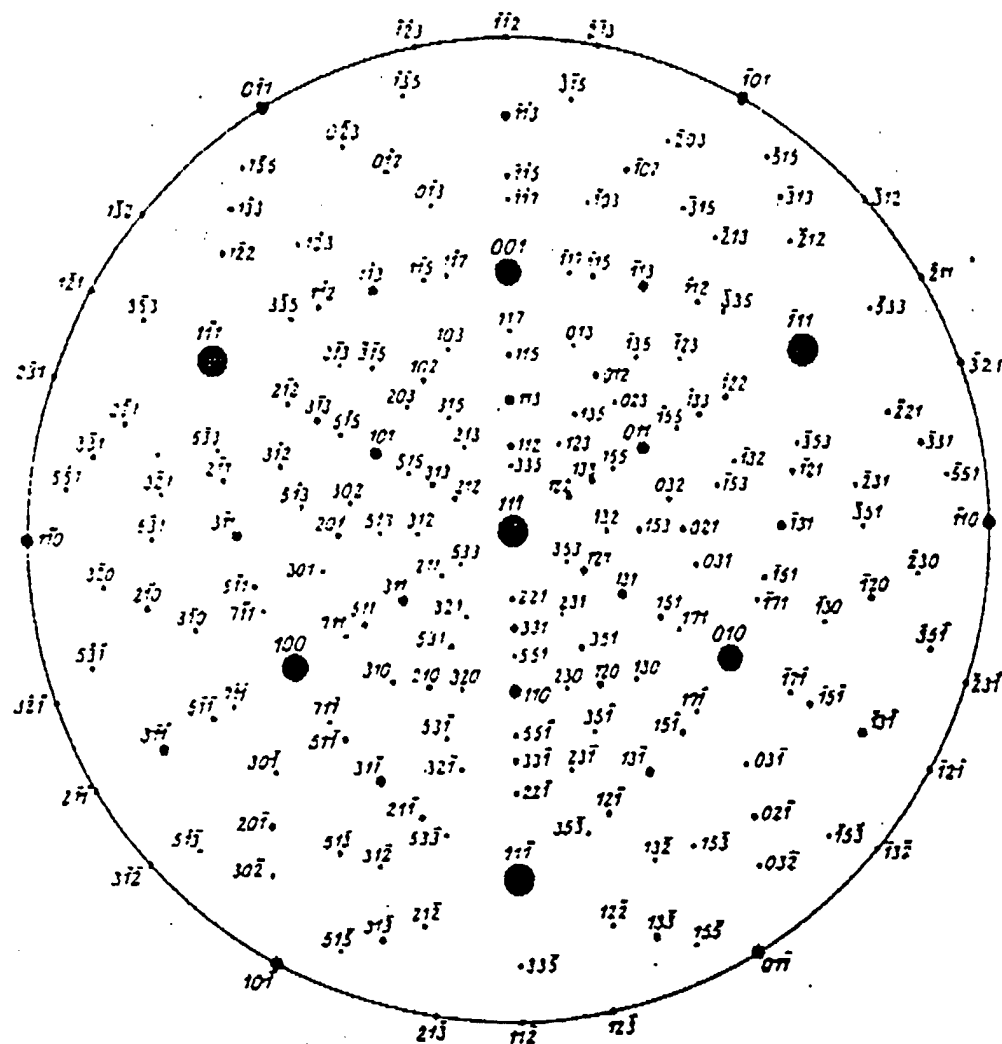


FIG. 3.8 Stereograph for a fcc cubic structure along the (111) pole.

was thermally flashed out at 450 °C under a phosphorus beam flux for about 5 min. in the growth chamber. The (111)B substrates were found thermally more stable than (100) substrates. InP layers were homoepitaxially grown with a substrate temperature (T_s) ranging from 410 to 510 °C, and a V/III incorporation ratio (the ratio of incorporation

rates of phosphorus over indium as respectively determined by group-V- and group-III-induced RHEED oscillations[18]) from 1 to 5. A (2×1) surface reconstruction was identified from the RHEED pattern for a clean InP surface after thermal flashing and during growth. Even though a wide range of the PH_3 gas flow was used we have never seen the $\sqrt{19}\times\sqrt{19}$ pattern on InP (111)B surface.[2]

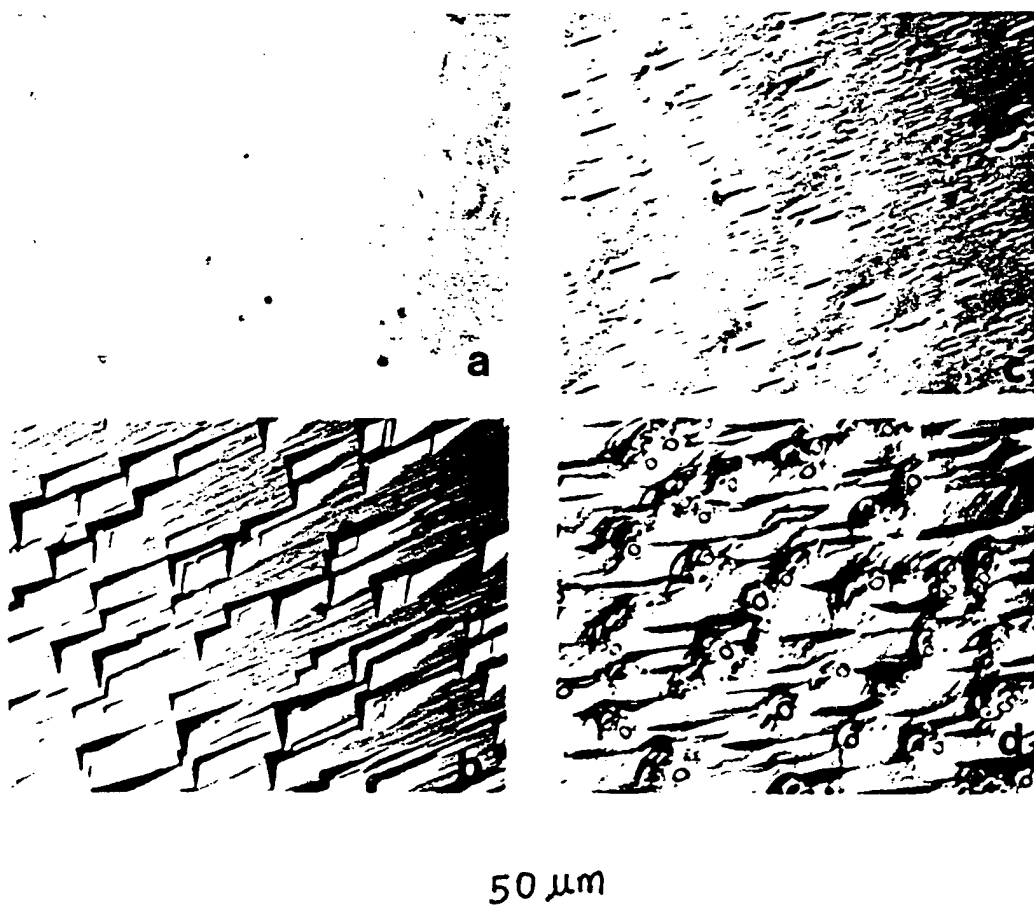


FIG. 3.9 Nomarski micrographs of the surface of 1 μm InP epilayers grown on InP (111)B substrates with misorientation of 0.5° toward $\langle 110 \rangle$ under different substrate temperatures and V/III incorporation ratios. (a) $T_s=470^\circ\text{C}$, V/III~1; (b) $T_s=470^\circ\text{C}$, V/III~3; (c) $T_s=490^\circ\text{C}$, V/III~1; and (d) $T_s=490^\circ\text{C}$, V/III~3.

Since atoms on a (111)B surface have only a single dangling bond, whereas they have two on a (100) surface, it is energetically more stable for group-III atoms to fall into the sites with two dangling bonds, resulting in pyramid-like surface defects due to the (100) facet growth. Thus, a key issue for obtaining a good surface morphology on a (111) surface is to introduce a small misorientation so that the surface step permits the growth to be governed by a step-flow mode.[3] At the edge of these steps an adatom shares two dangling bonds, thus resembling the case of a (100) surface. This type of adsorption is more stable than that by a single dangling bond existing on a flat (111)B surface.[19] Therefore, we used exactly oriented, misoriented 0.5° , 1° or 2° toward $\langle 100 \rangle$ or $\langle 110 \rangle$ InP (111)B substrates in the present study.

Figures 3.9(a)-(d) show Nomarski interference contrast micrographs of the surface morphology of $1\text{ }\mu\text{m}$ InP films grown on (111)B substrates with 0.5° off toward $\langle 110 \rangle$ at various substrate temperatures and V/III incorporation ratios. Our results show that the surface morphology is generally better when the film was grown at higher temperature. However, some hexagonal voidlike surface defects begin to appear when the T_s is higher than 490°C , as shown in Figs. 3.9(c) and (d). These surface defects are likely due to the evaporation of phosphorus from decomposed InP. On the other hand, poorer surface morphology was observed with increasing the phosphorus flux (or V/III incorporation ratio) because of a retardation of indium migration by the excess phosphorus on the surface, as depicted in Figs. 3.9(b) vs. (a), and 3.9(d) vs. (c). We further examine the surface morphology of the films grown at higher T_s ($>490^\circ\text{C}$) with a higher phosphorus flux (up to V/III~5) protection. we find that voidlike surface defects always exist when the T_s is higher than 490°C even with higher V/III ratio. Therefore, an optimal growth condition is identified as $T_s \sim 470^\circ\text{C}$ and V/III ratio ~ 1 for the InP growth on (111)B with 0.5° off toward $\langle 110 \rangle$. Featureless surfaces are obtained with these optimized growth conditions, as shown in Fig. 3.9(a). Since the migration length

may differ slightly for substrates with different misorientations, a small deviation of the optimal conditions are observed for 1° and 2° misoriented substrates. We find that the higher T_s is better for the substrate with more misorientation, such as 2° off, yet the voids appear subsequently on the surface. Hence, it is more readily to obtain a good surface with 0.5 - 1° misorientation.

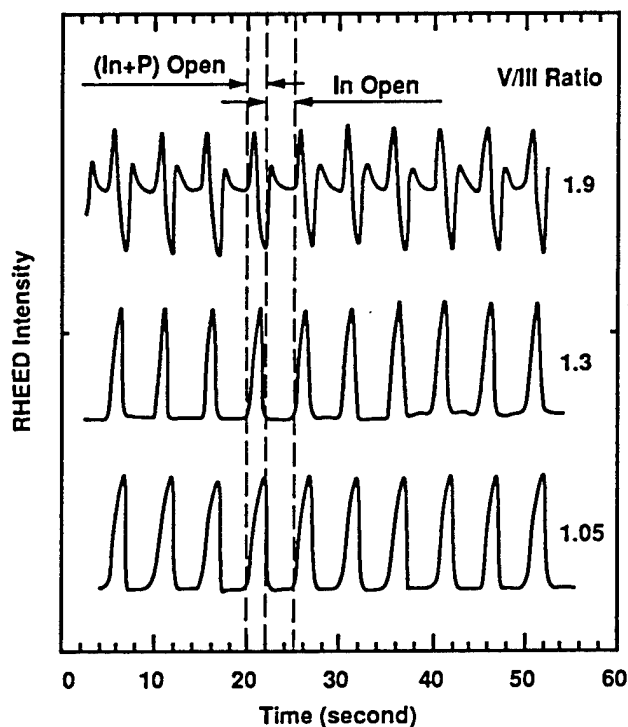


FIG. 3.10 RHEED oscillations during modulated phosphorus beam growth with different V/III incorporation ratios. The sequence of the shutter operation is also indicated.

An alternative method to improve the surface morphology was performed by modulating the phosphorus beam while supplying the indium beam continuously, a manner similar to migration-enhanced epitaxy (MEE).[20] The termination of the phosphorus beam flux is to enhance the migration of surface indium atoms. A typical growth sequence of modulated beam epitaxy is shown in Fig. 3.10. Different V/III incorporation ratios were employed. The unity V/III incorporation ratio represents the growth condition that the phosphorus flux is just enough to compensate the deposited indium atoms in a cycle. The RHEED intensity oscillations are shown in Fig. 3.10. The persistence of equal amplitude oscillations indicates a step-flow growth mode was achieved in all of these growth runs.[20] However, the temporal change of the RHEED intensity differs significantly with different V/III ratios. With increasing V/III ratio, the retardation of the indium atom migration results in a decrease of the RHEED intensity during the indium and phosphorus supply. The unity V/III ratio increases the intensity monotonically, indicating the most efficient migration of indium atoms at this condition. This result is consistent with the surface morphology observation. We have obtained featureless surface morphology of InP epitaxial layers grown on all of the misoriented and exact (111)B substrates by using the modulated-beam technique.[21] It has been reported recently that mirror-like surfaces can also be achieved on exactly (111)B GaAs substrates by either carefully controlling the growth condition by monitoring the intensity of the RHEED [22] or by MEE.[20]

3.4.3 Optimization of the growth condition for InAsP/InP heterostructures

InP (111)B substrates with 0.5° , 1° or 2° misorientation toward $\langle 100 \rangle$ or $\langle 110 \rangle$ were used in this study because a step-flow growth mode likely produces a mirror-like surface morphology. The $\text{InAs}_x\text{P}_{1-x}/\text{InP}$ strained quantum well structures were grown under the optimal conditions determined for InP. A typical structure consists of 15-period

InAsP(80 Å)/InP(120 Å) MQWs. In order to compare the optical property of (111) MQWs directly with (100) MQWs, the same structure was also grown consecutively on a (100) substrate with identical growth conditions except that the InP buffer layer on the (100) substrate was grown with a V/III incorporation ratio of approximately 1.5 [since a unity ratio usually results in a hazy surface for (100) growth]. Shown in Figs. 3.11(a)-(d) are Nomarski micrographs of the surface morphology from 15-period InAs_{0.21}P_{0.79}(80 Å)/InP(120 Å) strained MQWs grown side-by-side on (111)B substrates with 0.5 and 1°

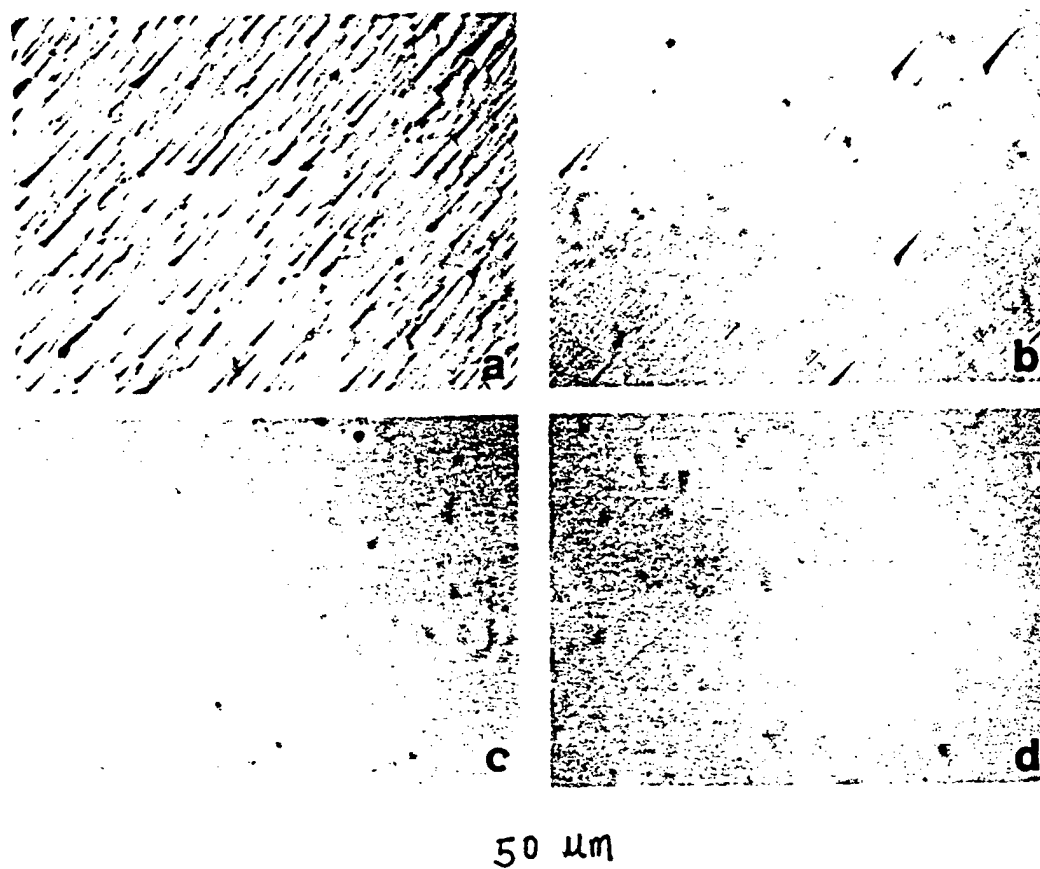


FIG. 3.11 Nomarski micrographs of surfaces of 15-period InAsP(80 Å)/InP(120 Å) strained MQW structures grown on InP (111)B substrates with various misorientations. (a) 0.5° off toward <110>; (b) 1° toward <110>; (c) 0.5° toward <211>; and (d) 1° toward <211>.

off toward $\langle 110 \rangle$ and $\langle 211 \rangle$ directions, respectively. As can be seen in Fig. 3.11(a) and (c), some pyramid-like structures exist. These are believed to appear during InAsP growth since the InP films grown at the same condition show specular surfaces. It is reasonable that the optimal growth conditions for InP and InAsP could be slightly different. The hatch lines, intersecting at 120° , can be seen from Fig. 3.11(d); these are attributed to strain relaxation in the InAsP layer. However, we can obtain a specular surface from the same structure grown on a (111)B substrate with 1° off toward $\langle 110 \rangle$ direction, as shown in Fig. 3.11(b). These results suggest that the misorientation with 1° off toward $\langle 110 \rangle$ direction is the most desirable for growing InAsP/InP strained heterostructures.[17]

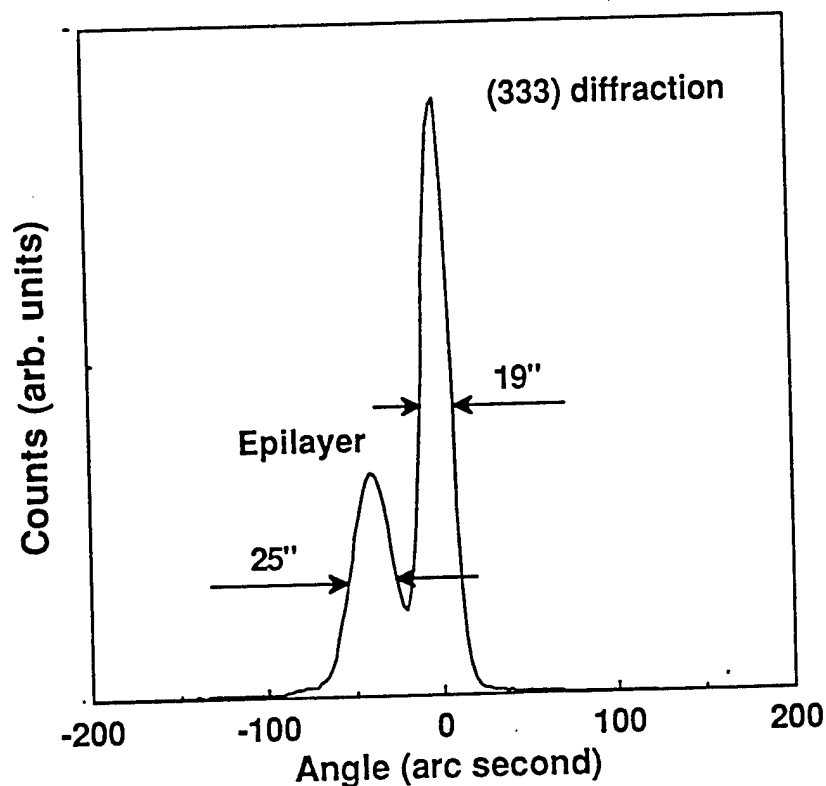


FIG. 3.12 A symmetric (333) x-ray rocking curve taken from a $1\text{ }\mu\text{m}$ thick InP (111)B epilayer with 0.5° misorientation.

3.4.4 Characterization of (111)B InP epilayers

Specular InP epilayers were examined by high-resolution x-ray rocking curves. A symmetric diffraction from a monochromatic radiation of the Cu $K\alpha_1$ line was recorded in the vicinity of the (333) reflection. A typical x-ray rocking curve from a 1 μm thick InP film is shown in Fig. 3.12. The peak located at the 0 position is identified to be from the InP (111)B substrate, with a full width at half maximum (FWHM) of 19 arcsec. The peak appearing at a smaller angle is from the InP epilayer. The small angular separation from the substrate peak is due to a small arsenic contamination in the MBE chamber. The incorporation of the As in InP layer, InP(As), is estimated to be only about 1%. This offset makes the characterization of epilayer even easier. The FWHM from the InP epilayer is as narrow as 25 arcsec. This indicates a good macroscopic crystalline quality.

Photoluminescence measurements were carried out at about 20 K. The luminescence was excited by the 5145 Å line of an argon ion laser. Shown in Fig. 3.13 are PL spectra taken from three 1.0 μm thick InP epilayers grown on 0.5° off to <110> InP (111)B substrates at $T_s=450$, 470 and 490 °C, respectively. These peaks are attributed to the bound exciton transitions. The smallest FWHM was achieved from the sample grown at $T_s=470$ °C (3.5 meV). This result is consistent with the observation of the best surface morphology. A slightly larger linewidth (5.3 meV) and smaller emission energy were observed from the InP layer grown at 450 °C than the film grown at 470 °C. This may be due to more impurity incorporation when it was grown at lower temperature. An intense and broad (FWHM=9.7 meV) peak was seen for the InP layer grown at 490 °C. This strong peak at low energy is assigned as the defect-related transition since many voidlike defects exist on the sample surface. A lower impurity incorporation at this high growth temperature could also be responsible for the high PL intensity from this sample. The PL intensity is as intense as those from (100) InP films grown side-by-side.[21]

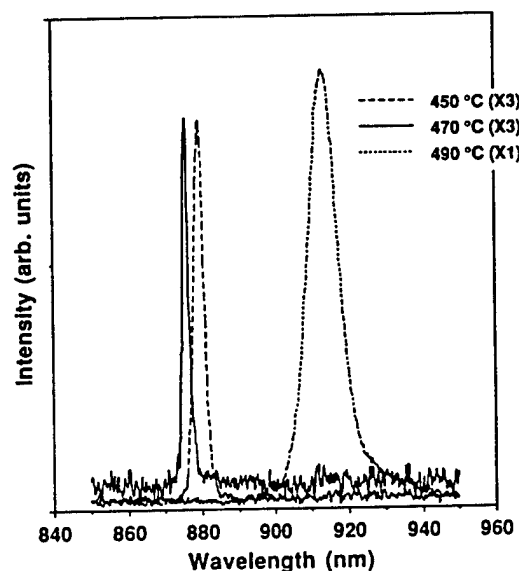


FIG. 3.13 Low-temperature PL spectra taken from 1 μm thick homoepitaxial InP layers grown at $T_s = 450, 470$ and 490 °C. The FWHMs for these three samples are 5.3, 3.5 and 9.7 meV, respectively.

Our recent experimental results from high-resolution PL measurements at low temperature[23] indicate that phosphorus vacancies are likely produced in the InP growth by modulated-beam technique. As a result, some fine spectral structures with emission energies slightly smaller than the InP bandgap are resolved. In addition, the frequent shutter operation in this technique makes the modulated-beam growth technique undesirable. Thus, the (111)B samples were primarily grown under the optimal conditions determined above using continuous growth.

Room-temperature Hall measurements of a 2 μm undoped InP show a mobility of 4000 cm^2/Vs with an n -type background carrier concentration of $3 \times 10^{15} \text{ cm}^{-3}$. A Si-doped InP film has a mobility of 2800 cm^2/Vs with an electron concentration of $3 \times 10^{18} \text{ cm}^{-3}$. These results are comparable to those obtained from (100) InP layers.[16]

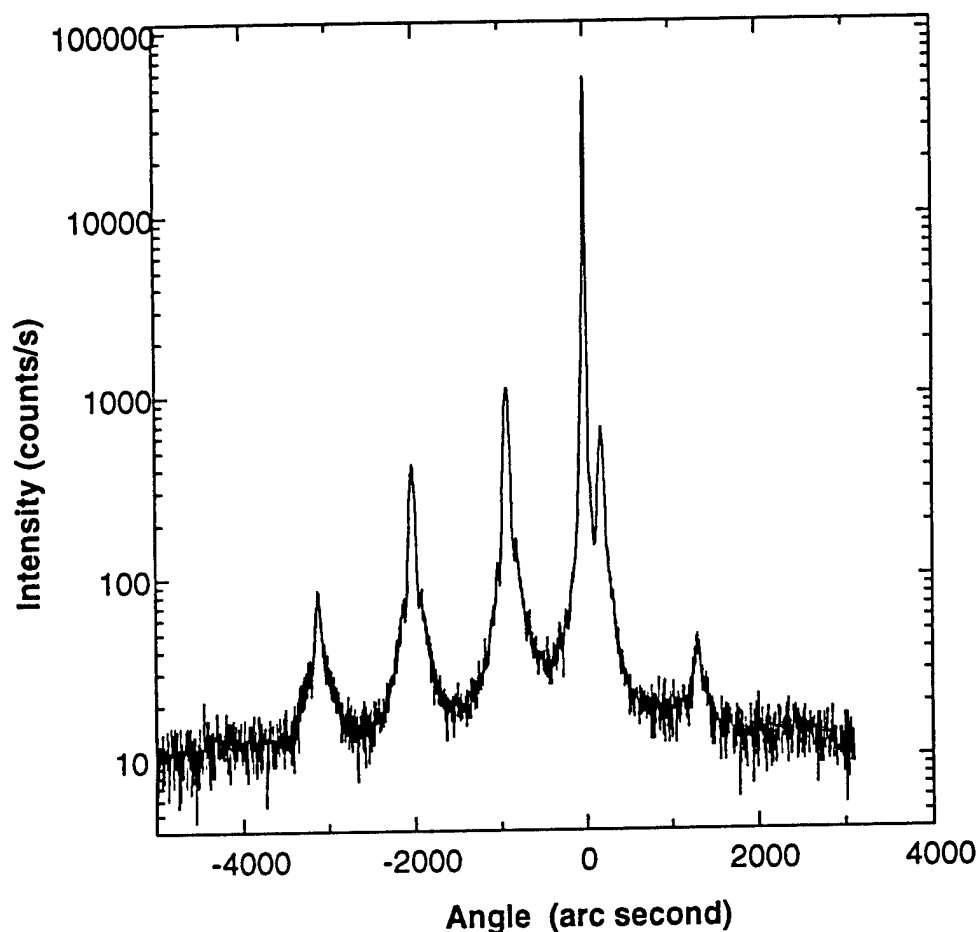


FIG. 3.14 A typical x-ray rocking curve of a symmetric (333) diffraction from a 15-period $\text{InAs}_{0.21}\text{P}_{0.79}$ (80 Å)/InP (120 Å) strained MQW structure. Intense and sharp satellite peaks can be seen up to the third order, and Pendellösung fringes appear on the wings of the substrate and adjacent satellite peaks.

3.4.5 Characterization of (111)B InAsP/InP strained MQWs

Specular InAsP/InP MQW structures were examined by high-resolution x-ray rocking curves. A symmetric (333) diffraction from a 15-period $\text{InAs}_{0.21}\text{P}_{0.79}$ (80 Å)/InP(120 Å) strained MQW structure is shown in Fig. 3.14. Sharp and distinct satellite peaks can be observed up to the third order, and the Pendellösung fringes due to the interference of diffraction from the whole MQW structure can be observed, indicating good crystalline quality, lateral uniformity and vertical periodicity. Simulations to rocking curves (see details in the next section) taken from the samples grown on both (111)B and (100) substrates based on the dynamical theory show that almost the same growth rate and group-V incorporation behavior exist for the growth on these two differently oriented substrates.

Specimens for XTEM were thinned by chemical polishing, and ion milling at 77K, which effectively reduced indium segregation. Shown in Fig. 3.15(a) is an XTEM micrograph from a 15-period $\text{InAs}_{0.21}\text{P}_{0.79}$ (80 Å)/InP(120 Å) strained MQW structure possessing a specular surface morphology grown on an InP (111)B substrate with 1° miscut to <110>. We see very sharp and uniform InAsP/InP interfaces. No defects were observed even when the specimen was tilted around. The lattice mismatch (~0.7%) between $\text{InAs}_{0.21}\text{P}_{0.79}$ and InP is apparently accommodated coherently. However, for the same structure grown on an InP (111)B substrate with 1° miscut to <100>, we observed some hatch lines on the surface due to strain relaxation. The surface morphology for this sample is shown in the inset of Fig. 3.15(b). We observed misfit dislocations, some of which even penetrate into the InP buffer layer as a consequence of the strain energy relief, as illustrated in Fig. 3.15(b).

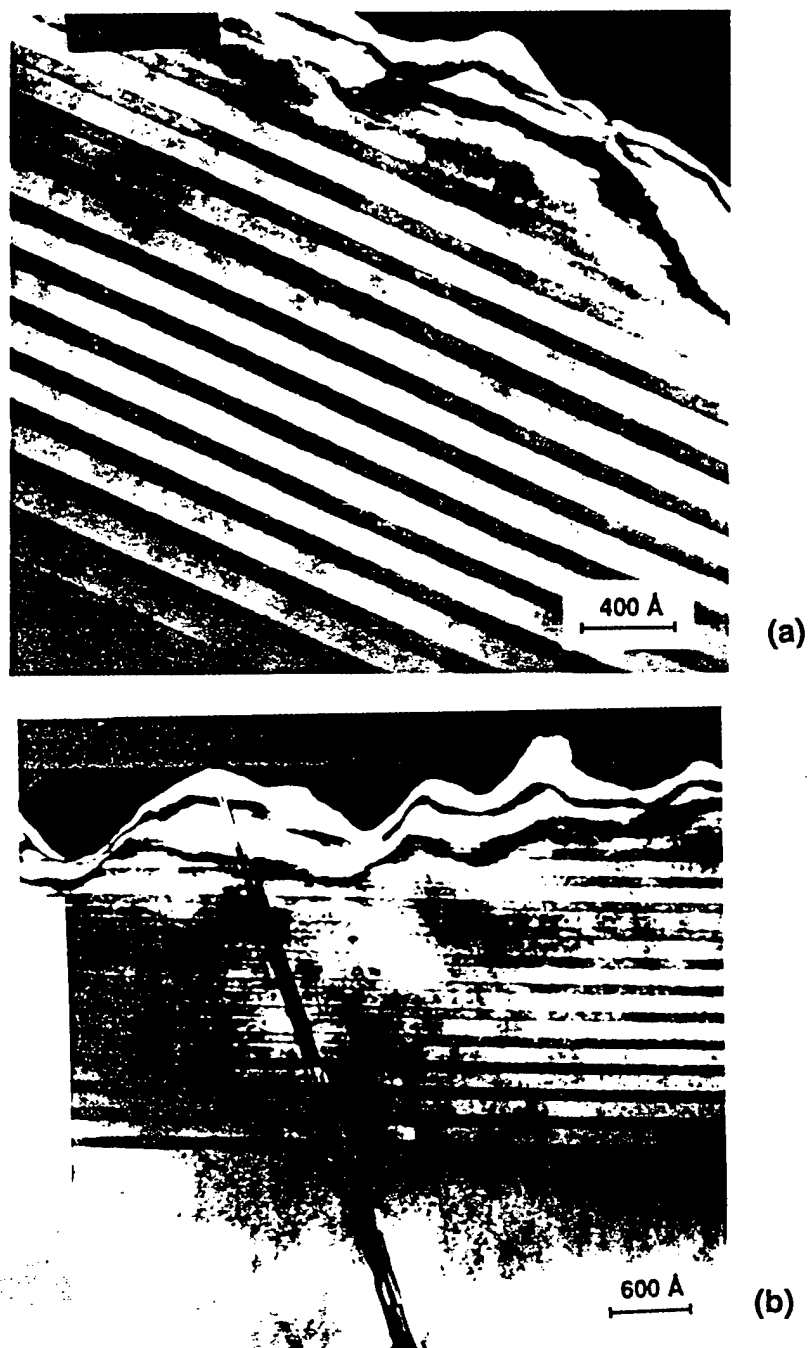


FIG. 3.15 XTEM micrographs taken from InAsP/InP MQWs grown on InP (111)B substrates with a 1° misorientation toward to (a) $\langle 110 \rangle$ direction, and (b) $\langle 100 \rangle$ direction. The inset of (b) shows the Nomarski microscopic picture of the surface morphology. Hatch lines are due to strain relaxation.

3.5 Simulation of x-ray rocking curves

3.5.1 High-resolution x-ray rocking curves

Specular InAsP/InP MQW structures were examined by high-resolution x-ray rocking curves. Symmetric diffraction [(400) for (100) samples and (333) for (111)B samples] from a monochromatic radiation of the Cu $K\alpha_1$ line was recorded. The four-reflection monochromator consists of two channel-cut Ge crystals (220 reflections), as described by Bartels.[24] The diffraction signal was detected at an angle of $2\theta_B$ when the sample was scanned in the vicinity of Bragg angle θ_B . The diffraction configuration is depicted in Fig. 3.16. The θ_B satisfies the Bragg diffraction condition:

$$2d\sin\theta_B = n\lambda, \quad (3.3)$$

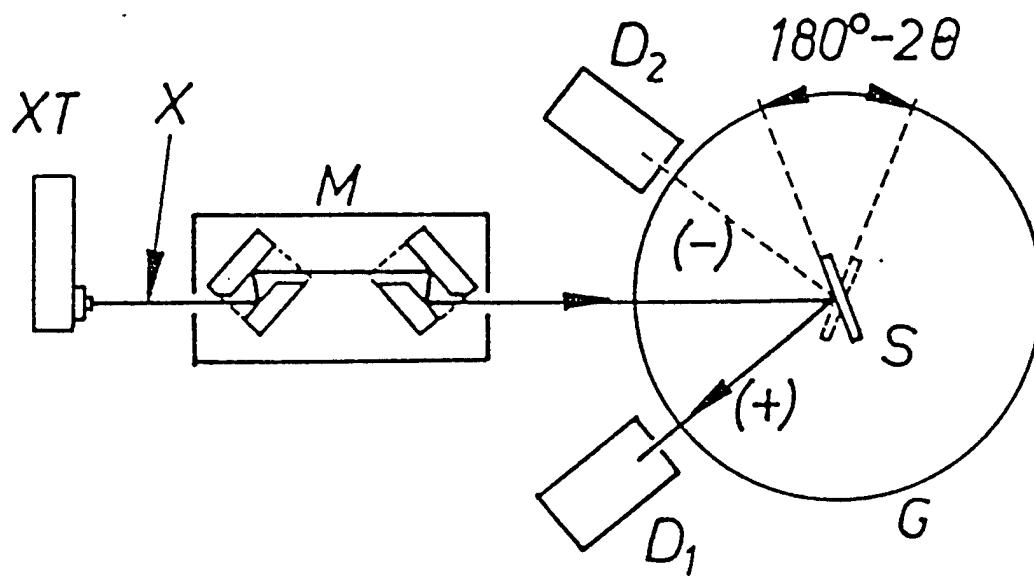


FIG. 3.16 Schematic diagram of the diffraction configuration of the x-ray diffractometry.

where λ is the x-ray wavelength and is approximately 1.5406 Å for the Cu K α_1 line; d is the spacing of diffraction planes; it depends on both the lattice constant and the crystal plan indices (h, k, l):

$$d = \frac{1}{\sqrt{\frac{h^2}{a_x^2} + \frac{k^2}{a_y^2} + \frac{l^2}{a_z^2}}} . \quad (3.4)$$

Some structural information can be obtained from the x-ray rocking curve even without running simulations. For instance, the total layer thickness ($L_z + L_b$) for one period can be obtained from the angular separation of adjacent satellite peaks, $\Delta\theta_{0,\pm 1}$ from

$$L_z + L_b = \frac{\lambda}{2\Delta\theta_{0,\pm 1} \cos\theta_B} . \quad (3.5)$$

Moreover, the composition of InAs $_x$ P $_{1-x}$ can be estimated from the angular separation between the zeroth order satellite peak of MQWs and the substrate peak, $\Delta\theta_{0,s}$ from the derivative to the Bragg condition, Eq. (3.3). It reads

$$\frac{\Delta d'}{d'} = -\cot\theta_B \Delta\theta_{0,s}, \quad (3.6)$$

where d' is the average plane spacing of the MQW structure. The alloy composition can be easily calculated from d' .

3.5.2 Elastic deformation and anisotropy of the elastic tensor

For a pseudomorphic multi-layered structure, the alloy composition can be determined from its average lattice-plane spacing in the growth direction. In the tetragonal distortion approximation of a strained layer with respect to the film

coordinates, the strain tensor for a strained layer on a (100) surface possesses only nonzero diagonal elements, and these elements can be expressed as[25,26]

$$\begin{aligned}\varepsilon_{xx} = \varepsilon_{yy} &= \frac{a_f - a_o}{a_f} \equiv \varepsilon_o, \\ \varepsilon_{zz} &= -\frac{2C_{12}}{C_{11}}\varepsilon_o,\end{aligned}\tag{3.7}$$

where a_f and a_o are the respective lattice constants of the free-standing $\text{InAs}_x\text{P}_{1-x}$ layer and the InP substrate. C_{11} and C_{12} are elastic stiffness constants.

However, the elastic deformation in the (111) direction is anisotropic, as demonstrated in Refs. 25 and 26. Basically, the lattice-mismatch between $\text{InAs}_x\text{P}_{1-x}$ and InP generates a tetragonal distortion with respect to the growth surface, but not with respect to the cubic axes (crystalline coordinates). Therefore, the off-diagonal elements of the strain tensor, which measure shear deformations, are nonzero. After an orthogonal basis transformation, the strain tensor elements, written with respect to the coordinates of the film [(111)B surface], are

$$\begin{aligned}\varepsilon_{11} = \varepsilon_{22} &= \frac{a_f - a_o}{a_f} \equiv \varepsilon_o, \\ \varepsilon_{33} &= \frac{-2C_{11} - 4C_{12} + 4C_{44}}{C_{11} + 2C_{12} + 4C_{44}}\varepsilon_o, \\ \varepsilon_{23} = \varepsilon_{31} = \varepsilon_{12} &= 0.\end{aligned}\tag{3.8}$$

Corresponding to a transformation of the strain tensor, diffraction indices must be transformed by the same basis matrix.[26] The symmetric (333) diffraction, for example, was transformed to $(0, 0, \sqrt{27})$ accordingly in the film coordinates.

3.5.3 Computer simulation and structural parameter determination

To simulate the x-ray rocking curve there are mainly two diffraction theories popularly used, the kinematical model and dynamical model. The former takes into account of only a single reflection, but the physical picture is intuitive;[27,28] while the latter takes into account of multiple reflections, and therefore are more rigorous.[29,30] We have carried out computer simulations based on the dynamical diffraction theory. We will not present the details for this model here. Interested readers can refer to the Refs. 29 and 30.

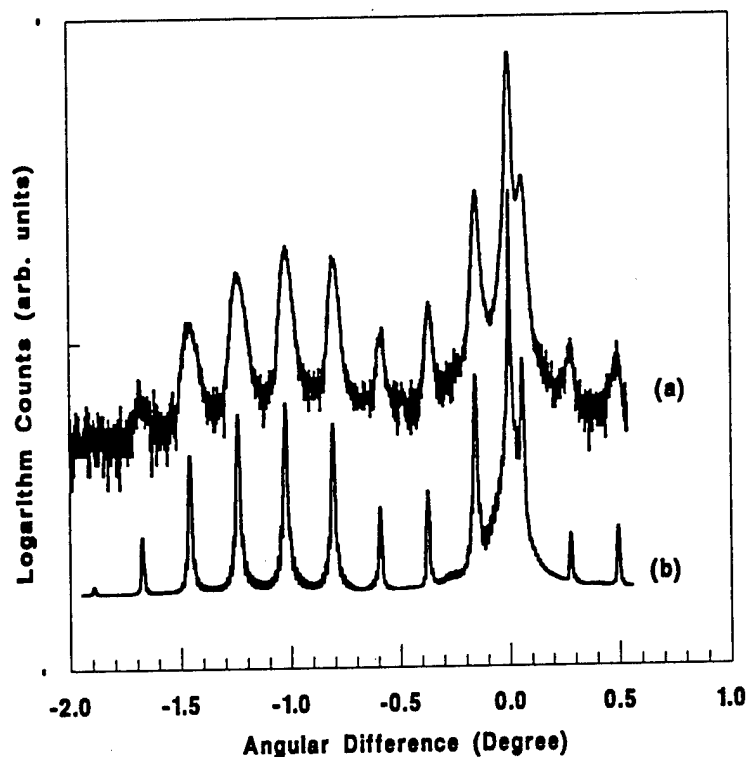


FIG. 3.17 (a) A high-resolution x-ray rocking curve and (b) a dynamic-theory simulation for a 15-period (100) $\text{InAs}_{0.5}\text{P}_{0.5}$ (76 Å)/ InP (162 Å) strained MQW structure. The best fit allows a precise determination of the arsenic composition and well and barrier layer thicknesses.

We assume that interfaces are abrupt and flat, and the chemical composition in the alloy layer is uniform. The elastic deformation is a tetragonal distortion in the growth direction. The simulation was conducted by assuming that $\text{InAs}_x\text{P}_{1-x}$ layers are pseudomorphically strained and that InP layers are unstrained.

Shown in Fig. 3.17(b) is the best fit to the symmetric (400) rocking curve Fig. 3.17(a), which was taken from a nominal structure of 16-period $\text{InAs}_{0.5}\text{P}_{0.5}$ (73 Å)/InP(158 Å) strained MQWs. Satellite peaks, resulting from diffraction of strained MQWs, can be observed up to the seventh order, and they are sharp and distinct. This indicates that this highly-strained (1.7%), multi-layered structure possesses a good periodicity. The best fit suggests that the strained MQW consists of 16-period $\text{InAs}_{0.5}\text{P}_{0.5}$ (76 Å)/InP(162 Å), which is in excellent agreement with the nominal parameters given by the growth condition. The slight broadening of the actual rocking curve shown in Fig. 3.17(a) may be attributed to As carryover into the InP layer at the interface during growth interruption. Another possibility is the incorporation of residual As. This small, but not periodic *contamination* in the InP layer could result either from the cracker or from the chamber, which were not considered in the simulation.

Figure 3.18 depicts a typical symmetric (333) x-ray rocking curve and simulation taken from a (111)B $\text{InAs}_x\text{P}_{1-x}$ /InP strained MQW structure. Figure 3.18(b) is the best fit to the experimental curve Fig. 3.18(a) with a special consideration for the strain distortion and diffraction conversion discussed above. The structural parameters used in the best fit are for a 15-period $\text{InAs}_{0.21}\text{P}_{0.79}$ (79.5 Å)/InP(119 Å) MQW structure. These parameters are very close to the nominal parameters [15-period $\text{InAs}_{0.2}\text{P}_{0.8}$ (80 Å)/InP(120 Å)], implying a very good control in the MBE growth. Excellent fits for peak positions and profiles suggest an excellent periodicity and structural accuracy of the MQWs. From this discussion, we can see that the x-ray rocking curve and computer

simulations are very powerful in characterizing structural properties and determining structural parameters precisely.

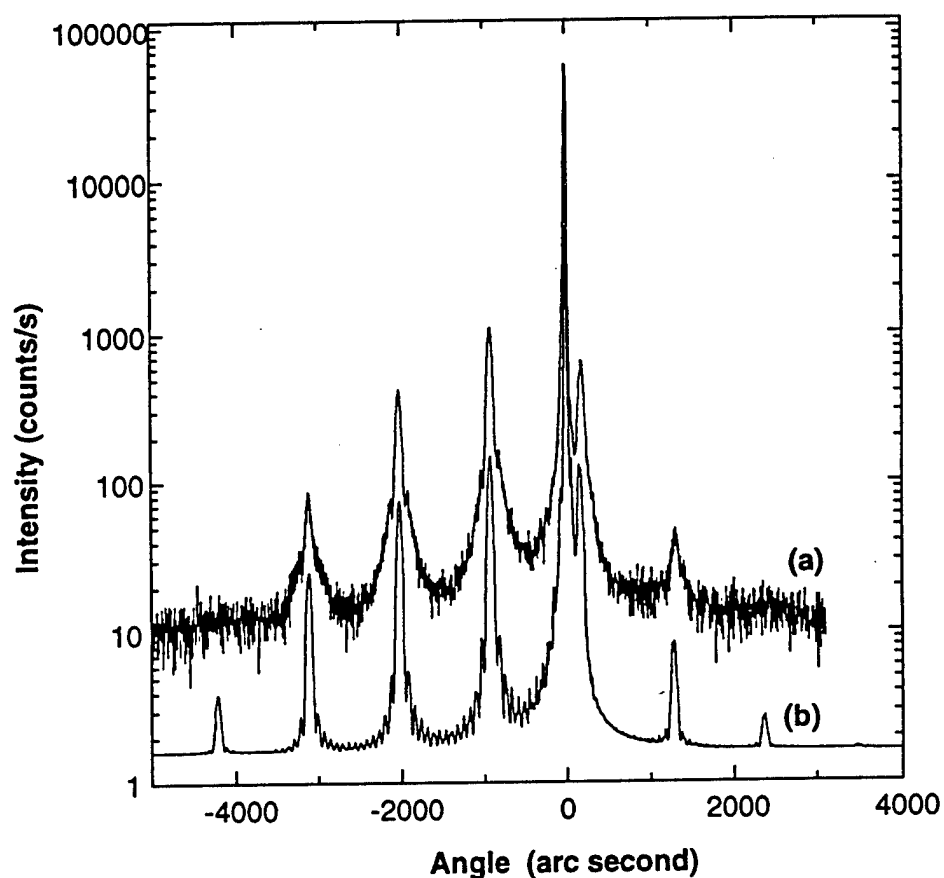


FIG. 3.18 (a) An x-ray rocking curve from (111)B 15-period $\text{InAs}_{0.21}\text{P}_{0.79}(80 \text{ \AA})/\text{InP}(120 \text{ \AA})$ strained MQWs in the vicinity of symmetric (333) diffraction. Satellite peaks and Pendellösung fringes show good crystalline quality. (b) A dynamical-theory simulation considering the anisotropy of the strain tensor in (111) orientation.

3.6 Conclusion

In summary, we have presented studies on the epitaxial growth and structural properties of strained (100) and (111)B $\text{InAs}_x\text{P}_{1-x}/\text{InP}$ strained MQWs in this chapter. Critical layer thickness for pseudomorphic epitaxial growth was calculated based on the mechanical equilibrium model and determined experimentally by XTEM images and PL spectra. The growth optimization with respect to the substrate temperature, V/III incorporation ratio, and the substrate misorientation enables us to achieve specular surfaces for InP and $\text{InAs}_x\text{P}_{1-x}/\text{InP}$ MQWs on InP (111)B substrates. The arsenic composition in $\text{InAs}_x\text{P}_{1-x}$ was successfully controlled over a wide range, from 0.1 to 0.7, by using different techniques. Characterizations by XTEM and high-resolution x-ray rocking curve measurements reveal excellent structural uniformity, periodicity, and accuracy. Computer simulations to x-ray rocking curves based on the dynamical theory, with anisotropy of the strain tensor taken into account, were performed for both (100) and (111)B $\text{InAs}_x\text{P}_{1-x}/\text{InP}$ MQW structures. Excellent fits were achieved, from which the structural parameters were extracted precisely. This growth and structural characterization studies provide a solid background to the investigation of optical properties of $\text{InAs}_x\text{P}_{1-x}/\text{InP}$ quantum structures in the next chapters.

References

- [1] J. W. Matthews and A. E. Blakeslee, *J. Cryst. Growth* **27**, 118 (1974).
- [2] A. Y. Cho, *J. Appl. Phys.* **41**, 2780 (1970).
- [3] J. H. Neave, P. J. Dobson, B. A. Joyce, and J. Zhang, *Appl. Phys. Lett.* **47**, 400 (1985).
- [4] R. Ito, H. Nakashima, and O. Nakada, *Jpn. J. Appl. Phys.* **12**, 1272 (1973).
- [5] R. People and J. C. Bean, *Appl. Phys. Lett.* **47**, 322 (1985); **49**, 229(E) (1986).
- [6] S. M. Hu, *J. Appl. Phys.* **69**, 7901 (1991).
- [7] T. G. Andersson, Z. G. Chen, V. D. Kulakovski, A. Uddin, and J. T. Vallin, *Appl. Phys. Lett.* **51**, 752 (1987).
- [8] I. J. Fritz, S. T. Picraux, L. R. Dawson, and T. J. Drummond, *Appl. Phys. Lett.* **46**, 967 (1985).
- [9] P. J. Orders and B. F. Usher, *Appl. Phys. Lett.* **50**, 980 (1987).
- [10] H. Q. Hou, T. P. Chin, B. W. Liang, and C. W. Tu, *Mat. Res. Soc. Symp. Proc.* **228**, 231 (1992).
- [11] R. P. Schneider, Jr. and B. W. Wessels, *Superlattices and Microstructures*, **6**, 287 (1989); and *Mat. Res. Soc. Symp. Proc.* **145**, 145 (1989).
- [12] H. Q. Hou, C. W. Tu and S. N. G. Chu, *Appl. Phys. Lett.* **58**, 2954 (1991).
- [13] D. L. Smith and C. Mailhot, *Solid State Commun.* **57**, 919 (1986), and *Phys. Rev. Lett.* **58**, 1264 (1987).
- [14] L. Pfeiffer, H. L. Stormer, K. W. Baldwin, K. W. West, A. R. Goni, A. Pinczuk, R. C. Ashoori, M. M. Dignam, and W. Wegscheider, *J. Cryst. Growth* **127**, 849 (1993).
- [15] E. Kapon, J. P. Harbison, C. P. Yuin, and N. G. Stoffel, *Appl. Phys. Lett.* **56**, 660 (1990).
- [16] L. Vina and W. I. Wang, *Appl. Phys. Lett.* **48**, 36 (1986).
- [17] H. Q. Hou and C. W. Tu, *J. Cryst. Growth* **127**, 199 (1993).

- [18] H. Q. Hou, B. W. Liang, T. P. Chin, and C. W. Tu, *Appl. Phys. Lett.* **59**, 292 (1991).
- [19] K. Tsutsui, H. Mizukami, O. Ishiyama, S. Nakamura, and S. Furukawa, *Jpn. J. Appl. Phys.* **29**, 468 (1990).
- [20] Y. Takano, Y. Kanaya, T. Orihaya, K. Pak, and H. Yonezu, *J. Cryst. Growth* **102**, 343 (1990).
- [21] H. Q. Hou and C. W. Tu, *Appl. Phys. Lett.* **62**, 283 (1993).
- [22] P. Chen, K. C. Rajkumar, and A. madhukar, *Appl. Phys. Lett.* **58**, 1771 (1991).
- [23] P. W. Yu, H. Q. Hou and C. W. Tu, *Phys. Rev. B*, (submitted).
- [24] W. J. Bartels, *J. Vac. Sci. Technol. B* **1**, 338 (1983).
- [25] J. Hornotra and W. J. Bartels, *J. Cryst. Growth* **44**, 513 (1978).
- [26] E. A. Caridi and J. B. Stark, *Appl. Phys. Lett.* **60**, 1441 (1992).
- [27] M. Quillec, L. Goldstein, G. Le Roux, J. Burgeat and J. Primot, *J Appl. Phys.* **55**, 2904 (1984).
- [28] V. S. Speriosu and T. Vreeland, Jr. *J. Appl. Phys.* **56**, 1591 (1984).
- [29] S. Bensoussan, C. Malgrange, and M. Sauvage-Simkin, *J. Appl. Cryst.* **20**, 222 (1987).
- [30] B. K. Tanner, *Adv. X-ray Anal.* **33**, 1 (1990), and references therein.

Chapter IV

Optical Properties of InAsP/InP Strained Quantum Wells Grown on InP (100) and InP (111)B Substrates

4.1 Introduction

It was pointed out in Chapter 2 that the InAsP/InP quantum well structures can provide excitonic emission from 0.98 to 1.55 μm at room temperature. Basically the InAsP/InP quantum structure can be an alternative material system to the more complex quaternary InGaAsP/InP quantum wells for some optoelectronic device applications. The As composition in $\text{InAs}_x\text{P}_{1-x}$ can be controlled with an *in situ* technique to achieve the desired wavelength in this spectral region very easily. Chapter 3 shows that the InAsP/InP strained MQWs possess high structural quality. This chapter therefore serves as a study of the general optical property of the InAsP/InP strained quantum wells. The first goal for the work presented in this chapter is to characterize the optical quality of heterostructure materials using various optical techniques. Second, the valence band offset is an essential property of the heterostructure for engineering transition energies from a quantum well for optoelectronic devices,[1-3] and it is determined by comparing a theoretical calculation with the experimental spectra.

Furthermore, we extended our study of the optical properties to InAsP/InP quantum wells grown on InP (111)B substrates. It has been demonstrated recently, that compound semiconductor heterostructures grown on (111)B substrates have some novel physical properties.[4] The large heavy-hole effective mass along the growth direction in (111)B GaAs/AlGaAs quantum wells gives rise to a 50-fold enhancement of the quantum efficiency of interband transitions.[5,6] As a result, a reduction of the threshold current in

a heterostructure laser fabricated from a GaAs/AlGaAs quantum well structure grown on a GaAs (111)B substrate was achieved.[5] In addition, this larger effective mass along the growth direction leads to a larger energy shift in quantum confined Stark effect (QCSE). More interestingly, a net displacement of the positive and negative charges can be generated in a strained quantum well grown on a (111)B substrate due to the lack of inversion symmetry in the zincblende structure.[4] As a result, an internal electric field can be produced from the piezoelectric effect.[7] Some novel nonlinear optoelectronic devices, such as the self electrooptic-effect devices (SEEDs)[8] and optical switches, were proposed by using the blue-shifted electroabsorption[7] and the large optical nonlinearity resulting from screening of the internal electric field, respectively.[9]

Work to date for the study of (111)B heterostructures, however, has been primarily performed for structures grown on GaAs substrates. Little has been accomplished for structures on InP (111)B substrates.[10-12]

In this chapter, we present optical properties of both (111)B and (100) InAsP/InP strained multiple quantum wells (MQWs) grown by gas-source molecular beam epitaxy (GSMBE). This study is intended to explore the quantum size effect of the (111) and (100) heterostructures, and to provide a better understanding of the dependence of the optical property on substrate orientations. In Section 4.2, we present theoretical models, with various effects on band-structure modulation taken into account, for calculating transition energies from (100) and (111)B quantum wells. Section 4.3 describes various optical techniques and typical optical spectra as general material characterizations. In Section 4.4, optical properties of (100) and (111)B InAsP/InP MQWs are studied in a comparative manner, and the emphasis is on resolving the difference in the quantum-size effect and on determining the valence-band discontinuity. Section 4.5 focuses on the screening of piezoelectric field by photo-generated carriers in (111)B InAsP/InP quantum structures.

4.2 Band structure and energy-level calculations

4.2.1 Envelope-function model

Energy levels of confined particles in a quantum well can be obtained by solving the one-dimensional single-particle Schrödinger equation which we write within the envelope-function and effective-mass approximation as:

$$\left[-\frac{\hbar^2}{2m_o} \left(\nabla \frac{1}{m^*(z)} \nabla \right) + V_o(z) \right] \Psi(z) = E \Psi(z) \quad (4.1)$$

where $m^*(z)$ is the carrier effective mass (different in the well- and the barrier-layer materials) and $V_o(z)$ is the effective potential energy which, in the case of a square well, is the height of the potential step,

$$V_o(z) = \begin{cases} V_o & \text{for } z \leq L/2 \\ 0 & \text{for } z > L/2, \end{cases} \quad (4.2)$$

where L is the well thickness.

By applying boundary conditions that the wavefunction and the probability current are continuous across the heterointerface, the solution for a square potential well can be written in the well known implicit form as:[13]

$$\begin{aligned} \tan\left(k_w \frac{L}{2}\right) &= \frac{m_w^* k_b}{m_b^* k_w} && \text{for even states,} \\ \tan\left(k_w \frac{L}{2}\right) &= -\frac{m_b^* k_w}{m_w^* k_b} && \text{for odd states,} \end{aligned} \quad (4.3)$$

where $k_w^2 = 2m_w^* E / \hbar^2$ and $k_b^2 = 2m_b^* (V_o - E) / \hbar^2$, and m_w^* and m_b^* refer to effective masses of the well and the barrier materials, respectively.[13] The wave function is well known to have a form of sinusoidal oscillations in the well and an exponential decay in the barrier layer. Eqs. (4.3) can be solved numerically. Since the bandgap of InAsP layer is usually small (~ 1 eV), the conduction band nonparabolicity may not be neglected. In a

two-band model, the electron effective mass (m_e^*) is corrected as $m_e^*(E) = m_e^*(1 + 2E/E_g)$, [13] where E_g is the bandgap energy.

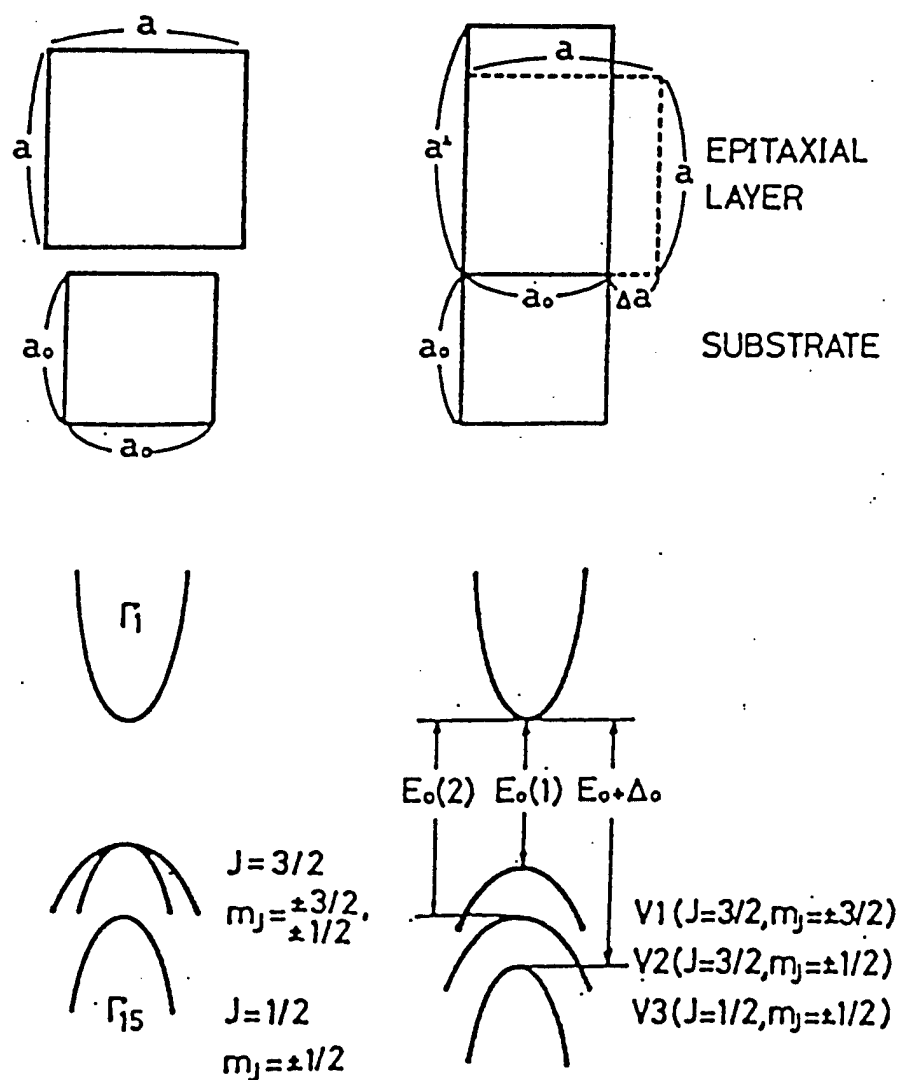


FIG. 4.1. Schematic diagram of the tetragonal distortion of a strained InAsP layer grown on an InP substrate. The InAsP layer is biaxially strained, while there is no strain in the InP layer.

4.2.2 Strain-induced change of the band structure

The method of the energy-level calculation is the same for (111)B and (100) quantum wells, but there are some fundamental differences in the orientation-dependent material parameters between (111)B and (100) bulk materials (such as elastic deformation, strain-induced bandedge shift, and valence-band anisotropy), and between the quantum structures grown on these different oriented substrates (e.g., the piezoelectric effect).

A. Elastic deformation

In an approximation of elastic deformation, a biaxial compressive strain will be present in the InAsP layer when the $\text{InAs}_x\text{P}_{1-x}$ layer is pseudomorphically grown on an InP substrate. The strain is assumed only in the InAsP layer because the thickness of the InP substrate is far larger than that of the InAsP layer. This results in a tetragonal distortion with respect to the growth surface. Shown in Fig. 4.1 is a schematic diagram of the accommodation of the lattice mismatch between the two layers. When the InAsP layer is grown on a (100) substrate, off-diagonal strain-tensor elements vanish, and the three major diagonal elements, ϵ_{ii} ($i=x,y,z$), can be expressed as[14]

$$\begin{aligned}\epsilon_{xx} = \epsilon_{yy} &= \frac{a_f - a_o}{a_f} \equiv \epsilon_o, \\ \epsilon_{zz} &= -\frac{2C_{12}}{C_{11}}\epsilon_o,\end{aligned}\tag{4.4}$$

where a_f and a_o are respective lattice constants of the free-standing InAsP and InP substrate; C_{11} and C_{12} are the elastic stiffness constants. In the case of (111)B substrate, however, the tetragonal distortion is with respect to the (111) direction (film coordinates), but not to the cubic axes (crystalline coordinates); consequently, the off-diagonal strain-tensor elements are nonzero in this case. Caridi and Stark [14] have

reported a detailed calculation of the strain tensors for all the $[hkk]$ orientations. For the (111) orientation, the strain-tensor elements can be expressed as

$$\begin{aligned}\epsilon_{ii} &= \frac{4C_{44}}{C_{11} + 2C_{12} + 4C_{44}} \epsilon_o, \\ \epsilon_{ij} &= \frac{-(C_{11} + 2C_{12})}{C_{11} + 2C_{12} + 4C_{44}} \epsilon_o \quad (i \neq j),\end{aligned}\quad (4.5)$$

where $i, j = x, y, z$, and ϵ_{ij} ($i \neq j$) represent shear components of the strain tensor.

B. Shift of the bandedge induced by strain

The biaxial compressive strain in the $\text{InAs}_x\text{P}_{1-x}$ well layer can be equalized by a hydrostatic (compressive) pressure and a uniaxial stress along the growth direction. For the QW grown on a (100) substrate, the hydrostatic pressure component enlarges the bandgap, while the uniaxial stress component splits the valence band degeneracy. On the other hand, the bandedge change for the (111)B quantum structure is related to the shear component of the deformation potential due to the nonzero off-diagonal strain-tensor elements. Finally the changes of the bandedge of the conduction band (CB), δE_c , and of the valence band (VB), δE_v , read[15]

$$\begin{aligned}\delta E_c &= 2a_c \frac{C_{11} - C_{12}}{C_{11}} \epsilon_o \\ \delta E_v &= 2a_v \frac{C_{11} - C_{12}}{C_{11}} \epsilon_o \pm b \frac{C_{11} + 2C_{12}}{C_{11}} \epsilon_o\end{aligned}\quad \text{for (100),} \quad (4.6)$$

$$\begin{aligned}\delta E_c &= 3a_c \epsilon_{ii} \\ \delta E_v &= 3a_v \epsilon_{ii} \pm \sqrt{3}d \epsilon_{ij}\end{aligned}\quad \text{for (111)B,} \quad (4.7)$$

where the strain-tensor elements, ϵ_{ii} and ϵ_{ij} , have been given by Eqs. (4.5); parameters a_c and a_v are respective hydrostatic deformation potentials of the CB and the VB; b and d are shear deformation potentials. The signs "+" and "-" are for the heavy hole (hh) and the light hole (lh) bandedge, respectively. Usually the hydrostatic deformation potential,

a , is obtained from the measured change of the total bandgap rather than the absolute bandedge shift. For the sake of discussions, a_c was chosen to be $\frac{2}{3}a$, and $a_v \sim \frac{1}{3}a$. [16] However, the final results are not sensitive to the change in the assumed ratio.

C. Valence-band anisotropy

Another important difference between the quantum structures grown on (100) and (111)B substrates is the VB anisotropy effect; namely, different effective hole masses for these two orientations. This difference affects the quantization shift in the quantum well. Expressed in terms of Luttinger parameters (γ_1 , γ_2 and γ_3) the effective mass in the vicinity of the zone center ($k=0$) reads

$$\begin{aligned} m_{lh}^* &= \frac{m_o}{\gamma_1 \mp 2\gamma_2} & \text{for (100),} \\ m_{hh}^* &= \frac{m_o}{\gamma_1 \mp 2\gamma_3} & \text{for (111)B,} \end{aligned} \quad (4.8)$$

where m_o is the free electron mass. Lawaetz [17] calculated Luttinger parameters for all the III-V compounds. The resultant hole effective masses are calculated and listed in Table 4.1. The hh effective mass in (111)B direction is found to be about 2.5 times as large as that in the (100) direction. On the other hand, the lh effective mass is rather less dependent on the orientation. This large VB anisotropy was studied experimentally for GaAs/AlGaAs (111)B quantum structures by Hayakawa *et al.* [18] Many superior optical characteristics for (111)B quantum structures are related to the large heavy-hole effective mass. [5,18]

Figure 4.2 shows a schematic diagram of the bandedge shift calculated from Eqs. (4.6) and (4.7) for strained $\text{InAs}_{0.21}\text{P}_{0.79}$ layers grown on both (111)B and (100) substrates. We can see the clear effect of the biaxial compressive strain in enlarging the bandgap and splitting the VB degeneracy. Furthermore, it is noteworthy that the bandgap enlargement by the hydrostatic component for the (111)B strained InAsP layer is about

13 meV larger than the same layer grown on the (100) substrate, as a result of the different bandgap dependence on the strain.

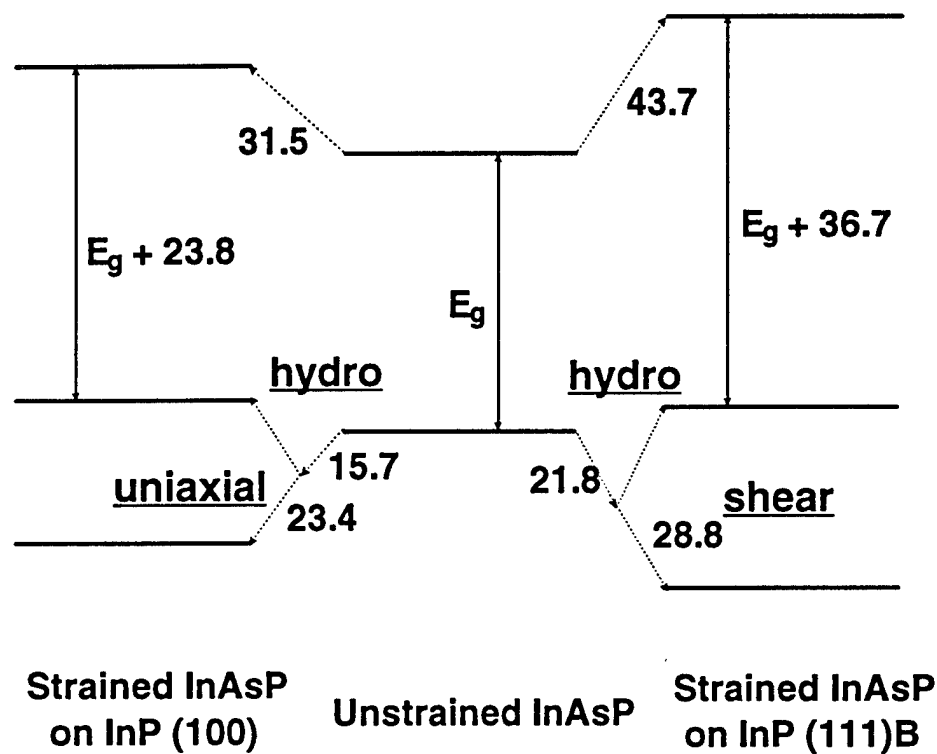


FIG. 4.2. Schematic diagram of the band structure modification for $\text{InAs}_{0.21}\text{P}_{0.79}/\text{InP}$ heterostructures pseudomorphically grown on InP (111)B and (100) substrates, respectively. The energy changes due to hydrostatic pressure, uniaxial stress and shear components are designated respectively.

4.2.3 Piezoelectric effect of (111) InAsP/InP strained quantum wells

An important difference between (111) and (100) heterostructures is that there is a piezoelectric effect for strained quantum wells grown on a (111) substrate. A large

electric field can be generated in the strained-layer region. The direction of the field is dependent on the strain direction (compressive or tensile) and the (111) orientation [(111)B or (111)A], and the magnitude of this field is dependent on the *shear* strain component and the piezoelectric constant (e_{14}).

$$|F_{piezo}| = \frac{2\sqrt{3}e_{14}\epsilon_{ij}}{\epsilon_m\epsilon_r}, \quad (4.9)$$

where ϵ_m and ϵ_r are dielectric constants of the vacuum and the material, respectively. It has been reported theoretically and experimentally[4,7] that the piezoelectric field can be as large as 200 kV/cm for a strained InGaAs/GaAs quantum well structure with a lattice mismatch of ~1%. However, this field is relatively smaller for the InAsP/InP system (e.g., ~70 kV/cm field for a lattice mismatch of 1%) because of a smaller piezoelectric constant. Figure 4.3 shows the magnitude of the built-in piezoelectric field in the quantum well calculated from Eq. (4.9) as a function of the As composition in strained InAsP/InP quantum wells grown on InP (111)B substrates.

As we see from the above discussion, it is more complicated to calculate the confined energy levels for (111) quantum structures due to the built-in electric field. The effect of this field is to tilt the bandedge of the well layer. As a result, the wave function of electrons and holes will be separated. A decrease of the overlap integral will reduce the oscillator strength, and therefore lead to a decrease of the emission intensity as compared to the same structure grown on a (100) substrate. Another effect is that the confined energy shifts to the bottom of the quantum well when the bandedge is tilted with applying an electric field, resulting in a red shift of the emission energy. This is the so-called quantum confined Stark effect (QCSE). To account for the transition energy effectively for (111) quantum wells, the energy shift due to this QCSE has to be considered. Miller *et al.*[19] reported an "effective well width" model, where a quantum well with a finite barrier is approximated by one with an infinite barrier and an effective

well width. The effective well width is chosen to give the correct energies of the actual quantum well with the finite barrier in the absence of an electric field. With this approximation, the Schrödinger equation under an electric field can be solved analytically. The energies can be obtained as a function of the electric field from a numerical calculation of the Airy functions.

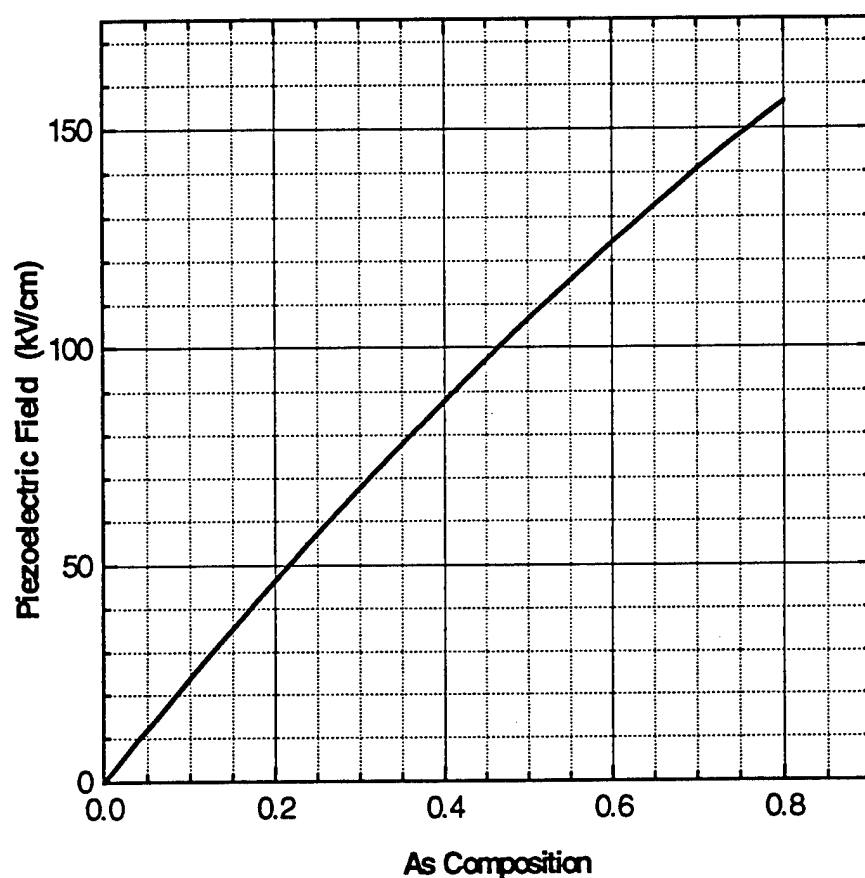


FIG. 4.3. The magnitude of the piezoelectric field in an $\text{InAs}_x\text{P}_{1-x}/\text{InP}$ strained quantum well grown on an InP (111)B substrate.

TAB. 4.1. Physical constants of InP and InAs used in the present calculation^a

	InP	InAs
Lattice constant (Å)	5.8687	6.0584
C_{11} (10^{11} dyn/cm ²)	10.11	8.33
C_{12} (10^{11} dyn/cm ²)	5.61	4.526
C_{44} (10^{11} dyn/cm ²)	4.56	3.96
a (eV)	-7.4 ^b	-6.9 ^b
b (eV)	-1.7	-1.7
d (eV)	-5.0 ^b	-4.0 ^b
m_e^* (m_o)	0.076	0.0231
m_{hh}^* (111) (m_o)	1.316 ^c	0.92 ^c
m_{hh}^* (100) (m_o)	0.472 ^c	0.34 ^c
m_{lh}^* (111) (m_o)	0.085 ^c	0.026 ^c
m_{lh}^* (100) (m_o)	0.096 ^c	0.027 ^c
ϵ_r	12.4	14.6
e_{14} (Cm ⁻²)	-0.042 ^d	-0.045 ^e

^aLandolt-Börnstein New Series, Edited by O. Madelung, Vol. 22a, (Springer-Verlag, 1986).

^bD. D. Nolte, W. Walukiewicz, and E. E. Haller, Phys. Rev. Lett. **59**, 501 (1987).

^cP. Lawaetz, Phys. Rev. B **4**, 3460 (1971).

^dS. Adachi, J. Appl. Phys. **53**, 8775 (1982).

^eE. A. Caridi, T. Y. Chang, K. W. Goossen, and L. F. Eastman, Appl. Phys. Lett. **56** 659 (1990).

For unstrained $\text{InAs}_x\text{P}_{1-x}$ compound the fundamental bandgap was chosen to be $E_g(x) = 1.416 - 1.36x + 0.36x^2$ (eV) at 15K and $E_g(x) = 1.351 - 1.315x + 0.32x^2$ (eV) at 300K, respectively.[24] Knowing the bandgap discontinuity between the InP barrier layer and InAsP well layer, we assumed Q_v ($\Delta E_v/\Delta E_g$)=0.30[20,21] and calculated the confined energy levels for electrons and holes by using the envelope-function model, where ΔE_v is the valence band discontinuity, and ΔE_g is the difference of the band gap energy between the well layer and the barrier layer. The physical constants used in this calculation are summarized in Table 4.1. The parameters for $\text{InAs}_x\text{P}_{1-x}$ are obtained by assuming that Vegard's law applies and by linearly interpolating from the values between end binary compounds. Furthermore, the QCSE energy shift of the confined energy levels was calculated using the effective well-width model. Illustrated in Fig. 4.4 is the QCSE energy shift as a function of the electric field for the first confined electron, hh and lh levels, respectively. This field can be either applied externally or built in internally. Note that the energies of the hh and lh shift much faster than that of the electron level. Using a variational method for an infinite quantum well, Bastard *et al.*[22] calculated the field-induced energy shift, in the weak-field limit, to be

$$\delta E_{\text{QCSE}} \propto m^* F^2 L^4, \quad (4.10)$$

where F and L are the electric field and the well width, respectively. Therefore, the larger energy shift from the hh level, compared to the electron level, can be attributed to the larger hh effective mass. On the other hand, the lh confined level shifts even more than the hh level even though the lh effective mass is similar to that of the electron. From Fig. 4.2 we see that the lh quantum well can be very shallow due to the strain-induced splitting of the valence bandedge. The confined energy level is thus very close to the bottom of the quantum well of the lh bandedge. This small confined energy can be equalized by a wider but infinite quantum well in the effective well-width model, so the

energy shift should be very significant for the lh level owing to the L^4 dependence. Hence, we may conclude that *a larger energy shift is from a level with a smaller confined energy, which can be induced by a larger effective mass, a smaller well depth, or a wider well width.* Another result we can expect from Eq. (4.10) is a larger energy shift for a (111) quantum well than a (100) well because of the larger hh effective mass in the (111) direction. This was observed in GaAs/AlGaAs quantum wells experimentally.[23]

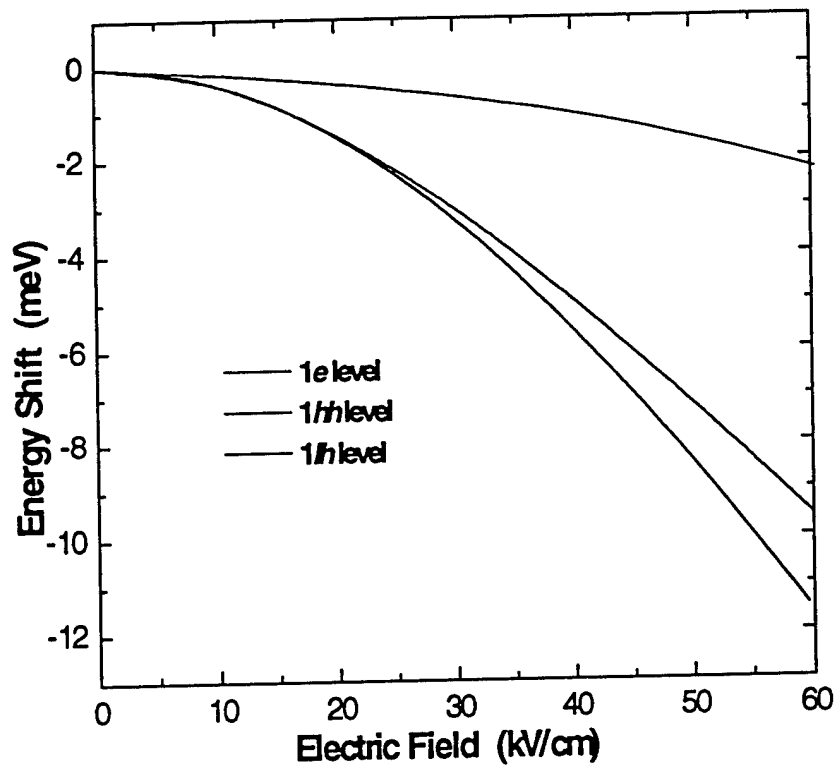


FIG. 4.4. Energy shift of the first electron, hh and lh levels in $\text{InAs}_{0.21}\text{P}_{0.79}(80 \text{ \AA})/\text{InP}(120 \text{ \AA})$ strained MQWs under an electric field due to QCSE. The calculation is based on the effective well width model. Larger shifts are obtained from levels with smaller confined energies.

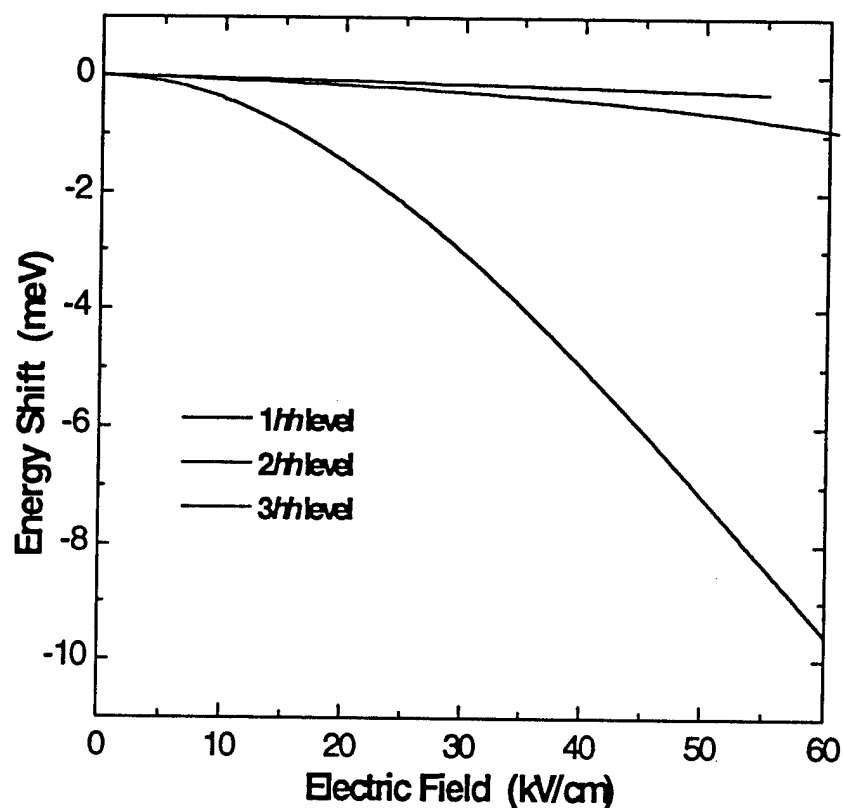


FIG. 4.5. Energy shift of different hh subbands as a function of the applied electric field across the quantum well region. Significant difference of the energy shift is predicted. This result indicates that the energy shift of the higher subband excitonic transition is very small.

Figure 4.5 depicts the QCSE energy shift for different hh subbands as a function of the electric field. The energy shift is seen to differ significantly, and it is very small for the higher subbands.[28] This implies that a correction in transition energy for the higher subband excitonic transition is often unnecessary.

4.2.4 Energy calculation of excitonic transition

After calculating the confined energy levels, E_e and E_h , for electrons and holes, respectively, the energy for excitonic transition is given by

$$E_{trans} = E_g + E_e + E_h - E_b + \delta E_{QCSE} , \quad (4.11)$$

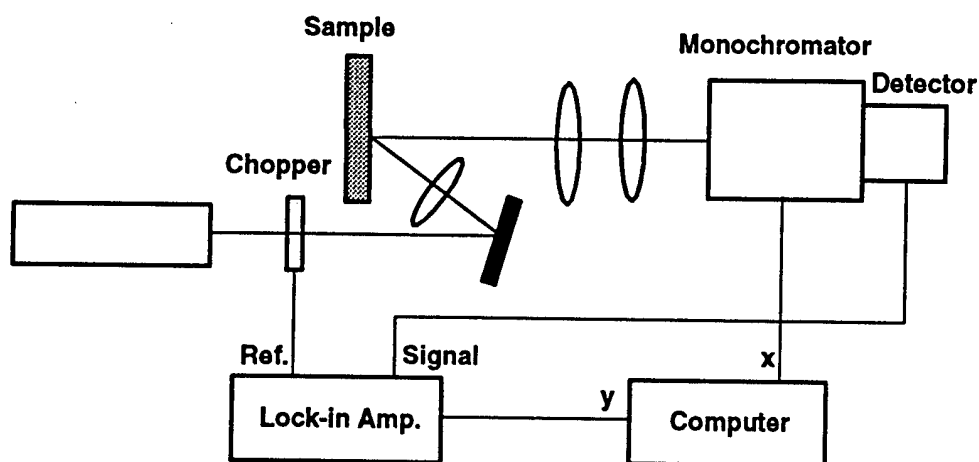
where E_g is the bandgap of the *strained* InAsP well layer; δE_{QCSE} is the energy shift due to QCSE of the internal field in the (111) quantum well structure [this value is zero for the (100) quantum well]. Another factor that should be considered in this calculation is the change of the exciton binding energy with an applied electric field. Variational calculations can yield a theoretical determination[19,25] of the exciton binding energy, but it changes only about 3 meV even when the field is as high as 100 kV/cm.[19] We therefore use a constant E_b (8.5 meV) as the exciton binding energy at zero field,[25] and deduct a constant amount (1.5 meV) to account for the change in the exciton binding energy under the electric field.

4.3 Optical characterization techniques

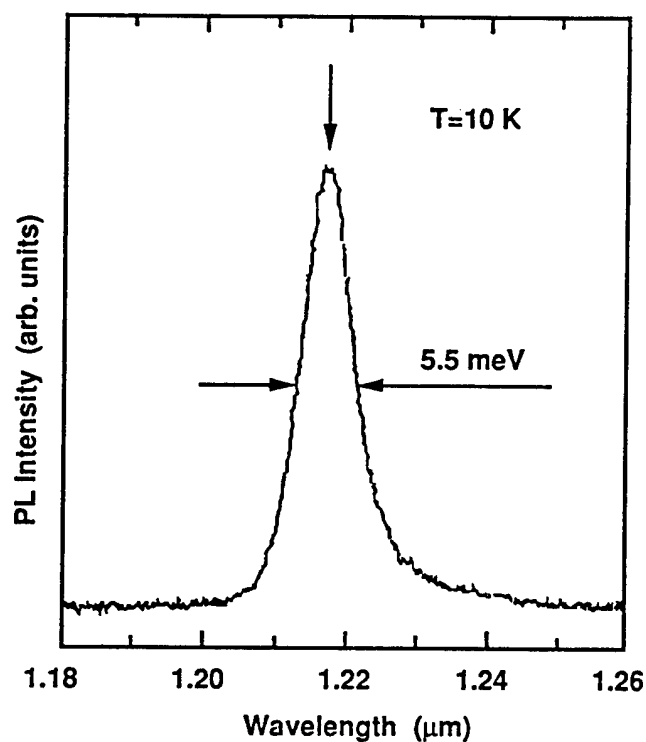
Various optical techniques were employed to resolve the excitonic transitions from quantum wells. This section describes photoluminescence (PL), PL excitation (PLE), absorption, and photo-modulated transmission (PT) spectroscopy.

4.3.1 Photoluminescence measurements

Photoluminescence spectroscopy is a sensitive and simple technique to characterize the optical quality of materials. By comparing the emission energy with a calculation for the energy levels, the alloy composition or well thickness of the structure can be deduced. Low-temperature PL measurements were carried out at 15 K in a closed-cycle cryostat. The samples were mounted to a cold finger in the vacuum chamber. The



(a)



(b)

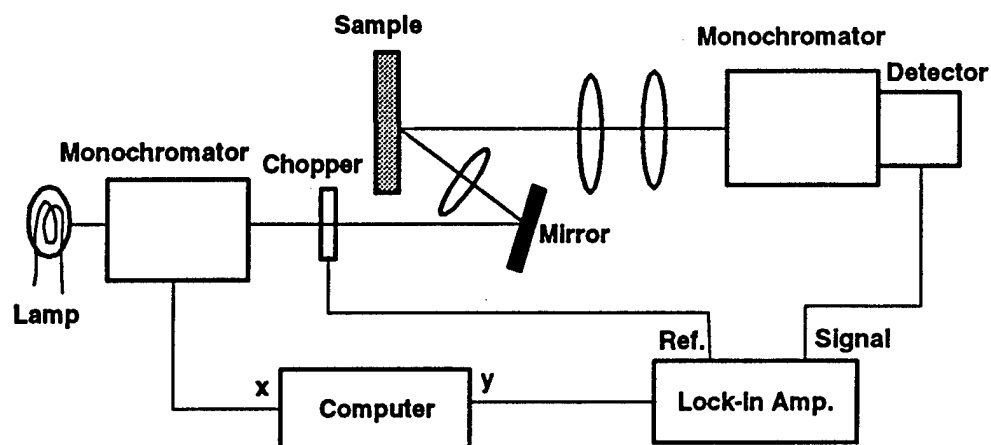
FIG. 4.6. (a) Schematic diagram of PL setup; (b) low-temperature PL spectrum taken from a 1.3 μm modulator structure consisting of 30-period $\text{InAs}_{0.4}\text{P}_{0.6}$ (92 Å)/ InP (138 Å) MQWs. Sharp and intense peak is attributed to the heavy-hole excitonic emission. The arrow in the figure indicates the calculated transition energy.

quantum-well structures were excited by the 5145-Å line from an argon-ion laser with a typical pumping power of 10 W/cm². The luminescence was collected in a back scattering configuration, focused into and dispersed with a 50-cm monochromator. The signal was detected by a thermo-electrically cooled Ge photodiode, and measured by a lock-in technique. The spectral resolution was approximately 2 Å. Figure 4.6(a) shows the schematic diagram of the PL setup.

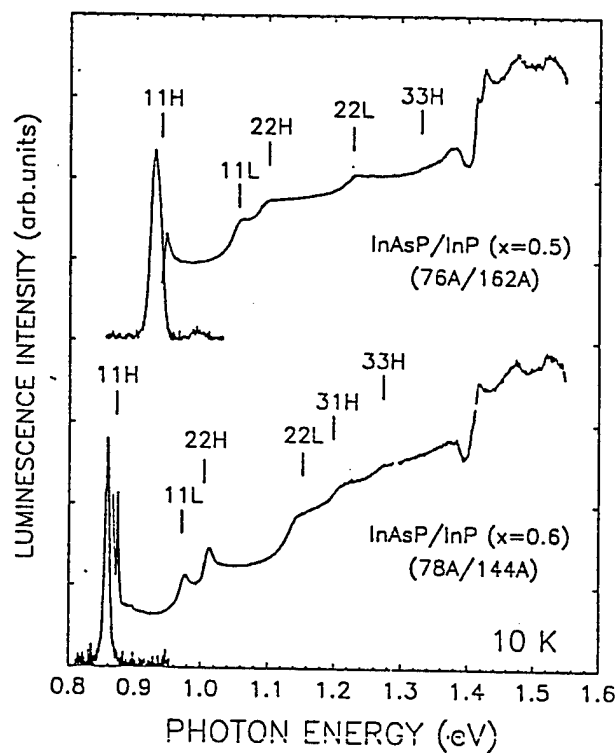
Figure 4.6(b) shows a typical PL spectrum taken from a 1.3-μm modulator structure consisting of 30-period InAs_{0.4}P_{0.6}(92 Å)/InP(138 Å) strained MQWs. Very intense emission was observed, attributable to the first heavy-hole subband excitonic transition. The full-width of half maximum (FWHM) is about 5.5 meV, indicative of good lateral uniformity and vertical repeatability of this strained heterostructure. The FWHMs for lightly strained InAs_{0.2}P_{0.8}/InP MQW structures emitting at 1.06 μm at room temperature is typically 4 meV. These results are among the best ever reported for InAs_xP_{1-x}/InP strained MQWs,[20] and even for lattice-matched In_{1-x}Ga_xAs_yP_{1-y}/InP quantum wells. The arrow shown in Fig. 4.7 is the calculated transition energy on the basis of the structural parameters determined from the x-ray rocking curve. We assumed the valence band offset ratio $Q_v = \Delta E_v / \Delta E_g = 0.3$ since the emission energy is not very sensitive to this value. An excellent agreement was reached between the calculation and measurements. We will present our results for the Q_v determination in the next section.

4.3.2 Photoluminescence excitation measurements

Photoluminescence excitation spectroscopy is a more sensitive optical technique to resolve transitions from higher excited states, even for a ^{single} quantum well, but the measurement is usually carried out at low temperature to have enough luminescence intensity. Low-temperature PLE, performed at Oklahoma State University, was measured by using a tunable monochromatic light generated by a tungsten lamp and a 32-cm



(a)



(b)

FIG. 4.7. (a) Schematic diagram of PLE setup; (b) PLE spectra taken at 15 K for two highly-strained InAsP/InP MQW samples. Also shown are PL spectra measured at the same temperature. The labels refer to the identifications for spectral features and the vertical bars indicate calculated interband transitions using $Q_v=0.3$.

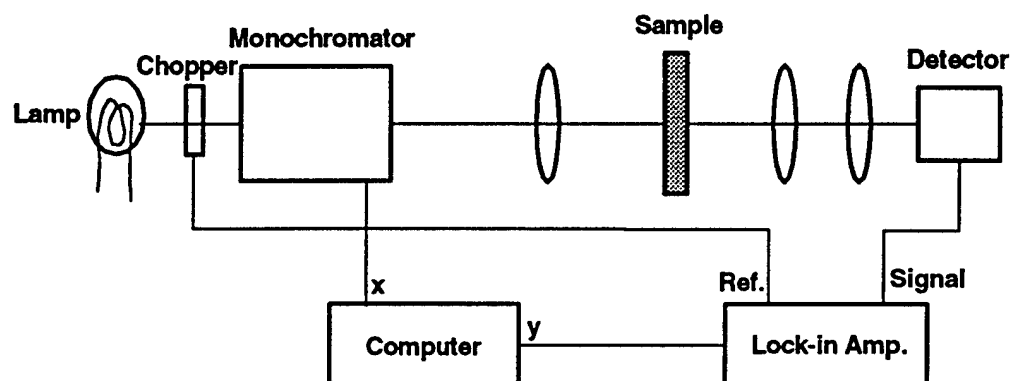
monochromator, but the analyzing spectrometer was set to monitor the wavelength corresponding to the energy of the PL emission peak. The signal was again measured by a cooled Ge detector and the lock-in technique. A schematic diagram of the setup is shown in Fig. 4.7(a).

Figure 4.7(b) shows the low-temperature PLE spectra from two highly-strained $\text{InAs}_x\text{P}_{1-x}/\text{InP}$ MQWs. The structural parameters, determined from x-ray measurements, are given in the figure. The transitions from higher subband excitons can be obtained up to the 3rd order. The step-like density-of-state can be seen clearly from the background PL intensity between subband excitonic transitions. The vertical bars in the figure indicate calculated interband transitions. The assignment for various spectral signatures is based on calculations, and the transitions are labeled in the figure. The energy-level calculation was carried out using the envelope-function model as presented in the last section. The best fit to the transition energies in the spectra suggests that the valence-band offset ratio $Q_v = \Delta E_v / \Delta E_g = 0.3$. Some more detailed discussion of the Q_v determination will be given in the next section.

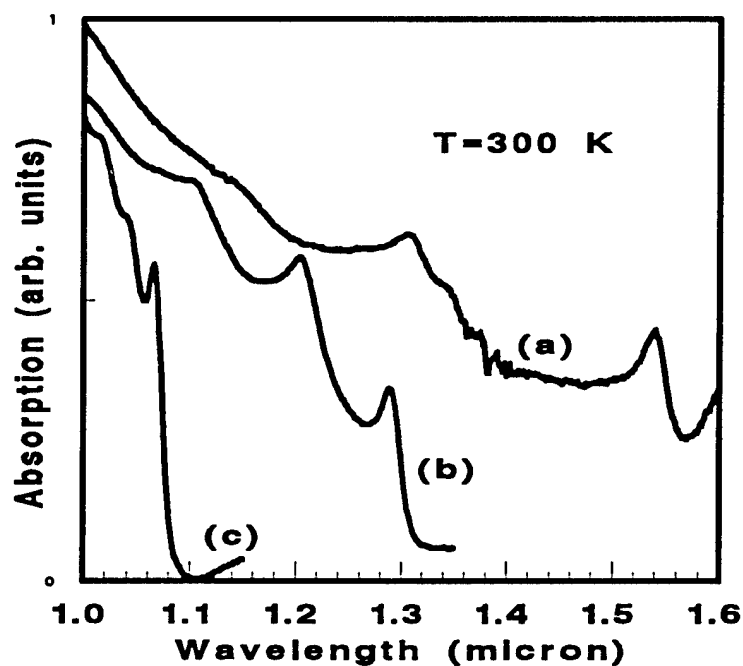
4.3.3 Absorption measurements

Absorption measurement is a very simple and powerful means for optical studies, but the sample should consist of many quantum wells to accumulate enough absorption. Absorption from higher subband excitons can be observed even at room temperature. Figure 4.8(a) shows a schematic diagram of the experimental setup. Absorption spectra were taken by measuring the transmission through the sample from a monochromatic light. The samples are usually polished from the backside to minimize light scattering through the structure; but it is not necessary to remove the InP substrate since it is transparent to interband excitonic transitions in the InAsP/InP quantum well. The final

spectra were corrected with calibrations to the intensity profile of the lamp and spectral responses of the grating and the detector.



(a)



(b)

FIG. 4.8. (a) Schematic diagram of absorption setup; (b) room-temperature absorption spectra from three InAsP/InP strained MQW samples. Very sharp absorption peaks are obtained at 1.06, 1.3 and 1.55 μm for these samples, respectively, indicative of the potential usefulness for optoelectronic devices.

Figure 4.8(b) shows the room-temperature absorption spectra from three $\text{InAs}_x\text{P}_{1-x}/\text{InP}$ MQW samples with different x in the ternary alloy. The structural parameters are listed in Table 4.2. It can be seen that sharp and strong absorption peaks appear at about 1.06, 1.3 and 1.55 μm for these three samples, respectively. The composition control for these three samples was according to the *in situ* calibration technique described in Chapter 2. Absorption between higher excited states can also be seen, which suggests good sample quality even with the period number exceeding the critical value. The linewidth broadens with increasing As composition in the $\text{InAs}_x\text{P}_{1-x}$ quantum well. This may be due to the increased alloy scattering in the quantum well or strain relaxation for the very highly strained samples.

Table 4.2. Description of the sample structures.

Sample	x	$L_{\text{InAsP}} (\text{\AA})$	$L_{\text{InP}} (\text{\AA})$	Period	FWHM(meV)	Absorption(μm)
HI06	0.60	78	144	15	7.0	1.55
HI35	0.40	92	138	30	5.5	1.30
HI32	0.20	92	138	30	4.0	1.06

Figure 4.9 shows absorption spectra taken from Sample #HI35 at various temperatures. The absorption peak is sharper for lower temperature as a result of reduced thermal scattering. Furthermore, the transition energy increases when the temperature becomes lower because the band gap becomes larger. Shown in Fig. 4.10 is the transition energy from the first heavy-hole excitons as a function of temperature. The least-square fitting with Vashini' relation $[E_g(T) = E_g(0) - \alpha T^2/(T+\theta)]$, where α and θ are fitting parameters, see for example, Chapter 5, *Heterostructure Lasers*, by H. C. Casey,

Jr and M. B. Panish, (Academic, New York, 1978)] to the experimental data can well account for the temperature dependence of the bandgap.

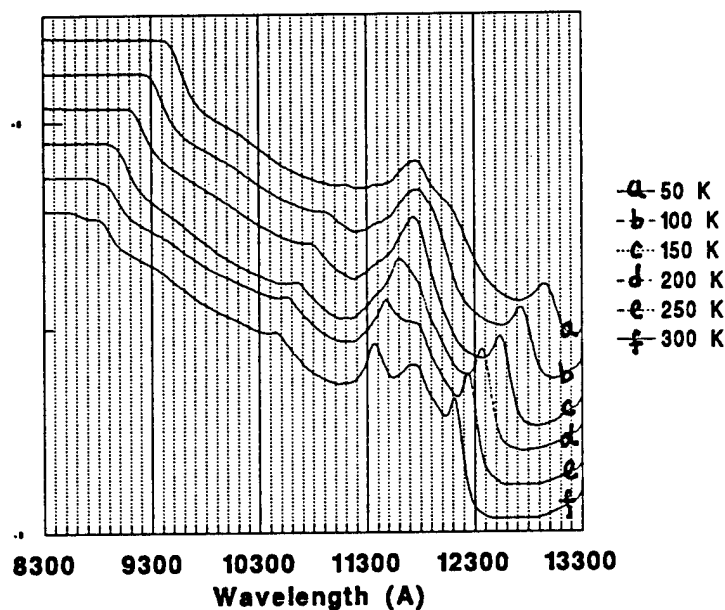


FIG. 4.9 Absorption spectra taken from a 1.3 μm modulator structure consisting of 30-period $\text{InAs}_{0.4}\text{P}_{0.6}$ (92 Å)/ InP (138 Å) MQWs at various temperatures. The narrower absorption peak at lower temperature is due to reduced thermal scattering. The energy bandedge shifts to higher energy, resulting in an increase of transition energy at low temperature.

Finally, another optical technique, which we call photo-modulated transmission (PT) spectroscopy,[26] was also employed. A He-Ne laser beam ($\sim 2\text{mW}$) was used to modulate the dielectric constant of the material, and the transmission signal was detected from a monochromatic pump beam irradiated on the same spot. This is a very sensitive technique, similar to photoreflectance spectroscopy,[27] but the interpretation of the spectral signatures is much easier. Shown in Fig. 4.11 is a comparison of a PT spectrum,

a transmission spectrum and the first-order derivative of the transmission spectrum for an $\text{InAs}_{0.21}\text{P}_{0.79}$ (100 Å)/InP strained MQW structure taken at low temperature. It is apparent that the PT spectrum reveals the same information as the derivative of the transmission spectrum, yet PT is a more sensitive technique. Basically, the zero crossing of the PT signal gives the energies of subband excitonic transitions.

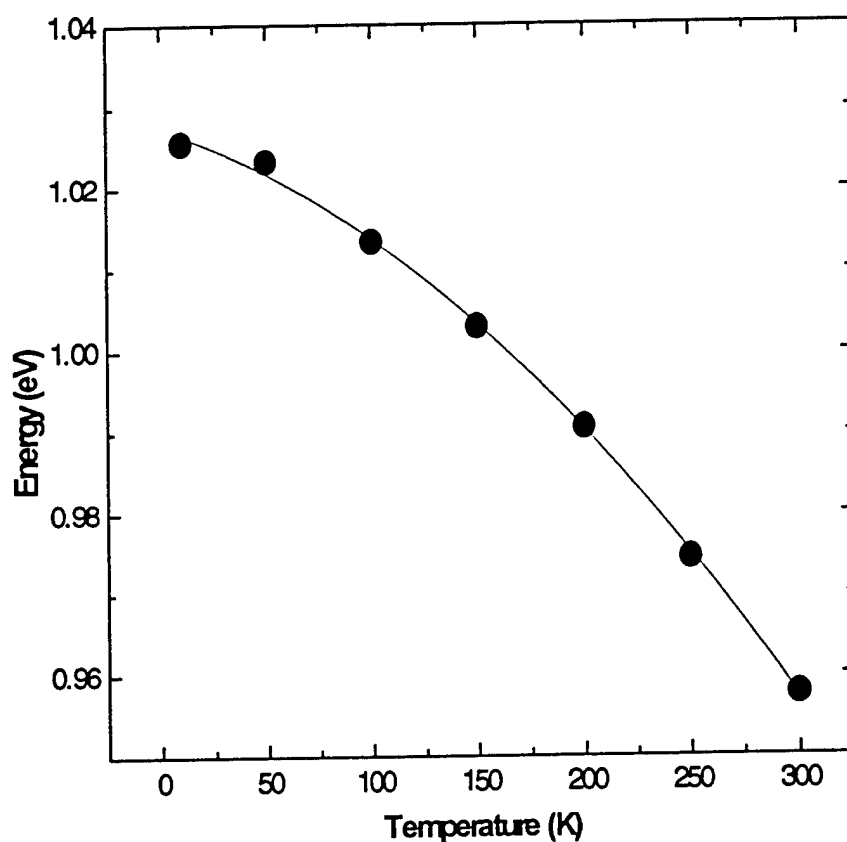


Fig. 4.10 The energy of the 1e-1hh excitonic transition as a function of the measuring temperature. The curve through the data points is the calculated temperature dependence of the bandgap energy of $\text{InAs}_{0.4}\text{P}_{0.6}$ interpolated from the known temperature coefficients of InAs and InP.

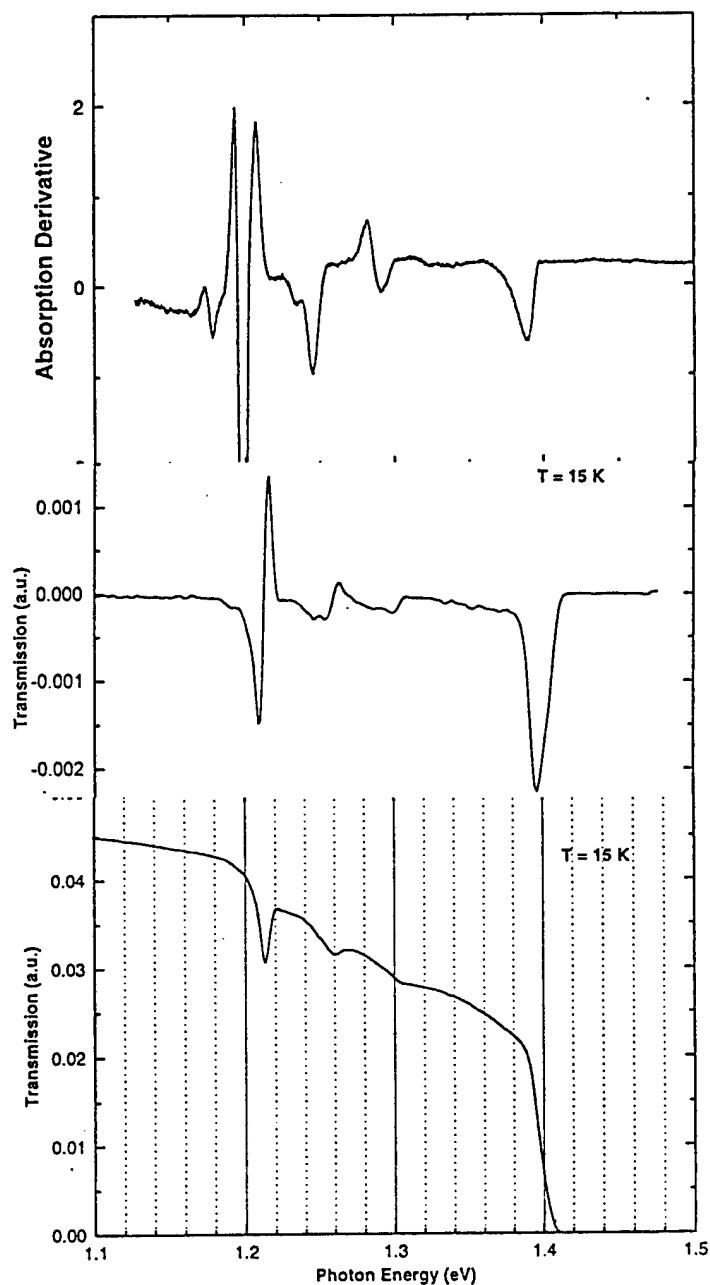


FIG. 4.11. Comparison of (a) a photo-modulated transmission (PT) spectrum, (b) transmission spectrum and (c) the first-order derivative of a transmission spectrum for a $\text{InAs}_{0.21}\text{P}_{0.79}$ (100 Å)/InP strained MQW structure taken at low temperature. It is apparent that the PT spectrum reveals the same information as the transmission derivative, yet the PT is a more sensitive technique.

4.4 Optical property of (111)B and (100) InAsP/InP strained quantum wells

Specular surfaces for InAsP/InP strained MQW samples, as determined in Chapter 3, were obtained under optimized growth conditions on InP (111)B substrates with 1° off to $\langle 110 \rangle$ direction. A typical structure consists of 15 periods of $\text{InAs}_x\text{P}_{1-x}$ (80 Å)/ InP (120 Å) strained MQWs. The structural parameters were extracted from the x-ray rocking curve measurement and computer simulation as demonstrated in the previous chapter. In order to understand the difference in optical properties between (111) and (100) samples, control samples on (100) substrates were grown consecutively to (111)B structures. In this section, optical properties are discussed in a comparative manner for (111)B and (100) quantum well structures. The samples (HB30 and HI70) are 15-period $\text{InAs}_{0.21}\text{P}_{0.79}$ (80 Å)/InP (120 Å) strained MQWs grown consecutively on (111)B and (100) substrates under the same conditions.

4.4.1 PL spectra

Shown in Fig. 4.12 are PL spectra taken at about 15 K. The pump-power density was kept sufficiently low so that the screening effect by photo-generated carriers could be negligible.[10,27] The full widths at half maximum (FWHMs) are 5.5 and 9.0 meV for (100) and (111) MQWs, respectively, indicating a good crystalline quality and good periodicity of the MQW structure. The narrow line width also implies a good interface quality since both the well layer and the barrier layer were excited by the 5145-Å laser line. These sharp and intense transitions are attributed to emissions from the first hh subband excitons. The emission from the (111) MQWs has as strong a peak intensity as that from the (100) MQWs. However, an internal electric field may exist in the (111)B InAsP quantum well layer due to the piezoelectric effect. The high built-in field leads to a localization of electron and hole wave functions to different sites of the quantum well in real space. Considering the reduction of the oscillator strength due to the internal

electric field in (111)B MQWs, we expect a higher PL emission intensity and narrower FWHM from (111)B MQWs if an electric field is applied to balance the band tilting.[28] It is noteworthy from Fig. 4.12 that the emissions from (111) and (100) MQWs occur at approximately the same photon energy even though the built-in electric field and quantization for the (111)B MQWs would shift the emission to a lower energy. This will be discussed in a greater detail later.

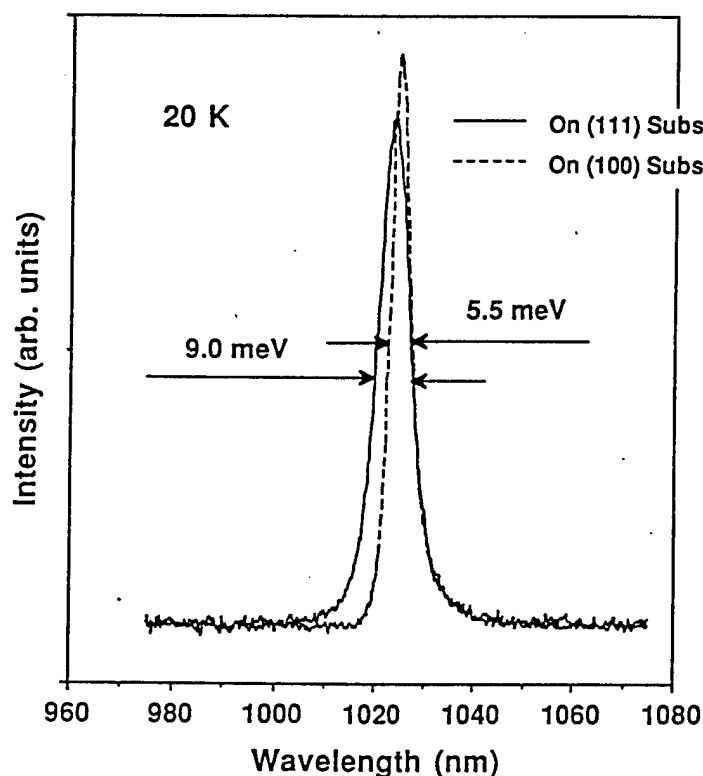


FIG. 4.12. Low-temperature PL spectra taken from two $\text{InAs}_{0.21}\text{P}_{0.79}(80 \text{ \AA})/\text{InP}(120 \text{ \AA})$ strained MQW samples grown on InP (111)B and (100) substrates, respectively. Comparable emission intensity was obtained from these two samples. The slight broadening of the emission peak from (111) MQWs may be due to the internal QCSE.

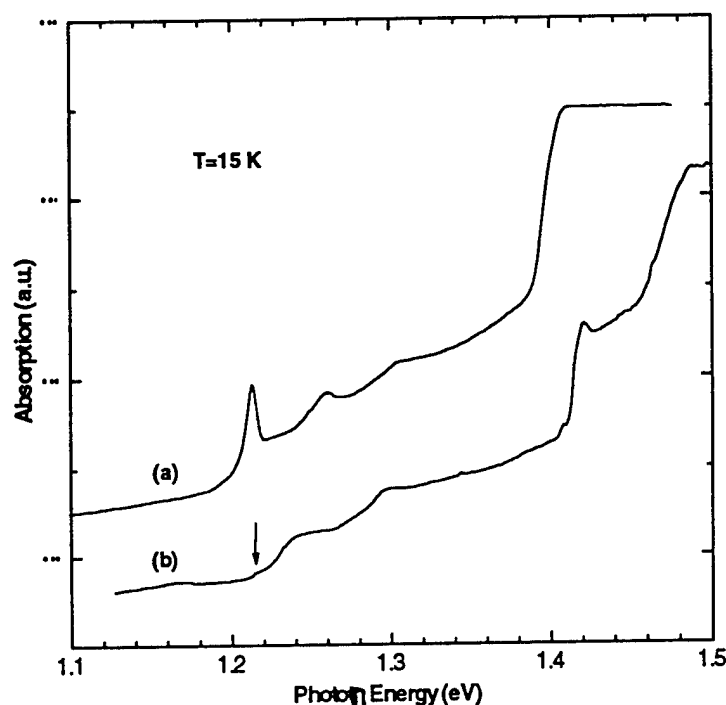


FIG. 4.13. Low-temperature absorption spectra from $\text{InAs}_{0.21}\text{P}_{0.79}(80 \text{ \AA})/\text{InP}(120 \text{ \AA})$ strained MQWs grown on (a) (100), and (b) (111)B substrates. The different absorption behavior is believed to result from the internal QCSE in the (111) quantum structure.

4.4.2 Low-temperature absorption spectra

Low-temperature ($\sim 15 \text{ K}$) absorption spectra taken from these two samples are shown in Fig. 4.13. The higher subband excitonic emissions are well resolved for (100) MQWs as shown in Fig. 4.13(a). However, Figure 4.13(b) shows that the absorption from (111)B InAsP/InP strained MQWs is remarkably different. First, the $1e-1hh$ excitonic absorption is hardly observable. [The peak should be around the position

indicated by the arrow in Fig. 4.13(b)]. This is attributed to the loss of the oscillator strength in exciton absorption arising from a reduction of the overlap integral for a tilted-bandedge quantum well.[7] This phenomenon reflects the significance of QCSE in modulating the absorption coefficient in optical modulator operation.[1,19] Second, transmissions from higher excited states have different energy positions compared to those of (100) quantum wells. The difference will be explained later when we discuss PLE spectra and a model calculation. In addition, absorption from higher subband excitons are even more intense than from the 1e-1hh absorption, as shown in Fig. 4.14(b). This happens because the reduction of oscillator strength under an electric field is less severe for higher subbands. The lower reduction of the oscillator strength correlates with the much smaller energy shift for higher subbands as shown in Fig. 4.5. Finally, the bandedge absorption of InP (111)B layer occurs at a higher energy, which we do not understand at present.

4.4.3 PLE spectra and valence band offset determination for (111) heterostructures

In order to resolve the transitions from higher excited states more clearly, low-temperature PLE measurements were performed. Shown in Figs. 4.14(a) and (b) are PLE spectra taken from the strained InAsP/InP (100) MQWs (Sample HI70) and (111)B MQWs (Sample HB30), respectively. (PL spectra are shown in the same figures with dotted curves). Distinct transitions from the higher subband excitons can be observed. In addition, a very sharp peak appears adjacent to the first hh exciton transition for both samples. They are believed to be parity-forbidden transitions.[23] The selection rule may be somewhat relaxed owing to a built-in field or strain-induced band-structure modulation. We performed an energy-level calculation based on the structural parameters determined by x-ray diffraction and the models described in Section 4.2. For the (111)B quantum well, the built-in electric field was calculated to be 53.8 kV/cm, which includes

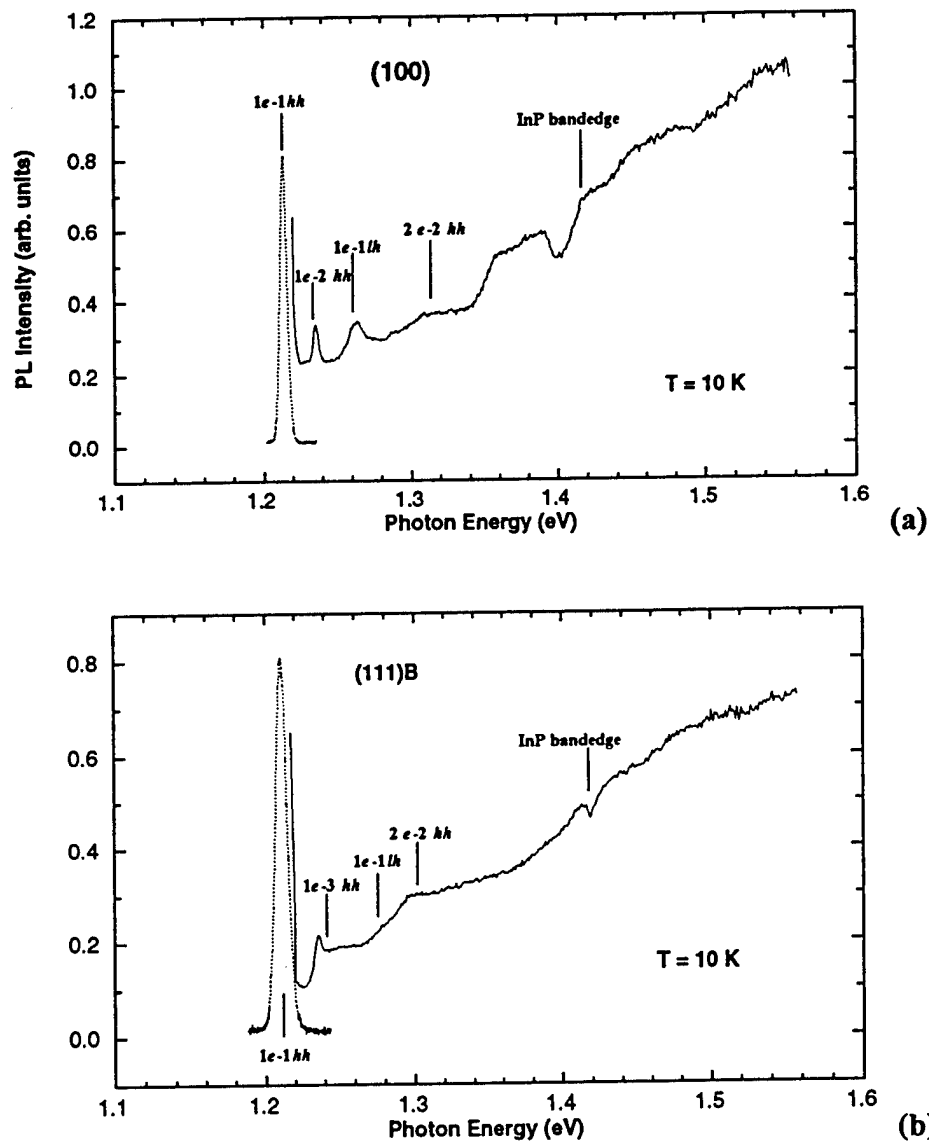


FIG. 4.14. PLE spectra taken at low temperature from $\text{InAs}_{0.21}\text{P}_{0.79}(80 \text{ \AA})/\text{InP}(120 \text{ \AA})$ strained MQWs grown on (a) (100) and (b) (111)B substrates. Very distinct transitions from higher subbands, and parity-forbidden transitions are observed. The assignments for the transitions are based on an energy-level calculation from the envelope-function model and the effective well width model [for the (111) quantum well only]. The vertical bars indicate calculated results.

the piezoelectric field from Eq. (4.9) and a correction to the band bending of the undoped epilayer on the n^+ substrate. The QCSE energy shifts for 1e and 1hh levels at the field of 53.8 kV/cm are calculated to be 1.8 and 8.1 meV, respectively, as shown in Fig. 4.4. We took Q_v as the only adjustable parameter to calculate the transition energies. A self-consistent procedure was carried out to include properly the contribution from the QCSE energy shift in (111) MQWs.

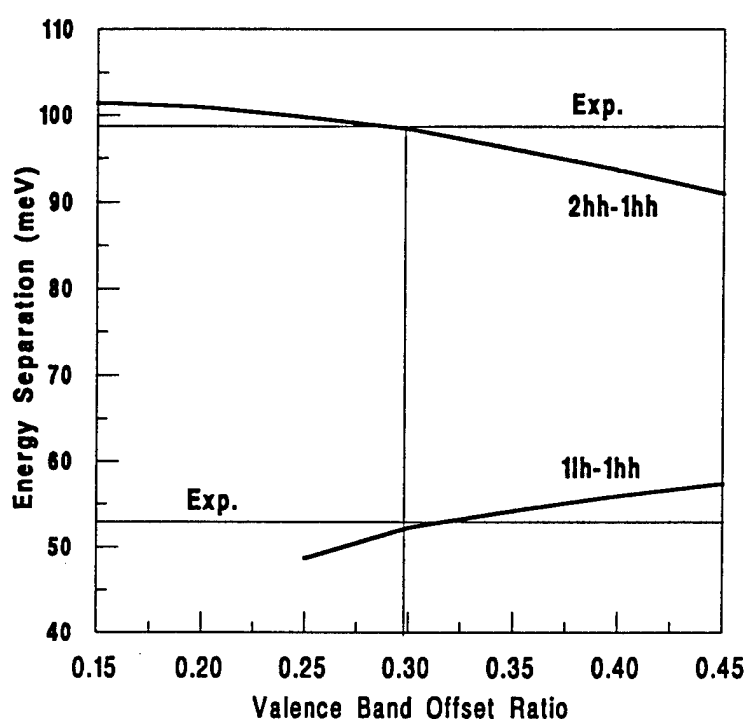


FIG. 4.15. Energy difference between 2e-2hh and 1e-1hh, and between 1e-1lh and 1e-1hh excitonic transitions calculated as a function of Q_v . The best fit between experimental and theoretical results can be obtained for $Q_v \sim 0.3$.

The differences in transition energies between higher excited state transitions and the 1e-1hh were calculated as a function of the Q_v since the transition energy from the first confined levels, 1e-1hh, is not very sensitive to Q_v . Figure 4.15 illustrates the theoretical and experimental results for energy differences of (2e-2hh)-(1e-1hh) and (1e-1lh)-(1e-1hh) for the (100) $\text{InAs}_{0.21}\text{P}_{0.79}/\text{InP}$ heterostructure. The best fit of the energy level calculation to the experimental spectra suggests that Q_v for (100) $\text{InAs}_{0.21}\text{P}_{0.79}/\text{InP}$ heterostructure is 0.30. The result from a similar calculation for (111)B $\text{InAs}_{0.21}\text{P}_{0.79}/\text{InP}$ heterostructure is 0.35. Vertical bars in Figs. 4.14 indicate the calculated transition energies. The peaks are assigned as various interband excitonic transitions according to the calculation. Excellent agreement between the calculation and experimental results is achieved.

The determination of Q_v for (100) InAsP/InP heterostructures was reported [20,21] by using different optical techniques. Our result is consistent with the results reported there. It should be mentioned that in determining Q_v there is definitely an uncertainty, which is from both the experimental accuracy and the theoretical model. Although this uncertainty is believed to be larger than the difference in the Q_v between (111)B and (100) heterostructures, we can still extract the difference in optical properties through a *comparative* study because the samples were grown under the same conditions and had the same structural parameters and the same optical techniques and theoretical models were employed.

It is interesting to note that a slightly larger value of Q_v was obtained for the (111)B heterostructure. This is believed to result from the strain dependence of the bandedge shift. As depicted in Fig. 4.2 the bandedge shift from the CB and hh VB in the (100) direction are 31.5 and 7.7 meV, respectively. On the other hand, these shifts in the (111)B strained InAsP layer are 43.7 and 7.0 meV, respectively. It was reported that the band offset distribution was governed by the core levels of the constituent atoms in the

compound.[29] As a result, the band lineup for InAsP with respect to InP (not heterostructure) should be independent of the substrate orientation. The band structure of (100) InAsP/InP heterostructures have been studied substantially,[20,21] and the results are consistent with that determined here ($Q_v=0.30$). From this and the fact that the strain leads to a larger reduction in the CB discontinuity for (111)B InAsP/InP heterostructures than for (100), we should be able to determine the valence band offset of the (111)B InAsP/InP heterostructure. Illustrated in Fig. 4.16 is the schematic diagram of the band lineup of strained InAsP layers grown on InP (111)B and (100) substrates with respect to the bandedge of InP. The relative bandedge lineup of the (111) InAsP/InP heterostructure is obtained from Fig. 4.2. The Q_v determined by this way for the (111) InAsP/InP quantum structure (~ 0.32) is in qualitative agreement with the result determined by the energy-level calculation (~ 0.35).

Wang *et al.* reported[30] in 1986 a determination of the CB discontinuity of the GaAs/AlGaAs heterostructures grown on both (100) and (311) substrates by Hall measurements. They found that Q_v does not depend on the substrate orientation. This is consistent with our findings here since the GaAs/AlGaAs is a lattice-matched material system, in which there is no strain-induced bandedge shift as in the InAsP/InP structure. Because of strain, Q_v is slightly larger for InAsP/InP (111) structures than for (100).

Now we compare the PL emission energy between spectra from (111)B and (100) MQWs shown in Fig. 4.12. Competing effects govern the transition energies. On one hand, the quantization effect due to the larger hh effective mass and the QCSE shift would decrease the emission energy from (111)B MQWs by approximately 2 and 10 meV, respectively. This would lead to a red shift of the PL peak spectrally; On the other hand, the same strain yields a larger bandgap increase (~ 13 meV) for (111)B strained InAsP bulk layer than for a (100) bulk layer, as shown in Fig. 4.2. As results of these two

compromising processes, the emission energies are almost the same for (111) and (100) quantum wells as shown in Fig. 4.12.

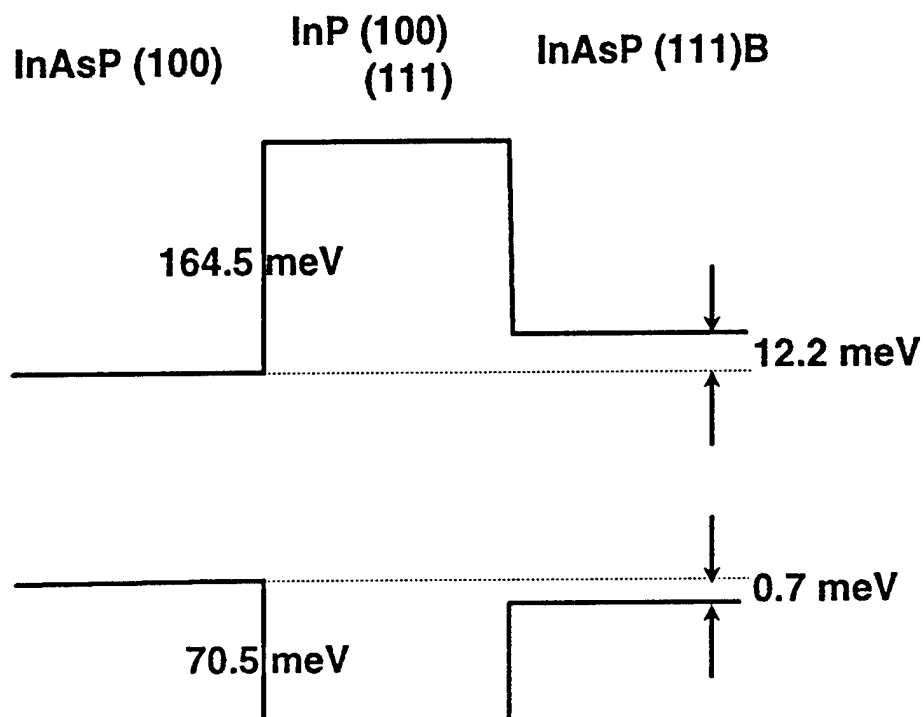


FIG. 4.16. Schematic diagram of the band lineup for strained InAsP layers grown on (111)B and (100) substrates with respect to the InP layer. The energy reference of the InAsP bandedges is obtained from Fig. 4.2.

4.5 Screening of piezoelectric field in (111)B InAsP/InP strained quantum wells

As discussed in Section 4.2, a built-in electric field exists in the strained (111)B InAsP/InP heterostructure. In this section, we will demonstrate the existence of this field by low-temperature PL measurements. To ensure pumping uniformity in the quantum

well, the samples used in this investigation consisted of a *single* InAsP/InP QW, grown on a 5000-Å thick InP buffer layer and capped with a 400-Å thick InP layer. The epilayers were nominally undoped. The composition and layer thickness calibration were performed on an InAsP/InP *multiple* QW structure grown consecutively under the same conditions as the single QW sample. The structural parameters were extracted from a computer simulation to x-ray rocking curves for the multilayered structure (see Section 3.5.3 for details).

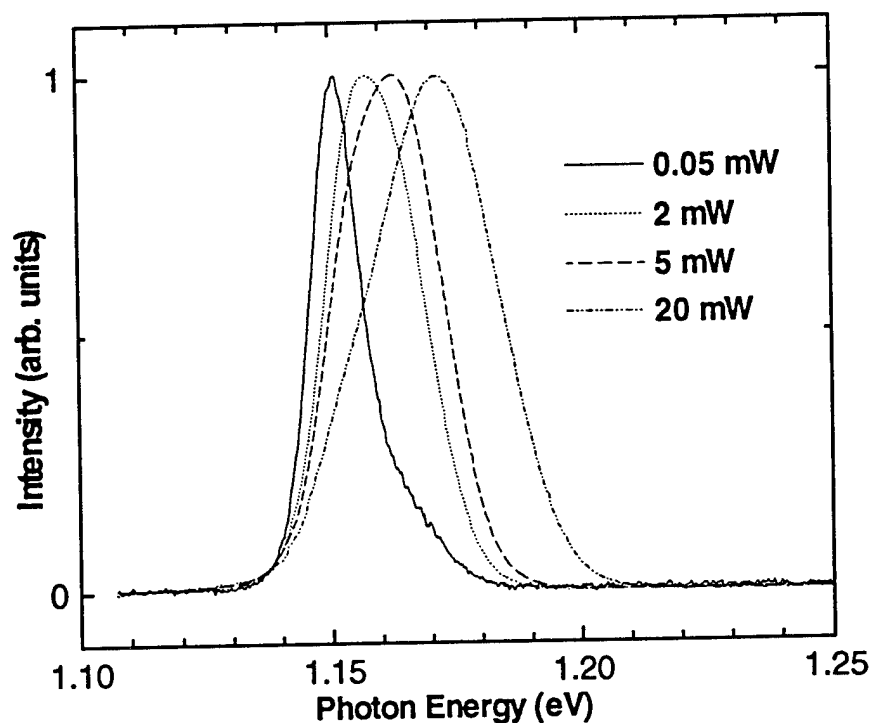


FIG. 4.17. Low-temperature PL spectra taken from a (111) InAsP(100 Å)/InP single QW under different pumping density. The PL peaks shift to higher energy and broaden in linewidth as the pumping density increases.

4.5.1 Low-temperature PL measurements at various pumping densities

Photoluminescence measurements were carried out at about 15 K in the same setup as described before. The QW structures were excited by the 5145-Å line from an argon-ion laser. The spectral resolution was approximately 1 meV. The pumping power ranged from 8 μW to 200 mW by using neutral density filters, and the laser beam was focused to a spot with an approximately 100- μm diameter. Correspondingly, the pumping density ranged from 0.1 W/cm^2 to 2.5 kW/cm^2 .

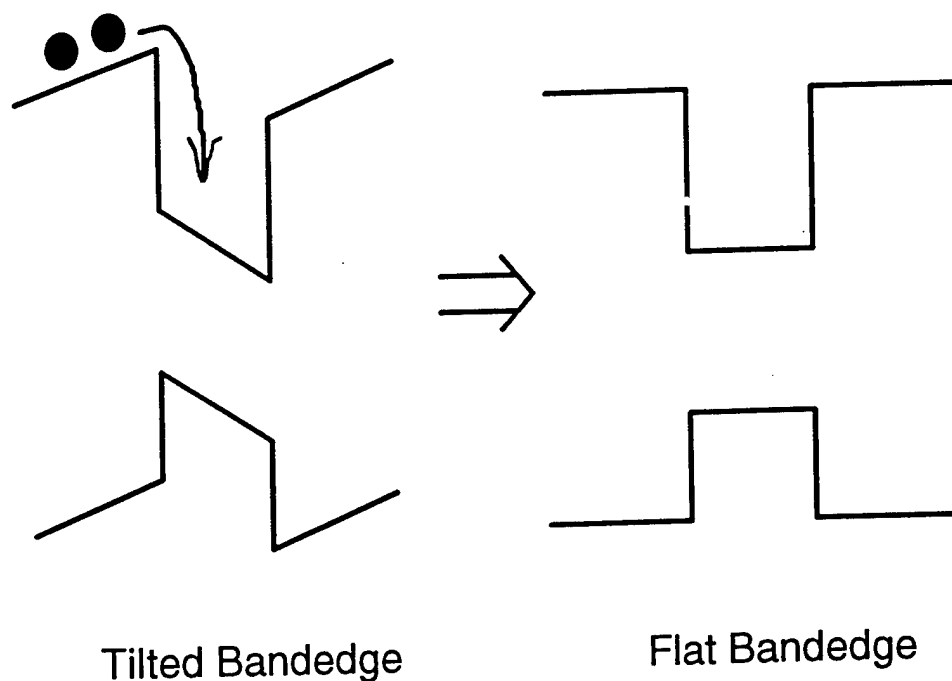


FIG. 4.18. Schematic diagram of the screening effect of the piezoelectric field by photo-generated carriers during PL measurements at high pumping power. A flat band condition can be reached when the built-in field is screened entirely.

Figure 4.17 shows PL spectra taken from an $\text{InAs}_{0.28}\text{P}_{0.72}(100 \text{ \AA})/\text{InP}$ single QW grown on an InP (111)B substrate under different pumping densities. The peak intensity was normalized for the sake of comparison. Sharp (FWHM~12 meV) and intense PL emission was observed at very low pumping density ($\sim 0.6 \text{ W/cm}^2$), indicative of good optical quality of the sample. Increasing the pumping density shifts the PL peak to higher energy side due to the screening of the built-in piezoelectric field. This phenomenon was observed previously for GaSb/AlSb[31], InGaAs/GaAs,[28] and InGaAs/InAlAs[10] strained quantum structures. As shown in Eq. (4.9), the piezoelectric field is proportional to the shear component of the strain tensor in (111)B heterostructures.[4,7] It was calculated to be 64 kV/cm for this highly strained $\text{InAs}_{0.28}\text{P}_{0.72}(100 \text{ \AA})/\text{InP}$ ($\epsilon_o \sim 0.9\%$) QW, and the bandedges of both the quantum well and the barrier will be tilted, as shown in Fig. 4.18. The confined energy levels in the QW shifts down to the bottom of the QW due to QCSE.[19] When a high-density laser beam is irradiated on the sample, free electrons and holes are generated in both the well and the barrier layers. The photo-generated free carriers then diffuse and are quickly trapped in the QW, neutralizing some interface piezoelectric charges. As a result, the piezoelectric field is partially screened and the bandedge tilting becomes smaller. The confined energy levels will then shift back to higher energy; therefore, a blue energy shift is observed for the PL emission when a higher pumping power is applied.

4.5.2 Field screening and blue energy shift

Depicted in Fig. 4.19 is the energy shift as a function of the laser pumping density. The blue shift starts at about 6 W/cm^2 pumping power, and is as large as 35 meV at 2.5 kW/cm^2 . Moreover, the amount of the energy shift was found to depend on the pumping density exponentially. We do not understand this dependence at present. We ruled out, however, the possibility of the band filling effect, instead of the free-carrier

screening, for the energy shift since the same experiments performed on a control sample with the same structure grown on an InP (100) substrate showed negligible energy shift. A possible reason for the exponential dependence lies in complications of the pumping situation for both well layer and barrier layer. An excitation with an energy between the InP and InAsP bandgaps may help in resolving this puzzle.

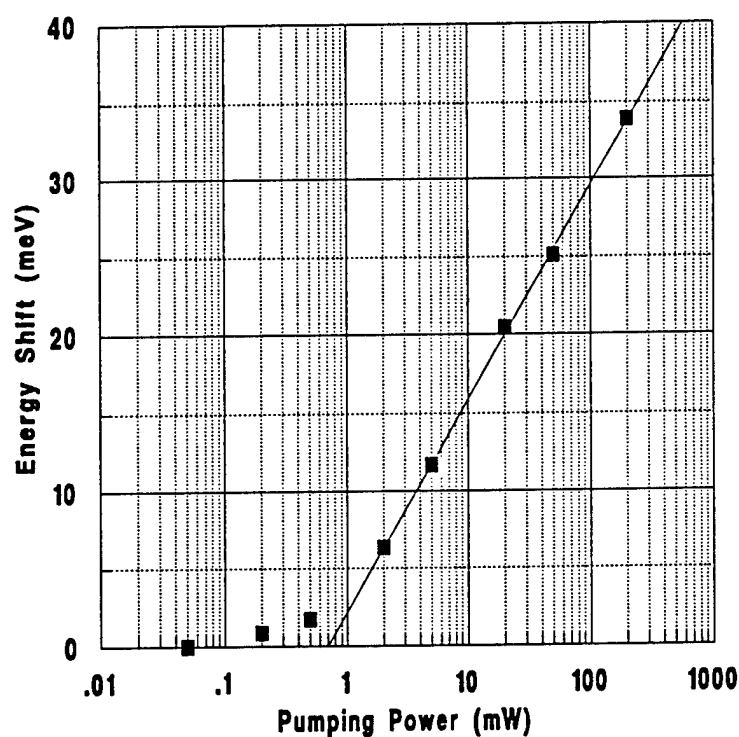


FIG. 4.19. Emission energy shift as a function of the pumping density for a highly strained InAsP (100 Å)/InP QW with a lattice-mismatched of $\epsilon_0 \sim 0.9\%$. The energy shift is as high as 35 meV when the sample was pumped with a very high density.

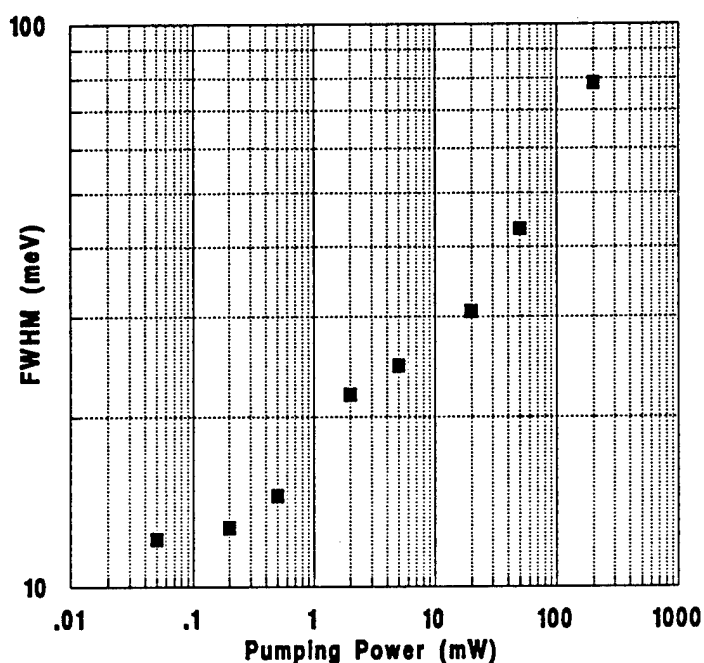


FIG. 4.20. The FWHM of the PL peaks measured from for an InAsP/InP strained quantum well as a function of the pumping density.

Another noteworthy point in the spectra in Fig. 4.17 is the broadening of the PL peaks with increasing the pumping density. Figure 4.20 shows the FWHM as a function of the pumping density for this sample. A narrower linewidth is expected for the emission under a smaller built-in field (or higher pumping power) since the lower electric field reduces less the overlap integral.[19] However, increasing the pumping power produces more hot carriers, resulting in broader FWHM. This broadening observed could be partially from the nonuniform intensity distribution of the laser spot on the sample. If the same experiment is performed on a strained quantum well with a very small strain in

the quantum well layer, where the piezoelectric charge density is very small, the effect of field screening on the line width may be noticeable before the carriers become hot. Consequently, the linewidth of the PL peak may become narrower first at a medium pumping density, and then become broad again at a very high pumping density.[28]

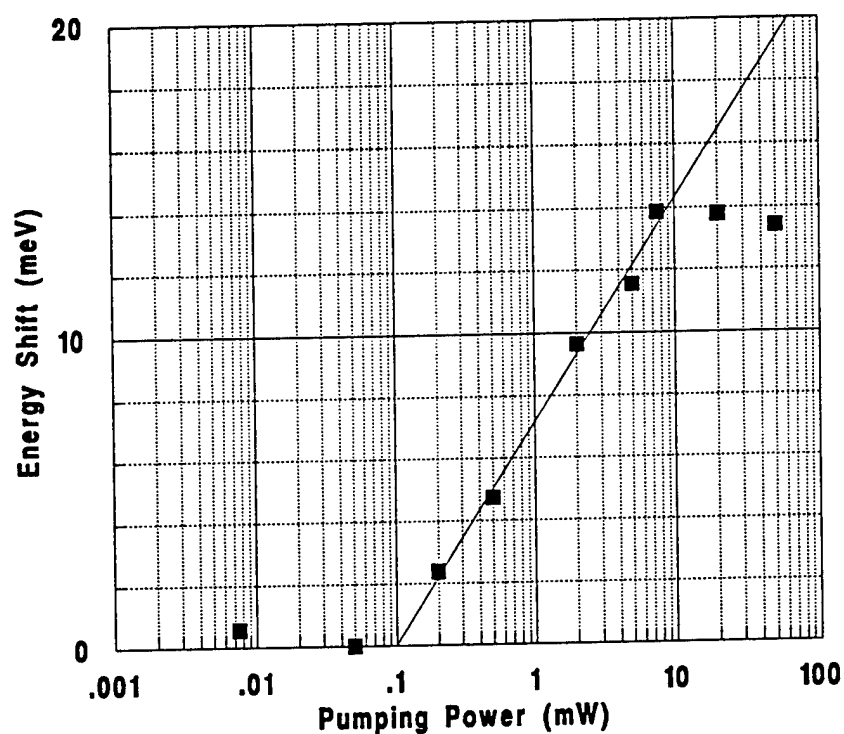


FIG. 4.21. Emission energy shift as a function of the pumping density for a slightly strained InAsP (100 Å)/InP QW with a lattice-mismatched of $\epsilon_0 \sim 0.65\%$. A saturation of the energy shift (~ 13.8 meV) indicates a flat-band condition.

4.5.3 Deduction of the valence band anisotropy

Figure 4.21 shows the blue energy shift as a function of the pumping density for a $\text{InAs}_{0.19}\text{P}_{0.81}(100 \text{ \AA})/\text{InP}$ ($\epsilon_p \sim 0.65\%$) single QW, which has a smaller built-in strain than the previous sample. The energy shift, starting at $\sim 1 \text{ W/cm}^2$, is again dependent on the pumping power exponentially. When the pumping density increases to $\sim 120 \text{ W/cm}^2$, however, the energy shift saturates at a value of $\sim 13.8 \text{ meV}$. When the sample is pumped with even higher density the PL linewidth broadens, but the photon energy remains the same. This saturation indicates that a flat-band condition is reached. This is a clear evidence of the existence of the piezoelectric field in strained InAsP/InP (111) QWs, and a direct measurement of the piezoelectric field-induced energy shift in the QW structures due to QCSE. We can deduce the heavy-hole effective mass of the InAsP [111] layer from this experimentally determined energy shift (ΔE_{QCSE}), 13.8 meV , which results from changes in the electron level (ΔE_{1e}), the heavy-hole level (ΔE_{1hh}), and the exciton binding energy (ΔE_b), i.e.,

$$\Delta E_{\text{QCSE}} = \Delta E_{1e} + \Delta E_{1hh} + \Delta E_b . \quad (4.12)$$

We assume *a priori* that the (111) InAsP/InP heterostructure possesses the same valence band offset ratio as the (100), i.e. $Q_v = 0.3$. The lowest confined electron level, E_{1e} , is calculated by using an envelope-function model with the known electron effective mass, as discussed in Section 4.2. From Eq. (4.9) the built-in piezoelectric field equals 44.4 kV/cm for $\text{InAs}_{0.19}\text{P}_{0.81}$. By employing an "effective well-width" model[19] for QCSE-induced energy shift, ΔE_{1e} was determined to be 2.1 meV . ΔE_b was taken to be 1.5 meV . [19] Deducting these amounts from Eq. (4.12), we obtain ΔE_{1hh} to be 10.2 meV . Then a best-fit calculation was performed to determine m_{hh}^* . The hh energy E_{1hh} was calculated by assuming an initial value of the effective mass, $m^*(i)$. Then ΔE_{1hh} was calculated for an electric field of 44.4 kV/cm . This value was compared to 10.2 meV , the

experimentally determined value. An iteration of $m^*(i)$ gives a final, consistent output of $m_{hh}^* = 1.2m_o$, where m_o is the free electron mass. This result agrees with the theoretical results reported by Lawaetz,[17] and furthermore suggests a large anisotropy of the valence band in the (111) InAsP layer since $m_{hh}^* = 0.52m_o$ for (100) InAs_{0.19}P_{0.81}. A more rigorous calculation may better account for various effects, but this calculation is a good approximation since most of the QCSE shift results from the shift of the heavy-hole energy level.

4.6 Conclusion

In summary, we have presented optical properties of InAs_xP_{1-x}/InP strained quantum wells by various optical techniques, including PL, PLE, absorption and photo-modulated transmission measurements. Intense and sharp excitonic transitions were clearly resolved from the InAs_xP_{1-x}/InP quantum wells grown on both InP (111)B and (100) substrates, suggesting the viability of InAsP/InP MQWs for 1.06, 1.3 and 1.55 μ m optoelectronic device applications. Low-temperature PL, absorption and PLE measurements all suggest excellent optical quality of these samples. Optical transitions from higher subband excitons and parity-forbidden transitions were observed. A detailed model calculation considering the effects of strain, VB anisotropy, piezoelectricity, and QCSE was carried out. An excellent agreement between the calculation and experimental results was achieved, and the VB offset ratio was determined to be 0.30 and 0.35 for the InAs_{0.21}P_{0.79}/InP heterostructures grown on InP (100) and (111)B substrates, respectively. This study provides a better understanding on the dependence of the band offset ratio upon the substrate orientation, and on the difference of the quantum-size effect. The free-carrier screening effect was observed for strained InAsP/InP single quantum wells grown on InP (111)B substrates. A flat-band condition was identified from the saturation of the blue energy shift in PL spectra with increasing pumping

density. From the measured QCSE energy shift and the model calculation, the heavy-hole effective mass is deduced, which is consistent with theoretical results.

The optical characterizations also indicate that we have successfully synthesized, on InP (111)B substrates, a state-of-the-art InAsP/InP strained MQW structure, which is a promising material system for the realization of nonlinear optical devices in the long-wavelength region by the use of the internal field and the unique electro-optic property of the carrier-screening of the internal field.

References:

- [1] T. K. Woodward, T. Sizer, and T. H. Chiu, Appl. Phys. Lett. **58**, 1366(1991).
- [2] H. Q. Hou, C. W. Tu, and S. N. G. Chu, Appl. Phys. Lett. **58**, 2954 (1991);
H. Q. Hou and C. W. Tu, J. Electron. Mater. **21**, 137 (1992);
and H. Q. Hou, A. N. Cheng, H. H. Wieder, W. S. C. Chang, and C. W. Tu, Appl.
Phys. Lett. **63**, Sept. 27 (1993).
- [3] T. Fukushima, A. Kasukawa, M. Iwase, T. Namegaya, T. Kikuta, IEEE Photon.
Technol. Lett. **5**, 117 (1993).
- [4] D. L. Smith and C. Mailhot, Solid State Commun. **57**, 919 (1986); and Phys. Rev.
Lett. **58**, 1264 (1987).
- [5] T. Hayakawa, K. Takahashi, M. Kondo, T. Suyama, S. Yamamoto, and T. Hijikata,
Jpn. J. Appl. Phys. **26**, L302 (1987).
- [6] H. Imamoto, F. Sato, K. Imanaka, and M. Shimura, Appl. Phys. Lett. **55**, 115 (1989).
- [7] E. A. Caridi, T. Y. Chang, K. W. Goossen, and L. F. Eastman, Appl. Phys. Lett. **56**
659 (1990).
- [8] K. W. Goossen, E. A. Caridi, T. Y. Chang, J. B. Stark, D. A. B. Miller, and R. A.
Morgan, Appl. Phys. Lett. **56**, 715 (1990).
- [9] I. Sela, D. E. Watkins, B. K. Laurich, D. L. Smith, S. Subbanna, and H. Kroemer,
Phys. Rev. B **43**, 11884 (1991).
- [10] K. Nishi and T. Anan, J. Appl. Phys. **70**, 5004 (1991).
- [11] H. Q. Hou and C. W. Tu, Appl. Phys. Lett. **62**, 281 (1993).
- [12] H. Q. Hou and C. W. Tu, J. Cryst. Growth **127**, 199 (1993).
- [13] G. Bastard and J. A. Brum, IEEE J. Quantum Electron. **QE-22**, 1625 (1986).
- [14] E. A. Caridi and J. B. Stark, Appl. Phys. Lett. **60**, 1441 (1992).
- [15] J. Y. Marzin, in *Heterostructures and Semiconductor Superlattices*, edited by G.
Allan *et al.* (Springer, Berlin, 1986), p. 161.

- [16] W. Pötz and D. K. Ferry, *J. Vac. Sci. Technol.* **B4**, 1006 (1986).
- [17] P. Lawaetz, *Phys. Rev. B* **4**, 3460 (1971).
- [18] T. Hayakawa, K. Takahashi, M. Kondo, T. Suyama, S. Yamamoto, and T. Hijikata, *Phys. Rev. Lett.* **60**, 349 (1988).
- [19] D. A. B. Miller, D. S. Chemla, T. C. Damen, A. C. Gossard, W. Wiegmann, T. H. Wood, and C. A. Burrus, *Phys. Rev. B* **32**, 1043 (1985).
- [20] P. J. Wang and B. W. Wessels, *Appl. Phys. Lett.* **44**, 766 (1984).
- [21] S. J. Hwang, W. Shan, J. J. Song, H. Q. Hou, and C. W. Tu, *J. Appl. Phys.* **72**, 1645 (1992).
- [22] G. Bastard, E. E. Mendez, L. L. Chang, and L. Esaki, *Phys. Rev. B* **28**, 3241 (1983).
- [23] Y. Kajikawa, M. Hata, N. Sugiyama, and Y. Katayama, *Phys. Rev. B* **42**, 9540 (1990).
- [24] *Landolt-Börnstein New Series*, Edited by O. Madelung, Vol. 22a, (Springer-Verlag, 1986).
- [25] H. Q. Hou, Y. Segawa, Y. Aoyagi, S. Namba, and J. M. Zhou, *Phys. Rev. B* **42**, 1284 (1990).
- [26] W. Shan, X. M. Fang, D. Li, S. Jiang, S. C. Shen, H. Q. Hou, W. Feng, and J. M. Zhou, *Phys. Rev. B* **43**, 14615 (1991).
- [27] See, for example, D. E. Aspnes in *Handbook on Semiconductors*, Vol 2, edited by T. S. Moss (North Holland, N.Y. 1980), p. 109.
- [28] T. S. Moise, L. J. Guido, J. C. Beggy, T. J. Cunningham, S. Seshadri, and R. C. Barker, *J. Electron. Mater.* **21**, 119 (1992); and T. S. Moise, L. J. Guido, R. C. Barker, J. O. White, and A. R. Kost, *Appl. Phys. Lett.* **60**, 2637 (1992).
- [29] S. P. Kowalczyk, W. J. Schaffer, E. A. Kraut, and R. W. Grant, *J. Vac. Sci. Technol.* **20**, 705 (1982), and references therein.

- [30] W. I. Wang, T. S. Kuan, E. E. Mendez, and L. Esaki, Phys. Rev. B **31**, 6890 (1985).
- [31] B. V. Shanabrook, D. Gammon, R. Beresford, W. I. Wang, R. P. Leavitt, and D. A. Broido, *Proceedings of the 20th International Conference on the Physics of Semiconductors*, edited by E. M. Anastassakis and J. D. Joannopoulos (World Scientific, Singapore, 1990), p. 901.

Chapter V

Electrooptical Properties of (100) InAsP/InP Strained Quantum Wells

5.1 Introduction

Optoelectronic devices operating at 1.3 μm wavelength are of great importance for long-haul fiberoptic communication due to minimum dispersion at this wavelength for several varieties of optical fibers.[1] An external optical modulator can provide a high bit-rate, low noise and large-depth light modulation.[2] Furthermore, a waveguide modulator is used to confine the optical beam over an arbitrary interaction length. The usual structures for 1.3 μm emission can be realized by InGaAsP/InP[3] or InGaAlAs/InAlAs[4] quantum well structures lattice-matched to InP substrates, but the composition control of the quaternary layers can be difficult, particularly when a specific absorption wavelength has to be obtained. The quaternary-alloy quantum-well layer also possesses a high level of alloy disorder.[5] Moreover, the Al-containing compound has a problem of deterioration of the cleaved facets due to oxidization.

On the other hand, optoelectronic devices operating at 1.06 μm wavelength are also important for various optical information processing systems under development. An important device is the quantum well *p-i-n* diode optical modulator. If two-dimensional arrays of surface-normal modulators are used, the information processing capability can radically increase the aggregate information flow. These systems will require large amounts of optical powers with high spectral and spatial quality. It is not clear that semiconductor diode lasers can supply this power. A strong alternative is the Nd:YAG laser operated at 1.06 μm . Recent advances in diode pumping of solid-state lasers have resulted in making these lasers an efficient and compact source of coherent radiation. To

date, the requirement at this wavelength is satisfied by using lattice-matched InGaAsP/InP,[6] highly strained InGaAs/GaAs,[7] and strain-balanced InGaAs/GaAsP multiple quantum wells (MQWs).[8]

Strained $\text{InAs}_x\text{P}_{1-x}/\text{InP}$ quantum structure has been demonstrated to be an alternative material system to the quaternary layers for the spectral region of 0.98–1.5 μm . [9] An independent control of the layer thickness and alloy composition can be achieved for $\text{InAs}_x\text{P}_{1-x}$ in gas-source molecular beam epitaxy (GSMBE). [10] The alloy composition for this compound can be determined *in situ* easily in GSMBE. [11] Recently, it was demonstrated that the 1.06 μm modulator could be fabricated from 50 periods of $\text{InAs}_{0.19}\text{P}_{0.81}/\text{InP}$ MQWs, [12,13] which are less strained ($\sim 0.7\%$) than the InGaAs/GaAs system ($\sim 1.8\%$). Improved performance over 1.06 μm InGaAs/GaAs modulators has been achieved. However, to obtain a sufficient contrast ratio, the surface-normal modulator has to be made in a Fabry-Perot cavity [14] or use many periods of the MQWs. The number of periods will be a limiting factor for implementing *strained* MQWs. For *waveguide* modulator applications, on the other hand, a smaller number of periods (typically 10–15) of absorbing layers are needed so as to keep the intrinsic region thin enough for low driving power operation. Therefore, the large lattice mismatch in 1.3 μm $\text{InAs}_x\text{P}_{1-x}/\text{InP}$ MQWs may not be a stringent problem, and the $\text{InAs}_x\text{P}_{1-x}$ layer thickness and the MQW period number can be kept within the pseudomorphic limit.

In this chapter, we will present electroabsorption (EA) properties of 1.06 and 1.3 μm modulators using strained InAsP/InP MQWs. The quantum confined Stark effect (QCSE) is clearly demonstrated by the absorption peak shift and the change of the absorption coefficient. The impact of the structural degradation as examined by cross-sectional transmission electron microscopy (XTEM) on the EA property is presented. Excellent electrooptical properties are obtained, for the first time, from a 10-period

InAs_{0.41}P_{0.59}(100Å)/ InP(150Å) MQW structure, which can be used as the core absorber of a 1.3 μm waveguide modulator.

This chapter is organized as follows. In Section 5.2, the theoretical and experimental background of EA study will be presented. In Section 5.3, the EA and photocurrent property will be discussed for two typical modulator structures operated at 1.06 and 1.3 μm, respectively. Section 5.4 follows as a correlation study of the electrooptical property with the structural property.

5.2 Device principle, fabrication, and measurement

5.2.1 *Quantum-confined Stark effect and effective well-width model*

The electronic states in a quantum well can be modulated significantly under an external perturbation, such as an electric field,[15] magnetic field,[16] and hydrostatic pressure.[17] The operation of optical modulators is based on the change of optical properties in a moderate electric field due to QCSE.[18] When an electric field is applied along the quantum well plane, the effect is mostly carrier heating and consequent exciton dissociation.[18,19]. However, the bandedge will be tilted by an electric field applied across an intrinsic quantum well, as shown in Fig. 5.1(a). This results in a significant modulation on the band structure. (1) The quantized energy levels in the quantum well will shift down towards the well bottom as a result of the Stark effect, namely a red energy shift of a charged particle in an electric field. (2) The wavefunction for electrons and holes will be localized at the opposite sides of the quantum well. This leads to a reduction of the overlap integral, and therefore a decrease of the exciton oscillator strength. (3) Carriers may penetrate into or tunnel through the barrier layer at a high field; consequently, the exciton can be ionized by the electric field.[18] For an absorption spectrum, as shown schematically in Fig. 5.1(b), the effect (1) causes a red energy shift of the absorption peak; (2), a reduction of the absorption intensity; and (3), a broadening

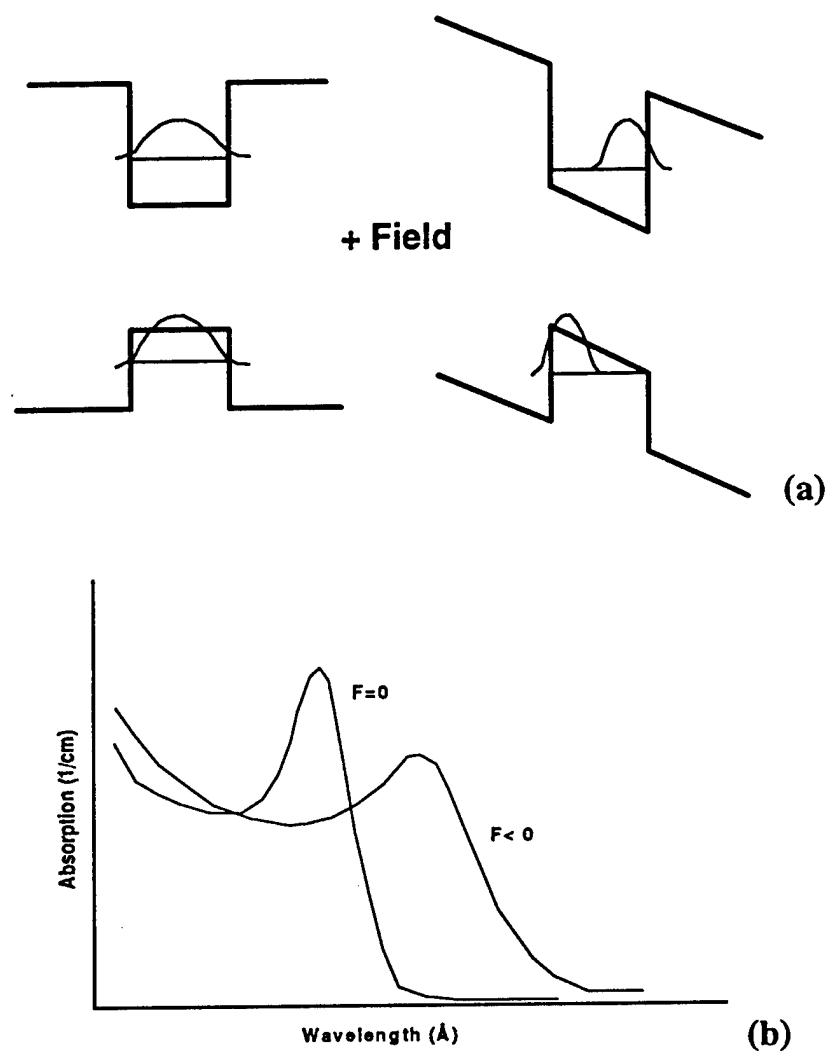
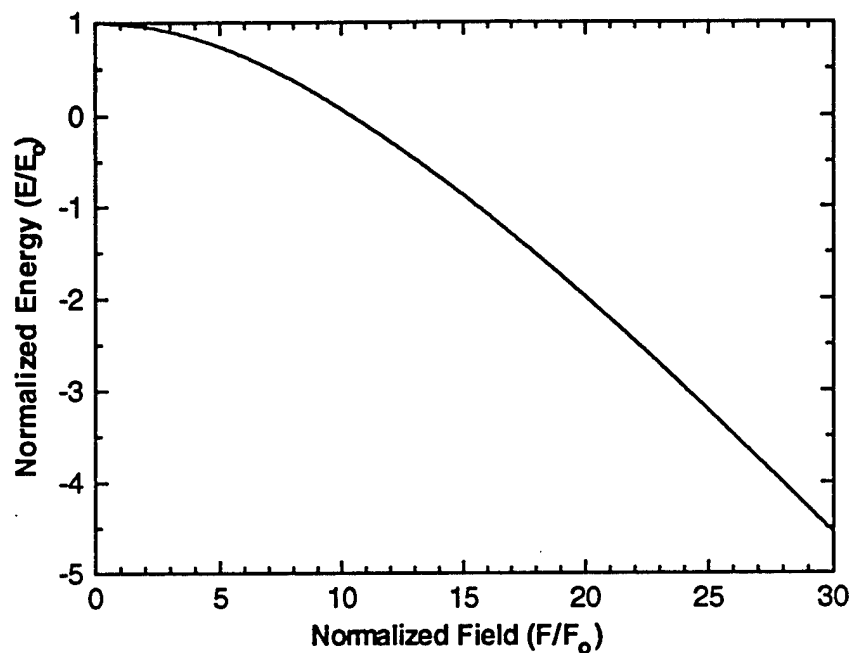


FIG. 5.1. (a) Schematic diagram of electroabsorption effect in MQWs. The left figure shows quantum wells formed by conduction and valence bandedges. The energy levels of the ground states for electrons and holes are shown, along with the wavefunction envelopes. The right figure shows these items when an electric field is applied perpendicular to the quantum well layers. (b) Schematic diagram of the absorption spectra from the corresponding quantum wells with and without field. Changes of the absorption energy, intensity and the line shape are due to QCSE



$$E_0 = \frac{\hbar^2}{2m^*} \left[\frac{\pi}{L_z} \right]^2 \quad \text{and} \quad F_0 = \frac{E_0}{eL_z}, \quad \text{where } L_z \text{ is the effective well width.}$$

FIG. 5.2. Universal curve for the energy of the first confined state in an infinite quantum well in the presence of a uniform electric field perpendicular to the well. The variables are energy and electric field normalized to those of the ground state.

of the absorption peak. The effects (2) and (3) can be modeled qualitatively,[20] but it is not easy to simulate the experiments accurately since these properties strongly depend on the material quality. On the other hand, the change in energy levels under a vertical electric field has been accounted for by several theoretical models. The perturbation and

variational[21] models are generally good for low-field region, but a significant discrepancy appears when the field is high. The tunneling-resonance and "effective well-width" models[18] were shown to be very effective in determining the energies. The basic concept of the effective well-width model was described in Chapter 4 already, and will not be repeated here. Basically, the Schrödinger equation is reduced to a standard nonlinear second-order differential equation, and its solution is a combination of Airy functions. By applying the boundary conditions, the electric field dependence on the energy levels can be solved numerically. Figure 5.2 shows the normalized energy (to the first confined energy level, E_0) as a function of the normalized field (to $F_0 = E_0 / eL_z$). This curve is universal, and can be applied to any quantum structure by simply de-normalizing the field and energy by calculating F_0 and E_0 for the real quantum well structure.[18]

5.2.2 Device processing technology

In order to apply a reverse electric field, a diode structure must be fabricated for the *p-i-n* structure. A transmission window is formed for EA or photocurrent (PC) measurements. A typical device structure and its ring-shaped *p*-layer ohmic contact are shown in Figs. 5.3(a) and (b), respectively. The flow chart for device processing is shown in Fig. 5.4. To reduce the scattering loss of the transmission light, the sample is polished on the backside by mounting the sample on a lapping chuck and then mechanically polishing with alumina powder on a lapping/polishing machine. After degreasing with organic solvent, we evaporate AuGe(2000 Å)/Ni(100 Å) *n*-type contact strips, which are defined by photo-lithography, on the backside of the n^+ -InP substrate. The sample is subsequently annealed at 400 °C for 30 sec in a forming gas to ensure a good ohmic contact. Then a second lithography is performed to define a ring-shaped contact area for the front side of the sample. The inner diameter of the ring is 200 μm for the probing light beam. The *p*-type non-alloyed, non-spiking contact metal, consisting of

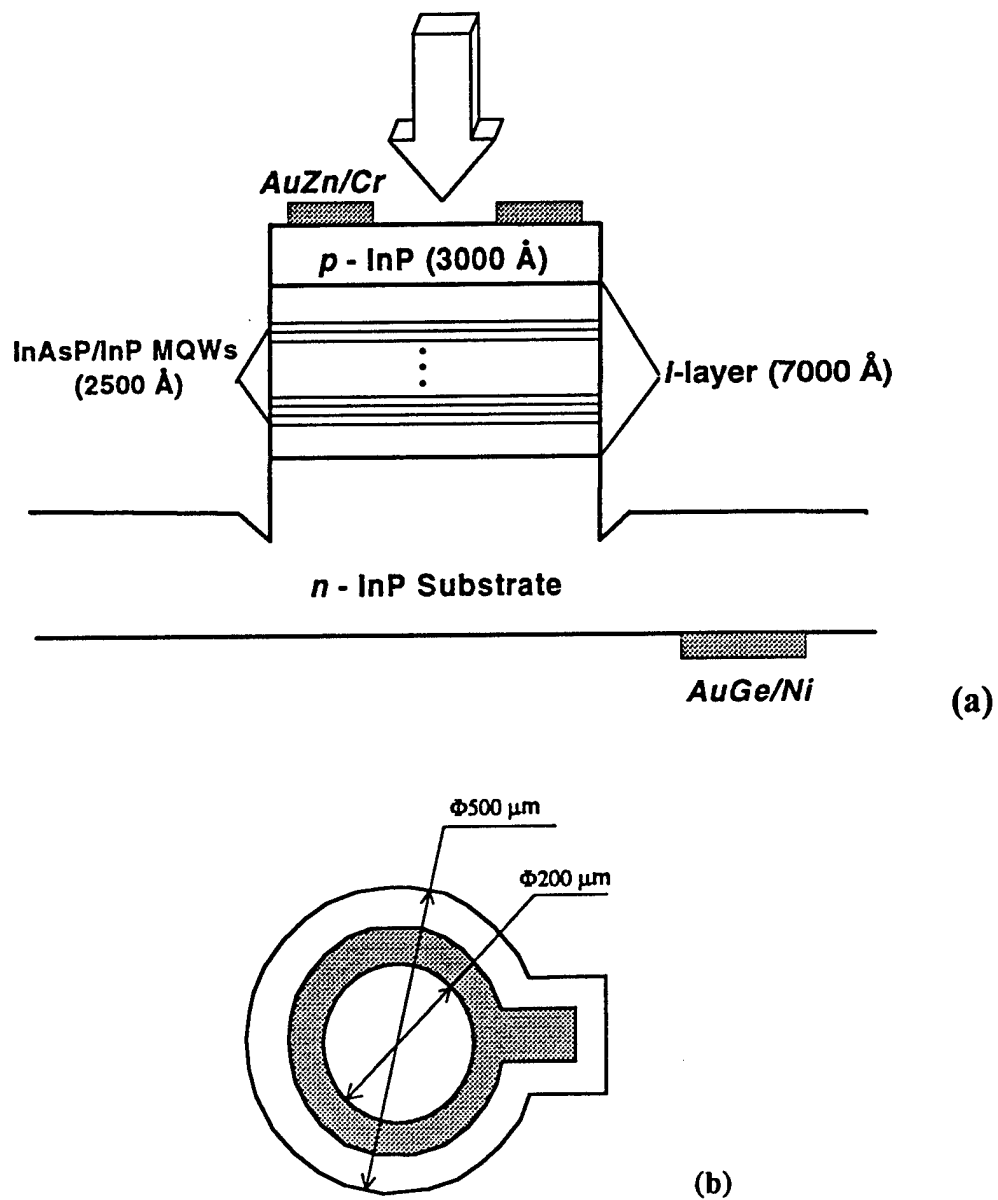


FIG. 5.3. (a) Schematic diagram of the cross section of a $p-i-n$ ring diode consisting of 10 periods of InAsP/InP strained MQWs in the intrinsic layer region. (b) The top view for the p -type ohmic contact of a ring diode.

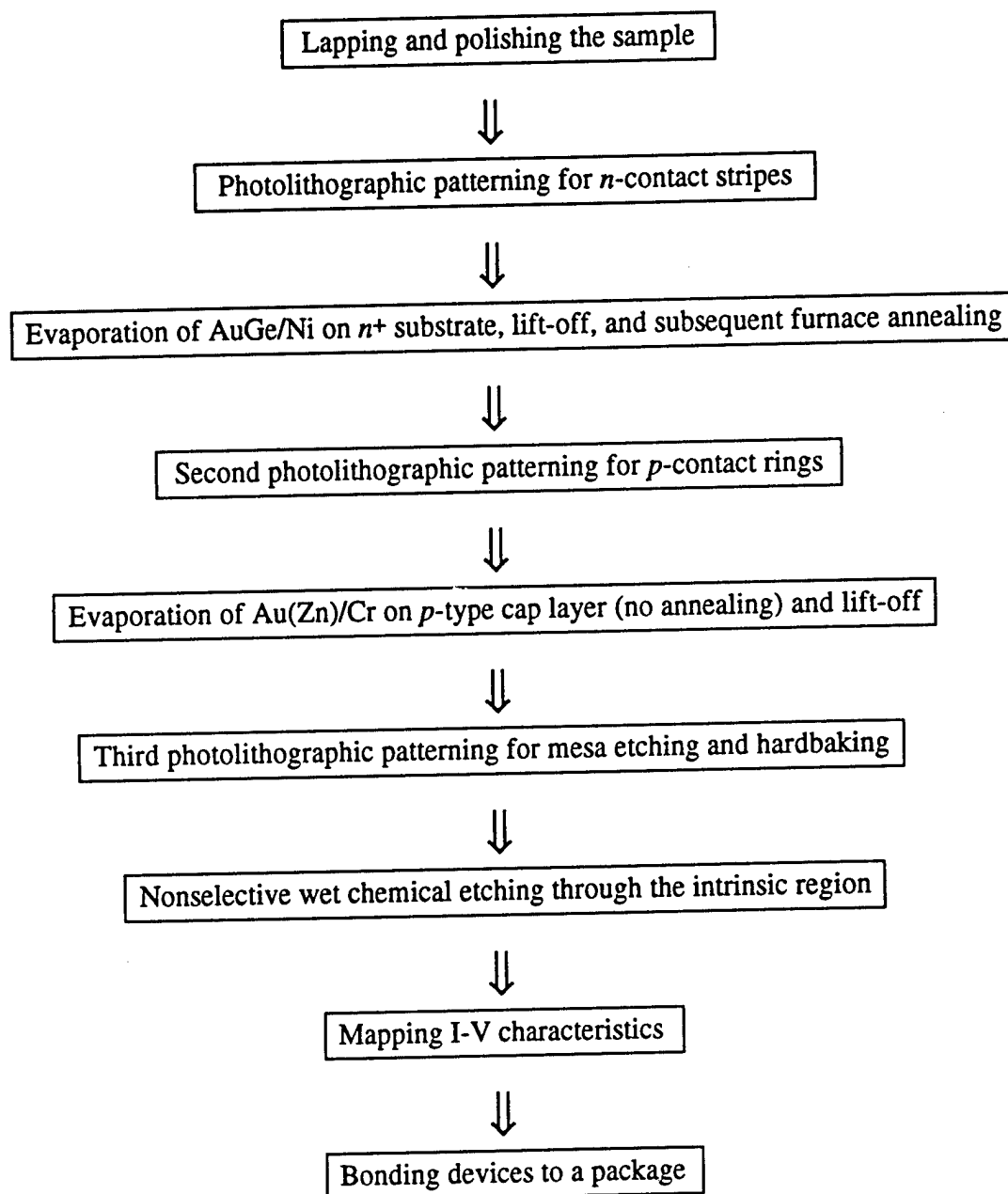


FIG. 5.4. Flow chart of the processing procedure for fabricating $p-i-n$ ring diodes.

2000 Å AuZn (or Au) on top of 100 Å Cr, is then evaporated by a thermal evaporator. Chromium improves the adhesion of Au and also serves as a barrier to zinc diffusion. After lifting off the evaporated metal, a third lithography defines a 500 μm diameter diode mesa around the *p*-type ring contact pattern. Wet chemicals are used to etch a 3 μm high mesa. The solution of (Br:HBr):H₂O in a content ratio of (1:17):30 provides a nonselective etching of both InP and InAsP with an etching rate of approximately 1 $\mu\text{m}/\text{min}$. At the mesa edge the etching trench is deeper by about 35%, as seen from the Dektak profile across a diode mesa. This may lead to a better isolation for the mesa.

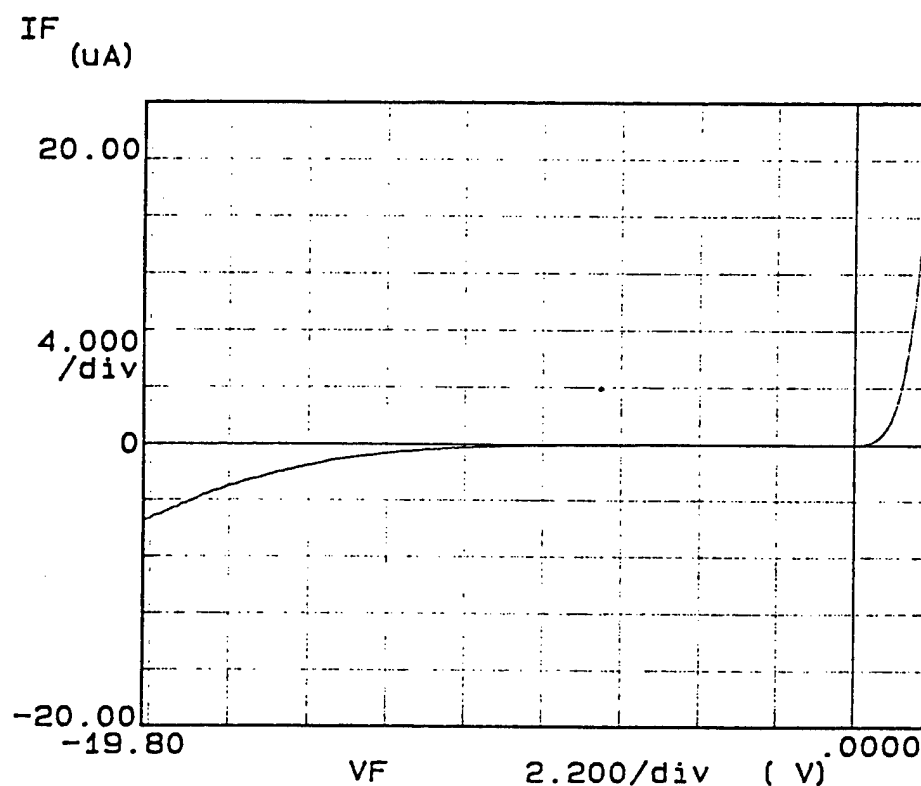


FIG. 5.5. I-V curve for a 1.3 μm InAsP/InP strained MQWs *p-i-n* diode modulator. Sharp turn-on under forward bias and hard breakdown under reverse bias suggest good electrical characteristics.

An I-V mapping for all the ring-diode modulators are carried out using a curve tracer. Typically, the device shows a sharp turn-on at about 2V and hard breakdown at >10 V for an intrinsic layer thickness of 7000 Å. Figure 5.5 depicts a typical I-V curve from a ring diode. This suggests a good electrical characteristic, such as good uniformity of the electric field in the intrinsic layer. The *p-i-n* diodes are also evaluated by C-V measurements. The result shows a $\sim 3 \times 10^{15} \text{ cm}^{-3}$ *n*-type background in the intrinsic layer region.

5.2.3 *Electroabsorption and photocurrent spectra*

Electroabsorption measurements are performed in the same absorption setup as illustrated in Fig. 4.6. Devices are soldered and wire bonded to a package. The reverse bias (negative to the *p* contact) is provided by a DC voltage supply. A μA meter is connected in series in the circuit to monitor the leakage current, which is typically less than 20 μA in the measured modulation voltage range. The alignment of the device in the optical path is made by adjusting x-y-z positions of the device while monitoring the photocurrent (PC) extracted from the device. The maximum PC indicates an optimal alignment of the device position. The transmission through the ring diode is normalized to the transmission from a bare InP area on the same wafer, where the MQW is etched out. We have fabricated several MQW modulators with different structural parameters and good EA property. Photocurrent spectra can be an alternative technique to EA with the same setup.

Since there is no antireflection (AR) coating for the sample surface, interference fringes are observed for some devices with thick layers. This makes the determination of the residual absorption very difficult. A special normalization procedure, however, can solve this problem.[4] The EA and PC spectra are taken consecutively from the same device with an identical alignment. Because the PC signal $[I(\lambda)]$ is related to the

transmission $[T(\lambda)]$ by $I(\lambda) = A(\lambda)[1 - T(\lambda)]$ at zero bias, the factor $A(\lambda)$ can be determined at the absorption peak λ_0 by correlating the EA spectrum with the PC spectrum. After assuming that the $A(\lambda)$ is independent of the wavelength in a narrow spectral range around the absorption peak, the transmission spectrum can be normalized from the PC spectrum through the factor $A(\lambda)$ in the whole spectral region. The normalized transmission at zero field is designated as $T_N(\lambda)$. The interference effect for transmission spectra under reverse biases, $T^V(\lambda)$, can then be canceled out by taking

$$T_N^V(\lambda) = T^V(\lambda) \cdot T_N(\lambda) / T(\lambda), \quad (5.1)$$

as normalized transmission spectra with biases. Spectral features were found to be the same as those measured from the devices with AR coating,[4] provided that the normalization is made in the vicinity (± 100 meV) of the absorption peak, suggesting the viability of this normalization procedure. The EA spectra discussed in this chapter are shown in terms of the absorption coefficient (α) by $T = T_0 \exp(-\alpha L)$, where L is the total thickness of the absorbing layer only, i.e., the thickness of the well layers.

5.3 Electroabsorption at 1.06 and 1.3 μm

5.3.1 $\text{InAs}_x\text{P}_{1-x}/\text{InP}$ MQWs for 1.3 μm waveguide modulators

The modulator samples are grown with an elemental In source and thermally decomposed hydride gas sources (AsH_3 and PH_3) from two separate gas injectors in a GSMBE system. The detailed growth conditions and composition control have been presented in Chapters 2 and 3. The sample structure, as shown in Fig. 5.3(a), consists of 10 periods of $\text{InAs}_{0.41}\text{P}_{0.59}$ (100 Å) / InP (150 Å) MQWs in the middle of a 7000-Å-thick intrinsic region, on a S-doped n^+ -InP (100) substrate and capped with a 3000-Å-thick Be-doped ($1 \times 10^{18} \text{ cm}^{-3}$) p -type contact layer. A calculation of the critical layer thickness suggests that the strained $\text{InAs}_{0.41}\text{P}_{0.59}$ quantum wells can be grown within the critical

limit for the layer thickness and period number of the MQW used in this work (see Figs. 3.1 and 3.2). The structural parameters are determined by x-ray rocking curves and computer simulations. Devices are fabricated after characterizations by absorption and low-temperature PL measurements.

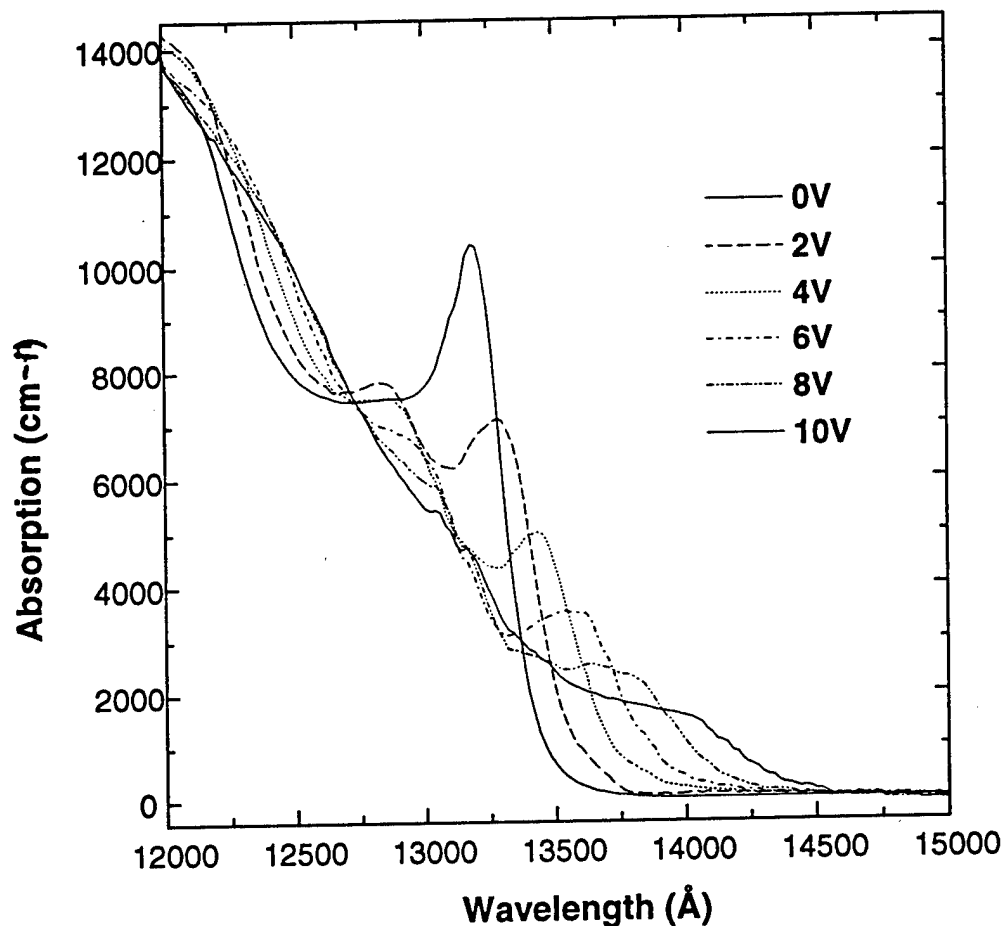


FIG. 5.6. EA spectra taken at various reverse biases for a 1.3 μm modulator structure. The sharp excitonic transition shows a significant red energy shift, a reduction of the absorption intensity, and a broadening of the linewidth due to QCSE and field ionization effect.

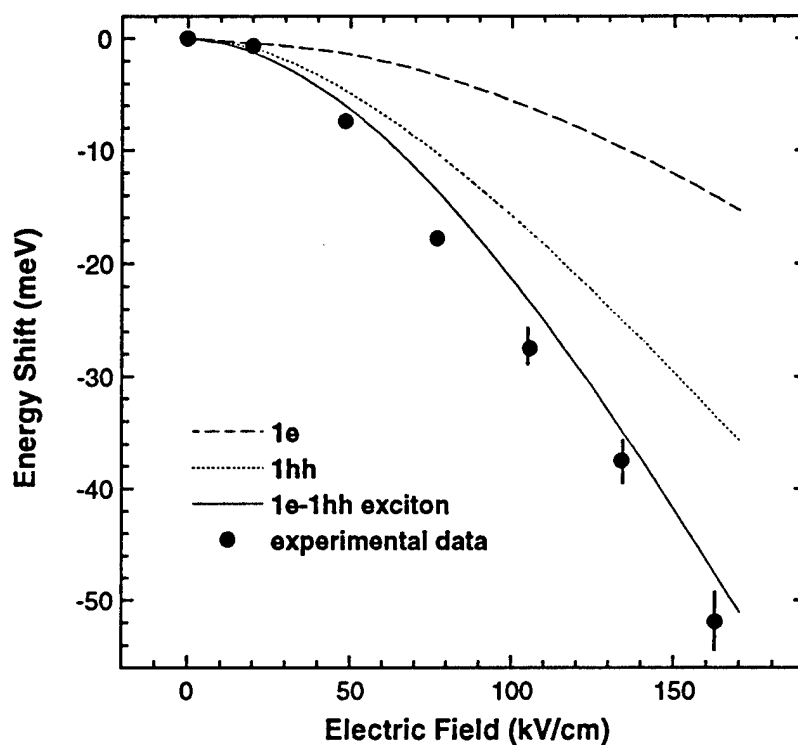


FIG. 5.7. Energy shift from the heavy-hole excitonic absorption as a function of the electric field across the quantum well. The calculated results are illustrated for the shift of electron (dashed curve) and heavy-hole (dotted curve) subbands, as well as for the energy of excitonic transitions (solid curve). A good agreement between theoretical and experimental (solid circles) results is obtained.

Shown in Fig. 5.6 are room-temperature EA spectra taken at various applied reverse biases. The absorption from the first heavy-hole subband exciton at zero-external bias shows a sharp peak with a half width at half maximum of 8.9 meV, indicative of good optical quality of this highly strained ($\sim 1.3\%$) MQW sample. The absorption coefficient is normalized to the total thickness of the quantum well layer (1000 Å). This

may be different from other conventions for spatial-light modulators in normalizing the absorption coefficient.[2] Several characteristics can be identified from the spectra shown in Fig. 5.6. First, the absorption peak shifts to lower energy with applying an electric field due to QCSE for excitons in the quantum wells. An additional feature is observable at the higher energy shoulder, which is believed to be from a parity-forbidden transition under the electric field. Second, the absorption intensity decreases with increasing the electric field across the quantum wells as a result of the reduction of the exciton oscillator strength as discussed in the last chapter. Finally, the absorption peak becomes broader under high field because the excitons are field-ionized.

Figure 5.7 shows the energy shift (solid circles) measured from the EA spectra in Fig. 5.6 as a function of the applied electric field. The uncertainties in determining the peak positions for broad peaks are given in Fig. 5.7 with error bars. The field is corrected for the inherent band bending in this *p-i-n* structure. Since the conduction band edge for n^+ InP and the valence band edge for p -InP are very close to the Fermi level at equilibrium, the built-in field was calculated to be ~ 19.3 kV/cm (1.35 V across the 7000-Å-thick intrinsic layer). This is evidenced by an EA measurement at a small forward bias (1V), which gives a small blue shift (~ 1.2 meV). We obtained a large energy shift up to 52 meV for a field of 160 kV/cm (10 V external reverse bias). Employing the physical constants provided in Table 4.2 and the recently determined band discontinuity (see Ref. 22 and Chapter 4), we carried out a calculation based on the effective well-width model for the energy shift in the $\text{InAs}_{0.41}\text{P}_{0.59}(100 \text{ \AA})/\text{InP}(150 \text{ \AA})$ MQWs. Illustrated in Fig. 5.7 by the dashed and dotted curves are the calculated energy shifts from the first electron and heavy-hole subbands, respectively. The solid curve gives the energy shift for the excitonic transition, where we neglected the change of the exciton binding energy under the electric field since it changes only about 2 meV in this region of the electric field.[18] We obtained a good agreement between the experimental and theoretical

results. The experimental results show a generally 2~3 meV larger shift than the calculation. If we take into account the change of the exciton binding energy, the discrepancy is even larger (4~5 meV). This discrepancy is not well understood presently. One possibility is that an effectively wider quantum well resulting from the interface diffusion probably exists and leads to a larger energy shift since the QCSE energy shift varies as the fourth power of the well width [Eq. (4.10)].

This large energy shift, e.g., ~18 meV at an *external* field of 57 kV/cm (4 V bias), is very desirable for low-power operation of the waveguide modulator. This energy shift is also remarkably larger than those from InGaAsP/InP[3] and InGaAlAs/InAlAs[4] systems. A reason for the superior EA property from InAsP/InP MQW modulators may be due to the smaller valence band offset. The bandgap discontinuities for these three heterostructures are about the same, but the distribution of this discontinuity to the valence band is significantly different, being about 60% for InGaAsP/InP and InGaAlAs/InAlAs,[23,4] and ~30% for InAsP/InP (Ref. 22 and Chapter 4). From the discussion in Section 4.2.3, the smaller confined energy resulting from a shallow quantum well will yield a larger QCSE energy shift. Therefore, we may attribute the remarkably large shift from the InAsP/InP modulator to the comparatively smaller valence band discontinuity.

In Fig. 5.8(a), we show the change of the absorption coefficient ($\Delta\alpha$) as a function of the detuning energy with respect to the absorption peak at zero bias. $\Delta\alpha$ can be as large as 4000 cm^{-1} with a detuning energy of 20 meV. The wide range (about 20~55 meV) of the effective absorption modulation enables the modulator to operate in a wide range of the voltage swing. The maximum $\Delta\alpha$ at the absorption peak position, however, is not useful for waveguide modulators because of a large residual absorption (α_0) at this position. Large $\Delta\alpha$ can also be obtained with a relatively low voltage that is important for low-power applications. A more direct figure of merit is the ratio $\Delta\alpha/\alpha_0$. Shown in Fig. 5.8(b) is $\Delta\alpha/\alpha_0$ as a function of the detuning energy. From Figs. 5.8(a)

and (b) we can see that a condition with $\Delta\alpha/\alpha_0 > 5$ can be achieved with a 22-meV detuning and the corresponding $\Delta\alpha$ can be as large as 3510 cm^{-1} ; or $\Delta\alpha/\alpha_0 > 10$ with a detuning of 28 meV with $\Delta\alpha \sim 2780 \text{ cm}^{-1}$. Compared to the best published results achieved from InGaAsP/InP[3] and InGaAlAs/InAlAs[4] MQWs for $1.3 \mu\text{m}$ modulators, our results show that InAsP/InP, which can be grown more readily, has superior EA property.

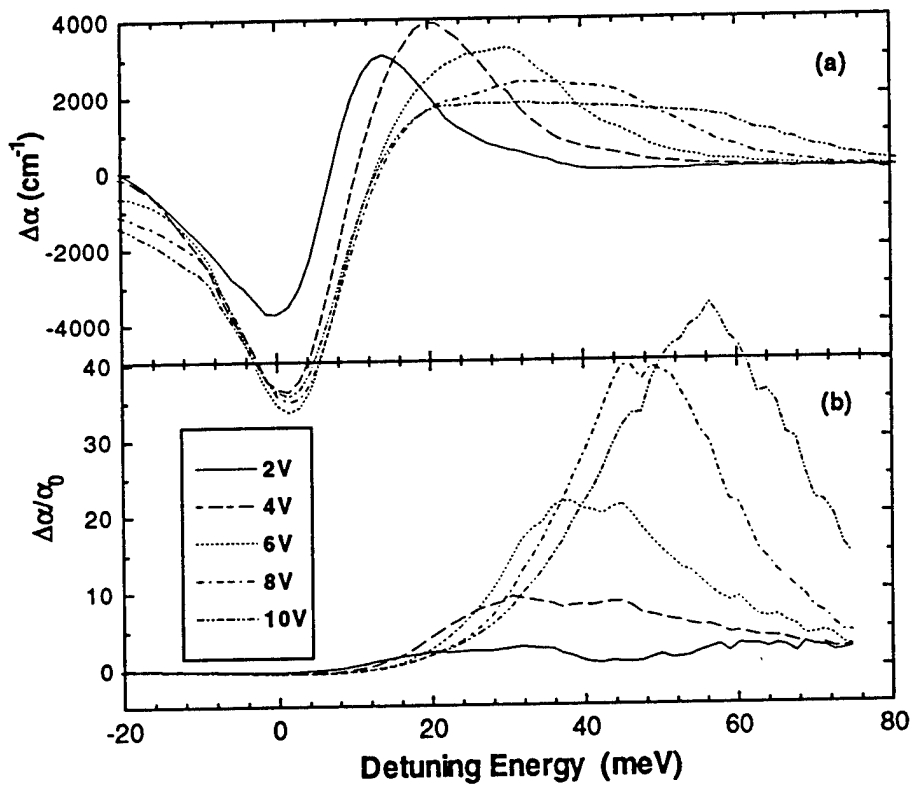


FIG. 5.8. (a) Change of the absorption coefficient as a function of the detuning energy with respect to the zero-field excitonic absorption; (b) $\Delta\alpha/\alpha_0$ as a function of the detuning energy. Both $\Delta\alpha$ and $\Delta\alpha/\alpha_0$ have to be maximized for waveguide modulator applications.

For waveguide modulator application, another important figure of merit is $\Delta\alpha/F^2$, [24] where F is the applied field. A large magnitude characterizes a large modulation depth with a small driving power. A dependence of $\Delta\alpha/F^2$ on the detuning energy is shown in Fig. 5.9 for various $\Delta\alpha/\alpha_0$ values. This result is significant for InAsP/InP waveguide modulators compared to other material systems.[4] A study of waveguide modulator using InAsP/InP strained MQWs is underway.

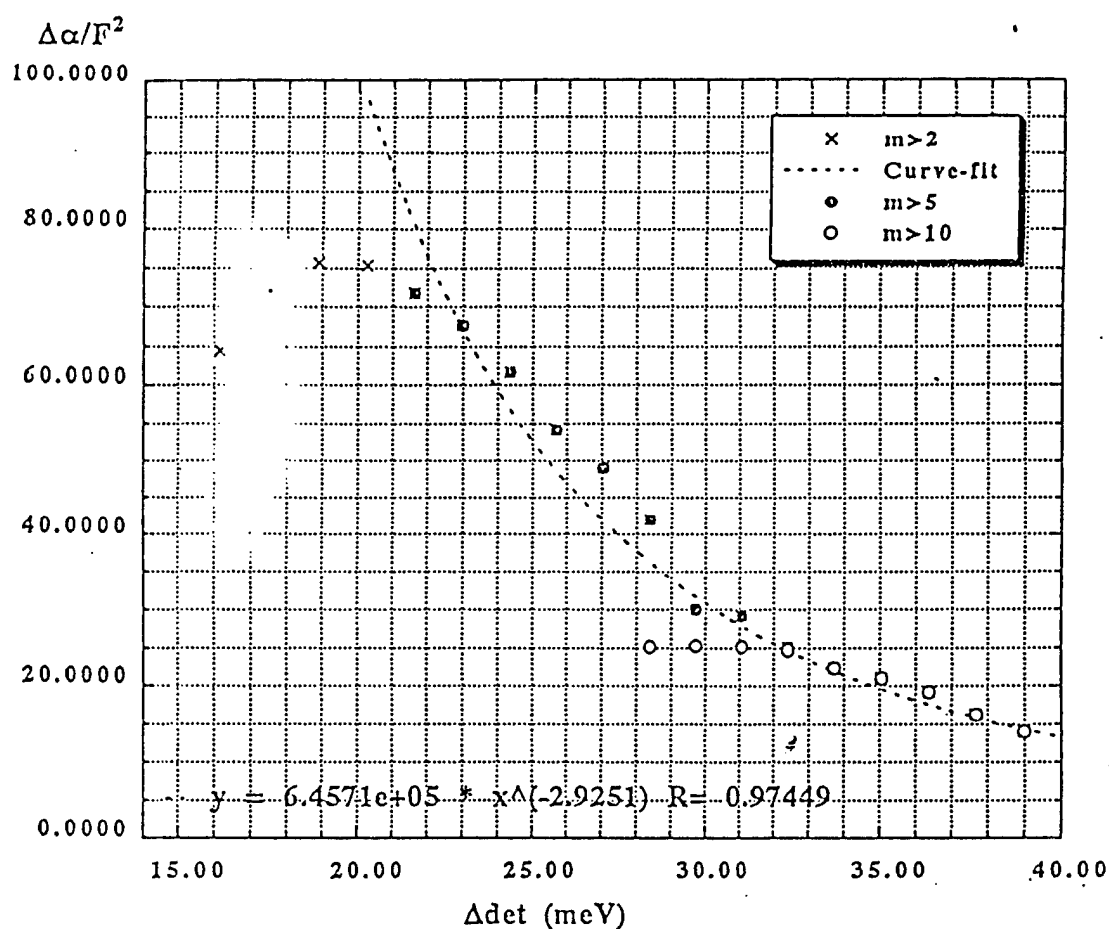


FIG. 5.9. $\Delta\alpha/F^2$ as a function of the detuning energy with various $\Delta\alpha/\alpha_0$. A large magnitude of $\Delta\alpha/F^2$ represents a high modulator depth with a small driving power.

5.3.2 Optical modulators at 1.06 μm

A number of 1.06 μm InAsP/InP MQW modulators show good EA property. The specific structure being discussed in this section is grown on a S-doped n^+ -InP substrate. Following an n^+ -InP buffer layer growth, a 30-period $\text{InAs}_{0.19}\text{P}_{0.81}$ (100 Å)/ InP (120 Å) strained MQW structure is sandwiched between 2000-Å thick undoped InP intrinsic layers, making the total intrinsic layer 10600 Å thick. The structure is then capped with a 3000-Å thick p -doped ($1 \times 10^{18} \text{ cm}^{-3}$) InP layer.

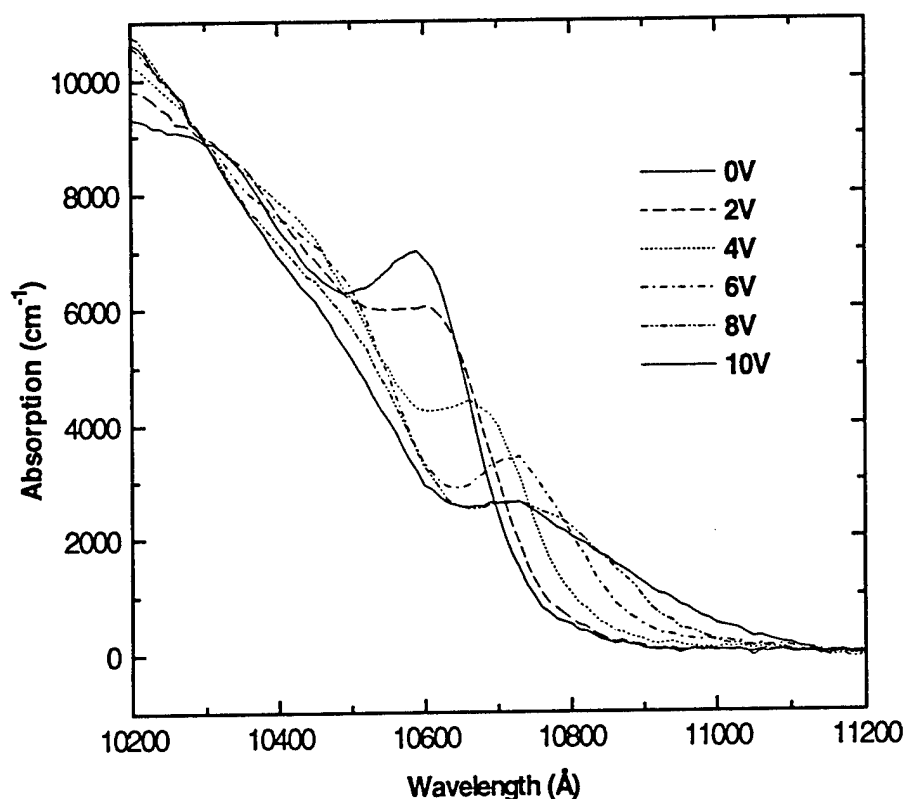


FIG. 5.10. Electro-absorption spectra taken at various reverse biases for a 1.06 μm InAsP/InP strained MQW modulator. The sharp excitonic transition shows a significant red energy shift, a reduction of the absorption intensity, and a broadening of the linewidth due to QCSE and field ionization effect.

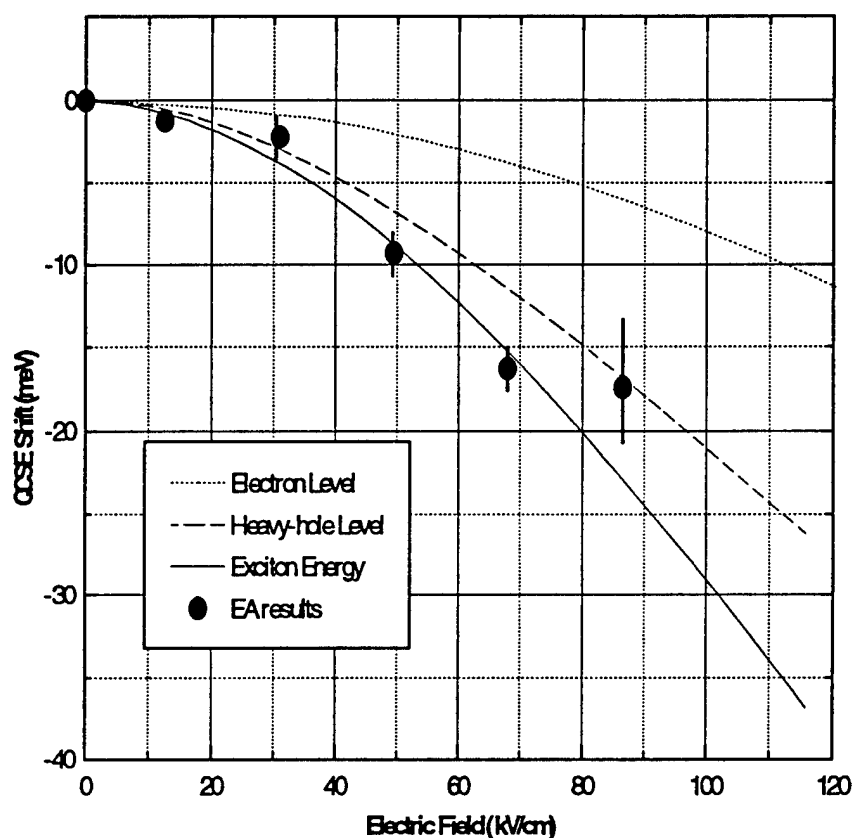


FIG. 5.11. Energy shift from the heavy-hole excitonic absorption as a function of the electric field across the quantum well for an $\text{InAs}_{0.19}\text{P}_{0.81}(100 \text{ \AA})/\text{InP}(120 \text{ \AA})$ MQW structure. The calculated results are illustrated for the shift of electron (dashed curve) and heavy-hole (dotted curve) subbands, as well as for the energy of excitonic transitions (solid curve). A good agreement between theoretical and experimental (solid circles) results is obtained.

Figure 5.10 shows typical EA spectra with various reverse DC biases taken at room temperature. The red energy shift and the large change of the absorption coefficient are attributed to QCSE discussed in the last section. The energy shift of the absorption

peak is illustrated in Fig. 5.11. Again the calculation was based on the effective well-width model. An even larger energy shift, e.g., ~ 20 meV shift in contrast to ~ 15 meV for a $1.3\text{ }\mu\text{m}$ modulator at a field of 80 kV/cm , is predicted. This is the direct result of the smaller confined energies of electrons and holes in a shallower well, compared to the quantum well in a $1.3\text{-}\mu\text{m}$ modulator, as discussed in Section 4.2.3. The energy shift from EA spectra are also shown in the same figure by considering the internal built-in field as described in the last section for the $1.3\text{ }\mu\text{m}$ modulator. The uncertainties in determining the absorption energy are given by vertical bars. An excellent agreement is obtained for the field smaller than 80 kV/cm , but a discrepancy arises at the field of $\sim 86.6\text{ kV/cm}$ (8 V external bias), probably from the exciton dissociation at the high electric field.

For spatial light modulators used in optical processing, an important figure of merit is the contrast ratio (CR) defined by $T(V)/T(0)$ in the positive contrast region and $T(0)/T(V)$ in the negative contrast region, where T denotes the transmission intensity. Shown in Fig. 5.12 is $\Delta T/T = \text{CR} - 1$ as a function of the wavelength. A $\sim 12\%$ change in the relative transmission can be achieved at $1.06\text{ }\mu\text{m}$ with a 10 V applied bias. However, a more significant contrast is desirable for device applications. A drastic increase of CR can be obtained by embodying this MQW structure in a Fabry-Perot cavity to facilitate multiple light passes[14] or by growing more quantum wells. The latter method, however, sacrifice the structural quality due to strain relaxation. Misfit dislocations will be generated in the strained MQW region when the number of periods is beyond a critical limit, and a high dislocation density can be expected if a larger number of quantum wells are grown. Recently, Woodward *et al.*[13] demonstrated that a strain-balanced InAsP/InGaP MQW structure shows an improved EA property. The built-in compressive strain can be balanced by the tensile strain in the InGaP layer so that the MQW structure can be grown, in principle, with an infinite number of periods. This

InAsP/InP material system is more satisfactory for 1.06 μm spatial-light modulators than the InGaAs/GaAs system.

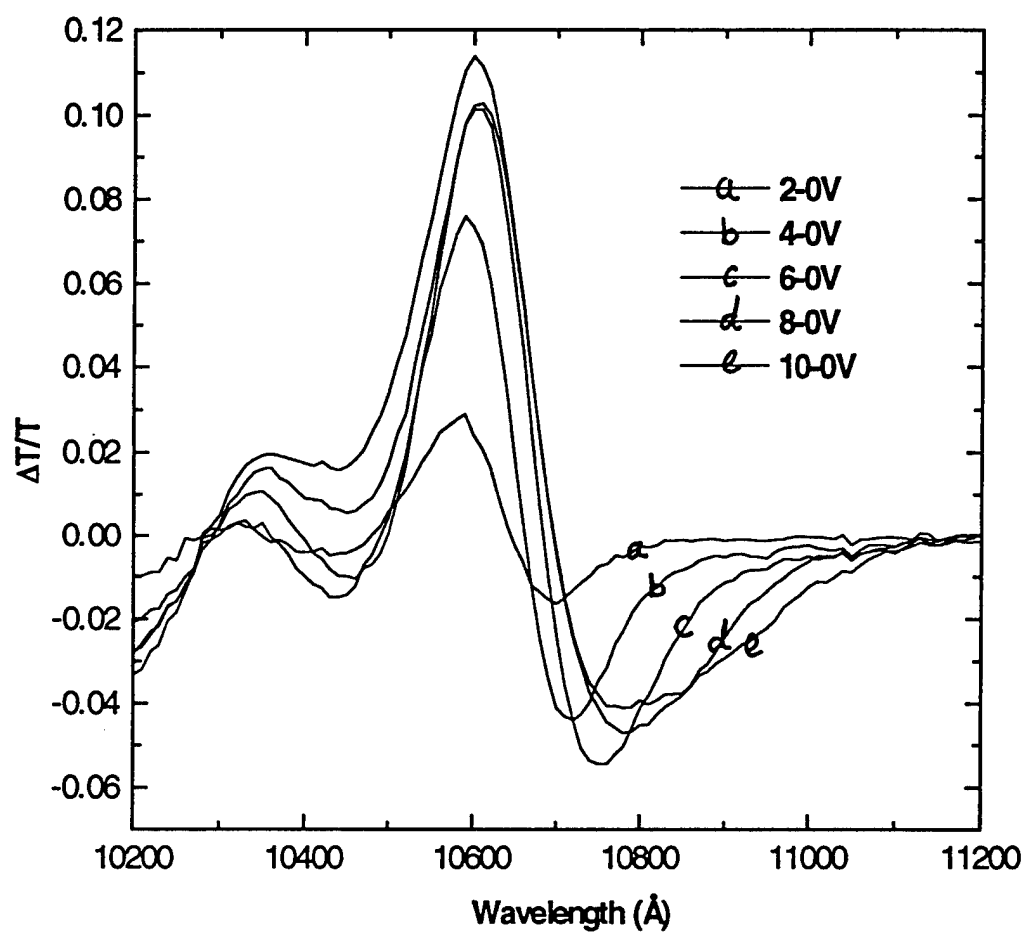


FIG. 5.12. $\Delta T/T$ data taken at various modulation voltages for a 1.06 μm InAs_{0.19}P_{0.81}(100 \AA)/InP (120 \AA) MQW modulator.

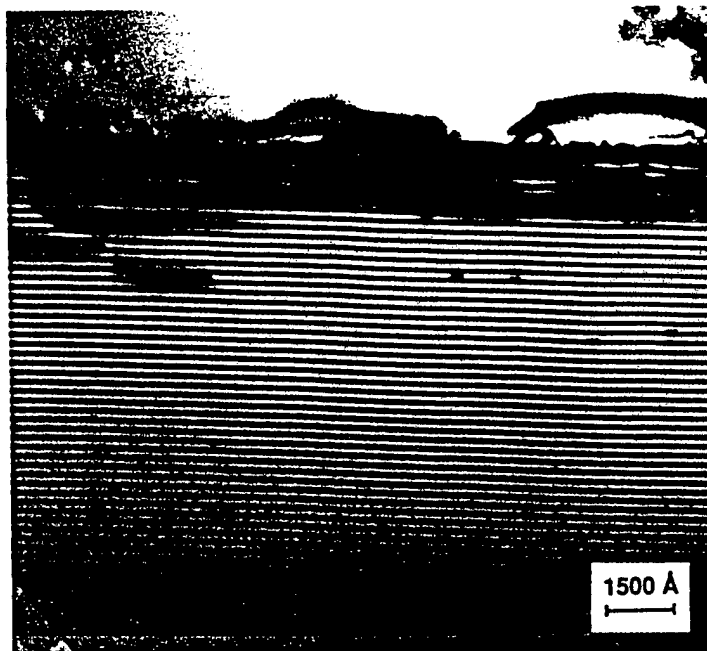


FIG. 5.13. XTEM micrograph for a 50-period $\text{InAs}_{0.39}\text{P}_{0.61}(100 \text{ \AA})/\text{InP}(120 \text{ \AA})$ MQW structure for a $1.3 \text{ }\mu\text{m}$ modulator.

5.4 Effect of strain relaxation on electro-absorption properties

As shown in the last section, InAsP/InP strained MQWs are excellent material system for $1.3 \text{ }\mu\text{m}$ waveguide modulators when the strained layer is grown pseudomorphically. As presented in Section 3.2, the critical layer thickness imposes on the number of periods in a strained MQW. The calculation shows in Fig. 3.2 that pseudomorphic growth can be achieved with as many as 15 periods for $\text{InAs}_{0.4}\text{P}_{0.6}(100 \text{ \AA})/\text{InP}(100 \text{ \AA})$ structure. In this section, we will take a closer examination of the impact

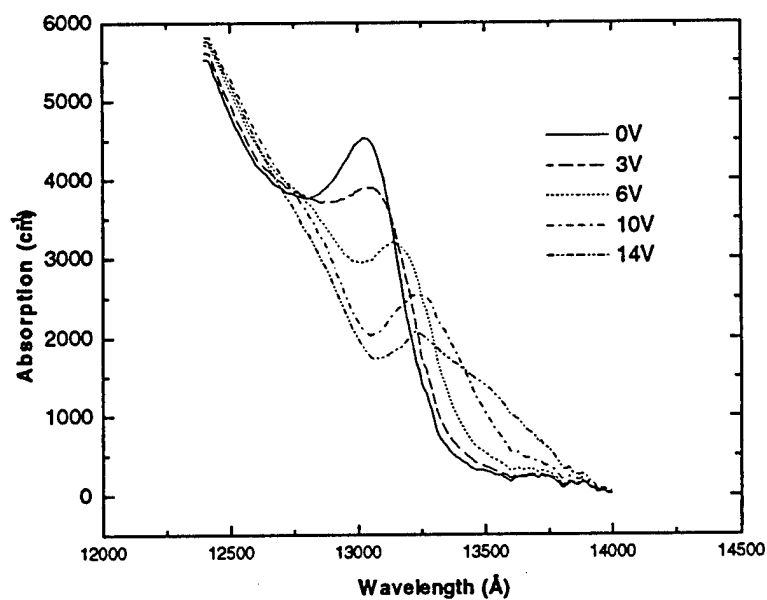
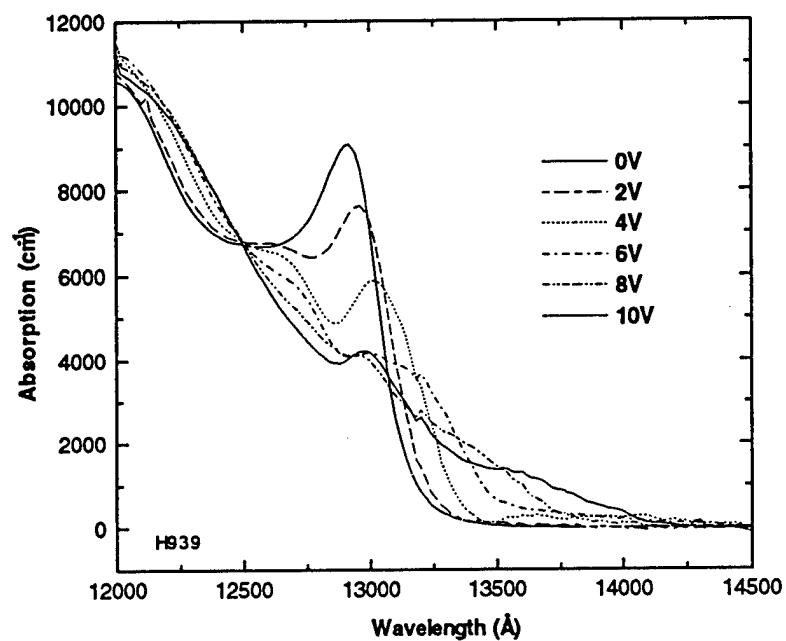


FIG. 5.14. EA spectra from two 1.3 μm modulators consisting of InAs_{0.39}P_{0.61}(100 Å)/InP (120 Å) MQWs (a) with 20 periods, and (b) with 50 periods.

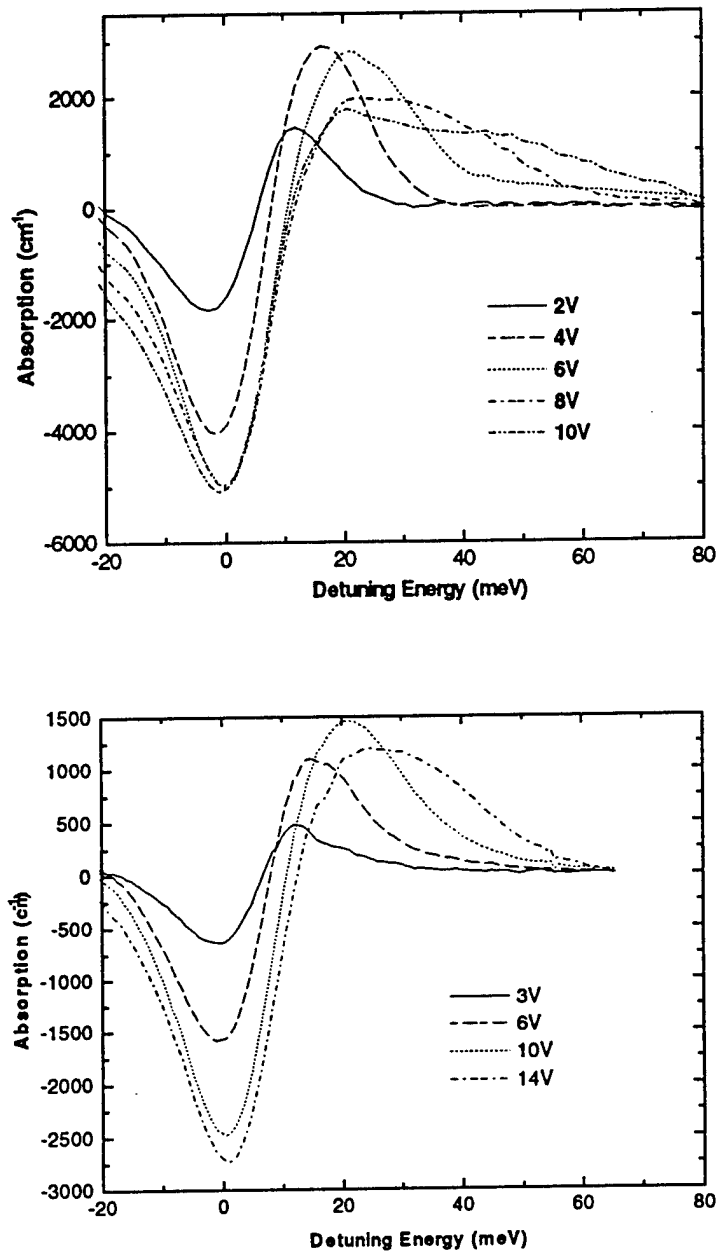


FIG. 5.15. Change of the absorption coefficient from two $1.3 \mu\text{m}$ modulators consisting of $\text{InAs}_{0.39}\text{P}_{0.61}(100 \text{ \AA})/\text{InP}(120 \text{ \AA})$ MQWs (a) with 20 periods, and (b) with 50 periods. Reduced $\Delta\alpha$ compared to Fig. 5.8(a)] is observed for the structure with more number of periods, in which a more severe strain relaxation is expected.

of strain relaxation on the EA property of 1.3 μm modulator structures. Devices are fabricated from three InAsP(100 Å)/InP(100~150 Å) MQW samples with 10-, 20-, and 50-period quantum wells, respectively. From Fig. 3.2, the 10-period structure is pseudomorphic, and 50-period structure is relaxed, as shown by a micrograph of cross-sectional transmission electron microscopy (XTEM) in Fig. 5.13. There might be a partial relaxation in the 20-period structure. The excellent EA property for the 10-period MQW structure has been presented. Figures 5.14(a) and (b) show EA spectra from the 20- and 50-period quantum well structure, respectively. Good characteristics of changes of absorption energy and absorption coefficient are obtained. Figure 5.15(a) and (b) show the respective change of the absorption coefficient as a function of the detuning energy for the 20- and 50-period structures. Compared with the $\Delta\alpha$ for the 10-period structure, shown in Fig. 5.8(a), a reduction of the absorption coefficient is observed for 20-period modulator, and an even more significant reduction for the 50-period structure. Furthermore, the QCSE energy shift determined from the EA spectra is also compared with the theoretical calculation in Fig. 5.16. The solid and open circles are the results from these two samples. The energy shift is found to be smaller than that predicted from the calculation. This is in contrast to the result for the 10-period structure. Over all, we observed an increasing degradation of the EA properties for increasing the number of periods, therefore, increased relaxation in the structure. This is understood as follows. When the period number exceeds the critical limit, strain relaxation occurs. A part of the external electric field may be pinned in the defective area, resulting in a reduced electric field applied across the quantum well region. Therefore, a smaller QCSE energy shift is observed even with the same applied bias. This strain relaxation also leads to a reduced $\Delta\alpha$ since the relaxed quantum-well area is not as absorptive as a perfect well.

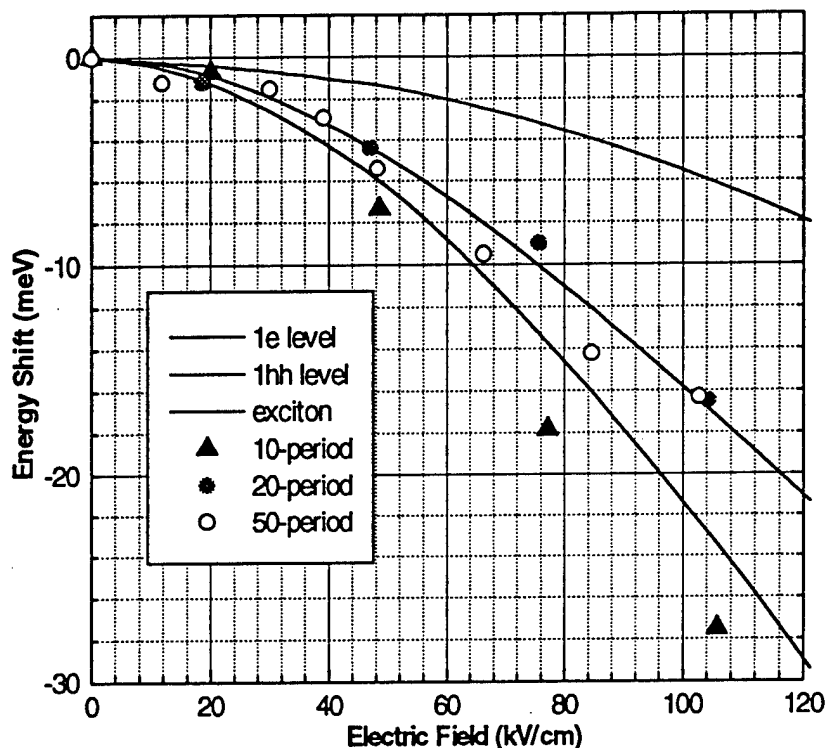


FIG. 5.16. Energy shift of the absorption peak as a function of the electric field across the quantum well for a $1.3\text{ }\mu\text{m}$ InAsP(100 Å)/InP (120 Å) MQW modulator. The calculated results are illustrated for the shift of electron (dashed curve) and heavy-hole (dotted curve) subbands, as well as for the energy of excitonic transitions (solid curve). Experimental results from a 20- and 50-period MQWs are denoted with solid and open circles, respectively. For the sake of comparison, the data for 10-period sample is also plotted with triangles.

5.5 Conclusion

We have discussed the electrooptical property of InAsP/InP strained MQW modulators, grown by gas-source molecular beam epitaxy. Electroabsorption is

demonstrated, for the first time, for InAsP/InP strained MQWs for 1.3 μm modulator applications. Very sharp excitonic absorption at room temperature was observed. Electroabsorption measurements performed on a ring-shaped *p-i-n* diode, consisting of 10-period $\text{InAs}_{0.41}\text{P}_{0.59}(100 \text{ \AA})/\text{InP}(150 \text{ \AA})$ strained MQWs, reveal a significant red shift of the absorption peak with increasing reverse bias due to the quantum-confined Stark effect. The energy shift is well accounted for in the effective well-width model. The energy shift is found to be much larger than from 1.3- μm InGaAsP/InP and InGaAlAs/InAlAs MQW modulator structure under the same electric field. This is attributed to the smaller valence band discontinuity in the InAsP/InP quantum structure. The change of the absorption coefficient at a 22-meV detuning is as large as 3510 cm^{-1} with a small residual absorption, which can be very useful for 1.3 μm waveguide modulators. Our results show that this quantum structure can be a good alternative to the more complex quaternary materials, such as InGaAsP/InP and InGaAlAs/InAlAs quantum wells. The composition and thickness control, moreover, can be greatly simplified in growing InAsP. These excellent EA characteristics suggest that the InAsP/InP strained MQWs can be a promising material system for 1.3 μm waveguide modulators.

The viability of using the strained InAsP/InP MQW structure for waveguide modulator is further examined through a correlation of the EA property with structural properties of MQW structures with different period numbers. The result shows that the strain relaxation can degrade the EA property by having a reduced energy shift and a smaller absorption coefficient. An excellent EA property can be obtained if the MQW is grown within the critical limit, approximately 15 periods of $\text{InAs}_{0.4}\text{P}_{0.6}(100 \text{ \AA})/\text{InP}(100 \text{ \AA})$ MQWs which are typically used as the core region of a 1.3 μm waveguide modulator.

Furthermore, the InAsP/InP strained MQW structure was also demonstrated for 1.06 μm spatial light modulators. Even though the ease in composition control, and

larger QCSE energy shift are very attractive, the pseudomorphic growth of a large number of periods of the MQW can be a limiting factor to obtain a large enough contrast ratio for optical information processing. Strain balanced InAsP/InGaP MQW may be a better material system for this application purpose.

References:

- [1] H. Tanaka, M. Suzuki, M. Usami, H. Taga, S. Yamamoto, and Y. Matsushima, J. Light. Tech. **8**, 1357 (1990).
- [2] T. H. Wood, J. Light. Tech. **6**, 743 (1988).
- [3] J. E. Zucker, I. Bar-Joseph, B. I. Miller, U. Koren, and D. S. Chemla, Appl. Phys. Lett. **54**, 10 (1989).
- [4] A. N. Cheng *et al.* (unpublished).
- [5] T. H. Chiu, J. E. Zucker, and T. K. Woodward, Appl. Phys. Lett. **59**, 3452 (1991).
- [6] J. E. Zucker, I. Bar-Joseph, C. H. Joyner, A. Dentai, M. D. Divino, D. S. Chemla, Electron. Lett. **25**, 973 (1989).
- [7] T. K. Woodward, T. Sizer II, D. L. Sivco, and A. Y. Cho, Appl. Phys. Lett. **57**, 548 (1990); and S. Niki, A. Cheng, J. C. P. Chang, W. S. C. Chang, and H. H. Wieder, Jpn. J. Appl. Phys. **29**, L1833 (1990).
- [8] J. E. Cunningham, K. W. Goossen, and W. Jan, J. Cryst. Growth, **127**, 184 (1993).
- [9] H. Q. Hou and C. W. Tu, J. Electron. Mater. **21**, 137 (1992).
- [10] H. Q. Hou, C. W. Tu, and S. N. G. Chu, Appl. Phys. Lett. **58**, 2954 (1991).
- [11] H. Q. Hou and C. W. Tu, Appl. Phys. Lett. **60**, 1872 (1992).
- [12] T. K. Woodward, T. Sizer, and T. H. Chiu, Appl. Phys. Lett. **58**, 1366(1991).
- [13] T. K. Woodward, T. H. Chiu and T. Sizer, Appl. Phys. Lett. **60**, 2846 (1992).
- [14] R. H. Yen, R. J. Simes, and L. A. Coldren, IEEE J. Quantum Electron. **QE-25**, 2272 (1989).
- [15] K. Ogawa, T. Katsuyama, and M. Kawata, Phys. Rev. B **46**, 13289 (1992).
- [16] H. Q. Hou, Y. Segawa, Y. Aoyagi, S. Namba, and J. M. Zhou, Phys. Rev. B **42**, 1284 (1990); and Solid State Commun. **74**, 159 (1990), and references therein.
- [17] H. Q. Hou, L. J. Wang, R. M. Tang, and J. M. Zhou, Phys. Rev. B **42**, 2926 (1990).

- [18] D. A. B. Miller, D. S. Chemla, T. C. Damen, A. C. Gossard, W. Wiegmann, T. H. Wood, and C. A. Burrus, *Phys. Rev. B* **32**, 1043 (1985).
- [19] J. D. Dow and D. Redfield, *Phys. Rev. B* **5**, 594 (1972).
- [20] J. A. Brum and G. Bastard, *Phys. Rev. B* **31**, 3893 (1985).
- [21] G. Bastard, E. E. Mendez, L. L. Chang, and L. Esaki, *Phys. Rev. B* **28**, 3241 (1983).
- [22] S. J. Hwang, W. Shan, J. J. Song, H. Q. Hou, and C. W. Tu, *J. Appl. Phys.* **72**, 1645 (1992).
- [23] B. Soucail, P. Voisin, M. Voos, D. Rondi *et al.* *Semicon. Sci. Technol.* **5**, 918 (1990).
- [24] M. K. Chin and W. S. C. Chang, *IEEE J. Quantum Electron.* (to be published).

APPENDIX

A

A kinetic model for As and P incorporation in III-V's

A kinetic model for As and P incorporation behaviors in GaAsP grown by gas-source molecular beam epitaxy

B. W. Liang and C. W. Tu

Department of Electrical and Computer Engineering, University of California at San Diego,
La Jolla, California 92093-0407

(Received 1 June 1992; accepted for publication 8 March 1993)

A kinetic model has been developed to explain As and P incorporation behaviors in $\text{GaAs}_{1-x}\text{P}_x$ epilayers grown on GaAs (001) by gas-source molecular beam epitaxy. The model can predict the P compositions for various substrate temperatures and flow rates. The model shows that an *in situ* determination of GaP molar fraction in $\text{GaAs}_{1-x}\text{P}_x$ can be performed by group V-induced intensity oscillations of reflection high-energy-electron diffraction at low substrate temperatures where desorption of group V species is negligible. At high substrate temperatures the compositions can be determined from the arsine and phosphine flow rates.

I. INTRODUCTION

Mixed group V ternary and quaternary III-V compounds, such as GaAsP, InAsP, and InGaAsP, are important for optoelectronic applications. Various growth techniques, such as metalorganic vapor-phase epitaxy (MOVPE), molecular beam epitaxy (MBE), metalorganic MBE, and gas-source MBE (GSMBE) have been used to grow these materials.¹⁻⁶ By GSMBE we mean using elemental group III sources and gaseous arsine and phosphine as the group V sources. One of the critical issues of growing mixed group V compounds is the control of the group V compositions.^{7,8} Most researchers use post-growth characterization techniques, such as x-ray rocking curve measurements and photoluminescence spectroscopy, to correlate the determined composition with growth parameters, such as flow rates or fluxes.

Recently our group has developed an *in situ* technique of determining the P composition in $\text{GaAs}_{1-x}\text{P}_x$ grown by GSMBE for $x < 0.4$.⁸ The P compositions of $\text{GaAs}_{1-x}\text{P}_x$ grown under normal MBE growth conditions (V/III incorporation ratio > 1 and the growth rate is limited by the Ga flux) can be obtained *in situ* from the difference in the oscillation periods of the As- and (As+P)-limited intensity oscillations of reflection high-energy-electron diffraction (RHEED) if the same flow rates and growth temperatures are used.⁸ This is because group V-limited RHEED intensity oscillations are obtained on a Ga-rich surface. On such a surface at the substrate temperature used (about 500 °C) the As incorporation rate is not affected by the presence of P. However, at higher substrate temperatures, both As and P desorb readily and there is a competition between As and P incorporation during the growth of GaAsP. Understanding this competition is the key to controlling the group V composition at any substrate temperatures and flow rates. Even though several models have been proposed in recent years for determining the composition of mixed group V ternary or quaternary compounds grown by MOVPE, MBE, and GSMBE,^{2,3,5} they cannot explain the agreement between the *in situ* determination of P composition in $\text{GaAs}_{1-x}\text{P}_x$ by group V-induced RHEED intensity oscillations and *ex situ* composition determina-

tion by, for example, x-ray rocking curves. In this article, taking into account adsorption and desorption of group V elements on the growing surface, we propose kinetic models for GSMBE of $\text{GaAs}_{1-x}\text{P}_x$ in the group III-limited and the group V-limited growth modes, respectively. We establish the temperature range where the *in situ* RHEED technique can be applied. We then expand our discussion to determining the P composition in $\text{GaAs}_{1-x}\text{P}_x$ grown under a wide range of growth conditions.

II. KINETIC MODELS

In epitaxy, the growth rate and composition may be controlled by three different processes, mass transfer (i.e., beam fluxes), adsorption and desorption, and surface reactions. In MBE or GSMBE, for binary compounds like GaAs grown under normal growth conditions (substrate temperature, T_s , between 450 and 650 °C, and growth rate, R_g , about 1 monolayer per second), the growth rate is expected to be limited by mass transfer. This means that surface reaction rates are much faster than the group III beam impingement rate. In this case the growth rate does not depend upon the substrate temperature. On the other hand, at much higher substrate temperatures the growth rate will be affected by desorption. The growth rate then will be sensitive to temperature variations. For mixed group III ternary compounds such as $\text{Al}_x\text{Ga}_{1-x}\text{As}$, the situation is almost the same as that of GaAs. Under normal growth conditions, the growth rate and composition are controlled simply by the Al and Ga beam fluxes and their ratio, respectively. For mixed group V ternary compounds, however, the situation is quite different. Even though the growth rate is still controlled by the group III beam flux, the composition is affected by surface chemical reactions between group III atoms and group V species and adsorption and desorption of group V species on the growing surface.

In our model of the MBE process, group V dimers (from a cracker in MBE or a gas cracker in GSMBE) in the gas phase first physisorb on the surface, in a so-called precursor state, then they are in a chemisorption state before incorporation into the lattice. Because of the high va-

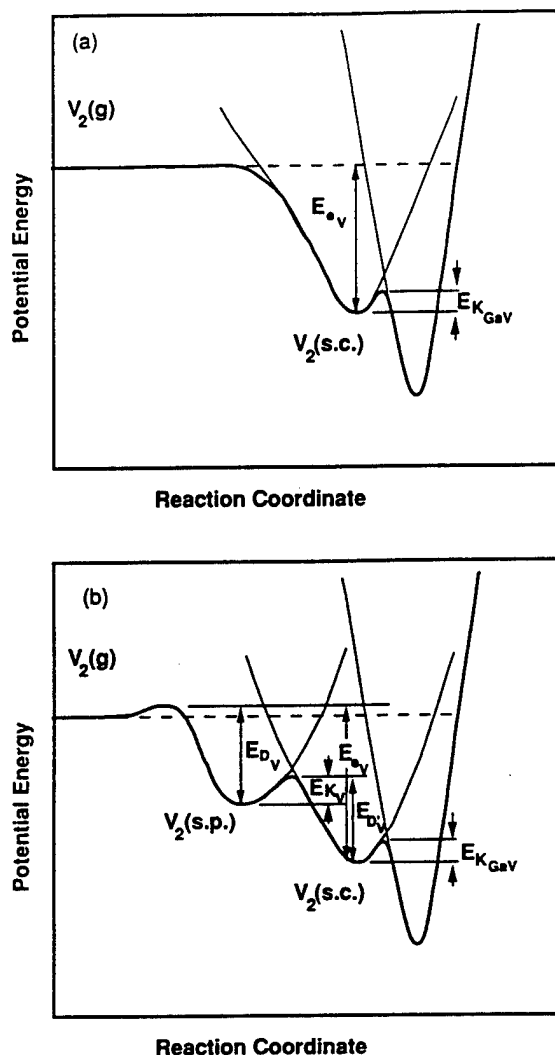


FIG. 1. Schematic diagrams of group V dimer adsorption and desorption reaction coordinates; (a) for a Ga-rich surface and (b) for a group V-rich situation. E_a is the activation energy for a group V dimer to desorb from its chemisorption state; E_{K_v} and E_{D_v} the activation energies for a group V dimer to change from a physisorption state to a chemisorption state and vice versa, respectively; E_{GaV} , the activation energy for group V elements to be incorporated into the lattice.

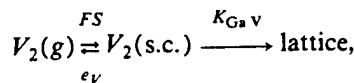
For pressures of As_2 and P_2 , desorption is important and can occur from both physisorbed and chemisorbed states. However, on a Ga-rich surface, Ga atoms are abundant, and the surface activity of Ga is thus unity. Therefore, once group V dimers arrive at the growing surface, they chemisorb immediately on the surface. Figure 1 shows the reaction coordinates for the two cases.

A. Group III-rich surface

The growth rate (R_g) of GaAsP on a Ga-rich surface, as obtained by RHEED intensity oscillations, is limited by the incorporation rates of As and P.⁹ We can write

$$R_g(GaAsP) = R_g(GaAs) + R_g(GaP). \quad (1)$$

The desorption of group V dimers is mainly from chemisorption states, as shown below:



where K_{GaV} is the incorporation rate constant; e_V the desorption rate constant; $V = As$ or P ; F the beam flux; S the sticking probability; g the gas phase; and s.c. the surface chemisorption state.

According to the mass action law, the net incorporation (desorption) rate of As and P, $R_g(R_e)$, can be written as the surface activity, a_i , where $i = As$ or P , multiplied by the incorporation (desorption) rate constant:

$$R_g(GaAs) = K_{GaAs} a_{As}, \quad (2)$$

$$R_g(GaP) = K_{GaP} a_P, \quad (3)$$

$$R_e(As) = e_{As} a_{As}, \quad (4)$$

$$R_e(P) = e_P a_P. \quad (5)$$

Under steady-state conditions, $R_g = FS - R_e$, so we have

$$a_{As} = (FS)_{As} / (K_{GaAs} + e_{As})$$

and

$$a_P = (FS)_P / (K_{GaP} + e_P).$$

Thus, growth rates of GaAs and GaP can be written as

$$R_g(GaAs) = (FS)_{As} / (1 + e_{As}/K_{GaAs}), \quad (6)$$

$$R_g(GaP) = (FS)_P / (1 + e_P/K_{GaP}). \quad (7)$$

Since the phosphorus composition (x) in the epilayer is determined by RHEED on a Ga-rich GaAs surface,

$$x = \frac{R_g(GaAsP) - r_g(GaAs)}{R_g(GaAsP)} = \frac{R_g(GaAs) + R_g(GaP) - r_g(GaAs)}{R_g(GaAs) + R_g(GaP)}, \quad (8)$$

where $r_g(GaAs)$ is the As-limited GaAs growth rate in the absence of P_2 . In principle, the As incorporation rate into $GaAs_{1-x}P_x$ will change upon injection of P_2 due to displacement of As by P. Foxon *et al.* reported a slight decrease of the As_4 sticking coefficient when P_4 was injected during MBE of $GaAs_{1-x}P_x$.⁷ The situation is similar if dimers are used. In our case, however, excess Ga atoms are deposited on the surface before the group V-limited RHEED oscillation measurements. Therefore, we can expect the displacement of As by P is negligible. In short, for a group III-rich surface, the As incorporation rate is independent of whether P is present or not, at least for the low x range. Therefore, $R_g(GaAs)$ and $r_g(GaAs)$ cancel out each other in Eq. (8). Substituting Eqs. (6) and (7) to Eq. (8), we obtain

$$x \approx \frac{1}{1 + [(FS)_{As}(1 + e_P/K_{GaP})] / [(FS)_P(1 + e_{As}/K_{GaAs})]}. \quad (9)$$

Since the As_2 and P_2 beam fluxes are proportional to the AsH_3 and PH_3 flow rates, respectively,¹⁰ we can write

$$x \approx \frac{1}{1 + \tilde{C}(f_{AsH_3}/f_{PH_3})} = \frac{1}{1 + \tilde{C}[(1 - X_f)/X_f]}, \quad (10)$$

where f 's are hydride flow rates; X_f the phosphine flow-rate fraction, and

$$\tilde{C} \equiv \frac{S_{As}}{S_P} \sqrt{\frac{M_{P_2}}{M_{As_2}}} \frac{(1 + e_P/K_{GaP})}{(1 + e_{As}/K_{GaAs})}, \quad (11)$$

where M 's are the molecular mass of P_2 and As_2 .

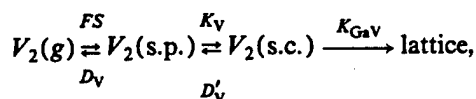
If the growth temperature is too low for As and P to desorb from their chemisorption states, we have $e_i/K_i \ll 1$, i.e.,

$$\tilde{C} \approx \frac{S_{As}}{S_P} \sqrt{\frac{M_{P_2}}{M_{As_2}}}. \quad (12)$$

The phosphorus composition in GaAsP epilayers, therefore, is independent of V/III ratio in the temperature range considered. This has been verified by experimental results in our group.⁸

B. Normal growth condition (V/III > 1)

Now we consider the normal GSMBE growth condition (group V rich), where there are fewer Ga atoms than group V species. In this case, as shown in Fig. 1(b), we assume the group V dimers undergo the following steps:¹¹



where s.p. stands for surface physisorption state, D_V the desorption rate constant, D'_V and K_V the rate constants for group V dimers between physisorption and chemisorption states. The growth-rate equation of GaAsP, in this case, is similar to Eq. (1), but it is limited by the Ga-beam flux:

$$R_g(\text{GaAsP}) = R_g(\text{GaAs}) + R_g(\text{GaP}) = F_{Ga}. \quad (13)$$

Therefore,

$$x = R_g(\text{GaP}) / (R_g(\text{GaAs}) + R_g(\text{GaP})). \quad (14)$$

Again, under steady-state conditions,

$$R_g(\text{GaAs}) = \frac{(FS)_{As}}{(D'_{As} D_{As} / K_{GaAs} K_{As}) + (D_{As} / K_{As}) + 1}, \quad (15)$$

$$R_g(\text{GaP}) = \frac{(FS)_P}{(D'_P D_P / K_{GaP} K_P) + (D_P / K_P) + 1}. \quad (16)$$

Combining Eqs. (14)–(16), we have

$$x = \frac{1}{1 + C(f_{AsH_3}/f_{PH_3})} = \frac{1}{1 + C[(1 - X_f)/X_f]}, \quad (17)$$

$$C \equiv \frac{S_{As}}{S_P} \sqrt{\frac{M_{P_2}}{M_{As_2}}} \frac{(D'_P D_P / K_{GaP} K_P) + (D_P / K_P) + 1}{(D'_{As} D_{As} / K_{GaAs} K_{As}) + (D_{As} / K_{As}) + 1}. \quad (18)$$

Equations (17) and (18) show the relationship between the phosphorus composition (x) and growth parameters. Since D'_i , K_i , and D_i obey Arrhenius relations, x is sensitive to the growth temperatures. If the growth temperature is low enough, however, Eq. (18) can be simplified into

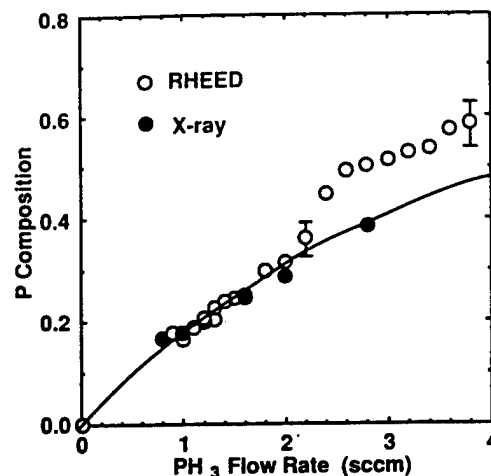


FIG. 2. The P composition in GaAsP as a function of the PH_3 flow rate at a AsH_3 flow rate of 1.6 sccm and growth temperature of 500 °C. Open circles are from group V-induced RHEED oscillations. Closed circles are from x ray diffraction measurements and simulations of GaAsP/GaAs SLs,⁸ and the line is a calculation based on Eqs. (10) and (12).

Eq. (12), i.e., $C = \tilde{C} = (S_{As}/S_P) \sqrt{(M_{P_2}/M_{As_2})}$. The assumption of the same S_{As}/S_P for both cases is reasonable for the low-temperature range.

Therefore, at low enough temperatures, one can obtain the P composition of $GaAs_{1-x}P_x$ in $GaAs_{1-x}P_x/GaAs$ strained-layer superlattices grown under normal conditions by *in situ* monitoring group V-induced RHEED intensity oscillations when the same hydride flow rates are used, as shown in Fig. 2. The open circles are from the RHEED oscillations, and the closed circles are determined *ex situ* from x-ray rocking curve measurements and simulations based on the dynamic theory. The solid line is a calculation from our model, which will be discussed in the next section. The agreement between *in situ* and *ex situ* results is very good for $x < 0.35$. In the high x range, however, the results from the *in situ* determination do not agree with the *ex situ* results. The reasons are believed to be (i) it is difficult to obtain reasonably good RHEED oscillations because of high strain; (ii) the strained-layer superlattice structure may be partially relaxed because the total layer thickness exceeds the critical layer thickness; and (iii) the assumptions in Eq. (8) that the As and P incorporation being independent of each other on a Ga-rich surface may not hold any more because of the existence of a relatively large amount of phosphorus on the growth front.

At higher substrate temperatures, however, the relationship between the P composition and phosphine flow-rate fractions in the normal growth conditions, Eq. (18), is different from that in the group III-rich conditions, Eq. (11), because As_2 and P_2 have different desorption and incorporation paths.

III. COMPARISON WITH EXPERIMENTAL RESULTS AND DISCUSSION

Equations (17) and (18) describe the relationship between phosphorus composition (x) in the epilayer and

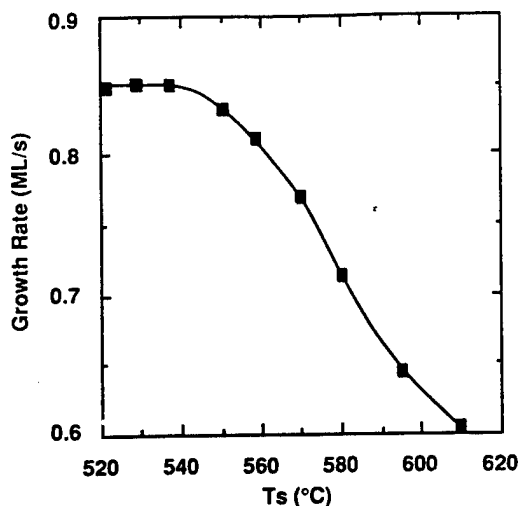


FIG. 3. The As incorporation rate obtained by As-induced RHEED intensity oscillations in GaAs as a function of reciprocal substrate temperature.

flow-rate fraction of PH_3 (X_f) as well as other parameters included in the parameter C . If we know these parameters, such as S , K , D' and D , we can obtain the parameter C and calculate x for different growth conditions. From the reaction-coordinate diagrams in Figs. 1(a) and 1(b), we note that the activation energy of D'_V/K_{GaV} plus that of D_V/K_V equals that of e_V/K_{GaV} for the case of a group III-rich surface, in Eq. (11). According to Eqs. (6) and (7), the activation energy of e_V/K_{GaV} can be obtained by group V-induced RHEED intensity oscillations at different substrate temperatures. Figure 3 shows the incorporation rate of As in GaAs obtained by As-induced RHEED intensity oscillations as a function of substrate temperature. From the data obtained in the temperature range between 540 and 610 °C, we obtain the activation energy of $e_{\text{As}}/K_{\text{GaAs}}$, or $(D'_{\text{As}}D_{\text{As}})/(K_{\text{GaAs}}K_{\text{As}})$, to be 88 kcal/mol. Using the same method, we obtain the activation energy of $e_{\text{P}}/K_{\text{GaP}}$, or $(D'_{\text{P}}D_{\text{P}})/(K_{\text{GaP}}K_{\text{P}})$, to be 79 kcal/mol.

From previous RHEED studies of desorption of excess As_2 or P_2 from a GaAs or GaP surface, we have obtained the activation energies of D_{As} and D_{P} , 58 and 43 kcal/mol, respectively, which are the same as the activation energies of the vapor pressure curves of As_2 and P_2 .¹² Since P_2 , As_2 , and Ga on a growing surface are very reactive, the activation energies for the reaction rate constants K_{As} and K_{P} are expected to be relatively small. We assume they be zero. Now the only unknown quantities in Eq. (18) are $S_{\text{As}}/S_{\text{P}}$ and four parameters involving prefactors since X_f is set by the flow rates used. Figure 4 shows the P compositions, obtained by x-ray rocking curves and simulations of GaAsP/GaAs strained layer superlattices,⁸ as a function of substrate temperature. The quantity of $S_{\text{As}}/S_{\text{P}}$ can be obtained from the data in the low-temperature range in Fig. 4 because from Eqs. (10) and (12) $S_{\text{As}}/S_{\text{P}} = \sqrt{(M_{\text{As}_2}/M_{\text{P}_2})}[(1-x)X_f]/[x(1-X_f)]$. Here we assume that $S_{\text{As}}/S_{\text{P}}$ is constant in the temperature range considered. Then we performed a best fit, shown by the solid line, to obtain the four factors involving pre-exponential

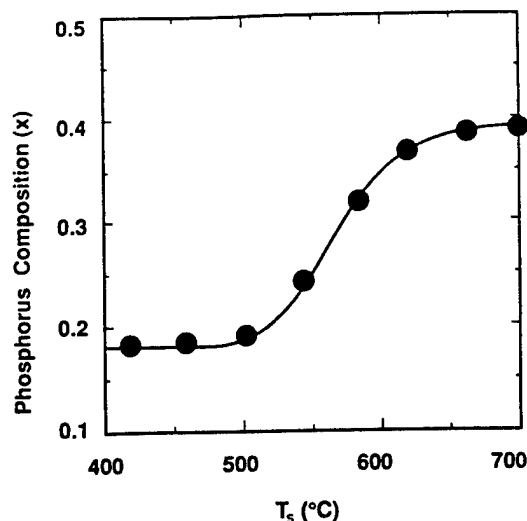


FIG. 4. The P composition in GaAsP as a function of substrate temperature. The solid line is the best fit to the experimental data (see Ref. 8).

factors. From this fitting, the parameter C in Eq. (18) becomes

$$C = \frac{2.7\{1 + 2.0 \times 10^{11} \exp[(21\,500)/(T_s)](1+B)\}}{1 + 5.4 \times 10^{15} \exp[(29\,250)/(T_s)](1+A)},$$

where

$$A = 5 \times 10^6 \exp(-15\,000/T_s),$$

$$B = 6 \times 10^8 \exp(-18\,000/T_s).$$

Thus, without any further adjustment of parameters, we can calculate phosphorus compositions as a function of phosphine flow rate for a given substrate temperature. Figure 2 compares the P compositions determined by x-ray rocking curves and simulations (solid circles) and calculations from our model (solid line). The substrate temperature was 500 °C, so $C=2.7$. The agreement is excellent.

We can also calculate P compositions as a function of flow-rate fractions in the gas phase for different growth temperatures, as plotted in Fig. 5. The lines are from our calculations, and the points are experimental results from GaAsP/GaAs strained-layer superlattices. It is interesting to note that the parameter C is almost unity when the growth temperature is about 620 °C. In this case the phosphorus composition is almost equal to the flow-rate fraction of PH_3 . This means that, despite strong desorption, the net incorporation rates of As and P are almost equal to each other. Therefore, the composition control then is even easier at high temperatures than at low temperatures.

IV. CONCLUSION

Simple kinetic models have been proposed to explain the arsenic and phosphorus incorporation behavior in $\text{GaAs}_{1-x}\text{P}_x$ grown on GaAs (001) by GSMBE for both Ga-rich surface ($V/\text{III} < 1$) and normal growth conditions ($V/\text{III} > 1$). For $\text{GaAs}_{1-x}\text{P}_x$ ($x < 0.4$) epilayers, one can use the *in situ* determination by RHEED to obtain the

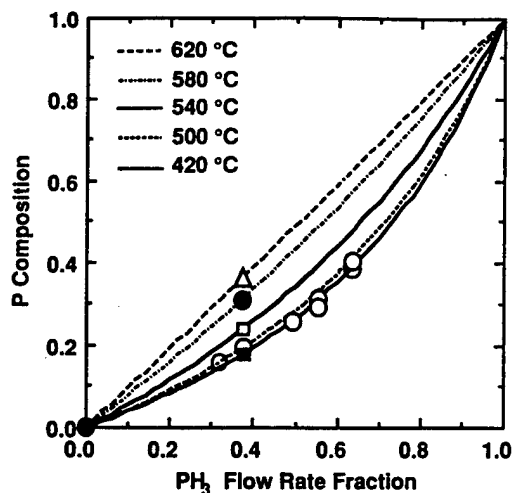


FIG. 5. The P composition in GaAsP as a function of the PH_3 flow rate fraction at different growth temperatures. The closed circles are from x-ray diffraction of GaAsP/GaAs SLSs grown at 500 °C. Other symbols indicate SLSs grown at different substrate temperatures. The lines are calculations from the kinetic model.

phosphorus composition at substrate temperatures below 500 °C. For substrate temperatures greater than 500 °C, the phosphorus composition increases with substrate tempera-

ture due to faster desorption of As_2 . At about 620 °C, phosphorus compositions in epilayers can simply be obtained from the flow-rate fractions because of nearly equal net incorporation of As and P.

ACKNOWLEDGMENTS

We wish to thank H. Q. Hou for part of his experimental data and T. P. Chin for assistance in GSMBE growth. This work is partially supported by the Office of Naval Research.

- ¹A. D. Huelsman, J. Electron. Mater. **18**, 91 (1989).
- ²L. Samuelson, P. Omling, and G. Grimmeiss, J. Cryst. Growth **61**, 425 (1983).
- ³H. Seki and A. Koukitu, J. Cryst. Growth **74**, 172 (1986).
- ⁴G. B. Stringfellow, J. Cryst. Growth **70**, 133 (1984).
- ⁵T. Nomura, H. Ogasawara, M. Miyao, and M. Hagino, J. Cryst. Growth (1991).
- ⁶M. B. Panish and S. Sumski, J. Appl. Phys. **55**, 3571 (1984).
- ⁷C. T. Foxon, B. A. Joyce, and M. T. Norris, J. Cryst. Growth **49**, 132 (1980).
- ⁸H. Q. Hou, B. W. Liang, T. P. Chin, and C. W. Tu, Appl. Phys. Lett. **59**, 292 (1991).
- ⁹R. Chow and R. Fernandez, Mater. Res. Soc. Symp. Proc. **145**, 13 (1989).
- ¹⁰T. P. Chin, B. W. Liang, H. Q. Hou, M. C. Ho, C. E. Chang, and C. W. Tu, Appl. Phys. Lett. **58**, 254 (1991).
- ¹¹Andrew Zangwill, in *Physics at Surface* (Cambridge University Press, Cambridge, 1988), p. 366.
- ¹²B. W. Liang and C. W. Tu, J. Appl. Phys. **72**, 2806 (1992).

Group-V Composition Control for InGaAsP Grown by Gas Source Molecular Beam Epitaxy

B.W. LIANG* and C.W. TU

Department of Electrical and Computer Engineering, University of California at San Diego, La Jolla, CA 92093-0407

Based on our kinetics models for gas source molecular beam epitaxy of mixed group-V ternary materials, the group-V composition control in $\text{In}_y\text{Ga}_{1-y}\text{As}_{1-x}\text{P}_x$ epilayers has been studied. The P or As composition in $\text{In}_y\text{Ga}_{1-y}\text{As}_{1-x}\text{P}_x$ (lattice matched to InP or GaAs) can be obtained from a simple equation for substrate temperatures below 500°C. This has been verified by a series of experimental results.

Key words: Composition control, $\text{In}_y\text{Ga}_{1-y}\text{As}_{1-x}\text{P}_x$, gas source molecular beam epitaxy (GSMBE), kinetics

INTRODUCTION

Because of its large wavelength coverage, mixed group-V quaternary InGaAsP is very important for optoelectronic applications. Various growth techniques, such as liquid-phase epitaxy (LPE), metal-organic vapor phase epitaxy (MOVPE), chemical beam epitaxy (CBE), and gas source molecular-beam epitaxy (GSMBE) have been used to grow this material.¹⁻⁵ One of the critical issues on the growth of such material is the control of the group-V composition.^{2,4} For MOVPE, a thermodynamic model was developed.⁶ For GSMBE, however, even though there are some experimental results,⁷ little work has been done theoretically. In this paper, based on the kinetics models for GSMBE of GaAsP and InAsP that we have developed,^{8,9} a simple equation has been derived for the determination of group-V composition in $\text{In}_y\text{Ga}_{1-y}\text{As}_{1-x}\text{P}_x$ epilayers grown by GSMBE.

EXPERIMENTAL PROCEDURE

The GSMBE growth was performed in a modified Intevac Gen-II MBE system, which can handle AsH_3 and PH_3 . A detailed description of this system can be

found elsewhere.¹⁰ InAsP and InGaAsP, samples were grown on semi-insulating InP (001) or GaAs (001) substrates. The growth temperature for InAsP was between 500 and 535°C, and for InGaAsP, it was fixed at about 470°C. X-ray rocking curve measurements and Rutherford backscattering (RBS) were performed to measure the P composition in InGaAsP and InAsP, respectively.

RESULTS AND DISCUSSION

For $\text{In}_y\text{Ga}_{1-y}\text{As}_{1-x}\text{P}_x$, one pair of the end ternary compounds are $\text{InAs}_{1-\beta}\text{P}_\beta$ and $\text{GaAs}_{1-\beta'}\text{P}_{\beta'}$, with a simple relation among x , y , β , and β' , i.e., $x = y\beta' + (1-y)\beta$. If β and β' are known, x can be calculated for a given y . This means that one can obtain the As or P composition in InGaAsP from InAsP and GaAsP. As and P incorporation behaviors in GaAsP have been studied extensively.¹¹⁻¹⁵ In Ref. 8, we obtained a general relation between P composition and growth conditions, such as substrate temperatures and flow-rate fractions, i.e., the ratio of the PH_3 flow rate over the total hydride flow rate. For InAsP, little work has been done.¹⁶ Figure 1 shows the P composition in InAsP grown on InP and in GaAsP grown on GaAs as a function of substrate temperature. For InAsP, the PH_3 flow-rate fraction (X_p) is 0.82, and the growth rate is 1 $\mu\text{m/h}$. The P compositions were obtained by RBS. For GaAsP, the PH_3 flow-rate fraction is 0.37, and the

(Received January 15, 1993; revised July 25, 1994)
*Present address: Hewlett-Packard Optoelectronics Division, San Jose, CA 95131

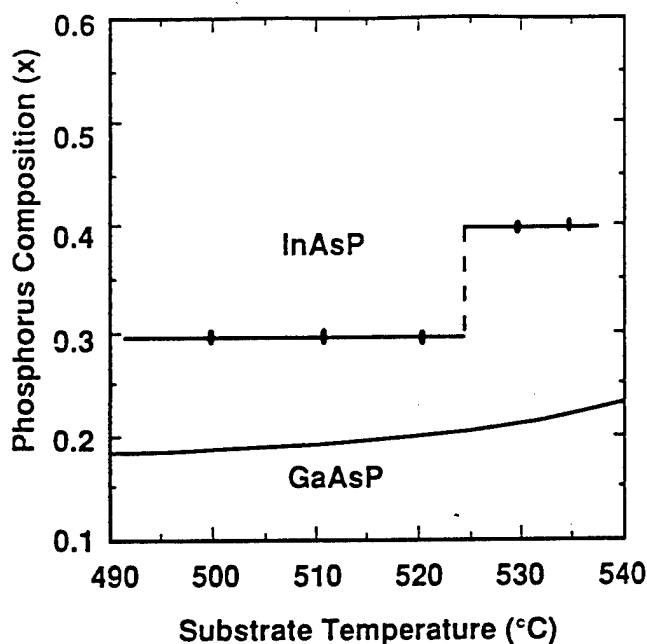


Fig. 1. The P composition in InAsP grown on InP and in GaAsP grown on GaAs as a function of substrate temperature. The experimental data for InAsP were obtained from RBS measurements of single epitaxial layers, and for GaAsP, from x-ray rocking curves and simulations of GaAsP/GaAs strained layer superlattices. The phosphine flow-rate fraction for InAsP is 0.82, and for GaAsP, 0.37.

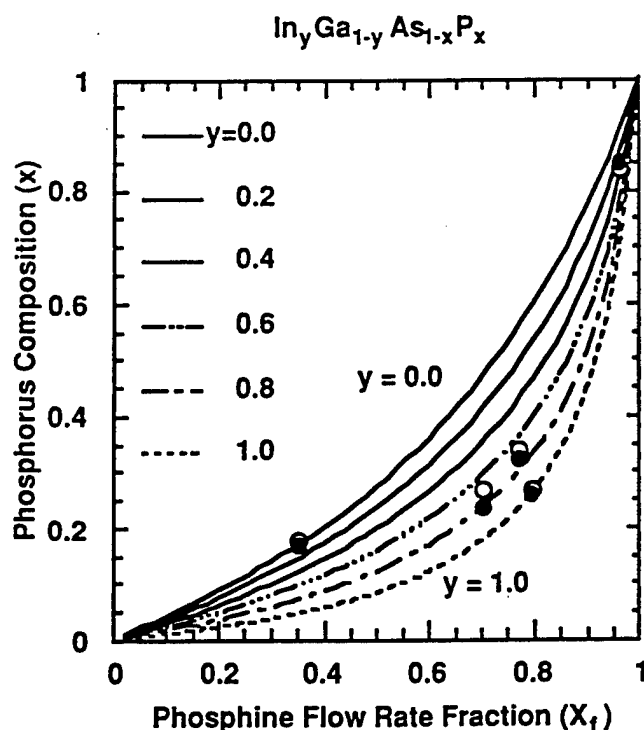


Fig. 2. The P composition in $\text{In}_y\text{Ga}_{1-y}\text{As}_{1-x}\text{P}_x$ as a function of phosphine flow-rate fraction for different Ga compositions at a substrate temperature below 500°C . The lines and open circles are calculated results and the solid circles are experimental data.

P compositions were obtained by x-ray rocking curves and simulations.⁸

If we extend our kinetic model for GSMBE of GaAsP_β to $\text{InAs}_{1-\beta}\text{P}_\beta$ for substrate temperatures below 520°C ,

the P composition β' in $\text{InAs}_{1-\beta}\text{P}_\beta$ as a function of arsine and phosphine flow rates or the phosphine flow-rate fraction can be written as

$$\beta' = \frac{1}{1 + \tilde{c} \frac{f_{\text{AsH}_3}}{f_{\text{PH}_3}}} = \frac{1}{1 + \tilde{c} \frac{(1 - X_f)}{X_f}} \quad (1)$$

with

$$\tilde{c} = \frac{S_{\text{As}}}{S_{\text{P}}} \sqrt{\frac{M_{\text{P}_2}}{M_{\text{As}_2}}}, \quad (2)$$

where f_s are hydride flow rates; X_f , the phosphine flow-rate fraction; S_s , sticking coefficients; and M_s , molecular weights. Equation (1) is similar in form to that for GaAsP.⁸ From Eq. (1) for InAsP and GaAsP and $x = y\beta' + (1 - y)\beta$, if y and \tilde{c} for both GaAsP and InAsP are known, one can obtain the P composition x in $\text{In}_y\text{Ga}_{1-y}\text{As}_{1-x}\text{P}_x$. For InAsP, according to the experimental results in Fig. 1, \tilde{c} is 11.2 for substrate temperatures below 520°C . For GaAsP, \tilde{c} is 2.7.⁸ Therefore, we have the P composition in $\text{In}_y\text{Ga}_{1-y}\text{As}_{1-x}\text{P}_x$ as a function of phosphine flow-rate fraction (X_f) and Ga composition ($1 - y$), as shown in Fig. 2.

$$x = \frac{y}{1 + \frac{11.2(1 - X_f)}{X_f}} + \frac{1 - y}{1 + \frac{2.7(1 - X_f)}{X_f}} \quad (3)$$

In Fig. 2, closed circles are experimental data, and open circles are expected values. We see the agreement is quite good, with an accuracy of about ± 0.02 . Even though such an accuracy may not be good enough for certain structures that have a stringent requirement on composition control, such as quantum-well modulators, our procedure replaces the usual initial trials and errors. Once the composition of the first sample is determined by x-ray rocking curves and simulations, the composition of the second sample can be fine-tuned to obtain the exact composition ($< \pm 0.01$). Reproducibility is a complicated issue because mass flow controllers may drift and the substrate temperature may vary slightly from run to run. The substrate temperature considered in our model is low ($< 500^\circ\text{C}$) such that the sticking coefficients of As and P are relatively insensitive of temperature and composition. The drift in mass flow controllers can be taken into account by determining the As and P incorporation rate at a given substrate temperature from group V-induced intensity oscillations of reflection high-energy electron diffraction (RHEED).¹⁰

Obviously, the ratio of As to P incorporation coefficient in InAsP is about four times larger than that in GaAsP. This may be explained by the difference in the binding energies between III-As and III-P for different group-III elements, such as Ga and In. The binding energy for GaP is about 1.65 eV, and for GaAs, about 1.52 eV. The difference is about 0.13 eV. However, the binding energy for InP is about 1.5 eV and

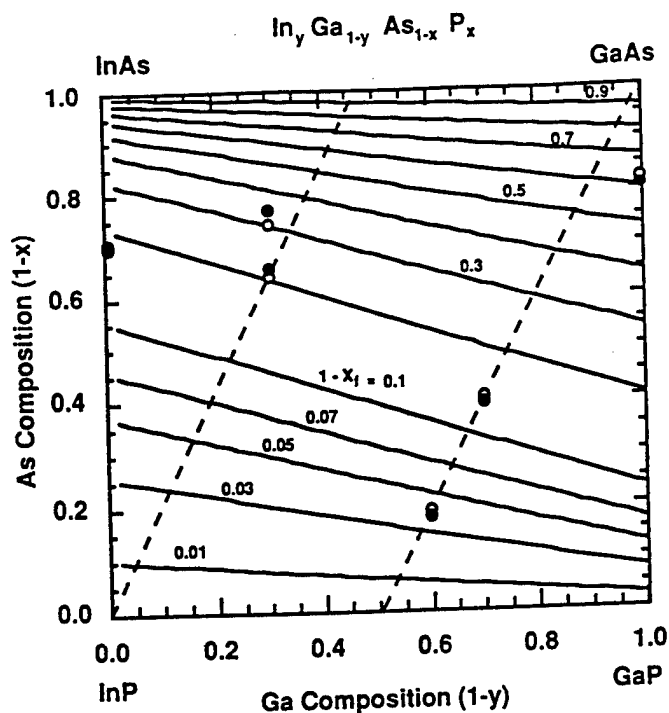


Fig. 3. The relationship among As and Ga compositions and arsine flow-rate fraction ($1 - X_i$) in $\text{In}_y\text{Ga}_{1-y}\text{As}_{1-x}\text{P}_x$ at a substrate temperature below 500°C . The open circles and the curves are calculation results, and the solid circles are experimental data.

InAs, 1.4 eV. So the difference is about 0.1 eV. This indicates that it is easier for P to desorb in InAsP than in GaAsP. Therefore, the ratio of P to As incorporation coefficient in InAsP is smaller than that in GaAsP. This was also found in MOVPE.¹⁷

Figure 3 shows the relationship between the As composition ($1 - x$) in $\text{In}_y\text{Ga}_{1-y}\text{As}_{1-x}\text{P}_x$ and arsine flow-rate fraction ($1 - X_i$) for different Ga compositions at growth temperature below 500°C . The curves and open circles are calculation results from Eq. (3) and the solid circles are experimental results from x-ray rocking curves. The two dashed lines indicate the compositions lattice-matched to GaAs and InP, respectively. Note that a small arsenic content in the gas phase produces a large arsenic composition in the solid phase, indicating that arsenic is incorporated much more efficiently than phosphorus. In Fig. 4, we compare a part of Fig. 3 with calculated results for InGaAsP grown by MOVPE, which were obtained from thermodynamics by Koukitu and Seki.¹⁷ One can see there are both similarity and difference between GSMBE and MOVPE. The similarity is that As has higher incorporation coefficient than P, and the As incorporation coefficient is even higher in InAsP than in GaAsP, as mentioned before. Thus, the As composition in InGaAsP decreases from In-rich to Ga-rich region. The difference between GSMBE and MOVPE is that in GSMBE there is no flat region for lower arsine flow-rate fractions and higher In compositions. This could be due to the fact that in GSMBE, arsine and phosphine are precracked to produce As_2 and P_2 ; whereas in MOVPE, arsine and phosphine have to react on the surface for As and P to be incorporated.

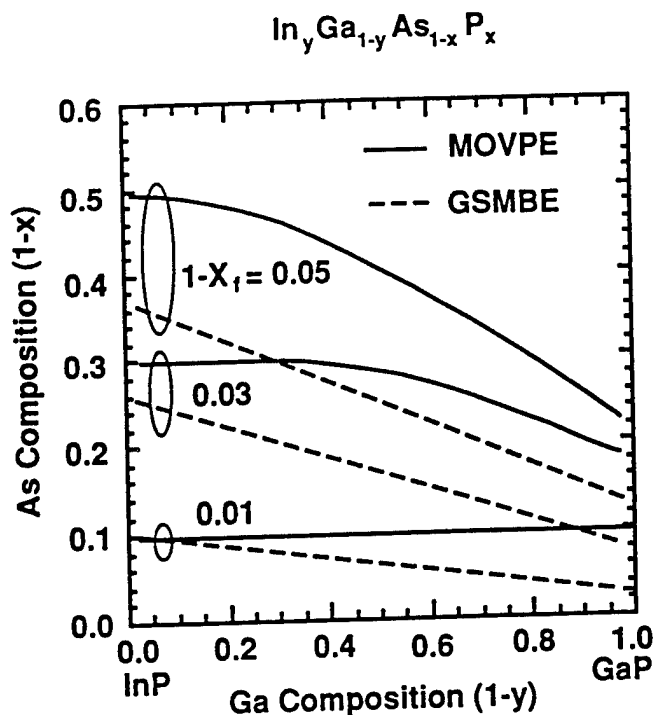


Fig. 4. A comparison of calculated As compositions as a function of gallium composition ($1 - y$) and arsine flow-rate fraction ($1 - X_i$) in $\text{In}_y\text{Ga}_{1-y}\text{As}_{1-x}\text{P}_x$ grown by GSMBE at a substrate temperature below 500°C (based on our kinetic model) with those grown by MOVPE at 650°C (based on Koukitu and Seki's thermodynamic model).¹⁷ The dash lines are for GSMBE and the solid lines, MOVPE.

Even though a different GSMBE system may cause different results due to possible systematic errors in the calibration of substrate temperatures and hydride flow rates, the equation should be the same for all systems. Once \bar{c} parameters are obtained for InAsP and GaAsP for a particular system, one can draw a similar figure to Fig. 3 and predict the group-V composition in InGaAsP easily.

CONCLUSION

We have investigated the group-V composition control in InGaAsP grown by GSMBE. Based on our kinetics models, a simple equation has been derived to predict the As composition in InGaAsP for a given Ga composition at substrate temperatures below 500°C . The calculated results agree with experimental results very well, and the control of group-V composition in InGaAsP is considerably simplified.

ACKNOWLEDGMENTS

We wish to thank T.P. Chin and H.Q. Hou for the assistance in GSMBE growth. This work is partially supported by the U.S. Office of Naval Research.

REFERENCES

1. A.Y. Cho, *J. Vac. Sci. Technol.* 16, 275 (1979).
2. W.T. Tsang, F.K. Reinhart and J.A. Ditzenberger, *Appl. Phys. Lett.* 41, 1094 (1982).
3. M. Lambert, L. Goldstein, A. Perales, F. Gaborit, C. Starck and J.L. Lievin, *J. Cryst. Growth* 111, 495 (1991).
4. H.C. Casey, Jr. and M.B. Panish, *Heterostructure Lasers, Part B* (New York: Academic Press, 1978).

5. M.B. Panish and S. Sumski, *J. Appl. Phys.* 55, 3571 (1984).
6. H. Seki and A. Koukitu, *J. Cryst. Growth* 74, 172 (1986).
7. K. Tappura, T. Hakkarainen, K. Rakenius, M. Hovinen and H. Asonen, *J. Cryst. Growth* 112, 27 (1991).
8. B.W. Liang and C.W. Tu, *J. Appl. Phys.* 74, 255 (1993).
9. C.W. Tu, B.W. Liang and H.Q. Hou, *J. Cryst. Growth* 127, 199 (1993).
10. T.P. Chin, B.W. Liang, H.Q. Hou, M.C. Ho, C.E. Chang and C.W. Tu, *Appl. Phys. Lett.* 58, 254 (1991).
11. A.D. Huelsman, *J. Electron. Mater.* 18, 91 (1989).
12. L. Samuelson, P. Omling and G. Grimmeiss, *J. Cryst. Growth* 61, 425 (1983).
13. G.B. Stringfellow, *J. Cryst. Growth* 70, 133 (1984).
14. T. Nomura, H. Ogasawara, M. Miyao and M. Hagino, *J. Cryst. Growth* 111, 61 (1991).
15. C.T. Foxon, B.A. Joyce and M.T. Norris, *J. Cryst. Growth* 49, 132 (1980).
16. H.Q. Hou and C.W. Tu, *Appl. Phys. Lett.* 60, 1872 (1992).
17. A. Koukitu and H. Seki, *J. Cryst. Growth* 76, 233 (1986).

APPENDIX

B

Lattice-mismatched structures with linearly graded buffer layers

Gas-source molecular beam epitaxial growth, characterization, and light-emitting diode application of $\text{In}_x\text{Ga}_{1-x}\text{P}$ on $\text{GaP}(100)$

T. P. Chin, J. C. P. Chang, K. L. Kavanagh, and C. W. Tu

Department of Electrical and Computer Engineering, University of California, San Diego, La Jolla, California 92093-0407

P. D. Kirchner and J. M. Woodall

IBM T. J. Watson Research Center, Yorktown Heights, New York 10598

(Received 24 September 1992; accepted for publication 15 February 1993)

Highly lattice-mismatched $\text{In}_x\text{Ga}_{1-x}\text{P}$ ($x < 0.38$) layers were grown on GaP substrates by gas-source molecular beam epitaxy. A relatively thin, compositionally linear-graded buffer layer was used to reduce the number of threading dislocations. Studies by double-crystal x-ray diffraction and transmission electron microscopy show this buffer layer to be 97% strain-relaxed along both $\langle 110 \rangle$ directions with dislocations well confined within the graded buffer and the substrate. Threading dislocation densities in the top layers were less than $1 \times 10^7 \text{ cm}^{-2}$. Room-temperature photoluminescence, ranging from 560 to 600 nm, is achieved. Heterojunction p - i - n diodes emitting at 560 nm at 300 K exhibit good rectifying and reverse breakdown characteristics.

Visible light-emitting diodes (LEDs) and laser diodes are useful for outdoor displays, signaling, and laser printers. Red $\text{GaAs}_x\text{P}_{1-x}$ LEDs and green GaP LEDs have been mass-produced for years by liquid- or vapor-phase epitaxy. In these indirect-band-gap materials impurity-induced transitions are responsible for the light generation. However, a typical external quantum efficiency for a $\text{GaAs}_x\text{P}_{1-x}$ LED at 590–630 nm, for example, is less than 1%. LEDs made with a direct-band-gap material show much higher efficiencies. Lattice-matched InGaAlP LEDs grown on GaAs , with the help of a thick GaP window layer, achieved a 6% external quantum efficiency at 590 nm.¹ At 560 nm the same structure with a higher aluminum content exhibits a lower efficiency ($\approx 0.2\%$), but still better than a conventional green GaP LED ($\approx 0.08\%$).¹

An alternative approach to indirect-gap GaAsP and direct-gap InGaAlP on GaAs for achieving room-temperature, short-wavelength visible light emission is to grow a lattice-mismatched epilayer of direct-gap $\text{In}_x\text{Ga}_{1-x}\text{P}$. When $x > 0.27$, this material has the highest direct-band-gap of any arsenide or phosphide, except $\text{In}_x\text{Al}_{1-x}\text{P}$. It grows tensilely strained on GaAs ($x < 0.49$) or compressively strained on GaP . In the composition range $0.27 < x < 0.49$, similar band gaps to that of InGaAlP lattice-matched to GaAs can be achieved without using aluminum, an advantage since aluminum is very sensitive to oxygen contamination. Recently, Masselink and Zachau reported the growth of $\text{In}_{0.35}\text{Ga}_{0.65}\text{P}$ on GaAs and obtained a room-temperature peak emission at 590 nm.² Stinson *et al.* have grown thick (10 μm) $\text{In}_x\text{Ga}_{1-x}\text{P}$ layers on a graded buffer layer on GaP by organometallic vapor-phase epitaxy and reported an LED external quantum efficiency of 0.9% at 590 nm.³ GaP substrates have the advantage that they are transparent to the emitted light, hence substrate absorption is greatly reduced. In this letter, we report the growth and characterization of $\text{In}_x\text{Ga}_{1-x}\text{P}$ layers

grown on a relatively thin (compared to Ref. 3), linearly graded buffer layer on GaP (100) by gas-source molecular beam epitaxy (GSMBE). The device characteristics of double-heterojunction $\text{In}_x\text{Ga}_{1-x}\text{P}$ green (560 nm) LEDs are also described.

Matthews *et al.*⁴ predicted that mismatched epilayers could have lower dislocation densities than the substrate because the misfit strain energy would cause existing threading dislocations to glide out of the epilayer. However, at large lattice mismatch this model breaks down since substrate dislocation densities are insufficient to relax the strain entirely. The nucleation of new dislocations is required, and this process is less well understood or controlled. Compositionally step-graded⁵ or linearly-graded buffer layers^{6–9} for strain relaxation and dislocation filtering in large mismatched systems have recently been reexamined. The results for both III-V and group IV semiconductor systems have been encouraging. Fitzgerald *et al.*⁶ demonstrated low threading-dislocation densities in $\text{Si}_x\text{Ge}_{1-x}/\text{Si}$ using a linearly graded buffer layer. Using a similar technique, Lord *et al.*⁷ reported 1.3 μm exciton resonance in an $\text{In}_{0.5}\text{Ga}_{0.5}\text{As}$ multiple quantum well structure grown on GaAs . Fischer-Colbrie *et al.*⁸ reported obtaining high-quality $\text{In}_{0.8}\text{Ga}_{0.2}\text{As}$ on InP , and Le Goues *et al.*⁹ reported low threading dislocation densities in both the $\text{Si}_x\text{Ge}_{1-x}/\text{Si}$ and $\text{In}_x\text{Ga}_{1-x}\text{As}/\text{GaAs}$ systems. Appropriately graded structures produce a sufficient amount of misfit dislocations to relax the film at a nucleation rate slow enough to apparently allow the glide of threading dislocations unimpeded to the edges of the sample. In this work we apply this growth technique to the $\text{In}_x\text{Ga}_{1-x}\text{P}/\text{GaP}$ system and obtain $\text{In}_x\text{Ga}_{1-x}\text{P}$ buffer layers with threading dislocation densities sufficiently low as to serve as a substrate for further growth.

The growth was performed in an Intevac Modular GEN-II MBE modified to handle arsine and phosphine.

Pure phosphine was introduced into the growth chamber through a cracker producing P_2 and H_2 . Solid gallium and indium were used for the group-III sources. More details about the GSMBE system have been described elsewhere.¹⁰ The *n*-type GaP (100) substrate was cleaned with a $HCl:HNO_3:H_2O$ (4:4:5) solution and mounted with indium onto a 3-in. Si wafer before it was loaded into the growth chamber. Oxide desorption occurred at about 660 °C. A thin GaP layer was grown first at 650 °C followed by the graded $In_xGa_{1-x}P$ buffer layer. For the buffer layer the indium cell temperature was changed at a rate such that the indium composition increased by 1% for every 40 nm of layer grown, approximately 2% lattice mismatch per micron. Because of the lower melting point of InP, compared to GaP, the optimal growth temperature is approximately in proportion to the In composition. Therefore, the substrate temperature was gradually decreased from 650 °C to the final temperature (490 to 550 °C) for the growth at the composition $x \approx 0.3$. The growth of the buffer layer was interrupted four times while the substrate was annealed for 5 min at 60 °C higher than the growth temperature. We found that this thermal cycling improved the surface morphology. After the required indium composition was reached, a constant-composition layer for x-ray diffraction measurements or diode fabrication was grown on top.

The surface of each sample was examined under a Nomarski optical interference microscope. Clearly defined surface cross-hatch patterns along both in-plane $\langle 011 \rangle$ directions were observed on these films, similar to previous work on lattice-mismatched epitaxial growth.⁹ This cross-hatched surface could be related to misfit dislocation multiplication sources whereby repeated glide occurs on closely spaced $\langle 111 \rangle$ planes.¹¹ We found the cross-hatched surface morphology to be associated with a low threading dislocation density and an intense photoluminescence (PL) emission.⁹ Another sample of $In_{0.32}Ga_{0.68}P$ grown with a four-step graded buffer layer (8% indium per step) has a rough textured surface and no PL response at room temperature. A clearly defined cross-hatched surface pattern then served as a first qualitative evaluation of the epilayers before further characterization.

Figure 1 shows a cross-section transmission electron micrograph (XTEM) of an $In_{0.32}Ga_{0.68}P$ epilayer grown on a linearly graded buffer on GaP(100). The TEM was carried out at an accelerating beam voltage of 300 kV. Dislocations are mostly confined to the graded buffer layer. Dislocation loop pile-ups in the substrate are also observed.¹² The top layer with a constant composition is clear and free of dislocations in XTEM. The threading dislocation density estimated from plan-view TEM is less than $1 \times 10^7 \text{ cm}^{-2}$.

The top epilayer composition and degree of strain relaxation were determined with (400) and (422) x-ray rocking curves. Figure 2 shows a typical (400) x-ray spectrum. The constant background is due to the linearly graded buffer layer. All of the layers examined were almost

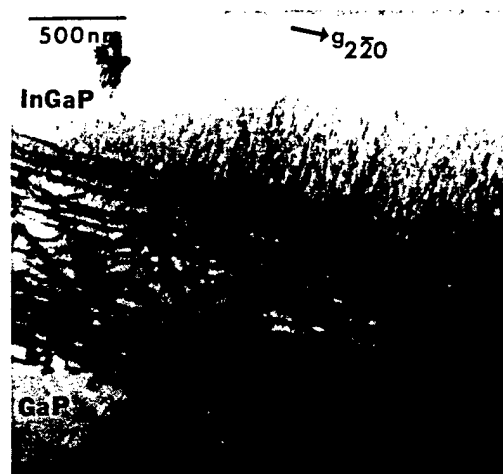


FIG. 1. Cross-section TEM micrograph of an $In_{0.32}Ga_{0.68}P$ epilayer grown on a linearly graded buffer layer on a GaP(100) substrate. The thickness of the linearly graded buffer is $1.15 \mu\text{m}$.

completely relaxed (around 97%) along both in-plane $\langle 011 \rangle$ directions. For $x \approx 0.3$, a top layer growth temperature of 540 °C is optimal with respect to the x-ray linewidth. The smallest linewidth measured for a $1.4\text{-}\mu\text{m}$ -thick $In_{0.32}Ga_{0.68}P$ layer grown on a 1.2-mm -thick graded buffer layer was 500 arcsec.

Room-temperature PL measurements were performed on samples with different In compositions. The highest luminescence intensity was obtained at 584 nm from a layer with 32% indium. The emission efficiency was low for lower indium concentrations because the direct-indirect band-gap crossover occurs at $x \approx 0.28$. In the case of higher indium concentrations above 32%, the PL intensity also decreased probably due to the increasing lattice mismatch. Consistent with x-ray results, the 300 K PL intensity for $x \approx 0.32$ is about 30% higher for a growth temperature of 520–540 °C than 480 °C. Photoluminescence at lower tem-

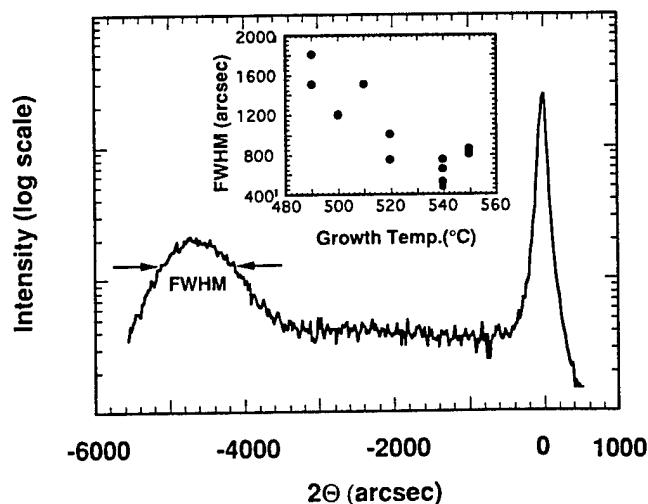


FIG. 2. (400) x-ray rocking curve of a $1.4\text{-}\mu\text{m}$ -thick $In_{0.3}Ga_{0.7}P$ layer grown on a linearly graded buffer layer on GaP(100). The insert shows the effect of growth temperature on the x-ray linewidth.

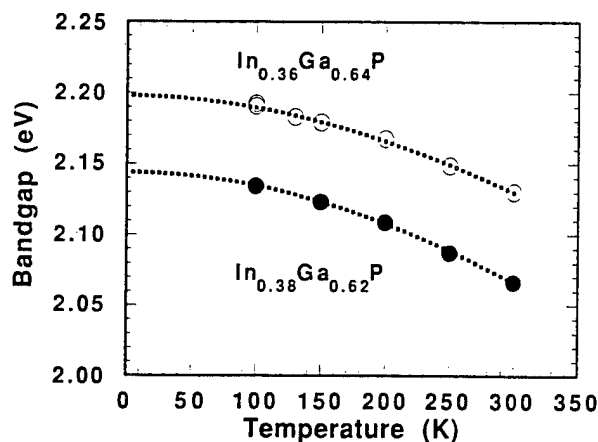


FIG. 3. Temperature dependence of the $\text{In}_x\text{Ga}_{1-x}\text{P}$ band-gap energy measured by photoluminescence. The dashed line is the result of fitting with the Varshni equation.

peratures was also measured, and the relationship between the peak energy and temperature was fit with the Varshni equations (Fig. 3).¹³ The extrapolated band-gap energy of $\text{In}_x\text{Ga}_{1-x}\text{P}$ versus indium composition at 4.2 K is consistent with the theoretical band gap for a relaxed $\text{In}_x\text{Ga}_{1-x}\text{P}$.¹⁴

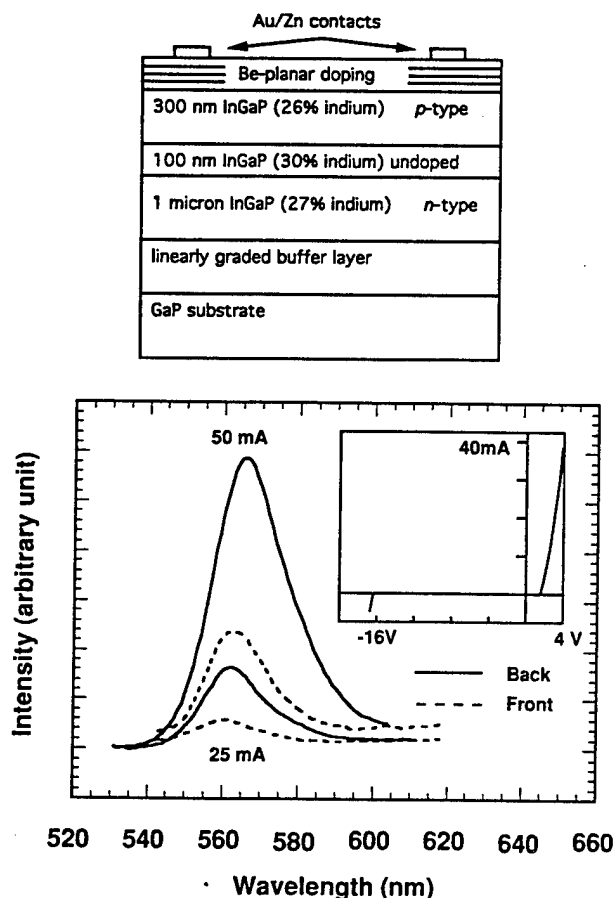


FIG. 4(a). Device structure of an $\text{In}_x\text{Ga}_{1-x}\text{P}$ heterojunction LED. The dose for the Be planar doping is $5 \times 10^{12} \text{ cm}^{-2}$. (b) Electroluminescence (EL) and I - V curve of the LED. The EL is measured at 25 and 50 mA from both the front side (dashed lines) and back side (solid lines).

Heterojunction $\text{In}_x\text{Ga}_{1-x}\text{P}$ p - i - n diodes with electroluminescence (EL) at peak wavelengths 560–565 nm were fabricated. The structure is shown in Fig. 4(a). The 100 nm active layer and the p -type cap layers were grown pseudomorphically on a relaxed $\text{In}_{0.27}\text{Ga}_{0.73}\text{P}$ layer. The cap layer contained three Be-planar doping regions to reduce the contact resistance. The I - V characteristics showed a high breakdown voltage ($\approx -16 \text{ V}$), and leakage currents less than 100 nA at -16 V despite the highly mismatched epilayer. However, a problem with this diode structure was the high series and contact resistance due to the difficulty in achieving high p -type doping in $\text{In}_x\text{Ga}_{1-x}\text{P}$.³ Although the Be planar doping in the ohmic contact layer (dose of each plane $\approx 5 \times 10^{12} \text{ cm}^{-2}$) reduced the contact resistance from 4.5×10^{-3} to $3 \times 10^{-3} \Omega \text{ cm}^2$ compared to a uniformly doped contact layer, poor current spreading results in light blocked by the metal contact when EL measurements are performed from the front side [dashed lines, Fig. 4(b)]. Light emission measured from the back side is improved by about a factor of 2 [solid lines, Fig. 4(b)] because the GaP substrate is transparent. Device geometry and the processing shall be further optimized to maximize light extraction.

In summary, we have demonstrated that a compositionally graded buffer can effectively reduce the number of threading dislocations in the $\text{In}_x\text{Ga}_{1-x}\text{P}/\text{GaP}$ system to obtain materials potentially useful for visible light emitting applications. X-ray and PL data show that the epilayer grown on a linearly graded buffer layer is fully relaxed, with a threading dislocation density less than $1 \times 10^7 \text{ cm}^{-2}$. Green LEDs (560 nm) with good rectifying and reverse breakdown characteristics were fabricated.

This work is supported by the Office of Naval Research and the National Science Foundation Presidential Young Investigator Award.

¹ K. H. Huang, J. G. Yu, C. P. Kuo, R. M. Fletcher, T. D. Osentowski, L. J. Stinson, M. G. Craford, and A. S. H. Liao, *Appl. Phys. Lett.* **61**, 1045 (1992).

² W. T. Masselink and M. Zachau, *Appl. Phys. Lett.* **61**, 58 (1992).

³ L. J. Stinson, J. G. Yu, S. D. Lester, M. J. Peanasky, and Kwang Park, *Appl. Phys. Lett.* **58**, 2012 (1991).

⁴ J. W. Matthews, S. Mader, and T. B. Light, *J. Appl. Phys.* **41**, 3800 (1970).

⁵ J. C. P. Chang, J. H. Chen, J. M. Fernandez, H. H. Wieder, and K. L. Kavanagh, *Appl. Phys. Lett.* **60**, 1129 (1992).

⁶ E. A. Fitzgerald, Y. H. Xie, M. L. Green, D. Brasen, A. R. Kortan, Y. J. Mii, J. Michel, and B. W. Weir, *Appl. Phys. Lett.* **59**, 811 (1991).

⁷ S. M. Lord, B. Pezeshki, S. D. Kim, and J. S. Harris, Jr., *J. Cryst. Growth* (to be published).

⁸ A. Fischer-Colbrie, R. D. Jacowitz, and D. G. Ast, *J. Cryst. Growth* (to be published).

⁹ F. K. LeGoues, B. S. Meyerson, J. F. Morar, and P. D. Kirchner, *J. Appl. Phys.* **71**, 4230 (1992).

¹⁰ T. P. Chin, B. W. Liang, H. Q. Hou, M. C. Hou, C. E. Chang, and C. W. Tu, *Appl. Phys. Lett.* **58**, 254 (1991).

¹¹ K. H. Chang, R. Gibala, D. J. Srolovitz, P. K. Bhattacharya, and J. F. Mansfield, *J. Appl. Phys.* **67**, 4093 (1990).

¹² J. C. P. Chang, T. P. Chin, C. W. Tu, and K. L. Kavanagh (unpublished).

¹³ Y. P. Varshni, *Physica* **34**, 149 (1967).

¹⁴ R. J. Nelson and N. Holonyak, Jr., *J. Phys. Chem. Solids* **37**, 629 (1976).

Heteroepitaxial growth of $\text{InP}/\text{In}_{0.52}\text{Ga}_{0.48}\text{As}$ structures on GaAs (100) by gas-source molecular beam epitaxy

T. P. Chin and C. W. Tu

Department of Electrical and Computer Engineering, 0407, University of California, San Diego, La Jolla, California 92093-0407

(Received 21 December 1992; accepted for publication 1 March 1993)

High quality $\text{In}_{0.52}\text{Ga}_{0.48}\text{As}$, InP, and $\text{In}_{0.52}\text{Ga}_{0.48}\text{As}/\text{InP}$ single quantum wells were grown on GaAs (100) by gas-source molecular beam epitaxy (GSMBE) with a 2- μm thick $\text{In}_x\text{Ga}_{1-x}\text{As}$ buffer layer where x was linearly graded from 0 to 0.52. Reflection high-energy electron diffraction patterns and specular beam intensity oscillations showed that the growth mode of $\text{In}_{0.52}\text{Ga}_{0.48}\text{As}$ and InP were layer by layer despite the lattice mismatch ($\Delta a/a = 3.8\%$) between InP and GaAs. Photoluminescence line widths at 10 K of a 1- μm thick InP and a 5-nm wide $\text{In}_{0.52}\text{Ga}_{0.48}\text{As}/\text{InP}$ single quantum well are 4.9 and 10 meV, respectively, which are comparable to the values measured from similar structures grown lattice matched on an InP substrate (3.5 and 7 meV, respectively) by the same GSMBE system. The quantum-well luminescence intensity is also comparable to lattice-matched samples.

$\text{In}_{0.53}\text{Ga}_{0.47}\text{As}$ and InP are critical materials in InP-based optoelectronic devices, which are important for the 1.3–1.55 μm fiber-optic communication technology. However, the integration of 1.3–1.55 μm optoelectronic devices with GaAs technology is difficult because of the large lattice mismatch between GaAs and InP. The control of the threading dislocations generated during the growth is essential to obtain good quality $\text{In}_x\text{Ga}_{1-x}\text{As}$ as x increases. Recently Ribas *et al.*¹ reported a device quality $\text{In}_{0.4}\text{Ga}_{0.6}\text{As}$ layer grown on a GaAs substrate by using a complicated step-graded buffer layer. Chen *et al.*² reported a three-step graded buffer layer for $\text{In}_{0.3}\text{Ga}_{0.7}\text{As}$ grown on GaAs. Using a linearly graded buffer layer has also resulted in low threading-dislocation density of $\text{Si}_x\text{Ge}_{1-x}/\text{Si}$, $\text{In}_x\text{Ga}_{1-x}\text{As}/\text{GaAs}$ (x up to 0.35), $\text{In}_{0.8}\text{Ga}_{0.2}\text{As}/\text{InP}$, and $\text{In}_x\text{Ga}_{1-x}\text{P}/\text{GaP}^{3-5}$ (x up to 0.38). In particular, excitonic resonance at 1.3 μm in multiple quantum well structures grown on GaAs have been reported.⁶ In this letter, we report the growth of $\text{In}_{0.52}\text{Ga}_{0.48}\text{As}$, InP, and $\text{In}_{0.52}\text{Ga}_{0.48}\text{As}/\text{InP}$ single quantum wells on GaAs by using a linearly graded buffer layer by gas source molecular beam epitaxy (GSMBE). These samples show good photoluminescence properties comparable to similar structures lattice-matched to InP substrates. Reflection high-energy electron diffraction (RHEED) patterns and intensity oscillations, recorded during growth, indicate a layer-by-layer growth mode.

Samples were grown on exactly oriented GaAs (100) substrates in a modified Intevac Modular GEN-II molecular beam epitaxy (MBE) system which has been described previously.⁷ To achieve a linear indium composition profile ($x=0-0.53$), the gallium cell temperature was kept constant and the indium cell temperature was adjusted gradually according to the calibration from InP RHEED oscillations. The real indium compositions of the samples discussed here were 0.52 ± 0.02 . The growth rate of $\text{In}_{0.52}\text{Ga}_{0.48}\text{As}$ was about 1.6 monolayers/s. The total thickness of this graded buffer layer was 2 μm before the indium composition reached 0.52. In other words, the overall gradient was about 2% mismatch/ μm . The sub-

strate temperature was decreased linearly from 600 to 450 $^{\circ}\text{C}$ across the 2 μm buffer layer, then another layer of $\text{In}_{0.52}\text{Ga}_{0.48}\text{As}$ (200–500 nm) thick was grown at 450 $^{\circ}\text{C}$ before further growth of InP or $\text{In}_{0.52}\text{Ga}_{0.48}\text{As}/\text{InP}$ single quantum wells at 450–510 $^{\circ}\text{C}$.

The RHEED pattern was monitored during growth and stored on a video tape. Streaky patterns were observed through the graded $\text{In}_x\text{Ga}_{1-x}\text{As}$ buffer layer up to the top InP. Figures 1(a) and 1(b) show the RHEED patterns of the $\text{In}_{0.52}\text{Ga}_{0.48}\text{As}$ surface. A four- and three-fold pattern was observed in $\langle 011 \rangle$ and $\langle 0\bar{1}1 \rangle$ directions, respectively. The RHEED patterns of InP grown on the top are (2×4) or (2×1) depending on the phosphine flow rate and the substrate temperature, as we observed on homoepitaxial InP (100) in GSMBE.⁸ Figures 1(c) and 1(d) are the InP (2×4) pattern along $\langle 011 \rangle$ and $\langle 0\bar{1}1 \rangle$ directions, respectively. RHEED intensity oscillations on both $\text{In}_{0.52}\text{Ga}_{0.48}\text{As}$ and InP surfaces were also recorded, as shown in Figs. 2(a) and 2(b), respectively. These RHEED results indicate that the growth of these highly mismatched $\text{In}_x\text{Ga}_{1-x}\text{As}$ and InP on GaAs was kept in a two-dimensional growth mode despite the large lattice mismatch. No island growth was observed by RHEED nor by microscopy analysis. Cross hatches along both $\langle 011 \rangle$ directions were observed under a Normaski phase-contrast microscope.

X-ray diffraction was used to measure the indium composition and the degree of relaxation. Rocking curves were taken on both (400) and (422) planes, and the perpendicular and lateral lattice spacing could then be calculated.⁹ The x-ray analysis shows that the top layers are typically more than 95% relaxed along both $\langle 011 \rangle$ directions, an indication of the effectiveness of strain relaxation by the graded buffer layer. This is similar to our previous work on linearly graded $\text{In}_x\text{Ga}_{1-x}\text{P}$ on GaP (100).⁵ The formation of the cross hatch is believed to be from the repeated gliding of dislocations on (111) planes.¹⁰ The typical distance between two cross-hatch lines are 500 nm and the height is around 10 nm. They do not seem to affect the single quantum wells in PL measurements as we shall see later.

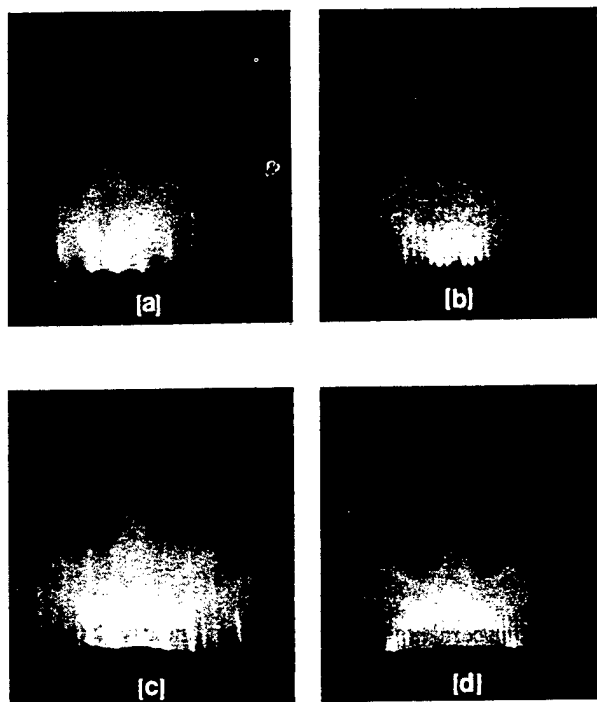


FIG. 1. (a) and (b) are (4×3) RHEED patterns along (011) and $(0\bar{1}1)$ directions of $\text{In}_{0.52}\text{Ga}_{0.48}\text{As}$ grown on GaAs (100) . (c) and (d) are (2×4) patterns of InP (5-nm thick) on top of the $\text{In}_{0.52}\text{Ga}_{0.48}\text{As}$ layer.

Photoluminescence measurements were performed at 10 K on $\text{In}_x\text{Ga}_{1-x}\text{As}$, InP, and $\text{In}_{0.52}\text{Ga}_{0.48}\text{As}/\text{InP}$ single quantum wells grown on GaAs. These samples are compared with similar structures grown lattice matched on InP in the same system. Figures 3(a) and 3(b) show the PL spectra of a 1- μm thick $\text{In}_{0.38}\text{Ga}_{0.62}\text{As}$ and a 0.8- μm thick $\text{In}_{0.52}\text{Ga}_{0.48}\text{As}$ layer, both grown on GaAs with a grader buffer layer. The PL full width at half maximum (FWHM) are 9 and 12 meV, respectively. These line widths are comparable to that obtained on a 0.2- μm thick $\text{In}_{0.53}\text{Ga}_{0.47}\text{As}$ layer (8 meV) grown on InP in the same

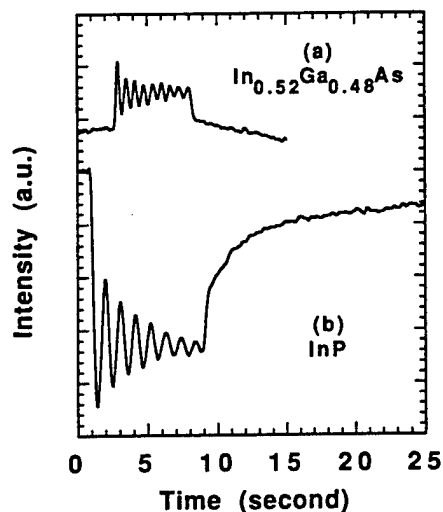


FIG. 2. RHEED intensity oscillations of (a) $\text{In}_{0.52}\text{Ga}_{0.48}\text{As}$ and (b) InP grown on GaAs substrate.

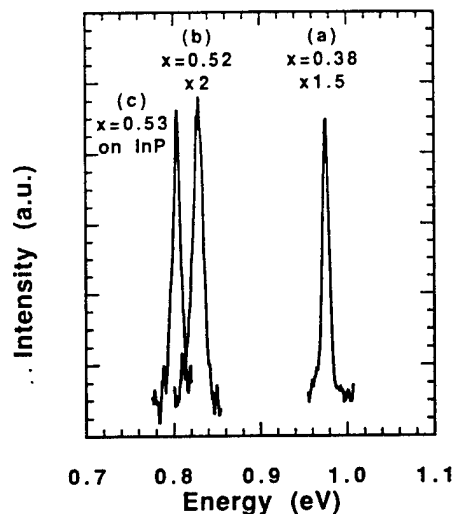


FIG. 3. 10 K PL spectra of (a) $\text{In}_{0.38}\text{Ga}_{0.62}\text{As}$ and (b) $\text{In}_{0.52}\text{Ga}_{0.48}\text{As}$ grown on GaAs with graded $\text{In}_x\text{Ga}_{1-x}\text{As}$ buffer layers. (c) is from a 0.2- μm thick $\text{In}_{0.53}\text{Ga}_{0.47}\text{As}$ grown lattice matched on InP. The FWHM are 9, 12, and 8 meV, respectively.

GSMBE system [Fig. 3(c)]. This PL result demonstrates that the optical quality of $\text{In}_{0.53}\text{Ga}_{0.47}\text{As}$ grown on GaAs with a linearly grader buffer layer could be comparable to that grown on InP. Our $\text{In}_{0.53}\text{Ga}_{0.47}\text{As}/\text{GaAs}$ result is also comparable to that reported by Ribas *et al.* who obtained a 7 meV line width on a 3- μm thick $\text{In}_{0.4}\text{Ga}_{0.6}\text{As}$ grown on GaAs with a buffer layer consisting of steps and superlattices.¹

Figure 4(a) shows the PL spectrum of a 1- μm thick InP layer grown at 480 °C on GaAs with a graded buffer layer, and Fig. 4(b) shows the PL obtained from a 0.6- μm thick InP layer grown directly on InP. For the homoepitaxial sample, the two peaks between 1.413 and 1.417 eV are identified to be D^0X and D^0h transitions. The peak centered at about 1.384 eV is believed to be from the electron-neutral-acceptor (eA^0) transition. The line width

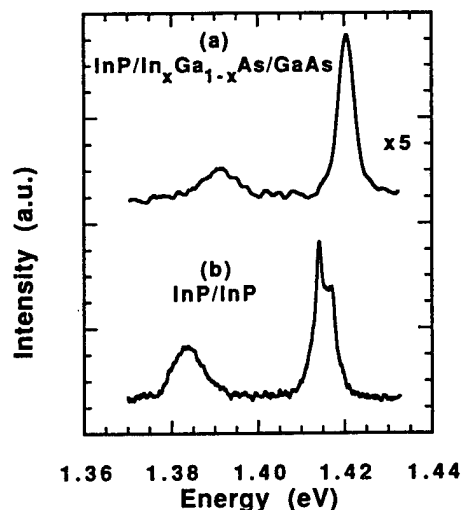


FIG. 4. 10 K PL spectra of (a) InP grown on GaAs with a graded $\text{In}_x\text{Ga}_{1-x}\text{As}$ buffer layer and (b) InP grown on InP.

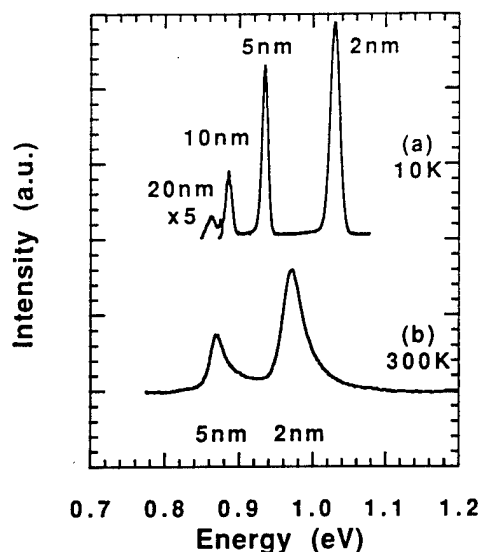


FIG. 5. (a) 10 K and (b) 300 K PL of four $\text{In}_{0.52}\text{Ga}_{0.48}\text{As}/\text{InP}$ single quantum wells grown on a GaAs with an $\text{In}_x\text{Ga}_{1-x}\text{As}$ buffer layer.

of the D^0h peak is estimated to be 3.5 meV, and the combined D^0X and D^0h peaks is about 5 meV. For the heteroepitaxial sample there is only one peak and the line width is 4.9 meV, comparable to that of the homoepitaxial sample. However, the luminescence efficiency of the heteroepitaxial InP is about 80% lower. This is probably due to the extra dislocations generated at the $\text{In}_{0.52}\text{Ga}_{0.48}\text{As}/\text{InP}$ interface, where a slight lattice mismatch occurs between these two layers. This is also supported by the fact that the peak position of these two InP PL spectra are different. The band-gap energy of the InP grown on the graded buffer layer is 6 meV higher than the homoepitaxial InP. If we assume that the strain at the $\text{In}_{0.52}\text{Ga}_{0.48}\text{As}/\text{InP}$ interface is 50% relaxed because the cross-sectional transmission electron microscopy (XTEM) result shows dislocations exist along only one $\langle 011 \rangle$ direction at this interface, we can conclude that this 6 meV band-gap shift corresponds to a lattice mismatch of $\Delta a/a = 1.4 \times 10^{-3}$ by considering the deformation potentials of InP.¹¹ The indium composition of the buffer layer is 51% by this estimation, which again agrees with the value (52%) obtained from PL and x-ray measurements. Our results should be compared with that reported by Razeghi *et al.* who grew InP on GaAs by MOCVD with a GaAs/GaInP buffer layer and achieved a 28 meV PL line width at 20 K.¹² Similar peak position shift towards higher energy was also observed. Yet the best PL result of InP on GaAs so far was reported by the same group in 1984, which was a 3 μm InP grown directly on GaAs with a 1 nm PL line width (equivalent to 1.6 meV).¹³

Single quantum wells were also grown on the graded buffer layer on GaAs and then characterized by PL. Single quantum wells with $\text{In}_{0.52}\text{Ga}_{0.48}\text{As}$ well width of 2, 5, 10, and 20 nm were separated by 50 nm InP barrier layers. The narrowest well is near the surface. Figure 5 shows the PL spectra of the single quantum well structure at 10 and 300 K. A higher excitation power is required to see the emis-

sion from the 20 nm well at 10 K, and the emission intensity of the 10 nm well is also lower than the top two wells. This could be explained as the effect of the small lattice mismatch between the InP and the $\text{In}_{0.52}\text{Ga}_{0.48}\text{As}$ buffer layer discussed above. Extra dislocations generated at this interface could affect the emission efficiency of the nearest two wells by nonradiative recombinations. However, intense excitonic peaks indicate good optical quality of the top two quantum wells (2 and 5 nm), whose intensities and line widths are comparable to those lattice-matched to an InP substrate. For example, the FWHM of the peak from the 5 nm well is 10 meV, as compared to a 7-meV FWHM from the control sample. These results are very encouraging.

In conclusion, we demonstrated that a high-quality $\text{In}_x\text{Ga}_{1-x}\text{As}$ could be grown on GaAs (100) by using a linearly graded buffer layer. This simple buffer layer successfully decoupled the lattice mismatch between the GaAs substrate and the subsequent InGaAs/InP heterostructures. Two-dimensional layer-by-layer growth was observed for $\text{In}_{0.52}\text{Ga}_{0.48}\text{As}$ and InP layers. We obtained InP, $\text{In}_{0.52}\text{Ga}_{0.48}\text{As}$ and $\text{In}_{0.52}\text{Ga}_{0.48}\text{As}/\text{InP}$ single quantum wells with PL intensities comparable to those grown lattice matched on InP substrates. One important question is how the cross-hatched surface morphology will affect the devices grown on top of the graded buffer layer.

The authors would like to thank P. D. Kirchner for valuable discussions. This work is partially supported by the Office of Naval Research, Hughes Aircraft Co., and the California MICRO program.

- ¹ P. Ribas, V. Krishnamoorthy, and R. M. Park, *Appl. Phys. Lett.* **57**, 1040 (1990).
- ² J. Chen, J. M. Fernandez, J. C. P. Chang, K. L. Kavanagh, and H. H. Wieder, *Semicond. Sci. Technol.* **7**, 601 (1992).
- ³ F. K. LeGoues, B. S. Meyerson, J. F. Morar, and P. D. Kirchner, *J. Appl. Phys.* **71**, 4230 (1992).
- ⁴ A. Fischer-Colbrie, R. D. Jacowitz, and D. G. Ast, *Conference Abstract of the 7th International Conference of Molecular Beam Epitaxy*, We 1.12, Stuttgart, Germany, 1992.
- ⁵ T. P. Chin, J. C. P. Chang, K. L. Kavanagh, C. W. Tu, P. D. Kirchner, and J. M. Woodall *Appl. Phys. Lett.* **62**, 2369 (1993).
- ⁶ S. M. Lord, B. Pezeshki, A. F. Marshall, J. S. Harris, Jr., R. Fernandez, and A. Harwit, *Mater. Res. Soc. Symp. Proc.* (1993).
- ⁷ T. P. Chin, B. W. Liang, H. Q. Hou, M. C. Ho, C. E. Chang, and C. W. Tu, *Appl. Phys. Lett.* **58**, 254 (1991).
- ⁸ T. P. Chin, B. W. Liang, H. Q. Hou, M. C. Ho, C. E. Chang, and C. W. Tu, *Mater. Res. Soc. Symp. Proc.* **216**, 517 (1991).
- ⁹ J. C. P. Chang and K. L. Kavanagh, *Mater. Res. Soc. Symp. Proc.* **263** (1992).
- ¹⁰ K. H. Chang, R. Gibala, D. J. Srolovitz, P. K. Bhattacharya, and J. F. Mansfield, *J. Appl. Phys.* **67**, 4093 (1990).
- ¹¹ K.-H. Hellwege, ed., *Landolt-Börnstein: Numerical Data and Functional Relationships in Science and Technology, New Series* (Springer, Berlin, Heidelberg, New York, 1982), Vol. 17, p. 281.
- ¹² M. Razeghi, *Prog. Cryst. Growth and Charact.* **19**, 21 (1989).
- ¹³ M. Razeghi, R. Blondeau, and J. P. Duchemin, *Inst. Phys. Conf. Ser.* **74**, 679 (1985).

Multiple dislocation loops in linearly graded $\text{In}_x\text{Ga}_{1-x}\text{As}$ ($0 \leq x \leq 0.53$) on GaAs and $\text{In}_x\text{Ga}_{1-x}\text{P}$ ($0 \leq x \leq 0.32$) on GaP

J. C. P. Chang, T. P. Chin, C. W. Tu, and K. L. Kavanagh

Department of Electrical and Computer Engineering, University of California, San Diego, La Jolla, California 92093-0407

(Received 16 February 1993; accepted for publication 11 May 1993)

We report transmission electron microscopy studies of dislocation structures in two lattice-mismatched III-V systems, $\text{In}_x\text{Ga}_{1-x}\text{As}$ ($0 \leq x \leq 0.53$)/GaAs and $\text{In}_x\text{Ga}_{1-x}\text{P}$ ($0 \leq x \leq 0.32$)/GaP, grown by gas-source molecular beam epitaxy. Multiple dislocation-loops, extending from within a linearly graded buffer layer to deep inside the substrate, were observed in both systems. All dislocations in each set of loops consisted of 60° dislocations with the same Burgers vector on a similar $\{111\}$ glide plane. The density in the graded buffer and the substrate was estimated to be $2 \times 10^9/\text{cm}^2$, and their appearance was associated with low threading dislocation densities and good optical quality in material grown on top of the buffer layer, $\text{InP}/\text{In}_{0.53}\text{Ga}_{0.47}\text{As}$ on GaAs or $\text{In}_{0.32}\text{Ga}_{0.68}\text{P}$ on GaP.

Fully relaxed lattice-mismatched semiconductor heterostructures, quantum wells, and superlattices devoid of threading dislocations have been the elusive goal of the international heteroepitaxy community for many years.¹ Recently, an old idea revisited, the use of a linearly or step-graded buffer layer between the substrate and the epilayer has produced some very promising results for large lattice-mismatched systems including $\text{Si}_x\text{Ge}_{1-x}/\text{Si}$,²⁻⁵ $\text{In}_x\text{Ga}_{1-x}\text{As}/\text{GaAs}$,⁵⁻¹⁰ and $\text{In}_{0.8}\text{Ga}_{0.2}\text{As}/\text{InP}$.¹¹ Close to 100% strain relaxation and a reduction in threading dislocation densities to below the detection limit of plan-view transmission electron microscopy (TEM), $10^6/\text{cm}^2$, have been reported. The demonstrated high efficiency of strain relaxation via the use of compositionally graded buffer layers is related to the control of misfit dislocation formation rates in the material. Although some data on dislocation mobilities are available, the dislocation source mechanism is system-dependent and remains unknown or controversial.

In this letter, we describe results from TEM studies of the strain relaxation occurring in the linearly graded buffer layers of two III-V systems, $\text{InP}/\text{In}_{0.53}\text{Ga}_{0.47}\text{As}$ on GaAs and $\text{In}_{0.32}\text{Ga}_{0.68}\text{P}$ on GaP. In both cases, the graded buffer layer resulted in close to 100% relaxation of the large compressive strain between the surface epilayer and the substrate, 3.8% for $\text{In}_{0.53}\text{Ga}_{0.47}\text{As}/\text{GaAs}$ and 2.5% for $\text{In}_{0.32}\text{Ga}_{0.68}\text{P}/\text{GaP}$. Unusual dislocation structures involving multiple dislocation loops (5–15) extending from within the graded buffer layer to deep inside the substrate were observed, similar to findings in compositionally graded $\text{Si}_x\text{Ge}_{1-x}/\text{Si}$.^{4,5} However, unlike SiGe ,¹² we observed fewer identifiable multiple loops in step graded buffer layers as compared to linearly graded material, suggesting that their formation may be dependent upon the composition step size.

Samples were grown on GaAs (001)¹³ or GaP (001)¹⁴ substrates by gas-source molecular-beam epitaxy (GSMBE)¹⁵ using elemental group-III effusion cells and thermally cracked arsine and phosphine. A compositionally linear-graded $\text{In}_x\text{Ga}_{1-x}\text{As}$ ($0 \leq x \leq 0.53$) or $\text{In}_x\text{Ga}_{1-x}\text{P}$ ($0 \leq x \leq 0.32$) buffer layer was grown first on the substrate,

GaAs or GaP, respectively, followed by a 0.5–1- μm -thick uniform composition layer grown on the graded buffer layer. The grading rate was about 2%-mismatch/ μm , or 26.5% and 25% $\text{In}/\mu\text{m}$ for $\text{In}_x\text{Ga}_{1-x}\text{As}$ and $\text{In}_x\text{Ga}_{1-x}\text{P}$, respectively. Four single quantum wells, consisting of 2-, 5-, 10-, and 20-nm-thick $\text{In}_{0.53}\text{Ga}_{0.47}\text{As}$ wells separated by 50-nm-thick InP barrier layers, were grown on top of the uniform $\text{In}_{0.53}\text{Ga}_{0.47}\text{As}$ layer for the evaluation of the optical properties. The narrowest well was grown nearest the surface. To compare linear grading with step grading, $\text{In}_{0.32}\text{Ga}_{0.68}\text{P}$ samples were grown on a four-step graded $\text{In}_x\text{Ga}_{1-x}\text{P}$ buffer layer (8% indium per step) on GaP. The grading rate, growth temperature variation, and total buffer layer thickness (1.2 μm) were the same as for the linearly graded sample. The perfection in the composition control was limited by the accuracy of the reflection high-energy electron diffraction (RHEED) oscillations. The actual indium composition of the nominal $\text{In}_{0.53}\text{Ga}_{0.47}\text{As}$ sample was $x=0.52$ as measured by photoluminescence (PL) and high-resolution x-ray diffraction (HRXD). Analysis of (224) and (004) reflections⁶ indicated complete relaxation of both the $\text{In}_{0.53}\text{Ga}_{0.47}\text{As}$ and $\text{In}_{0.32}\text{Ga}_{0.68}\text{P}$ surface layers. Other details of the growth, RHEED, and PL measurements will be published elsewhere.^{13,14}

The samples for cross-sectional TEM (XTEM) were prepared by standard Ar ion-thinning techniques. All TEM work was carried out using a Philips CM30 at a 300 kV operating voltage. Figure 1 shows a set of XTEM micrographs of the InGaAs sample first viewed in the $[110]$ direction (a), and then tilted by (b) 30° around the $[\bar{1}10]$ axis, and (c) 40° around the $[001]$ axis. The most striking feature is the presence of a 15 dislocation loops extending from the graded buffer layer to deep inside the substrate. The deepest loop observed penetrates into the substrate 2.5 μm . The dislocations clearly originate from a location within the graded layer, 0.4 μm above the buffer/substrate interface.

A Burgers vector analysis of the dislocations in Fig. 1 is shown in Fig. 2 using (a) g_{220} , (b) $g_{1\bar{1}1}$, (c) g_{004} , and (d) $g_{\bar{1}11}$ two-beam conditions. For every dislocation, a significantly reduced contrast occurs for the $g_{\bar{1}11}$ reflection

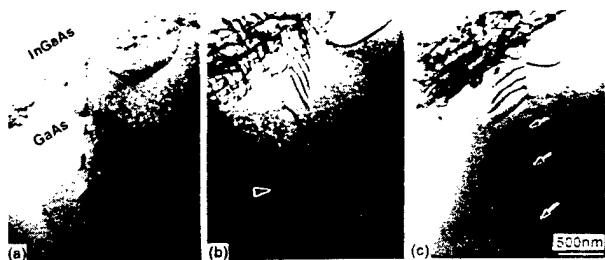


FIG. 1. [110] cross-sectional transmission electron micrographs of a linearly graded $\text{In}_x\text{Ga}_{1-x}\text{As}$ ($0 < x < 0.53$) layer grown on GaAs showing 11 dislocations inside the substrate with the sample (a) viewed in exact [110], (b) tilted by 30° about the $[110]$ axis, and (c) tilted by 40° about the $[001]$ axis. The arrows indicate dislocations at the bottom of the pileup.

[Fig. 2(d)], consistent with 60° dislocations with Burgers vectors \mathbf{b} equal to $\frac{1}{2}[\bar{1}01]$ and with a $(\bar{1}11)$ glide plane. We notice that a large dislocation loop with a $[1\bar{1}0]$ line direction located on the right side of this pileup (marked S in Fig. 2) disappears even more completely for $g_{\bar{1}11}$. This dislocation loop also has a Burgers vector equal to $\frac{1}{2}[\bar{1}01]$, but its glide plane is (111) . A fulfillment of the invisibility criteria $\mathbf{g} \cdot \mathbf{b} = 0$ but not the $\mathbf{g} \cdot (\mathbf{b} \times \mathbf{u}) = 0$ criteria, where \mathbf{u} is a unit vector in the dislocation line direction, is primarily responsible for the remaining visibility of these mixed screw- and edge-type dislocations.

Multiple dislocation loops deep inside the substrate or in the graded layer without penetration into the substrate were frequently seen in the thin areas of the TEM specimens. Other examples from the linearly graded $\text{In}_x\text{Ga}_{1-x}\text{As}$ sample are shown in Fig. 3, where two sets of multiple loops are visible $2.5 \mu\text{m}$ apart deep inside the

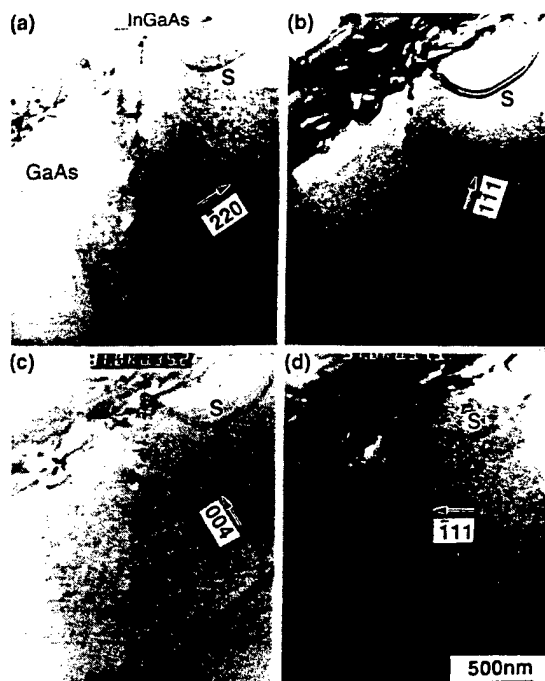


FIG. 2. A Burgers vector analysis of one set of dislocation loops and a single loop (marked S) next to them in the GaAs substrate: (a) g_{220} ; (b) g_{111} ; (c) g_{004} ; (d) g_{111} . For every dislocation, a significantly reduced contrast occurs for the g_{111} reflection.

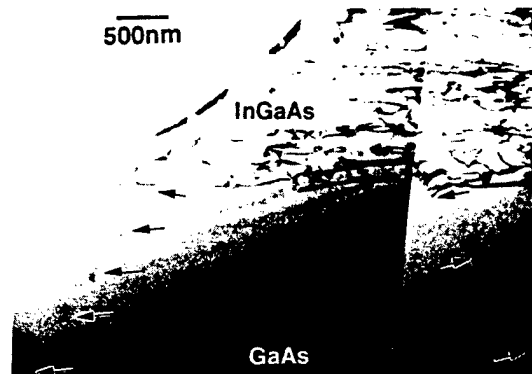


FIG. 3. A [110] cross-sectional transmission electron micrograph of a linearly graded $\text{In}_x\text{Ga}_{1-x}\text{As}$ ($0 < x < 0.53$) layer grown on GaAs showing two sets of dislocation loops deep inside the GaAs substrate.

GaAs substrate. The one with five loops aligned along the $[101]$ direction apparently formed by glide on a $(11\bar{1})$ plane, and the other one with three loops aligned along the $[01\bar{1}]$ direction formed by glide on a (111) plane. A rough estimate of the density of multiple loop structures in the graded region and substrate is $2 \times 10^9/\text{cm}^2$.

The $0.5\text{-}\mu\text{m}$ -thick $\text{In}_{0.52}\text{Ga}_{0.48}\text{As}$ layer, grown on the graded $\text{In}_x\text{Ga}_{1-x}\text{As}$ buffer layer on GaAs, had no threading dislocations detected within the resolution of plan-view (TEM), which is about $10^6/\text{cm}^2$. However, misfit dislocations with density $\approx 6 \times 10^4/\text{cm}$ running only in the $[110]$ direction were observed at the $\text{InP}/\text{In}_{0.52}\text{Ga}_{0.48}\text{As}$ interface. This is not surprising since the actual In composition was slightly off the lattice-matched target composition $x = 0.53$. Extra dislocations generated at this interface were observed to thread into the bottom two quantum wells (20 and 10 nm) resulting in a dislocation density of $2 \times 10^4/\text{cm}$ and $1 \times 10^3/\text{cm}$, respectively. Nevertheless, no threading dislocations were observed in the top two wells (2 and 5 nm wide). The perfection of the structural properties of these two quantum wells was supported by their optical properties.¹³ The intensities and linewidths of their excitonic peaks are comparable to similar structures grown lattice matched on an InP substrate.¹³

Multiple dislocation loops were also detected in the InGaP/GaP lattice-mismatched system, as shown in the TEM micrograph of Fig. 4. In this example, five loops are observed in the GaP substrate. Moreover, double sets of multiple loops,^{4,5,16} i.e., adjacent multiple loops on the (111) and the $(\bar{1}11)$ planes, are repeatedly seen in the graded region extending from the top, $x = 0.29$ region, to the lower part of the buffer and sometimes to the substrate. As the micrograph shows, no threading dislocations are visible in the uniform, $1.5\text{-}\mu\text{m}$ -thick, $\text{In}_{0.32}\text{Ga}_{0.68}\text{P}$ surface layer grown on top. Plan-view TEM indicated a threading dislocation density of less than $2 \times 10^6 \text{ cm}^{-2}$. Green light-emitting diodes (LED) (560 nm) with good rectifying and high reverse-breakdown characteristics ($\sim -16 \text{ V}$) at room temperature were fabricated with this material.¹⁴

XTEM of $\text{In}_{0.32}\text{Ga}_{0.68}\text{P}$ samples grown with a step-graded buffer layer showed a rough, textured surface

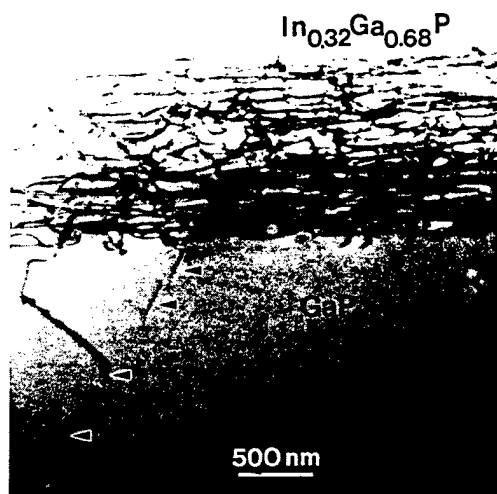


FIG. 4. A [110] cross-sectional transmission electron micrograph of a uniform $\text{In}_{0.32}\text{Ga}_{0.68}\text{P}$ layer grown on a linearly graded $\text{In}_x\text{Ga}_{1-x}\text{P}$ layer on GaP.

(wavelength ~ 50 nm) and no PL response at room temperature. Tangled dislocations were observed inside the step-graded buffer and isolated dislocation half-loops were found in the substrate. No multiple dislocation loops were detected either in the substrate or in the graded region. The top $\text{In}_{0.32}\text{Ga}_{0.68}\text{P}$ layer was highly defective with many threading dislocations, densities $\sim 3 \times 10^9/\text{cm}^2$. However, the presence of multiple loops is not a necessary condition for low threading dislocation densities. No multiple loops were observed in a three-step, step-graded $\text{In}_x\text{Ga}_{1-x}\text{As}$ buffer layer ($\Delta x = 0.1$ per step, each step $0.3 \mu\text{m}$ thick) on GaAs grown by solid-source MBE in a second system.^{6,7} Yet, the surface $\text{In}_{0.3}\text{Ga}_{0.7}\text{As}$ epilayer also had a low threading dislocation densities detected.^{6,7} Multiple loop formation is apparently inhibited by large composition steps.

Single loops both 60° and edge type apparently generated by strain relaxation in the surface epilayer are a common occurrence at lattice-mismatched interfaces.¹⁷ Reports of multiple dislocation loops in the substrate are much less common. Our results from a linearly graded buffer are very similar to those described in $\text{In}_{0.15}\text{Ga}_{0.85}\text{As}/\text{GaAs}$ strained-layer superlattices by Lefebvre and co-workers^{18,19} and also in the SiGe/Si system by LeGoues *et al.*¹⁶ Both groups have proposed that the multiple loops form by a type of Frank-Read mechanism²⁰ operating from a reaction between crossed misfit dislocations. LeGoues and co-workers further emphasize that a Frank-Read mechanism acts as a multiplication source for new misfit dislocations with the multiple loops as by-products.^{4,5,16} In our samples, we find that many multiple

loops occur inside the graded layer far above the initial interface without penetration into the substrate. Whatever the mechanism of formation, it operates at any time during the growth of the graded layer and does not necessarily require the introduction of dislocations into the substrate.

In conclusion, we have observed multiple dislocation loops, extending from within a linearly graded buffer layer to deep inside the substrate, occurring in two lattice mismatched III-V systems: $\text{In}_x\text{Ga}_{1-x}\text{As}$ ($0 < x < 0.53$)/GaAs and $\text{In}_x\text{Ga}_{1-x}\text{P}$ ($0 < x < 0.32$)/GaP. All dislocations in each set of loops consist of 60° dislocations with the same Burgers vector gliding on similar $\{111\}$ planes. Correlated with their appearance in the sample was a low threading dislocation density and good optical properties in epilayers grown on the surface, $\text{InP}/\text{In}_{0.53}\text{Ga}_{0.47}\text{As}$ on GaAs or $\text{In}_{0.32}\text{Ga}_{0.68}\text{P}$ on GaP. The multiple loops were sensitive to the composition step size, as we do not observe them in step-graded material of the same grading rate.

This work was supported in part by NSF (PYIDMR-9157714) and the Office of Naval Research.

- ¹ E. G. Bauer, D. J. Ehrlich, L. C. Feldman, C. P. Flynn, M. W. Geis, J. P. Harbison, R. J. Matyi, P. S. Peercy, P. M. Petroff, J. M. Philips, G. B. Stringfellow, and A. Zangwill, *J. Mater. Res.* **5**, 852 (1990).
- ² E. A. Fitzgerald, Y.-H. Xie, M. L. Green, D. Brasen, A. R. Kortan, J. Michel, Y.-J. Mii, and B. E. Weir, *Appl. Phys. Lett.* **59**, 811 (1991).
- ³ E. A. Fitzgerald, Y. H. Xie, D. Monroe, P. J. Silerman, J. M. Kuo, A. R. Kortan, F. A. Thiel, and B. E. Weir, *J. Vac. Sci. Technol.* **10**, 1807 (1992).
- ⁴ F. K. LeGoues, B. S. Meyerson, and J. F. Morar, *Phys. Rev. Lett.* **66**, 2903 (1991).
- ⁵ F. K. LeGoues, B. S. Meyerson, J. F. Morar, and P. D. Kirchner, *J. Appl. Phys.* **71**, 4230 (1992).
- ⁶ J. C. P. Chang, J. Chen, J. M. Fernandez, H. H. Wieder, and K. L. Kavanagh, *Appl. Phys. Lett.* **60**, 1129 (1992).
- ⁷ K. L. Kavanagh, J. C. P. Chang, J. Chen, J. M. Fernandez, and H. H. Wieder, *J. Vac. Sci. Technol. B* **10**, 1820 (1992).
- ⁸ V. Krishnamoorthy, Y. W. Lin, and R. M. Park, *J. Appl. Phys.* **72**, 1752 (1992).
- ⁹ K. Chang, P. Bhattacharya, and R. Lai, *J. Appl. Phys.* **67**, 3323 (1990).
- ¹⁰ S. M. Lord, B. Pezeshki, S. D. Kim, and J. S. Harris, Jr., *J. Cryst. Growth* **127**, 759 (1993).
- ¹¹ A. Fischer-Colbrie, R. D. Jacowitz, and D. G. Ast, *J. Cryst. Growth* **127**, 560 (1993).
- ¹² F. K. LeGoues, private communication.
- ¹³ T. P. Chin and C. W. Tu, *Appl. Phys. Lett.* **62**, 2708 (1993).
- ¹⁴ T. P. Chin, J. C. P. Chang, K. L. Kavanagh, C. W. Tu, P. D. Kirchner, and J. M. Woodall, *Appl. Phys. Lett.* **62**, 2369 (1993).
- ¹⁵ T. P. Chin, B. W. Liang, H. Q. Hou, M. C. Ho, C. E. Chang, and C. W. Tu, *Appl. Phys. Lett.* **58**, 254 (1991).
- ¹⁶ F. K. LeGoues, J. A. Ott, K. Eberl, and S. S. Iyer, *Appl. Phys. Lett.* **61**, 174 (1992).
- ¹⁷ E. A. Fitzgerald, D. G. Ast, P. D. Kirchner, G. D. Pettit, and J. M. Woodall, *J. Appl. Phys.* **63**, 693 (1988).
- ¹⁸ A. Lefebvre, C. Herbeaux, and J. Di Persio, *Philos. Mag. A* **63**, 471 (1991).
- ¹⁹ A. Lefebvre, C. Herbeaux, C. Bouiller, and J. Di Persio, *Philos. Mag. Lett.* **63**, 23 (1991).
- ²⁰ J. P. Hirth and J. Lothe, in *Theory of Dislocations*, 2nd ed. (Wiley, New York, 1982).

InGaAs/InP and InAsP/InP quantum well structures on GaAs (100) with a linearly graded InGaP buffer layer grown by gas-source molecular beam epitaxy

T. P. Chin,^{a)} H. Q. Hou,^{b)} and C. W. Tu

Department of Electrical and Computer Engineering, University of California, San Diego, La Jolla, California 92093-0407

J. C. P. Chang and N. Otsuka

School of Materials Engineering, Purdue University, West Lafayette, Indiana 47907

(Received 20 December 1993; accepted for publication 21 January 1994)

A linearly graded $\text{In}_x\text{Ga}_{1-x}\text{P}$ ($x=0.48-1$) buffer layer is used for growing a high-quality InP layer on a GaAs substrate. We show that an $\text{In}_x\text{Ga}_{1-x}\text{P}$ buffer layer is superior to an $\text{In}_y\text{Ga}_{1-y}\text{As}$ buffer layer because it is transparent to long wavelengths and allows a less stringent composition control. InGaAs/InP single quantum wells and InAsP/InP multiple quantum wells grown on the InP/ $\text{In}_x\text{Ga}_{1-x}\text{P}$ /GaAs substrate show comparable quality to similar structures grown on InP (100) substrates. Photocurrent spectra for the latter exhibit quantum-confined Stark effect near $1.3\text{ }\mu\text{m}$.

Recently, linearly graded buffer layers have been re-examined for growing device-quality semiconductor materials on highly mismatched substrates.¹⁻⁷ We have reported good results using a linearly graded $\text{In}_y\text{Ga}_{1-y}\text{As}$ ($y=0-0.53$) buffer layer for growing InP on a GaAs substrate.^{6,7} However, the $2\text{-}\mu\text{m}$ -thick $\text{In}_y\text{Ga}_{1-y}\text{As}$ buffer layer in the InP/ $\text{In}_y\text{Ga}_{1-y}\text{As}$ /GaAs system is not transparent to long wavelengths from InP-based devices. We also observed that misfit dislocations may occur at the InP/ $\text{In}_{0.53}\text{Ga}_{0.47}\text{As}$ (nominal composition) interface if the composition control is not accurate.^{6,7}

In this letter, we report the use of a linearly graded $\text{In}_x\text{Ga}_{1-x}\text{P}$ ($x=0.48-1$) buffer layer to grow InP on GaAs by gas-source molecular beam epitaxy (GSMBE). Similar to the InP/InGaAs/GaAs system, this structure is compressively strained. However, since $\text{In}_x\text{Ga}_{1-x}\text{P}$ has a larger bandgap than InP for all composition x , a fully transparent pseudosubstrate can be achieved. Furthermore, no composition control problem exists in this system since the transition between the top of the buffer layer ($\text{In}_x\text{Ga}_{1-x}\text{P}$, $x\rightarrow 1$) and the InP layer can be very smooth. InGaAs/InP single quantum wells (SQWs) and InAsP/InP multiple quantum wells (MQWs) were grown and characterized. Photocurrent spectra of an InAsP/InP MQW structure show absorption modulation at $1.3\text{ }\mu\text{m}$, which demonstrates the effectiveness of the $\text{In}_x\text{Ga}_{1-x}\text{P}$ buffer layer.

Samples were grown on exactly oriented GaAs (100) substrates in a modified Intevac modular Gen-II MBE system. Pure hydrides were thermally cracked as group-V sources. To achieve a linear indium composition profile ($x=0.48-1$), the indium cell temperature was kept constant and the gallium cell temperature was decreased gradually. The growth rate of $\text{In}_{0.48}\text{Ga}_{0.52}\text{P}$ was about 1.6 monolayers/s . The total thickness of the graded buffer layer was $2\text{ }\mu\text{m}$, corresponding to a gradient of roughly 2% mismatch/ μm .

The substrate temperature was decreased linearly from 580 to $480\text{ }^\circ\text{C}$. Then another layer of InP ($0.5-1\text{ }\mu\text{m}$ thick), grown at $480\text{ }^\circ\text{C}$, was then used as a substrate for further growth.

Reflection high-energy electron diffraction (RHEED) pattern was monitored during growth. Streaky patterns of a reconstructed surface were observed through the graded $\text{In}_x\text{Ga}_{1-x}\text{P}$ buffer layer the top InP. RHEED intensity oscillations on the InP surface were recorded, as shown in Fig. 1. The RHEED results indicate that the growth of the highly mismatched $\text{In}_x\text{Ga}_{1-x}\text{P}$ and InP on GaAs was kept in a two-dimensional growth mode, which is similar to our previous InP/ $\text{In}_y\text{Ga}_{1-y}\text{As}$ /GaAs work.^{6,7} Cross hatches along both (011) directions, which have been widely observed in strain-relaxed layers, were observed under a Nomarski phase-contrast microscope. (400) and (422) x-ray rocking curves were measured, and the top InP layers were found to be fully

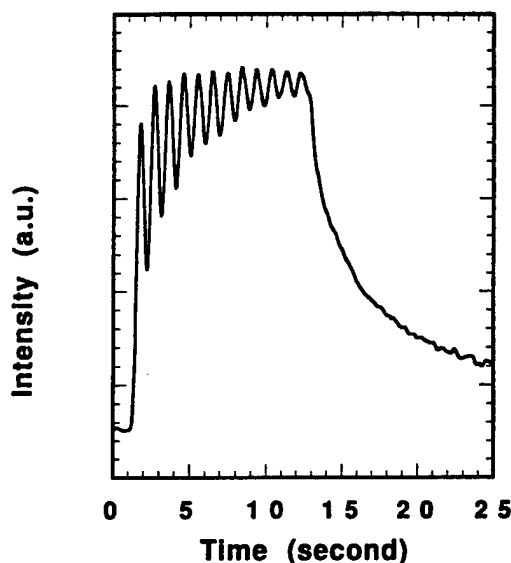


FIG. 1. RHEED oscillations of InP grown on GaAs with a linear-graded $\text{In}_x\text{Ga}_{1-x}\text{P}$ buffer layer.

^{a)}Present address: School of Electrical Engineering, Purdue University, West Lafayette, IN 47907.

^{b)}Present address: AT&T Bell Laboratories, Holmdel, NJ 07733.

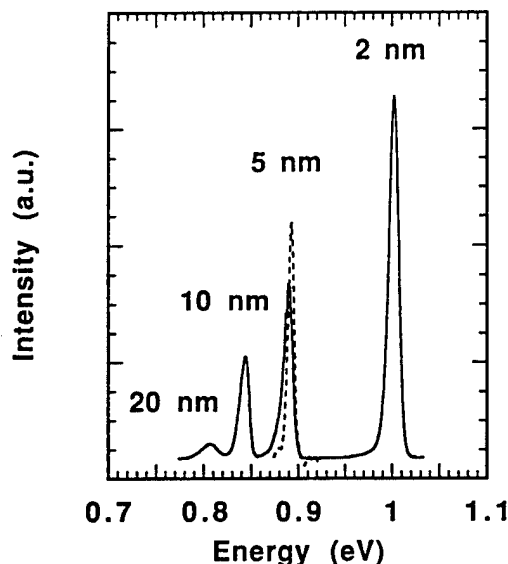


FIG. 2. 10 K PL spectra of an InGaAs/InP SQW structure grown on an InP/In_xGa_{1-x}P/GaAs substrate. The dashed curve is for a similar structure grown on an InP substrate. The two spectra are normalized to the same unit.

relaxed in the two perpendicular [110] directions, indicating that the In_xGa_{1-x}P buffer layer is effective in relieving the strain due to lattice mismatch between InP and GaAs.

To obtain a qualitative assessment of the InP layer, we grew an In_{0.53}Ga_{0.47}As/InP four-SQW structure on this pseudosubstrate and characterized it by low-temperature photoluminescence (PL) spectroscopy and [011] cross-sectional transmission electron microscopy (XTEM). As shown in Fig. 2, emission peaks from the four wells are well resolved and the peak intensities are strong. The PL line width at 10 K of a 5-nm-wide is 11 meV, which is comparable to the values measured from similar structures grown lattice matched on an InP substrate (7 meV, dashed curve) or on an InP/In_yGa_{1-y}As/GaAs pseudosubstrate (10 meV) by the same GSMBE system. Figure 3(a) is a (200) dark-field XTEM image of the SQWs structure. In the graded In_xGa_{1-x}P buffer layer we see an unusual dislocation structure⁷ consisting of a double set of multiple dislocation-loops glide on two different {111} planes. Surprisingly, unlike the case of graded In_yGa_{1-y}As/GaAs and In_zGa_{1-z}P/GaP,⁷ no dislocation loops are observed in the first 200 nm of the In_xGa_{1-x}P layer nor in the GaAs substrate, as shown in Fig. 3(b). More study of this phenomenon is underway. Dislocations are well confined within the graded In_xGa_{1-x}P buffer layer and no threading dislocations are observed in the top InP layer and the SQW structure within the sensitivity of XTEM. High resolution TEM images show the In_{0.53}Ga_{0.47}As-on-InP interface is atomically smooth with 1–2 monolayer roughness.

Recently, Hou *et al.* demonstrated that InAsP/InP is a promising alternative material system for obtaining 1.3 μm devices.^{8,9} A 10-period InAsP/InP (100 Å/150 Å) MQW *p-i-n* structure was grown on an InP/In_xGa_{1-x}P/GaAs substrate. The room-temperature, zero-volt photocurrent spectrum of this diode, with the light shined through the back [Fig. 4(a)], is comparable to that of the control sample [Fig.

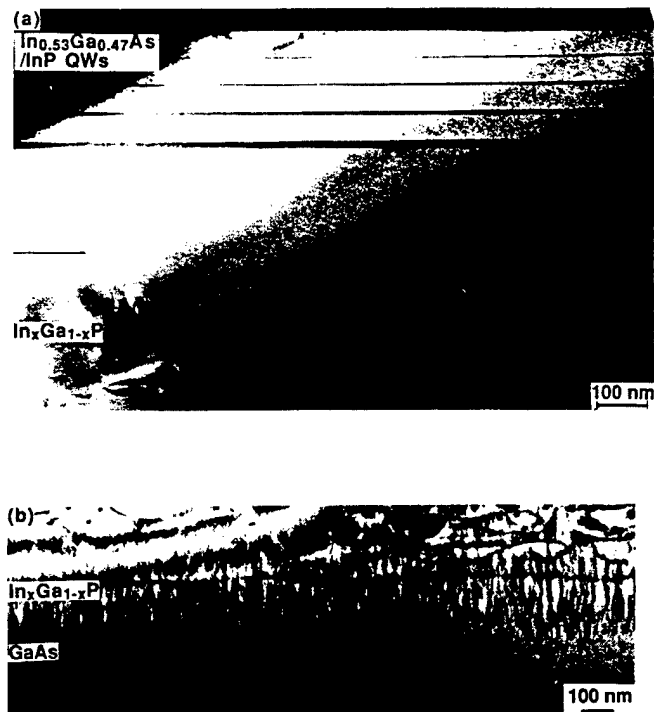


FIG. 3. (a) A (200) dark-field XTEM image of the In_{0.53}Ga_{0.47}As/InP SQW structure grown on an InP/In_xGa_{1-x}P/GaAs buffer layer. The In_{0.53}Ga_{0.47}As well layers appear darker than the InP barrier layers. (b) A (022) bright-field XTEM image of the interface between the graded In_xGa_{1-x}P buffer layer and the GaAs substrate. No dislocation loops are seen in the first 200 nm of the In_xGa_{1-x}P layer nor in the GaAs substrate.

4(b)], a similar structure grown directly on an InP substrate. The estimated half-width at half-maximum (HWHM) of these two samples are 12 and 9 meV, respectively. The different peak positions are due to the compositional variation

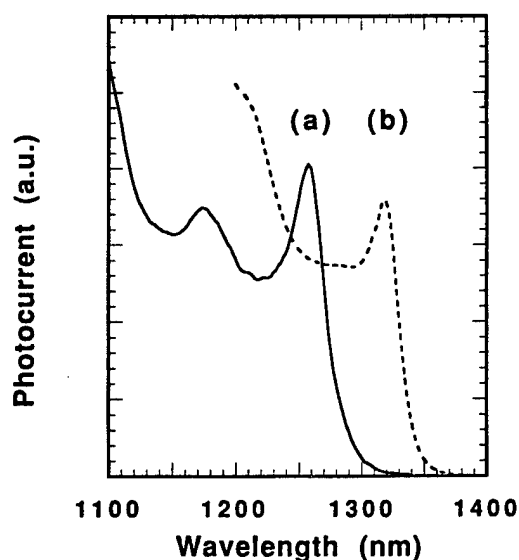


FIG. 4. Zero-volt photocurrent spectra of InAsP/InP MQW structures grown (a) on InP/In_xGa_{1-x}P/GaAs (solid line), and (b) on InP substrates (dashed line).

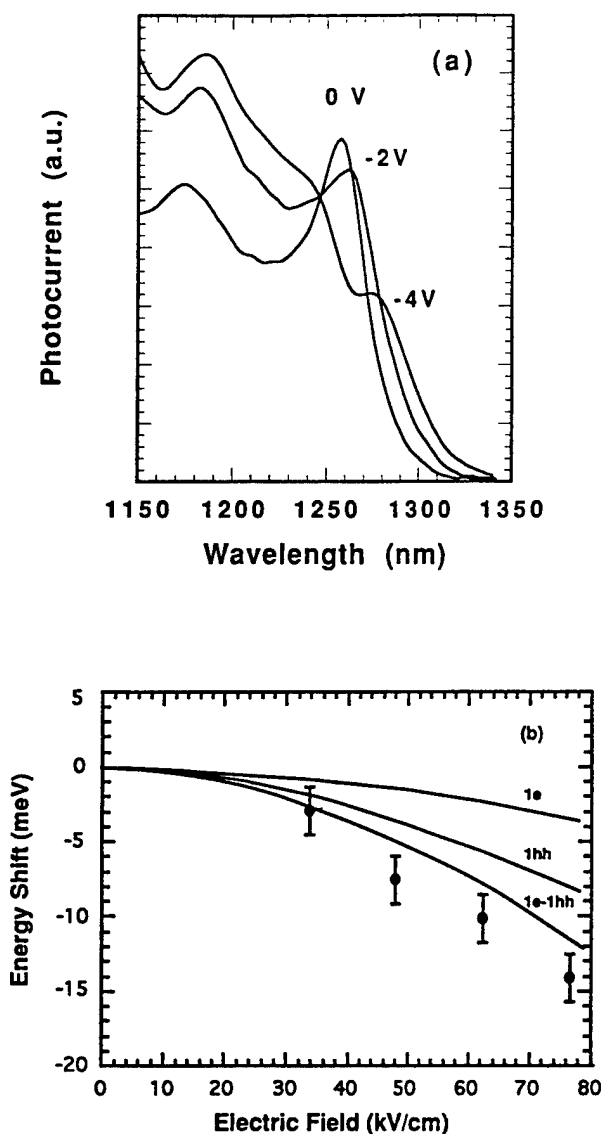


FIG. 5. (a) Photocurrent spectra under reverse bias. Absorption-peak shift due to QCSE is observed. (b) Calculated energy shifts of the electron and heavy hole levels under reverse bias. The summation represents the shift of absorption peak, which is compared with the experimental values (solid circles).

between the two runs. Our results also compare favorably to those reported by Lord *et al.*¹⁰ on a $1.3 \mu\text{m}$ (wavelength) $\text{Al}_{0.33}\text{Ga}_{0.67}\text{As}/\text{In}_{0.5}\text{Ga}_{0.5}\text{As}$ strained MQW structure on a linearly graded $\text{In}_y\text{Ga}_{1-y}\text{As}$ ($y=0-0.35$) buffer layer on a GaAs substrate. In their samples, the HWHM of the exciton absorption peak is 14 meV for a small gradient ($7.5\% \text{ In}/\mu\text{m}$) buffer layer but 21 meV for a large gradient ($30\% \text{ In}/\mu\text{m}$) buffer layer. Although a thicker buffer layer gives better results, the long growth time is not desirable. In our experiment, a narrow linewidth (12 meV) is obtained even with a large gradient ($25\% \text{ In}/\mu\text{m}$).

Figure 5 shows photocurrent spectra of the InAsP/InP

MQW $p-i-n$ structure under reverse bias (up to -4 V). Quantum confined stark effect (QCSE) is observed, which is one of the critical features of optical modulators. The amount of peak shift [Fig. 5(b), solid circles] is consistent with calculated shifts of electron and heavy-hole subbands under reverse bias based on an "effective well width" model.¹² The theoretical calculation and material parameters¹¹⁻¹³ have been discussed in a previous article,⁹ in which the results of InAsP/InP grown on InP were presented. The breakdown voltage of this diode, however, is smaller than the devices grown on InP. A soft breakdown is observed at -5 V , compared to -10 V . Nevertheless, the existence of QCSE in the photocurrent measurements indicates the structure has an appropriate material quality for device applications in the future.

In conclusion, we demonstrate that a linearly graded $\text{In}_x\text{Ga}_{1-x}\text{P}$ buffer layer is effective for obtaining a good-quality InP on GaAs(100). This linearly graded buffer layer successfully decouples the InP epilayer from the GaAs substrate and is superior to the previously reported InP/ $\text{In}_y\text{Ga}_{1-y}\text{As}/\text{GaAs}$ buffer layer. Two-dimensional growth mode was maintained during growth. InGaAs/InP SQWs with PL intensities comparable to those grown lattice matched on InP or InP/ $\text{In}_y\text{Ga}_{1-y}\text{As}/\text{GaAs}$ substrates were obtained. QCSE near $1.3 \mu\text{m}$ in photocurrent spectra was observed on InAsP/InP MQW structures grown on the InP/ $\text{In}_x\text{Ga}_{1-x}\text{P}/\text{GaAs}$ substrates. Our results show that a linearly graded, transparent $\text{In}_x\text{Ga}_{1-x}\text{P}$ buffer layer could be viable for integrating InP-based and GaAs-based devices.

The work at UCSD is partially supported by the Office of Naval Research and the ARPA Optoelectronic Technology Center.

- ¹ E. A. Fitzgerald, Y. H. Xie, D. Monroe, P. J. Silberman, J. M. Kuo, A. R. Kortan, F. A. Thiel, and B. E. Weir, *J. Vac. Sci. Technol. B* **10**, 1807 (1992).
- ² F. K. LeGoues, B. S. Meyerson, J. F. Moror, and P. D. Kirchner, *J. Appl. Phys.* **71**, 4230 (1992).
- ³ S. M. Lord, B. Pezeshki, S. D. Kim, and J. S. Harris, Jr., *J. Cryst. Growth* **127**, 759 (1993).
- ⁴ A. Fischer-Colbrie, R. D. Jacowitz, and D. G. Ast, *J. Cryst. Growth* **127**, 560 (1993).
- ⁵ T. P. Chin, J. C. P. Chang, K. L. Kavanagh, C. W. Tu, P. D. Kirchner, and J. M. Woodall, *Appl. Phys. Lett.* **62**, 2369 (1993).
- ⁶ T. P. Chin and C. W. Tu, *Appl. Phys. Lett.* **62**, 2708 (1993).
- ⁷ J. C. P. Chang, T. P. Chin, C. W. Tu, and K. L. Kavanagh, *Appl. Phys. Lett.* **63**, 500 (1993).
- ⁸ H. Q. Hou and C. W. Tu, *Appl. Phys. Lett.* **60**, 1872 (1992).
- ⁹ H. Q. Hou, A. N. Cheng, H. H. Wieder, W. S. C. Chang, and C. W. Tu, *Appl. Phys. Lett.* **63**, 1833 (1993).
- ¹⁰ S. M. Lord, A. F. Marshall, and J. S. Harris, Abstract of the 1993 Electronic Materials Conference, paper A2, p. A1, Univ. of California, Santa Barbara, June 23-25, 1993.
- ¹¹ D. A. B. Miller, D. S. Chemla, T. C. Damen, A. C. Gossard, W. Wiegmann, T. H. Wood, and C. A. Burrus, *Phys. Rev. B* **32**, 1043 (1985).
- ¹² S. J. Hwang, W. Shan, J. J. Song, H. Q. Hou, and C. W. Tu, *J. Appl. Phys.* **72**, 1645 (1992).
- ¹³ K.-H. Hellwege, Ed., *Landolt-Börnstein: Numerical Data and Functional Relationships in Science and Technology, New Series* (Springer, Berlin, Heidelberg, New York, 1986), Vol. 22a.

APPENDIX

C

List of Publications

Appendix C List of Publications

1. T.P. Chin, B.W. Liang, H.Q. Hou, M.C. Ho, C.E. Chang, and C.W. Tu, "Determination of surface V/III ratios of phosphide growth in gas-source molecular-beam epitaxy," *Appl. Phys. Lett.* **58**, 254-256 (1991).
2. C.E. Chang, T.P. Chin, and C.W. Tu, "A differential reflection high energy electron diffraction measurement system," *Rev. Sci. Instrum.* **62** (3), 655-659 (Mar. 1991).
3. J.C.P. Chang, T.P. Chin, K.L. Kavanagh, and C.W. Tu, "High-resolution x-ray diffraction of InAlAs/InP superlattices grown by gas-source molecular-beam epitaxy," *Appl. Phys. Lett.* **58** (14), 1530-1533 (1991).
4. H.Q. Hou, B.W. Liang, T.P. Chin, and C.W. Tu, "In situ determination of phosphorus composition in GaAs_{1-x}P_x grown by gas-source molecular beam epitaxy," *Appl. Phys. Lett.* **59** (3), 292-294 (15 July 1991).
5. H.Q. Hou, C.W. Tu, and S.N.G. Chu, "Gas-source molecular beam epitaxy growth of highly strained device quality InAsP/InP multiple quantum well structures," *Appl. Phys. Lett.* **58**, 2954-2956 (1991).
6. T.P. Chin, B.W. Liang, H.Q. Hou, and C.W. Tu, "Reflection high-energy-electron diffraction study of InP and InAs (100) in gas-source molecular beam epitaxy," *Mater. Res. Soc. Symp. Proc.* **216**, 517-522 (1990).
7. B.W. Liang, H.Q. Hou, and C.W. Tu, "Study of As and P incorporation behavior in GaAsP by gas-source molecular beam epitaxy," *Mater. Res. Soc. Symp. Proc.*, (1991).
8. T.P. Chin, P.D. Kirchner, G.D. Pettit, and J.M. Woodall, "Highly carbon-doped p-type Ga_{0.5}In_{0.5}As and Ga_{0.5}In_{0.5}P by carbon tetrachloride in gas-source molecular beam epitaxy," *Appl. Phys. Lett.* **59**, 865 (1991).
9. H.Q. Hou, T.P. Chin, B.W. Liang, and C.W. Tu, "Modulator structure using In(As,P)/InP strained multiple quantum wells grown by gas-source MBE," *Mat. Res. Soc. Symp. Proc.* **228**, 231-236 (1992).
10. C.W. Tu, B.W. Liang, J. Moore, H.Q. Hou, T.P. Chin, and M.C. Ho, "Comparison of various versions of molecular beam epitaxy for large-area deposition of III-V device structures," *Electrochem. Soc. Proc, Large Area/Scale Epitaxy for III-V Device Fabrication* **91-13**, 13-22 (1991).
11. H.Q. Hou and C.W. Tu, "Growth of GaAs_{1-x}P_x/GaAs and InAs_xP_{1-x}/InP strained quantum wells for optoelectronic devices by gas-source molecular-beam epitaxy," *J. Electronic Mater.* **21**, (2), 137-141 (1992).
12. H.Q. Hou, B.W. Liang, M.C. Ho, T.P. Chin, and C.W. Tu, "Growth studies of GaAs_{1-x}P_x in gas-source molecular beam epitaxy," *J. Vac. Sci. Technol.B*, 953-955 (1992).

13. H.Q. Hou and C.W. Tu, "InGaAsP/InP multiple quantum wells grown by gas-source molecular beam epitaxy," *J. Crystal Growth* **120**, 167-171 (1992).
14. M.C. Ho, Y. He, T.P. Chin, B.W. Liang, and C.W. Tu, "Enhancement of effective Schottky barrier height on n-type InP," *Electronics Lett.* **28**, (1), 68-71 (2 Jan. 1992).
15. H.Q. Hou, B.W. Liang, M.C. Ho, T.P. Chin, and C.W. Tu, "Growth studies of GaAsP in gas-source molecular beam epitaxy," *J. Vac. Sci. Technol. B* **10**, (2), 953-955 (Mar/Apr 1992).
16. X.Yin, Xinxin Guo, F.H. Pollack, G.D. Pettit, J.M. Woodall, T.P. Chin, and C.W. Tu, "Nature of band bending at semiconductor surfaces by contactless electroreflectance," *Appl. Phys. Lett.* **60**, (11), 1336-1338 (16 Mar. 1992).
17. H.Q. Hou and C.W. Tu, "In situ control of As composition in InAsP and InGaAsP grown by gas-source molecular beam epitaxy," *Appl. Phys. Lett.* **60**, (15), 1872-1874 (13 Apr. 1992).
18. B.W. Liang and C.W. Tu, "A study of group-V desorption from GaAs, GaP, InP and InAs by reflection high-energy electron diffraction," *J. Cryst. Growth* **128**, 538-542, (March 1993).
19. R.C. Gee, T.P. Chin, C.W. Tu, P.M. Asbeck, C.L. Lin, P.D. Kirchner, and J.M. Woodall, "InP/InGaAs heterojunction bipolar transistors grown by gas-source molecular beam epitaxy with carbon-doped base," *IEEE Trans. Electron Device Lett.* **13** (5), 247-249 (May 1992).
20. Y. He, B.W. Liang, N.C. Tien, and C.W. Tu, "Selective Chemical Etching of InP Over InAlAs," *J. Electrochem. Soc.* **139** (7), 2046-2048 (July 1992).
21. B.W. Liang and C.W. Tu, "A study of group-V desorption from GaAs and GaP by reflection high-energy electron diffraction in gas-source molecular beam epitaxy," *J. Appl. Phys.* **72** (7), 2806-2809 (1 October 1992).
22. S.J. Hwang, W. Shan, J.J. Song, H.Q. Hou, and C.W. Tu, "Interband transitions in InAs_xP_{1-x}/InP strained multiple quantum wells" *J. Appl. Phys.* **72** (4), pp. 1645-1647 (15 August 1992).
23. B.W. Liang and C.W. Tu, "A study of group-V desorption from GaAs and GaP by reflection high-energy electron diffraction in gas-source molecular beam epitaxy" *J. Appl. Phys.* **72** (7), pp. 2806-2809 (1 October 1992).
24. H.Q. Hou and C.W. Tu, "Homoepitaxial growth of InP on (111)B substrates by gas-source molecular beam epitaxy" *Appl. Phys. Lett.* **62**, pp. 281-283 (18 January 1993).
25. H.Q. Hou and C.W. Tu, "InP and InAsP/InP heterostructures grown on InP (111)B substrates by gas-source molecular beam epitaxy" *J. Crystal Growth* **127**, pp. 199-203 (February 1993).

26. B.W. Liang and C. W. Tu, "A study of group-V element desorption from InAs, InP, GaAs and GaP by reflection high-energy electron diffraction" *J. Crystal Growth* **128**, pp. 538-542 (March 1993).
27. C.W. Tu, B.W. Liang, and H.Q. Hou, "Growth kinetics and in situ composition determination of mixed-group-V compounds grown by gas-source molecular beam epitaxy" *J. Crystal Growth* **127**, pp. 251-254 (April 1993).
28. C.W. Tu (invited), "Carbon-doped p-type $\text{In}_{0.53}\text{Ga}_{0.47}\text{As}$ and its application to InP/ $\text{In}_{0.53}\text{Ga}_{0.47}\text{As}$ heterojunction bipolar transistors" *Proc. of 5th International Conf. on Indium Phosphide and Related Materials* pp. 695-698 (April 19-22, 1993).
29. W. Shan, S.J. Hwang, J.J. Song, H.Q. Hou, and C.W. Tu, "Valence band offset of $\text{GaAs}/\text{GaAs}_{0.68}\text{P}_{0.32}$ multiple quantum wells" *Appl. Phys. Lett.* **62** (17), pp. 2078-2080 (April 26, 1993).
30. T.P. Chin, J.C.P. Chang, K.L. Kavanagh, C.W. Tu, P.D. Kirchner, and J.M. Woodall, "Gas-source molecular beam epitaxial growth, characterization, and light-emitting diode application of InGaP on GaP (100)" *Appl. Phys. Lett.* **62** (19), pp. 2369-2371 (May 10, 1993).
31. T.P. Chin and C.W. Tu, "Heteroepitaxial growth of InP/ $\text{In}_{0.52}\text{Ga}_{0.48}\text{As}$ structures on GaAs (100) by gas-source molecular beam epitaxy" *Appl. Phys. Lett.* **62** (21), pp. 2708-2710 (May 24, 1993).
32. T.P. Chin, J.C.P. Chang, K.L. Kavanagh, and C.W. Tu, "Growth and characterization of $\text{In}_x\text{Ga}_{1-x}\text{P}$ ($x \leq 0.38$) on GaP(100) with a linearly graded buffer layer by gas-source molecular beam epitaxy" *Mater. Res. Soc. Symp. Proc.* **281**, pp. 227-232 (1993).
33. B.W. Liang and C.W. Tu, "A kinetic model for As and P incorporation behaviors in GaAsP grown by gas-source molecular beam epitaxy" *J. Appl. Phys.* **74** (1), pp. 255-259 (1 July 1993).
34. J.C.P. Chang, T.P. Chin, C.W. Tu, and K.L. Kavanagh, "Multiple dislocation loops in linearly graded $\text{In}_x\text{Ga}_{1-x}\text{As}$ ($0 < x < 0.53$) on GaAs and $\text{In}_x\text{Ga}_{1-x}\text{P}$ ($0 < x < 0.32$) on GaP" *Appl. Phys. Lett.* **63** (4), pp. 500-503 (26 July 1993).
35. H.Q. Hou, A.N. Cheng, H.H. Wieder, W.S.C. Chang, and C.W. Tu, "Electroabsorption of InAsP/InP strained multiple quantum wells for 1.3 μm waveguide modulators" *Appl. Phys. Lett.* **63** (13), pp. 1833-1835 (27 September 1993).
36. C.W. Tu, B.W. Liang, and T.P. Chin, "Heavily carbon-doped p-type GaAs and $\text{In}_{0.53}\text{Ga}_{0.47}\text{As}$ grown by gas-source molecular beam epitaxy using carbon tetrabromide" *J. Crystal Growth*, **136** (1-4), pp. 191-194, (March 1994).
37. H.Q. Hou, C.W. Tu, W. Shan, S.J. Hwang, J.J. Song, and S.N.G. Chu, "Structural and optical characterizations of InAsP/InP strained multiple quantum wells grown on InP (111)B substrates" *J. Vac. Sci. Technol. B* **12** (2), pp. 1116-1118 (March/April 1994).

38. T.P. Chin, H.Q. Hou, C.W. Tu, J.C.P. Chang, and N. Otsuka, "InGaAs/InP and InAsP/InP quantum well structures on GaAs(100) with a linearly graded InGaP buffer layer grown by gas-source molecular beam epitaxy", *Appl. Phys. Lett.* **64** (15), pp. 2001-2003 (11 April 1994).
39. H.Q. Hou and C.W. Tu, "Optical property of InAsP/InP strained quantum wells grown on InP (111)B and (100) substrates" *J. Appl. Phys.* , **75** (9), PP. 4673-4679, (1 May 1994).
40. C.W. Tu and H.Q. Hou, "InAsP/InP strained quantum wells grown by gas-source molecular beam epiaxy on InP (100) and (111)B substrates", *SPIE Proc.* **2140**, pp. 150-157, (1994).
41. C.W. Tu, T.P. Chin, J.C.P. Chang, K.L. Kavanagh, and N. Ostuka, "InGaAs/InP and InAsP/InP quantum wells on GaAs(100) with graded InGaAs or InGaP buffer layers grown by gas-source molecular beam epitaxy", *Proc. Sixth International Conference on Indium Phosphide and Related Materials*, pp. 543-546 (Santa Barbara, CA 27-31 March 1994). New York, NY, IEEE, 1994.
42. C.W. Tu and B.W. Liang, "Group V composition control for InGaAsP grown by gas-source molecular beam epitaxy", *Proc. of Electrochemical Society*, May 1994.
43. B.W. Liang and C.W. Tu, "Group-V composition control for InGaAsP grown by gas-source molecular beam epitaxy", *J. Electronic Mater.* **23**, pp. 1251-1254 (November 1994).